

REPORT DOCUMENTATION PAGE

Form Approved
OMB No. 0704-0188

Public reporting burden for this collection of information is estimated to average 1 hour per response, including the time for reviewing instructions, searching existing data sources, gathering and maintaining the data needed, and completing and reviewing the collection of information. Send comments regarding this burden estimate or any other aspect of this collection of information, including suggestions for reducing this burden, to Washington Headquarters Services, Directorate for Information Operations and Reports, 1215 Jefferson Davis Highway, Suite 1204, Arlington, VA 22202-4302, and to the Office of Management and Budget, Paperwork Reduction Project (0704-0188), Washington, DC 20503.

1. AGENCY USE ONLY (Leave blank)

2. REPORT DATE

Mar 95

3. REPORT TYPE AND DATES COVERED

4. TITLE AND SUBTITLE

The effects of the thermal Boundary Condition & Turbulence on Heat Transfer from a cylinder, Flat Plate, & Turbine Blade using the Transient Shroud & Heated-coating Techniques

5. FUNDING NUMBERS

6. AUTHOR(S)

Robert J. Butler

7. PERFORMING ORGANIZATION NAME(S) AND ADDRESS(ES)

AFIT Students Attending:

Univ of California

8. PERFORMING ORGANIZATION
REPORT NUMBER

AFIT/CI/CIA

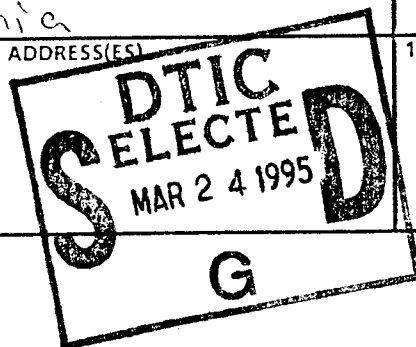
95-001D

9. SPONSORING/MONITORING AGENCY NAME(S) AND ADDRESS(ES)

DEPARTMENT OF THE AIR FORCE
AFIT/CI
2950 P STREET, BDLG 125
WRIGHT-PATTERSON AFB OH 45433-7765

10. SPONSORING/MONITORING
AGENCY REPORT NUMBER

11. SUPPLEMENTARY NOTES



12a. DISTRIBUTION/AVAILABILITY STATEMENT

Approved for Public Release IAW AFR 190-1
Distribution Unlimited
BRIAN D. GAUTHIER, MSgt, USAF
Chief Administration

12b. DISTRIBUTION CODE

Accession For

NTIS CRA&I
DTIC TAB

Unannounced

Justification

By

Distribution /

Availability Codes

Dist	Avail and/or Special
------	-------------------------

A-1

13. ABSTRACT (Maximum 200 words)

19950322 145

14. SUBJECT TERMS

15. NUMBER OF PAGES

271

16. PRICE CODE

17. SECURITY CLASSIFICATION
OF REPORT18. SECURITY CLASSIFICATION
OF THIS PAGE19. SECURITY CLASSIFICATION
OF ABSTRACT

20. LIMITATION OF ABSTRACT

99-001D

**The Effects of the Thermal Boundary Condition and Turbulence
on Heat Transfer from a Cylinder, Flat Plate, and Turbine Blade
using the Transient Shroud and Heated-Coating Techniques**

By

ROBERT JOHN BUTLER

B.S. (Embry-Riddle University) 1985
M.S. (University of Tennessee) 1989

DISSERTATION

Submitted in partial satisfaction of the requirements for the degree of

DOCTOR OF PHILOSOPHY

in

MECHANICAL ENGINEERING

in the

GRADUATE DIVISION

of the

UNIVERSITY OF CALIFORNIA

DAVIS

Approved:

James W. Baughn
Robert L. Capone
Bruce R. Johnson

Committee in Charge

1995

ACKNOWLEDGMENTS

I would like to thank the many individuals who have helped me throughout the writing of this dissertation. The guidance and energetic inspiration provided by Professor James W. Baughn helped make this intimidating once in a lifetime goal manageable. I am truly grateful that he insisted we visit U. C. Davis before making a decision on a graduate program. I would also like to thank Professor Bruce R. White and Professor Vincent R. Capece for their insightful advice and their time intensive review of this research.

Special thanks to Mr. Don Barnum and Mr. Dave Hook from the student machine shop, and Mr. Leo Palaima and Mr. Jim Mehlschau from the engineering shop. Their help in the design and construction of the experimental equipment was invaluable. The machine shop facilities at UC Davis are a truly great asset, but unfortunately they usually go unnoticed. In addition, I would like to thank the group in Electronic General Services for their help keeping all of the equipment operational.

I would also like to thank Greg Cho, Farshid Hashemi, Masood Mesbah, Kapila Perera, and Jon Roby for their help in the lab and their gracious sharing of equipment.

Most importantly, I wish to express my sincere love and gratitude to my wife Leigh. She unselfishly put her career and other desires aside during this program. Thanks.

ABSTRACT

A new technique to measure local heat transfer is developed, it and other methods are used to study the effects of the thermal boundary condition on local heat transfer and turbulence level effects on turbine blade heat transfer. The new technique is called the shroud technique and is a variation on the transient method. It is designed for use on arbitrarily shaped models in a wind tunnel. The shroud acts as a protective covering during in-situ heating of the model. A transient is produced by sudden removal of the shroud. Measurements on a cylinder in cross-flow are used as one method for validation of this technique. These measurements showed that the shroud technique produced good results except in the wake region where the duration of the flow development sometimes created problems. The shroud technique and a gold-film heated-coating method are both used for measurements on a flat plate with a laminar boundary layer to investigate the effect of thermal boundary conditions. The results are compared to numerical solutions, done as part of this study, for uniform temperature, uniform heat flux, and transient thermal boundary conditions. The experimental results agreed well with theory with the uniform heat flux producing 36% higher heat transfer rates than those for uniform temperature. The transient results were highly dependent on the nondimensional temperature used, producing heat transfer rates as low as the uniform temperature or higher than the uniform heat flux boundary conditions. Finally, the gold-film heated-coating method is used to investigate the effect of turbulence on turbine blade heat transfer at low Reynolds numbers (67,500 to 144,000) in a linear

cascade. For low turbulence levels (1%) the pressure side of the blade exhibited streaks of varying heat transfer possibly associated with Gortler vortices. With grid turbulence (10%) the streaks disappeared on the pressure side and the heat transfer increased to turbulent levels. Grid turbulence also increased the heat transfer on the leading edge and suction surface, while advancing the location of boundary layer transition. These cascade results compare favorably to those that have been reported for a rotating rig.

TABLE OF CONTENTS

ACKNOWLEDGMENTS	ii
ABSTRACT	iii
NOMENCLATURE	vii
LIST OF FIGURES	xi
LIST OF TABLES	xiv
CHAPTER 1 INTRODUCTION	1
CHAPTER 2 THE SHROUD TECHNIQUE	4
2.1 Background	4
2.2 Experimental Apparatus	6
2.3 Data Reduction	12
2.4 Uncertainty Analysis	14
CHAPTER 3 GOLD-FILM HEATED-COATING METHOD	17
3.1 Background	17
3.2 Experimental Apparatus	18
3.3 Data Reduction	22
3.4 Uncertainty Analysis	26
CHAPTER 4 CYLINDER IN CROSS-FLOW	29
4.1 Background	29
4.2 Results for the Shroud Technique	32
4.3 Discussion	34
CHAPTER 5 LAMINAR FLOW OVER A FLAT PLATE	48
5.1 Background	48
5.2 Numerical Solutions	55
5.3 Results for the Shroud Technique	68
5.4 Results for the Gold-Film Heated-Coating Method	73
5.5 Comparison, Correlation and Discussion	77

CHAPTER 6 TURBINE BLADE IN A LINEAR CASCADE	84
6.1 Background	84
6.2 Linear Cascade Apparatus	88
6.3 Aerodynamic Results	97
6.4 Results for the Gold-Film Heated-Coating Method	104
6.5 Extreme Grid Turbulence	116
6.6 Comparison of Cascade and Rotating Data	121
6.7 Comparison with USAF Academy Results	126
6.8 Discussion	135
CHAPTER 7 CONCLUSIONS AND RECOMMENDATIONS	138
REFERENCES	145
APPENDICES	156
Appendix A Shroud Heater and Control Program	156
Appendix B Thermocouple Calibration	163
Appendix C Liquid Crystal Calibration	167
Appendix D Shroud Technique Data Reduction	175
Appendix E Gold-Film Heated-Coating Data Reduction	179
Appendix F Model Wall Thickness Sensitivity	183
Appendix G Model Size and Thermal Property Determination	192
Appendix H Liquid Crystal and Paint Thickness Sensitivity	197
Appendix I Hot-Wire Calibration and Measurement	207
Appendix J Adiabatic Wall Temperature	219
Appendix K Inversion of the $\text{erfc}(\gamma)$ using Quattro Pro	221
Appendix L Flat Plate Computational Fluid Dynamics Codes	225
Appendix M Turbine Blade Geometry	241
Appendix N Cylinder in Cross-flow Data	244
Appendix O Flat Plate Data	253
Appendix P Turbine Blade Data	260

NOMENCLATURE

English Symbols

B_x	airfoil axial chord
C_f	coefficient of friction
C_p	specific heat for a constant pressure process
D	diameter
e	electric voltage
$\operatorname{erfc}()$	complementary error function
g	acceleration due to gravity
h	local heat transfer coefficient
i	electric current
k	thermal conductivity
l	length of gold sheet
L	thickness of wood substrate
Nu	Nusselt number (hD/k or hx/k)
p	pitch distance between turbine blades
P	pressure
Pr	Prandtl number
PRT	platinum resistance thermometer
q''	heat transfer flux
r	recovery factor

R	resistance or specific gas constant
R"	resistance per square
Re	Reynolds number based on inlet conditions ($\rho VD/\mu$ or $\rho Vx/\mu$ or $\rho VB_x/\mu$)
s	surface arc length
St	Stanton number ($h/\rho C_p V = Nu/RePr$)
t	time
T	temperature
T*	nondimensional temperature
T/C	thermocouple
Tu	turbulence intensity
u	velocity component in x-direction
v	velocity component in the y-direction
V	velocity
w	width of gold film
x	distance measured in the x-direction
y	distance measured in the y-direction

Greek Symbols

α	thermal diffusivity ($k/\rho C_p$)
β	relative cascade flow angle measured relative to the y-axis
γ	argument for 1-D semi-infinite conduction equation [$h\sqrt{t/(\rho C_p k)}$]
Δh	differential manometer height

Δt	time difference (step size)
ΔT	temperature difference
Δx	distance between nodes in the x-direction
Δy	distance between nodes in the y-direction
δ	analog-to-digital quantization error
δx	experimental uncertainty in the parameter x
ϵ	surface emissivity
μ	absolute viscosity
ν	kinematic viscosity
ρ	density
σ	Stefan-Boltzman constant

Subscripts

aw	adiabatic wall
c	convective
D	diameter
f	fluid
i	integer index for nodes in the x-direction
j	integer index for nodes in the y-direction
L	conduction losses
LC	liquid crystal
m	measured

mod1 model #1
mod2 model #2
oil manometer oil
p constant pressure process
r radiation
ref reference
s surface
w wood
x in the x or axial direction
1 cascade inlet
2 cascade exit
 ∞ free-stream conditions

Superscripts

n integer time-step index
* nondimensional

LIST OF FIGURES

Figure 2.2.1 Heating apparatus and control system	7
Figure 2.2.2 Heating shroud extraction	9
Figure 2.2.3 Heating shroud in the wind tunnel	10
Figure 2.2.4 Flat plate model after shroud removal	11
Figure 3.2.1 Gold-film heated-coating model surface	20
Figure 3.2.2 Gold-film flat plate model and associated equipment	21
Figure 3.2.3 Liquid crystal colors on the turbine blade model	23
Figure 4.2.1 Local heat transfer around the cylinder	33
Figure 4.3.1 Comparison of heat transfer around the cylinder	35
Figure 4.3.2 Spectrum analyzer data ($Re=34,000$)	40
Figure 4.3.3 Spectrum analyzer data ($Re=74,000$)	41
Figure 4.3.4 Spectrum analyzer data ($Re=106,000$)	42
Figure 4.3.5 Strouhal number for cylinder with and without end cavities	43
Figure 5.1.1 Effect of thermal boundary condition on wall temperature	51
Figure 5.2.1 Computed vs exact coefficient of friction on a flat plate	59
Figure 5.2.2 Computed vs exact local Nusselt number on a flat plate	60
Figure 5.2.3 Uniform temperature vs. constant heat flux boundary conditions	62
Figure 5.2.4 Wall temperature for a constant heat flux boundary condition	63
Figure 5.2.5 Nondimensional temperature effect on transient heat transfer	66

Figure 5.2.6 Variation of local heat transfer coefficient over time	67
Figure 5.3.1 Effect of the transient nondimensional temperature	70
Figure 5.3.2 Effect of Reynolds number (Transient $T^*=.8$)	72
Figure 5.4.1 Laminar flat plate heat transfer (uniform heat flux)	75
Figure 5.4.2 Effect of Reynolds number (uniform heat flux)	76
Figure 5.5.1 Numerical solutions compared to experimental ($T^*=.9$ and .7)	78
Figure 5.5.2 Numerical solutions compared to experimental ($T^*=.8$ and .6)	79
Figure 5.5.3 Transient numerical results corrected by correlation	81
Figure 5.5.4 Transient experimental results corrected by correlation	82
Figure 6.2.1 Wind tunnel with attached cascade section	90
Figure 6.2.2 Linear cascade geometry	91
Figure 6.2.3 Turbine blade geometry	94
Figure 6.2.4 Heat transfer turbine blade in the cascade	95
Figure 6.2.5 Turbulence grid in the cascade tunnel	96
Figure 6.3.1 Free-stream velocity	98
Figure 6.3.2 Free-stream turbulence	100
Figure 6.3.3 Wake velocity	102
Figure 6.3.4 Wake turbulence	103
Figure 6.3.5 Wake flow angle	105
Figure 6.4.1 Effect of grid turbulence ($Re=67,500$)	107
Figure 6.4.2 Spanwise heat transfer variation on the pressure surface	110
Figure 6.4.3 Effect of grid turbulence ($Re=134,000$)	112

Figure 6.4.4 Effect of Reynolds number (without grid)	114
Figure 6.4.5 Effect of Reynolds number (with grid)	115
Figure 6.5.1 Free-stream velocity and turbulence for close grid	117
Figure 6.5.2 Effect of very high turbulence (Re=67,500)	119
Figure 6.5.3 Effect of very high turbulence (Re=134,000)	120
Figure 6.6.1 Grid effect on Dring's rotating tests	123
Figure 6.6.2 Comparison of cascade and rotating rig results	125
Figure 6.7.1 Effect of Turbulence on USAFA Turbine Cascade	128
Figure 6.7.2 Comparison of UC/Davis and USAFA results (no grid)	130
Figure 6.7.3 Comparison of UC/Davis and USAFA results (with grid)	132
Figure B.1 Thermocouple calibration	165
Figure C.1 Liquid crystal calibration rig (from Yan)	170
Figure F.1 Effect of wall thickness on transition time	187
Figure F.2 Effect of wall thickness on calculated heat transfer coefficient	188
Figure G.1 Cylinder diameter analysis	195
Figure H.1 Effect of paint/liquid crystal thickness on the heat transfer	203
Figure I.1 Hot-film calibration (cross-flow)	209
Figure I.2 Hot-film calibration (endflow)	211
Figure L.1 Comparison of two methods for updating the wall temperature	234

LIST OF TABLES

Table 2.4.1 Uncertainty Analysis	16
Table 3.4.1 Uncertainty Analysis for Flat Plate	27
Table 3.4.2 Uncertainty Analysis for Turbine Blade	28
Table 4.3.1 Experimental Specifications	37
Table 6.2.1 Cascade Geometry	92
Table 6.6.1 Present cascade and UTRC test specifications	124
Table 6.7.1 Cascade tunnel comparison	127
Table 6.7.2 Flow angle effect on suction side heat transfer	134
Table B.1 Thermocouple calibration	164
Table C.1 Intrinsic Thermocouple Calibration	172
Table C.2 Liquid crystal calibration	173
Table D.1 Transient method data reduction spreadsheet	176
Table E.1 Gold-film heated-coating data reduction spreadsheet	180
Table F.1 Wall Thickness Sensitivity	186
Table G.1 Cylinder diameter analysis	194
Table H.1 Thermal properties for various materials	198
Table H.2 Paint/Liquid Crystal Thickness Sensitivity	201
Table I.1 Hot-film calibration (cross-flow)	208
Table I.2 Hot-film calibration (endflow)	210
Table K.1 Iterative inversion of the complementary error function	223
Table M.1 Turbine Blade Geometry	242

CHAPTER 1 INTRODUCTION

The objectives of the present investigation are four-fold. First, a new technique, called the shroud technique, is developed to measure local heat transfer. Second, local heat transfer measurements on a cylinder in cross-flow are used as one method for validation of this shroud technique. Third, the shroud technique and a gold-film heated-coating method are both used for measurements on a flat plate with a laminar boundary layer to investigate the effect of thermal boundary conditions. Numerical solutions for uniform temperature, uniform heat flux, and transient thermal boundary conditions are compared to the experimental results. Finally, the gold-film heated-coating method is used to investigate the effect of turbulence on the heat transfer distribution on a turbine blade in a linear cascade.

The new shroud technique is presented and explained in Chapter 2. The new technique is a variation on the transient method. It is designed for use on arbitrarily shaped models in a wind tunnel. The shroud acts as a protective covering during in-situ heating of the model. A computer controlled heater and fan are used to preheat the model to a uniform temperature, while the model is installed in the wind tunnel. The transient is produced by sudden removal of the shroud. Liquid crystals are used on the model to measure surface temperature. The theory of the transient method, background information, data reduction schemes, and a uncertainty analysis are also presented.

The gold-film heated-coating method is presented and explained in Chapter 3. This method uses a gold-film on the model surface to produce a uniform heat transfer flux (through electrical resistance heating) from the test surface. Liquid crystals are used on the model to measure surface temperature. The theory of the heated-coating method, background information, data reduction schemes, and a uncertainty analysis are also presented.

In Chapter 4, the local heat transfer measurement results for a cylinder in cross-flow using the shroud technique are presented. The cylinder in cross-flow is used as a test case to validate the shroud technique. The cylinder in cross-flow was chosen because it is well studied and it provides various types of flow conditions on one geometry (laminar, separated, and periodic shedding).

In Chapter 5, an investigation of the effect of the thermal boundary condition using laminar flat plate flow is presented. Laminar flow over a flat plate is used as a simple test case, but it is useful because it provides insight into more complicated flows. This chapter utilizes analytical, numerical, and experimental results in order to compare the uniform heat flux and transient boundary conditions. Three numerical codes are used to solve for the laminar flow over a flat plate with different thermal boundary conditions. Uniform wall temperature, constant heat flux, and unsteady wall temperature (transient) boundary conditions are used. Experimental tests are performed using the shroud technique and the gold-film heated-coating method. This allowed for a direct comparison of the two different techniques. Finally, the analytical, numerical, and

experimental solutions are all compared to fully understand the different experimental methods and their thermal boundary conditions.

This study is culminated in Chapter 5. In this chapter, the results for local heat transfer measurements on a turbine blade in a linear cascade are reported. The gold-film heated coating method is used to make these measurements. The effect of free-stream turbulence intensity ranging from the clean tunnel condition (1%) up to very high grid turbulence (25%) is presented. The present cascade results are also compared to data collected on the same turbine blade shape in an Air Force Academy cascade tunnel and a rotating facility at the United Technology Research Center.

CHAPTER 2 THE SHROUD TECHNIQUE

This chapter explains the shroud technique for measuring local heat transfer. The shroud technique is a variation on the transient method. Background information about transient methods and other methods in general is presented. The apparatus for the new shroud technique is explained. This new method uses liquid crystals to measure the surface temperature and a computer controlled heater and shroud to preheat and produce the required transient. The theory used in the data reduction and a uncertainty analysis is also presented.

2.1 Background

In general, any transient method determines the heat transfer rate by measuring the unsteady temperature response of a surface. The surface response can be produced by either exposing the surface to a fluid at a higher or lower temperature than the starting temperature of the surface itself. The end result is either the surface increasing or decreasing in temperature over time. By comparing the temperature transient to an assumed mathematical model, the heat transfer coefficient can be inferred.

Transient methods have a very long history. They were used extensively in shock tunnels where the short duration tests required transient techniques. In these tests, resistance thermometers were used on ceramic substrates (Schultz and Jones, 1973). Other transient methods used different techniques to measure the surface temperature.

Some earlier measurements used thermal-paints and they are reviewed in Schultz and Jones (1973) and Jones (1977). Clifford et al. (1983) used phase change paints on acrylic models to study heat transfer within gas turbine blade cooling passages and Metzger and Larson (1986) used melting point coatings to study heat transfer in rectangular ducts with turns. More recently Ireland and Jones (1985,1986), Jones and Hippensteele (1987), Metzger et al. (1991), and Baughn and Yan (1991) have used liquid crystals for the surface temperature measurement. Liquid crystals are very suitable to measure the surface temperature transient, since their response is repeatable and their colors can be easily recorded with a video system. More details about the early history of transient methods is available in Ireland and Jones (1985, 1986) and Ireland (1987).

For transient methods there are a variety of techniques used to accomplish the fluid temperature change relative to the surface. For example, Clifford et al. (1983), Ireland and Jones (1985, 1986), Metzger and Larson (1986) and Metzger et al. (1991) all used an ambient temperature sample and then suddenly raised the temperature of their flow with switching valves. All of these methods used a hot fluid and a room temperature model. This creates heat transfer to the upstream portion of the wind tunnel and produces somewhat unknown free-stream thermal conditions. O'Brien et al. (1986) used a preheated cylinder and inserted it into place across a channel with an ambient temperature flow field. Jones and Hippensteele (1987) preheated the wall of their wind tunnel and then initiated the flow using a diverter door. They also used multiple liquid crystal coatings to reduce the dependence of the results on the initial wall temperature

distribution. Baughn and Yan (1991) produced the transient with an insertion technique by suddenly connecting a preheated section of duct onto a fully developed duct to study enhanced heat transfer.

In the technique of the present study, the model is preheated in a removable shroud "in-situ" to a uniform temperature. It is then suddenly exposed to ambient temperature wind tunnel air by removing the heating shroud. This technique has the flexibility of allowing the model to have any shape.

2.2 Experimental Apparatus

Figure 2.2.1 is a diagram of the heating apparatus. The heating apparatus has two components, the heating unit and the heating shroud. Both parts are constructed from 5 inch PVC pipe, with 4 inch PVC pipe mounted in the middle to form concentric cylinders. The heating unit and shroud fit together to form one long set of concentric cylinders. The heating unit's center cylinder contains a fan and the top of the unit holds a 100 Watt light bulb. A data acquisition and control program was written to drive the light bulb and fan through an A/D card. Details and a listing of the data acquisition and control program are in Appendix A. Low voltage DC signals are switched to 110 AC through solid state relays. The control program measures model temperatures using calibrated special limit-of-error Type K thermocouples. The desired initial model temperature is entered through the computer and the control program turns the heater on and off as required to hold the model at a uniform temperature.

Figure 2.2.2 is a diagram showing the heating apparatus installed in the wind tunnel with the test model inside. Figure 2.2.3 is a photograph showing the shroud in

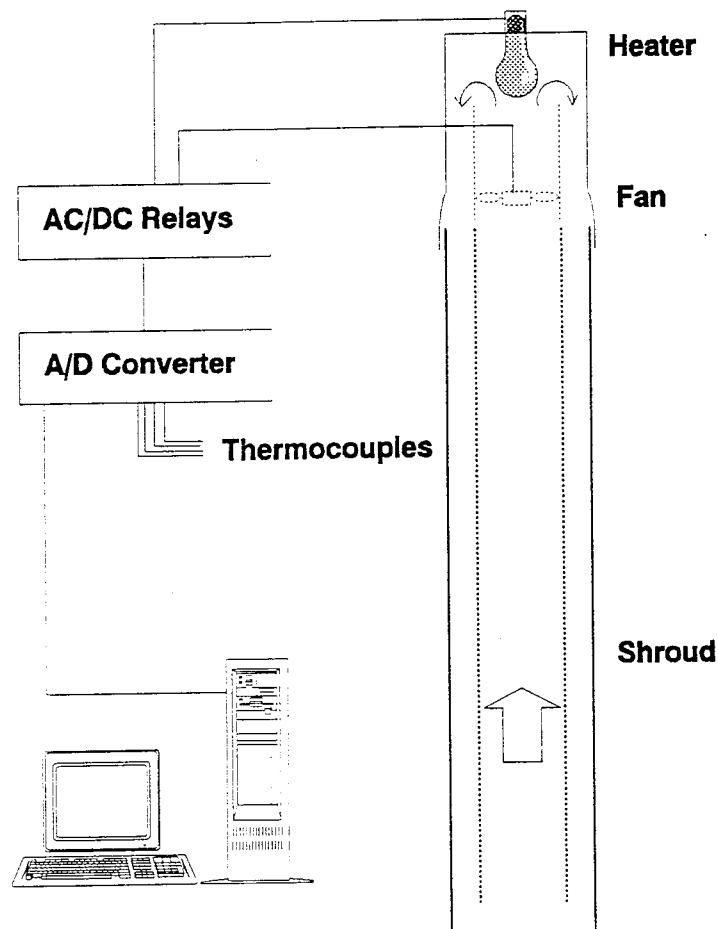


Figure 2.2.1 Heating apparatus and control system

place inside the tunnel. For this study, two models were used, the first was a 3 inch diameter plexiglas cylinder and the second was a 4 inch flat plexiglas plate. The models were air brushed with black paint and a thin layer of liquid crystals. The model is heated for 2-3 hours in the heating apparatus until it reaches a uniform temperature. With the video system recording, the heating shroud is rapidly extracted from the bottom of the wind tunnel and the model is exposed to the ambient temperature wind tunnel air. Figure 2.2.4 is a photograph showing the flat plate model after the shroud was removed. The wind tunnel test section is 24 inches high and 40 inches wide. The length of the model is 24 inches and it is mounted vertically in the tunnel. For the cylinder, the resulting blockage ratio is 7.5% and the aspect ratio is 8.0. The wind tunnel is open loop and is driven by a 50 HP constant speed motor operating a centrifugal compressor. A 16 to 1 stilling chamber with screens is used upstream of the wind tunnel nozzle to reduce free-stream turbulence. Adjustable vanes on the compressor allow for a variable speed from 6.5 to 21 m/s. The free-stream turbulence was measured with a hot-wire to be approximately 1.0% (see Appendix I).

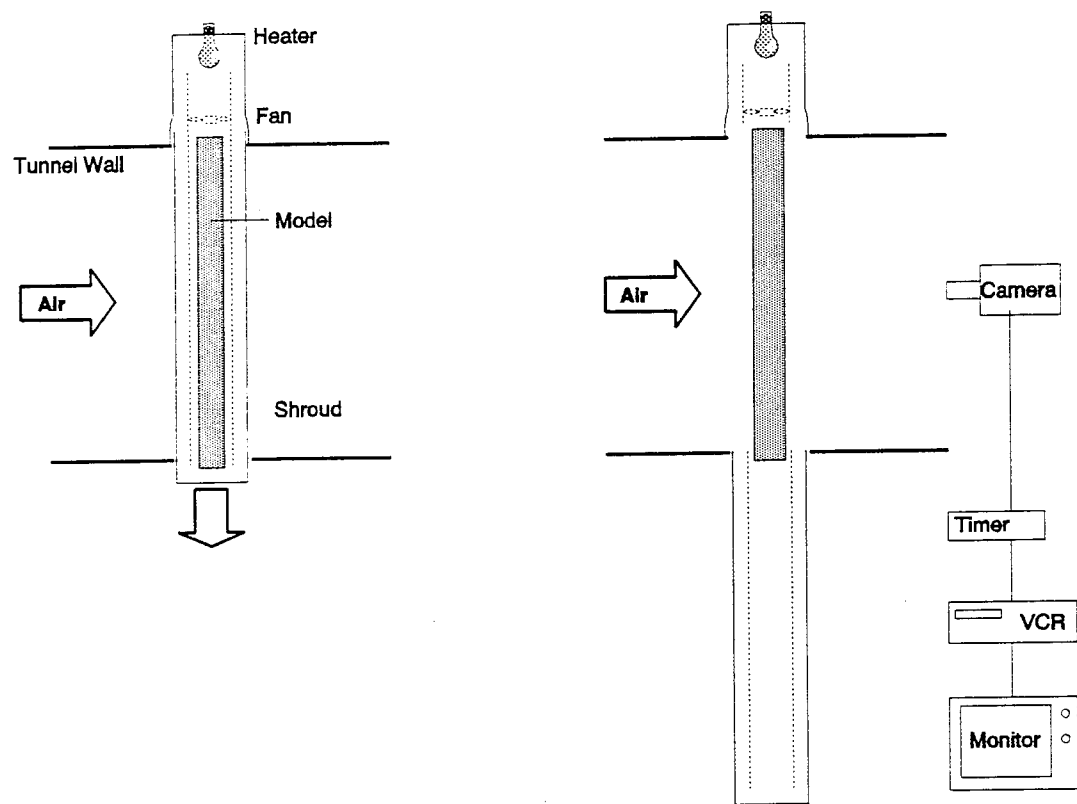


Figure 2.2.2 Heating shroud extraction

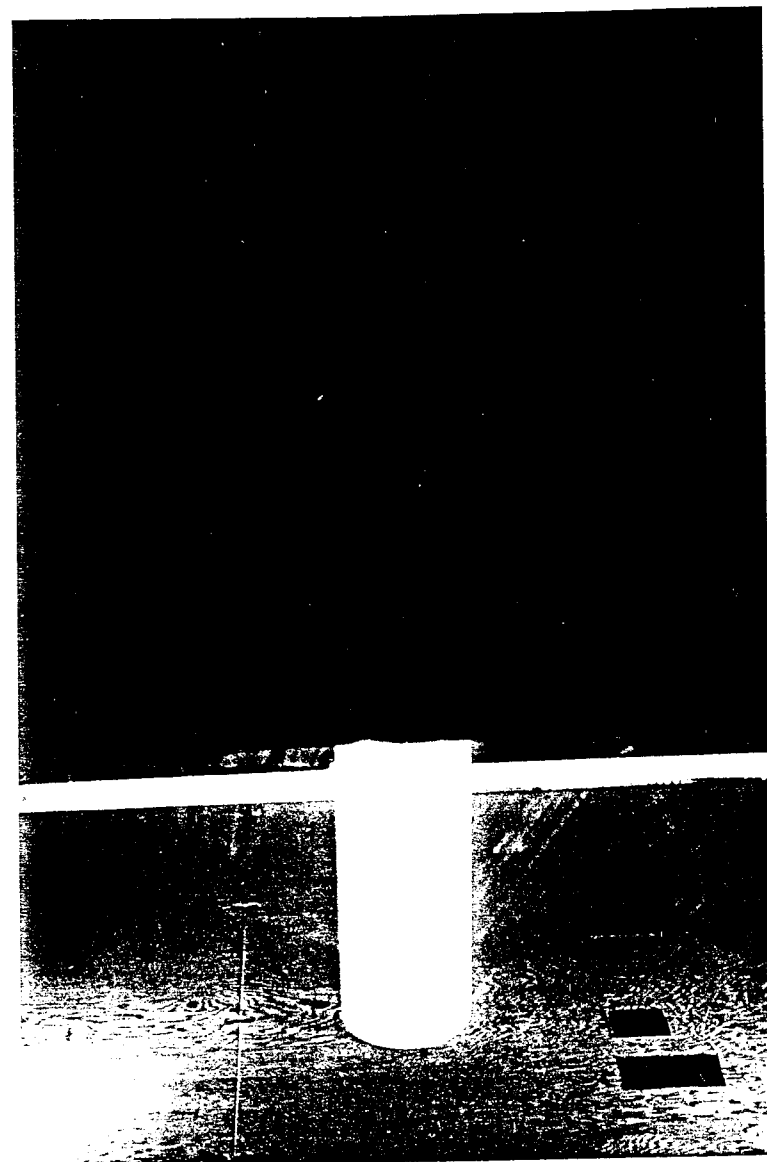


Figure 2.2.3 Heating shroud in the wind tunnel

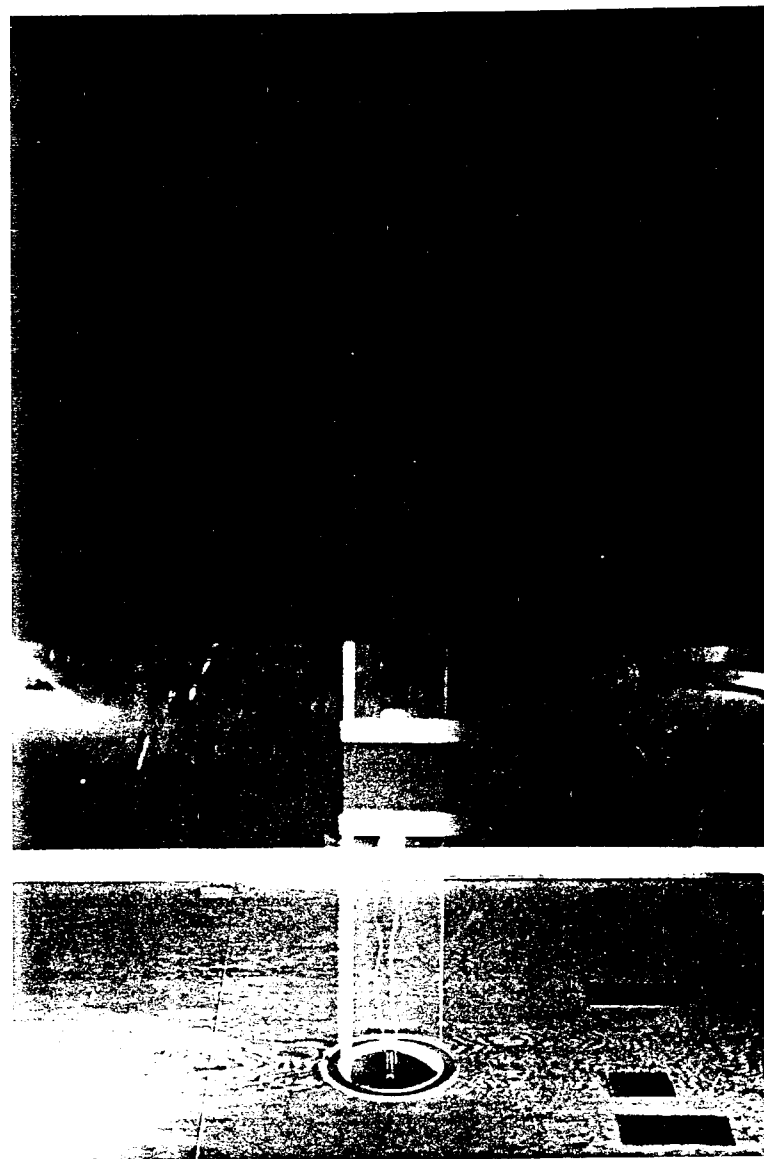


Figure 2.2.4 Flat plate model after shroud removal

2.3 Data Reduction

Data reduction for the shroud technique involves two steps. First, the video record is used to measure the temperature transient on the surface of a model. Secondly, a mathematical model is used to infer a heat transfer coefficient from the measured temperature transient.

A typical video record shows the model locally changing color depending on its surface temperature. A timer is also recorded into the video record in order to measure the starting time and the elapsed time until color transition for each location. Because the model aspect ratio is high, the data is two-dimensional and the video shows vertical isothermal color lines which run parallel to the vertical axis of the model. The liquid crystal color band clearly shows green, yellow, and red. As any given location cools, the surface will first turn green, followed by yellow and red. The time is measured when each location is between the colors yellow and red, which is called the color transition time.

Two liquid crystal calibrations were performed using two different techniques. First a method developed by Yan (1993) was used. This calibration system produced a linear temperature gradient on an aluminum bar. The bar was electrically heated on one end and cooled with a constant temperature bath on the other. This established the liquid crystal color play on the bar and a camera showed it on a video monitor. Four thermocouples established the temperature gradient and the location of the yellow color band was measured from the video monitor. For the first batch of liquid crystals, the center of the yellow color band was measured to be $35.73^\circ \pm 13^\circ \text{ C}$ using this method.

In addition, a simple method was developed using a thin Aluminum bar with an intrinsic special limit-of-error Type K thermocouple mounted to it. The bar was painted black and sprayed with liquid crystals. The entire bar/intrinsic thermocouple was calibrated against a platinum resistance thermometer (PRT). The bar was placed inside a plexiglas duct in order to reduce any conduction or radiation errors, but this allowed the bar to be viewed from the outside. The duct/bar was heated in order to produce the desired colors over the intrinsic thermocouple. The center of the yellow color band was measured to be $35.75^\circ \pm 10^\circ \text{ C}$ using this method. The transition temperature between yellow-red is used in the data reduction and was measured to be $35.68^\circ \pm 10^\circ \text{ C}$. More details about the calibration of the liquid crystals is available in Appendix C.

A mathematical model of the temperature transient is required to determine a heat transfer coefficient. A one-dimensional approximation is often used since the surface temperature response is limited to a thin layer near the surface and lateral conduction can be shown to be small (Dunne, 1983). Therefore, one-dimensional conduction into a semi-infinite medium with a convective boundary condition is assumed. The mathematical solution to this problem is available in Roby (1993). The result is well known and is:

$$T^* = \frac{T_{LC} - T_\infty}{T_o - T_\infty} = e^{-\gamma^2} \operatorname{erfc}(\gamma)$$

Where the liquid crystal transition temperature (T_{LC}), free-stream air temperature (T_∞), and the initial temperature (T_o) are all known. Using the video record, the time (t) for each location's local surface temperature to cool to the yellow-red liquid crystal

transition temperature is measured. The nondimensional temperature (T^*) is a very important parameter when using the transient method and its selection will directly effect the results. Its selection is only dependent on the starting, liquid crystal, and free-stream temperatures and is fixed for any given test. From this equation γ is determined (see Appendix K) and it is used in the following equation to calculate the local heat transfer coefficient.

$$h = \frac{\gamma \sqrt{\rho C_p k}}{\sqrt{t}}$$

Where the thermal properties of the Plexiglas model are known. This is a heat transfer coefficient which is a combination of both convection and radiation from the surface. The radiation is subtracted from the combined heat transfer coefficient in order to determine the convective component. The radiation component is determined using:

$$h_r = \epsilon \sigma (T_{LC} + T_\infty) (T_{LC}^2 + T_\infty^2)$$

The convective heat transfer coefficient is then used to calculate the Nusselt number.

2.4 Uncertainty Analysis

An uncertainty analysis (using standard uncertainty methods and 95% confidence) is summarized in Table 2.4.1. Every measured or assumed property is included in the estimate. The individual contribution of each measurement to the total uncertainty is given for typical conditions. The total uncertainty is estimated to be approximately 6%. The thermal properties of the model contribute the largest uncertainty in the

measurement. The most recent available properties for extruded plexiglass were used from the *Handbook of Industrial Materials* (1992). Properties from other sources are somewhat scattered, therefore, a large uncertainty is associated with this value. The thickness effect of the paint and liquid crystals is not included in this analysis, but is studied in detail in Appendix H. It was found that their thickness and thermal property variation could produce an error on the order of a couple of percent. We feel this is already covered by the relatively high uncertainty associated with the thermal properties of the plexiglas. Our comparison with previous results would suggest that 6% uncertainty is reasonable and probably conservative since Baughn et al. (1989) found the results were generally within 2% of the gold-film method.

Table 2.4.1 Uncertainty Analysis

Measured Parameter	Typical Value	$\delta X (\pm)$	Nu/ \sqrt{Re} Uncertainty %
P_∞	30.06 in Hg	.1	.08
T_∞	22.7° C	.1	.77
T_o	38.97° C	.1	3.05
Δh	1.16 in oil	.005	.11
D	.076556 m	.000127	.96
T_{LC}	35.85° C	.1	.93
$\sqrt{\rho C_p k}$	575	25	4.57
ϵ	.85	.15	.89
t	2 sec	.03	1.29
			Total=5.92%

CHAPTER 3 GOLD-FILM HEATED-COATING METHOD

This chapter gives the details about the gold-film heated-coating method for measuring local heat transfer. The background about other methods and uniform heat flux methods in general is presented. This method, uses a thin gold-film surface to produce a uniform heat flux and liquid crystals to measure the surface temperature. The theory used for the data reduction and a uncertainty analysis is also presented.

3.1 Background

The heated-coating method has a very long history. The general idea is to measure the local surface temperatures on a model which is producing a uniform heat transfer flux (typically electrical resistance heating) from a heated-coating on the test surface. The local heat transfer coefficient can be calculated by knowing the power into the surface, local surface temperature, heated area, and free-stream temperature. Variations on the uniform heat flux technique involve different ways to measure the surface temperature and different ways to produce the heat flux.

A general overview of the many researchers who have used uniform heat flux methods is included. Early work using this technique used thermocouples in order to measure the local surface temperature. Local heat transfer coefficients were measured for a cylinder in cross-flow by Giedt (1949) who used thermocouples and nichrome ribbon to produce the electrical resistance heat flux. Wilson and Pope (1954) used a similar technique to measure the heat transfer on turbine blade shapes in very early

cascade tunnel testing. Simonich and Bradshaw (1978) used steel shim strips to produce the needed heat flux to measure the effect of free-stream turbulence on turbulent boundary layers. O'Brien et al. (1986) used inconel foil and thermocouples on one of three different cylinder models to compare different heat transfer techniques. Some other more recent techniques have used liquid crystals on the test surface to measure surface temperature. Cooper et al. (1975) used carbon impregnated paper to produce the heat flux and liquid crystals to test a cylinder in cross-flow. A similar technique was used by Hippensteele et al. (1985) to measure the local heat transfer around a turbine blade in a cascade tunnel. Baughn et al. (1989) used a thin polyester surface with vacuum deposited gold and liquid crystals to compare uniform heat flux and transient tests on a pin fin. Endwall heat transfer in a cascade tunnel was investigated by Boyle and Russell (1990) using a thin metallic foil and liquid crystals.

In all cases, the test surface has to be wrapped with some type of heater element in order to produce the uniform heat flux. This requirement limits the application of this technique to flat surfaces or surfaces with curvature in only one direction.

The present research uses a similar gold-film to that of Baughn et al. (1989) and liquid crystals to compare the uniform heat flux, transient, and uniform temperature boundary conditions on a flat plate surface. In addition, the gold-film heated-coating method is applied to a turbine blade in a linear cascade.

3.2 Experimental Apparatus

The gold-film heated-coating method is applied to two different configurations: a flat plate model with a laminar boundary layer and a turbine blade shape in a linear

cascade. In each case, the model surface is constructed in a similar manner, but the model shape is different and is used in a different wind tunnel arrangement.

A diagram of a typical model surface is shown in Figure 3.2.1. Gold film is attached to the substrate (ponderosa pine wood for the flat plate and 2 lb/ft³ polystyrene for the turbine blade) using 3-M spray adhesive. The gold film was provided by Courtaulds Performance Films and is a thin 7-mil polyester sheet with vacuum deposited gold on the surface. The thin layer of gold provides the surface with uniform resistivity. Bus bars are formed using Copper tape attached to each end of the gold film. To ensure good electrical contact a silver based paint is applied between the copper tape and the gold film. The gold film is air brushed with flat black paint, followed by liquid crystals. The flat plate model used Hallcrest R35W1 (red beginning at 35° C and 1° bandwidth) liquid crystals, while the turbine blade used Hallcrest R40W1 (red beginning at 40° C and 1° bandwidth) liquid crystals. A diagram of the flat plate model in the wind tunnel with its associated equipment is shown in Figure 3.2.2. Constant voltage is provided by a DC power supply to the copper bus bars. The voltage across the gold film causes current to flow through the gold, the resistivity of the gold produces uniform Ohmic heating on the surface of the model. Current is measured using an Amperemeter in series with the power supply. The voltage is measured using a voltmeter with separate lead wires to the bus bars (this avoids any voltage drop due to the resistance of the lead wires). The power can be determined by using the voltage and the current, current and resistance, or voltage and resistance. Because the resistance of the gold film changes slightly with temperature, the local value (at the measuring locations temperature) of the gold's resistance should be used.

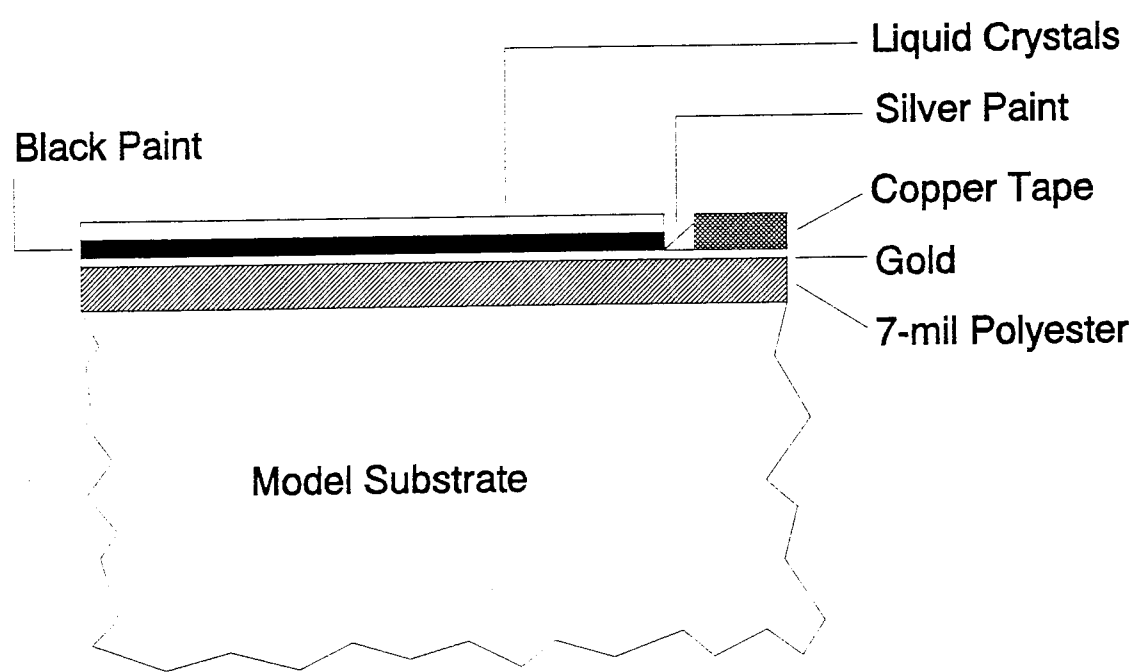


Figure 3.2.1 Gold-film heated-coating model surface

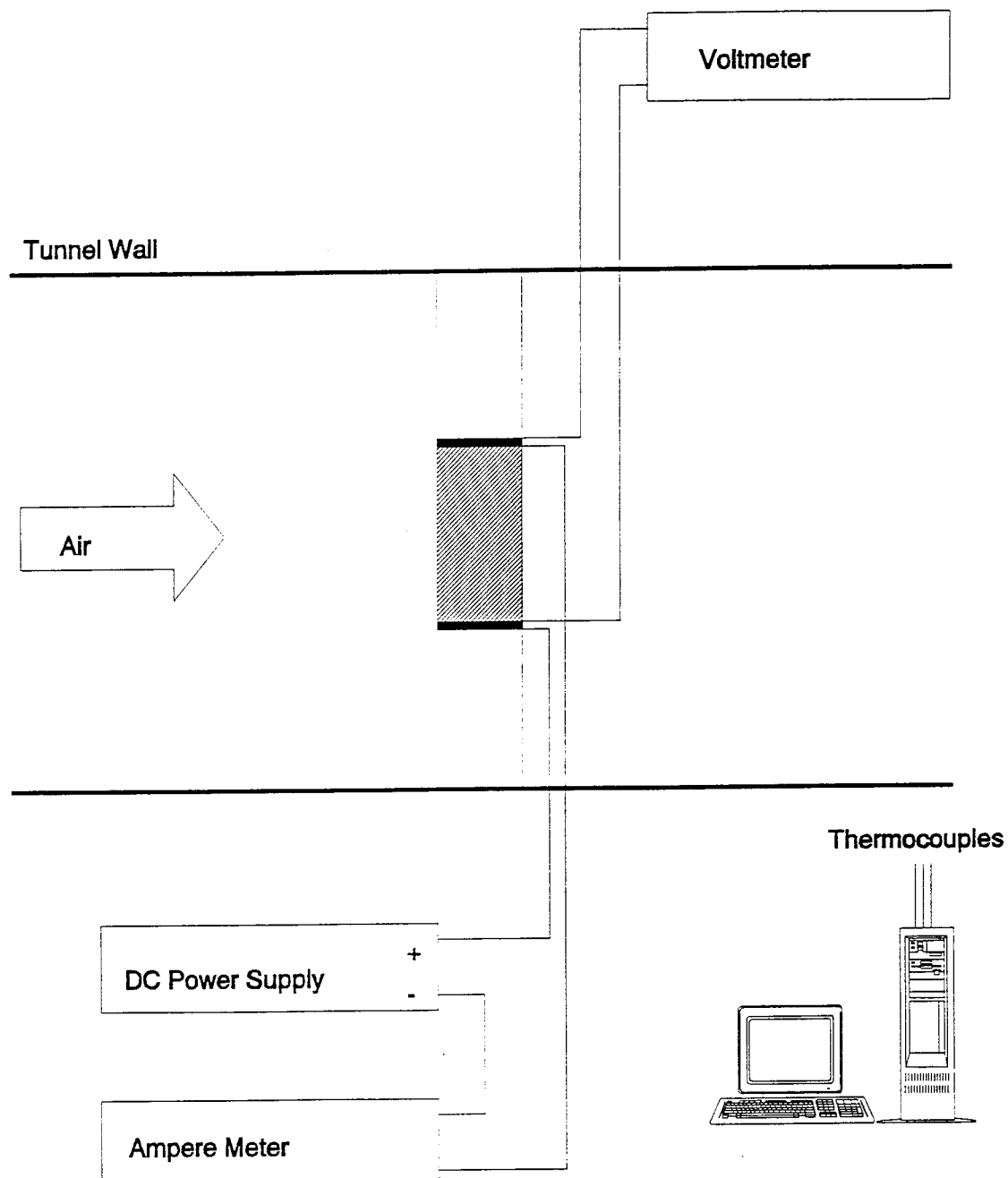


Figure 3.2.2 Gold-film flat plate model and associated equipment

Heat transfer measurements are performed by running the tunnel in a steady state fashion. For a given location on the model, the power is adjusted in order to produce the yellow color band (from the liquid crystals) on the selected region of the model. Figure 3.2.3 shows the liquid crystal colors on the surface of the turbine blade model. The model has very low thermal conductivity, therefore, each point is given adequate time to reach steady state. The free-stream tunnel air temperature is measured using a calibrated 30 gage Type K thermocouple attached to a 16-bit A/D card installed in an IBM AT computer (see Appendix A).

3.3 Data Reduction

The gold-film heated-coating method is very easy to apply with straight forward data reduction. The voltage across the gold film is adjusted to increase or decrease the surface temperatures. The power supply is set in order to produce the color yellow from the liquid crystals at any location from which data is being collected. When steady state is reached, the contours from the yellow color of the liquid crystals map isothermal lines, which represent lines of constant heat transfer coefficient. The local heat transfer coefficient is determined by:

$$h = \frac{q_c''}{(T_{LC} - T_\infty)}$$

The adiabatic wall temperature should be used in this equation as the reference temperature (T_∞). In this case, a thermocouple exposed to the free-stream tunnel air

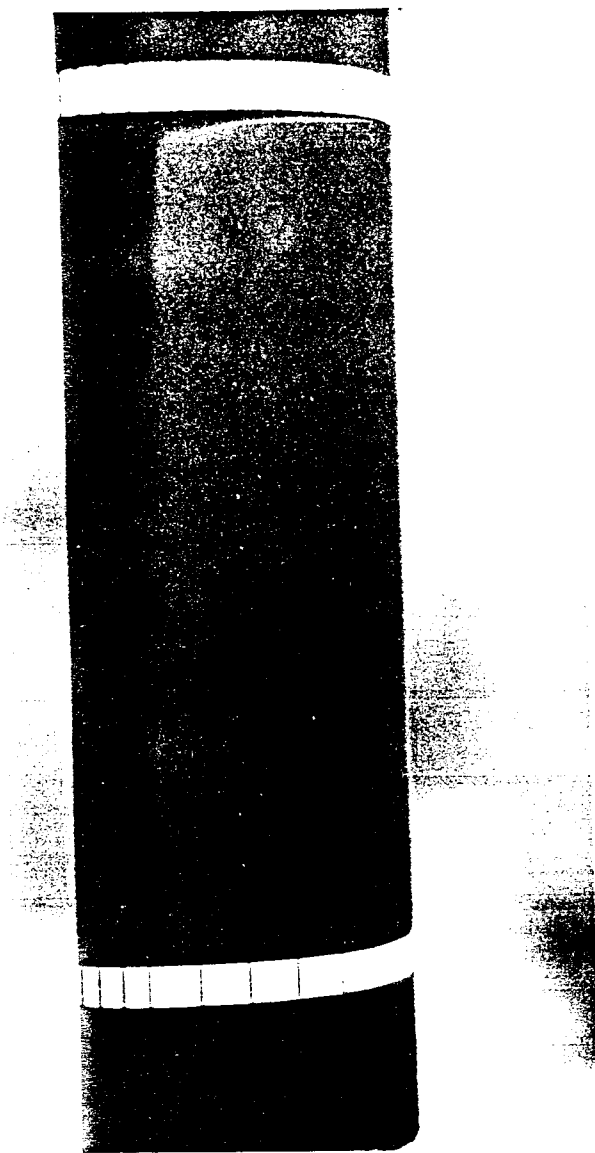


Figure 3.2.3 Liquid crystal colors on the turbine blade model

is used to measure temperature (T_∞). For this very low Mach number flow, the measured temperature is within 0.1° C of the total, static, and adiabatic wall temperatures (this measurement is analyzed in more detail in Appendix J). The heat flux due to convection (q_c'') is determined by subtracting radiation and conduction losses from the local heat flux (q'').

$$q_c'' = q'' - \epsilon \sigma (T_{LC}^4 - T_\infty^4) - q_L''$$

The local heat flux (q'') can be calculated many ways. It is desirable to account for the temperature sensitivity of the gold surface, therefore simply using the product of current and voltage divided by the surface area can yield a small error. Because this method requires data to be collected at a constant temperature associated with the color yellow from the liquid crystals, the local resistance of the gold is fixed at 40° C . Assuming the current is uniform through the model allows for the local heat flux to be calculated using:

$$q'' = \frac{i^2 R_{40}}{lw} = \frac{i^2 (R_{40}'' l/w)}{lw} = \frac{i^2 R_{40}''}{w^2}$$

The current, length and width of the gold are measured. The resistance of the gold at 40° C (R_{40}) is expressed in terms of the resistance per square (R''). The resistance per square is a common way to express the resistance of surface coatings and it is simply the resistance of any size square piece (note: due to scaling of the electrical path, any size square piece will have the same resistance). The actual resistance of a rectangular piece is proportional to its length and inversely proportional to its width. The resistance of the gold sample was measured using a four-wire arrangement at 25° C to be 5.63

Ohms. Baughn et al. (1985) measured the temperature coefficient of the gold coating to be .0011 (1/C°). Therefore, the resistance of the coating would be $R_{40} = 5.63(1+.0011(40-25)) = 5.72$ Ohms at 40° C. Accounting for the dimensions of the gold yields $R''_{40} = R_{40}(w/l) = 2.49$ Ohms/square. The conduction losses (q_L'') can be shown to be negligible for the turbine blade because the model is heated from both sides and is made from polystyrene. The conduction losses can not be ignored on the relatively thin wooden flat plate model, but the losses can be measured fairly accurately. Thermocouple measurements were taken on the opposing side of the flat plate model for each liquid crystal location. This allowed for an estimation of the conduction loss using Fourier's conduction law:

$$q_L'' = -k_w \frac{(T_{LC} - T_w)}{L_w}$$

The liquid crystal temperature (T_{LC}) is determined by using two different calibration techniques. These are the same techniques which were explained in Chapter 2. Though, the flat plate and turbine blade tests used different liquid crystals. The flat plate model used Hallcrest R35W1 (red beginning at 35° C and 1° bandwidth) liquid crystals, while the turbine blade used Hallcrest R40W1 (red beginning at 40° C and 1° bandwidth) liquid crystals. The R35W1 liquid crystals calibration results were given in Chapter 2. The R40W1 liquid crystals were calibrated using Yan's (1993) method and the simplified method with consistent results. The center of the yellow color band was measured to be $40.10^\circ \pm 15^\circ$ C. More detail about the calibration of the liquid crystals is available in Appendix C.

3.4 Uncertainty Analysis

An uncertainty analysis (using standard uncertainty methods and 95% confidence) was performed for the gold-film heated-coating method and applied to the flat plate model and the turbine blade model. The uncertainty of the local heat transfer coefficient is summarized in Table 3.4.1 for the flat plate model and in Table 3.4.2 for the turbine blade model. All of the measured or assumed properties are included in the estimates. For typical conditions, the individual contribution of each measurement to the total uncertainty in local heat transfer coefficient is given. For the flat plate tests, the local resistance of the gold, the thermal conductivity of the wood substrate, and the emissivity of the surface contribute the largest uncertainties in the local heat transfer coefficient. The requirement of a fairly thin flat plate leads to a large conduction correction, which becomes an uncertainty when the thermal conductivity of the wood substrate is estimated. The polystyrene turbine blade which is heated from both sides would not exhibit this uncertainty. The uncertainty for the surface emissivity is very conservative because actual measurements have not been performed, this uncertainty is lower in regions of high heat transfer. The variation of the gold's local resistivity is estimated to be approximately 5%. The flat plate data compares very favorably with theory suggesting that a total uncertainty of 6.7% is reasonable. Without the added uncertainty of the wood substrate, the total uncertainty for the turbine blade measurements is 5.5%. It is believed that this is conservative since the uniformity of the liquid crystal color during tests suggests the gold uniformity is probably better than the 5% estimate.

Table 3.4.1 Uncertainty Analysis for Flat Plate

Measured Parameter	Typical Value	$\delta X (\pm)$	h Uncertainty %
R''	2.49 Ohms/Square	.11	5.0
T_∞	20.25° C	.1	.9
T_{Lc}	35.85° C	.1	.9
L	6.375 in	.005	0
W	3.859 in	.008	1.2
k_w	.13 W/m°C	.02	3.5
ϵ	.85	.15	2.1
i	2.028 A	.005	.7
V	7.946 V	.005	0
			Total=6.7%

Table 3.4.2 Uncertainty Analysis for Turbine Blade

Measured Parameter	Typical Value	$\delta X (\pm)$	h Uncertainty %
R"	2.49 Ohms/Square	.125	5.0
T _x	26.3° C	.15	1.2
T _{LC}	40.1° C	.15	1.2
L	18.375 in	.008	0
W	8.00 in	.008	.2
ε	.85	.15	1.7
i	3.77 A	.005	.3
V	21.56 V	.005	0
			Total=5.5%

CHAPTER 4 CYLINDER IN CROSS-FLOW

In this chapter, the local heat transfer measurement results on a cylinder in cross-flow using the shroud technique are presented. The cylinder in cross-flow is used as a test case to validate the shroud technique. The cylinder in cross-flow is well studied and it provides various types of flow on one geometry (laminar, separated, and periodic shedding).

4.1 Background

Flow around a circular cylinder has been the subject of interest for several hundred years. The oscillating wake from a cylinder sparked very early interest due to its ability to make an elastic cylinder vibrate and produce sound. Leonardo da Vinci recorded drawings of the vortical flow produced by a stream in the wake region of pilings (Blevins, 1990). Today, the cylinder in cross-flow is often used as a simple test case, although the flow around a cylinder is very complex exhibiting many different features: laminar, turbulent, separated, reverse, unsteady, periodic, and asymmetric flows.

Understanding the fluid mechanics around a cylinder is critical to understanding the local heat transfer distribution. Flow approaches the front region of a cylinder and stagnates at the forward most region. The flow accelerates from the stagnation point building a laminar boundary layer. From this point on, and especially in the wake of the cylinder, the flow behavior is very Reynolds number dependent.

When the Reynolds number is less than 300,000 the laminar boundary layer will continue to grow and the wake region can be classified into one of four different types. When the Reynolds number is less than five, the boundary layer in the wake will stay attached and be symmetric in nature. For Reynolds number between 5 and 40, the laminar boundary layer separates and forms symmetric stationary laminar vortices in the wake region of the cylinder. For Reynolds number between 40 and 300, the laminar boundary layer separates near 80° and the vortices become unstable (though still laminar) and alternately shed downstream from the cylinder. For Reynolds number from 300 to 150,000 (called the subcritical range), the vortices are now turbulent, but still alternately shed from the cylinder (Blevins, 1990).

Strouhal (in 1878) determined that the frequency of sound generated by a vibrating wire was proportional to the velocity and inversely proportional to the wire diameter (Blevins, 1990). From this discovery came the Strouhal number:

$$St = \frac{fD}{V}$$

Which is a nondimensional parameter relating the unsteady vortex shedding frequency (f) with the diameter (D) and free-stream velocity (V). The shedding frequency (cycles per second, Hz) is based on the time between vortices shed from one side of the cylinder, therefore every other vortex. The present study is concerned with the subcritical range and over this range the Strouhal number is nearly a constant value of 0.21 (Schlichting, 1968).

For Reynolds numbers between 150,000 and 3,500,000 (called the transitional range), asymmetric regions of the boundary layer stay laminar, while some portions

transition to turbulent. This mixed flow condition produces a disorganized turbulent wake which disrupts the natural vortex shedding. When the Reynolds number is greater than 3,500,000 (called the supercritical range), the laminar boundary layer will transition to turbulent. The turbulent boundary layer allows the separation point to move downstream to roughly 140° on the cylinder and the vortex shedding reestablishes a natural shedding frequency. The vortex shedding is believed to persist up to Reynolds number of infinity. Vortex shedding of the wind around islands have been observed by satellite photos at Reynolds number up to 10^{11} (Blevins, 1990).

There have been numerous experimental investigations of the local heat transfer around a cylinder. Schmidt and Wenner (1943) measured local heat transfer on a uniform wall temperature model by using a heat flux sensor during steady state tests. Similar techniques were used by Achenbach (1975), Kraabel et al. (1982), and O'Brien and VanFossen (1985). The heat flux sensor used in these techniques usually subtends roughly 10° of the model. Meel (1962) tried to improve this by using a very small platinum-film resistance temperature gauge. Steady-state uniform heat flux methods have been used by Giedt (1949) and Baughn et al.(1986).

This portion of the present study used a transient method. The shroud technique uses a model constructed of plexiglas. without the requirement of internal heating and heat flux sensors. The original purpose for testing the cylinder in cross-flow was to validate the new shroud technique. The results were surprising and a lot of new information was learned about both transient methods and the heat transfer to a cylinder in cross-flow.

4.2 Results for the Shroud Technique

The local heat transfer was measured for Reynolds number of 34,000, 74,000, and 110,000. For flow around a cylinder, the local heat transfer is usually normalized using the Frössling (1958) number ($\text{Nu}/\text{Re}^{1/2}$). A plot of the local Frössling number for all three test runs is shown in Figure 4.2.1. The laminar boundary layer region starts at the stagnation point and continues around the cylinder until the boundary layer separates (78° - 86° depending on Reynolds number). In this region, the heat transfer decreases as the boundary layer grows. Boundary layer separation is recognized by the location of minimum heat transfer. The separation point moves forward with increasing Reynolds number from 86° ($\text{Re}=34,000$) to 78° ($\text{Re}=110,000$). These locations are consistent with studies by Son and Honratty (1969), Zukauskas (1972), Dwyer and McCroskey (1973), and Achenbach (1968). Although, Dwyer and McCroskey (1973) showed that the separation point actually oscillates, this may explain why there is a rather broad region of low heat transfer near separation for $\text{Re}=34,000$. The heat transfer data shows the separation region to be more distinct as the Reynolds number goes up. This also implies the upstream region feels the presence of the oscillatory wake more at low Reynolds number. Also shown in Figure 4.2.1 is data for Reynolds number of 74,000 and 110,000. The heat transfer in the wake region of the cylinder should correlate using $\text{Nu}/\text{Re}^{2/3}$. This would increase $\text{Nu}/\text{Re}^{1/2}$ as Reynolds number grows larger. The present data behaves in the opposite manner, which alerts us to a problem in this region.

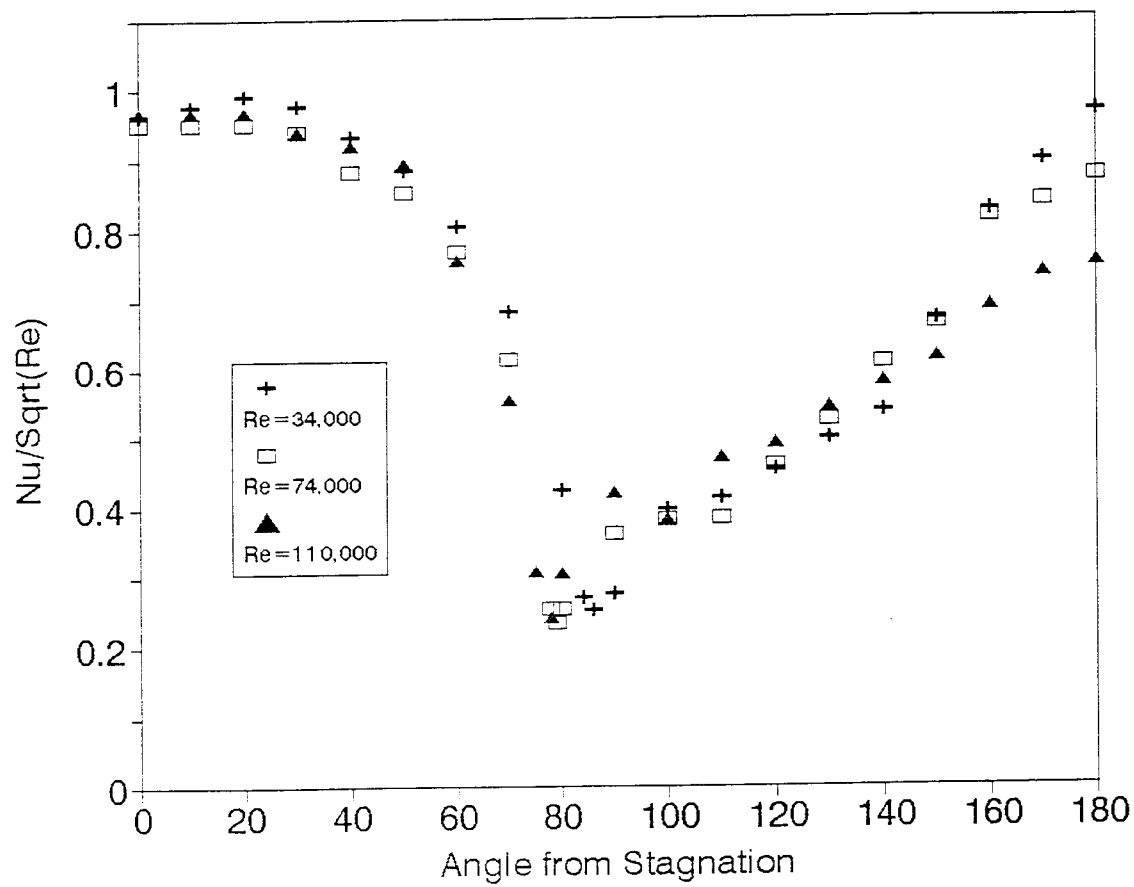


Figure 4.2.1 Local heat transfer around the cylinder

4.3 Discussion

In Figure 4.3.1, the 34,000 Reynolds number data is compared to data from Kraabel et al. (1982), Schmidt and Wenner (1943), O'Brien and VanFossen's (1985), and Meel (1962). Excluding Schmidt and Wenner's (250 mm cylinder), all of the results are roughly the same up to separation. For Reynolds number of 34,000, the maximum heat transfer didn't occur at the stagnation point, but was measured at 20°. This seemed strange, but it was repeatable. O'Brien and VanFossen⁴ also measured the local heat transfer at 10 and 20 degrees to be roughly 5% higher than that measured at stagnation, but they didn't speculate about their result. Dwyer and McCroskey (1973) showed that the unsteady wake actually causes the stagnation point to oscillate, which during portions of the cycle, produces higher shear stresses in the 10-30° region. This unsteady stagnation behavior would be more dominant at low Reynolds number, therefore could be the source of the slightly higher heat transfer measured at 20°. The slightly higher heat transfer at 20° could also be explained due to angular dependence of the liquid crystal. As the viewing angles increase, the liquid crystal appear to be at a higher temperature. In either case, the high heat transfer at 20° is less than the uncertainty of the technique and should not be over emphasized.

The separation region is very difficult to analyze using other techniques because the heat flux sensors which are used subtend a large angle of the model. This results in data which is broadened due to averaging and possibly shifted by unequal gradients on each side of the minimum. Many past researchers state the minimum heat transfer is aft of the separation point. This may be an error introduced by sensor

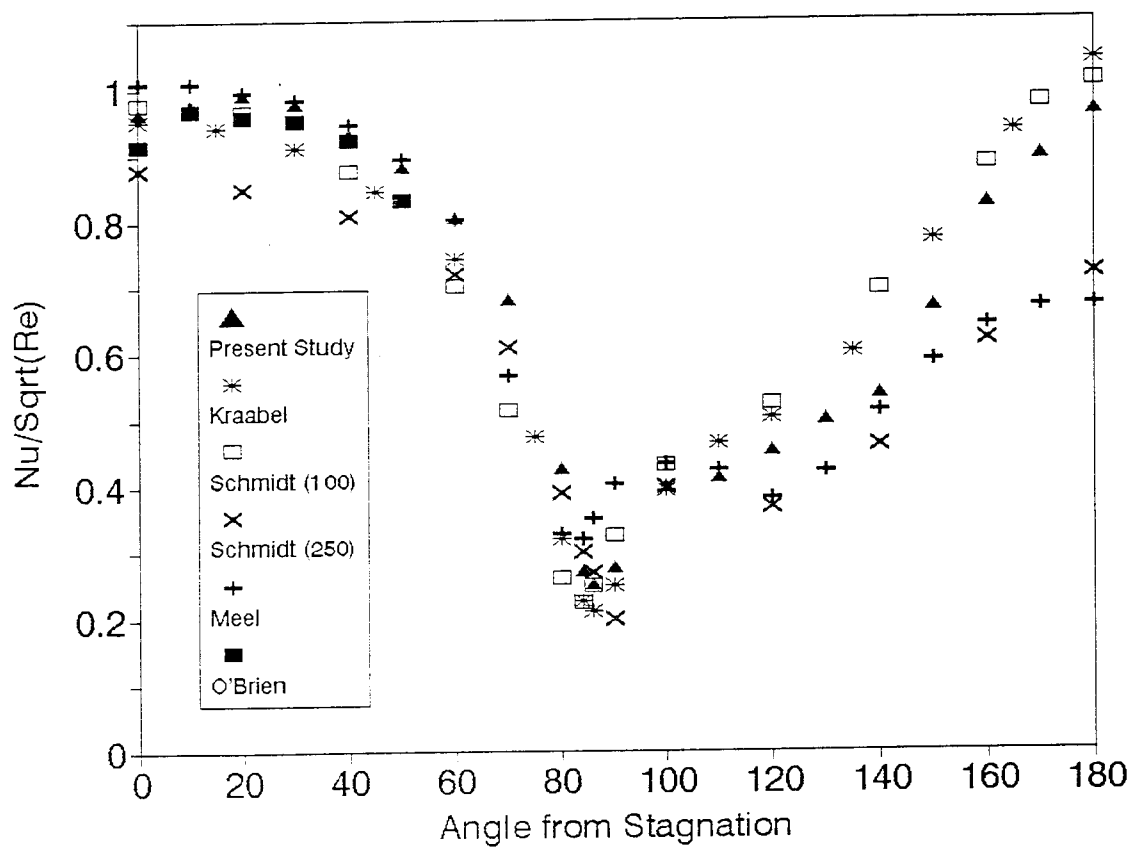


Figure 4.3.1 Comparison of heat transfer around the cylinder

averaging and shifting of the minimum heat transfer. The subtended sensor angle, along with other pertinent experimental data for the different studies is shown in Table 4.3.1.

Figure 4.3.1 shows that the wake region heat transfer data is very scattered, but falls into two types of profiles. Meel (1962) and Schmidt and Wenner's (1943) 250mm data has a second maximum and a second minimum after separation. While, the other data presented has an ever increasing heat transfer from separation to the rear stagnation point. Richardson (1963) tried to explain the large differences in the wake region heat transfer by looking at the experimental index of uncertainty, cylinder diameter, blockage, aspect ratio, and turbulence intensity. He concluded there must be some unrecognized factor. It is interesting to note that Schmidt and Wenner (1943) produced both type of results on their two different size cylinders, though most researchers ignore Schmidt and Wenner's 250 mm data. Richardson (1963) gave Schmidt and Wenner's 250 mm data the best index of uncertainty, although, we are not sure this should be the case. We must look at individual contributions in order to help explain the wake region heat transfer.

Tunnel blockage has been studied by Hiwada and Mabuchi (1982), West and Apelt (1982), and Hiwada et al. (1979). High blockage tends to move the separation point aft, and at very high blockage ($D/w=.6$) will produce a second maximum/minimum similar to the ones shown. The data presented is considered low blockage and shouldn't result in a measurable difference in heat transfer. We believe Schmidt and Wenner's 250 mm cylinder results have the characteristics of high blockage. Their separation point is further aft and the second heat transfer maximum exists. Their tests were performed in a freejet, but their model blocked over 40% of the nozzle exit.

Table 4.3.1 Experimental Specifications

	Reynolds Number	Blockage	Aspect Ratio	Subtended Sensor	Turbulence
	Re	D/w	h/D	Angle	Tu Re ^{.5}
Present Study	33,500	.075	8.0	Liquid Crystal	1.8
Kraabel	33,700	.083	20.0	9.5 °	.92
Schmidt & Wenner (100)	39,800	freejet (.167)	2.5	14.3 °	Unknown
Schmidt & Wenner (250)	39,200	freejet (.417)	1.0	5.8 °	Unknown
Meel	31,900	.093	6.9	3.5 °	.36
O'Brien & VanFossen	48,800	.096	2.3	10.0 °	1.33

The model aspect ratio needs to be considered if the test portion of the model is effected by the wall of the tunnel. Sparrow et al. (1984) concluded that wall effects are contained within one diameter of the wall. Therefore, for most of the data this shouldn't be a factor, and we believe it has a negligible effect.

Free-stream tunnel turbulence, surface roughness, and pulsating flows have been studied by many researchers, Achenbach (1977), O'Brien and VanFossen (1985), Newman et al. (1972), Lowery and Vachon (1975), Andraka and Diller (1985), and Ibrahim (1985). Very high free-stream turbulence can cause amplified stagnation point heating and premature boundary layer transition, which dramatically changes the heat transfer distribution. The levels of free-stream turbulence for the presented data are considered low and shouldn't change the heat transfer measurably.

With so many different test techniques, it is very hard to speculate why the heat transfer measurements in the separated wake region are so different. Though, it appears some factor is changing the unsteady characteristics of the wake. Hiwada et al. (1979) had a very interesting result. Their heat transfer measurements looked similar to Schmidt and Wenner's (1943) 100 mm and Kraabel's (1982) data, but when they added a splitter plate to the cylinder, the resulting heat transfer looked similar to that of Meel (1962). This suggests that some outside factor is interacting with the wake and changing the heat transfer profile. We found that the periodic vortex shedding frequency is very sensitive to outside influences. Because our model has a high aspect ratio, our initial tests were performed with each end of the model open to cavities produced by the heating unit and shroud fitted on the tunnel wall (see Figure 2.2.2). The shedding frequency was measured using a constant current hot-wire attached to a spectrum

analyzer. These measurements showed the Strouhal number changed dramatically if the cavities were covered. Raw spectrum analyzer data is shown in Figures 4.3.2 (Re=34,000), 4.3.3 (Re=74,000), and 4.3.4 (Re=106,000). For Reynolds number of 34,000, the shedding frequency is 18.438 Hz with the cavities covered. With the cavities, the frequency is less pronounced, but is clearly centered around 15.05 Hz. The same effect is evident at all three Reynolds numbers. A plot of the Strouhal number vs. Reynolds number is shown in Figure 4.3.5. The Strouhal number is about 0.2 with the cavities covered, which is the natural shedding frequency. The cavities produce an unsteady influence which effects the fluid dynamics. Barbi et al. (1986) found that many unsteady factors can interact with the wake. His work showed that the shedding frequency will decrease as the forcing frequency increases, until the shedding frequency "locks-on" to one-half the forcing frequency. Under some conditions, the vortices actually shed simultaneously, rather than alternating. These fluid dynamic changes would certainly effect the local heat transfer. The literature reveals some controversy over this point. Mabuchi et al. (1974) concluded that the rear stagnation heat transfer wasn't dependent on the Strouhal number. While Igarashi (1984) concluded that the wake region heat transfer is inversely related to the shedding frequency. In both cases, they used splitter plates and other cylinders behind the primary cylinder to produce the necessary changes in shedding frequency. These devices would contribute to other unnatural fluid dynamic changes, other than changing the shedding frequency. The present data was collected with and without the end cavities, therefore the only expected difference would be the shedding frequency.

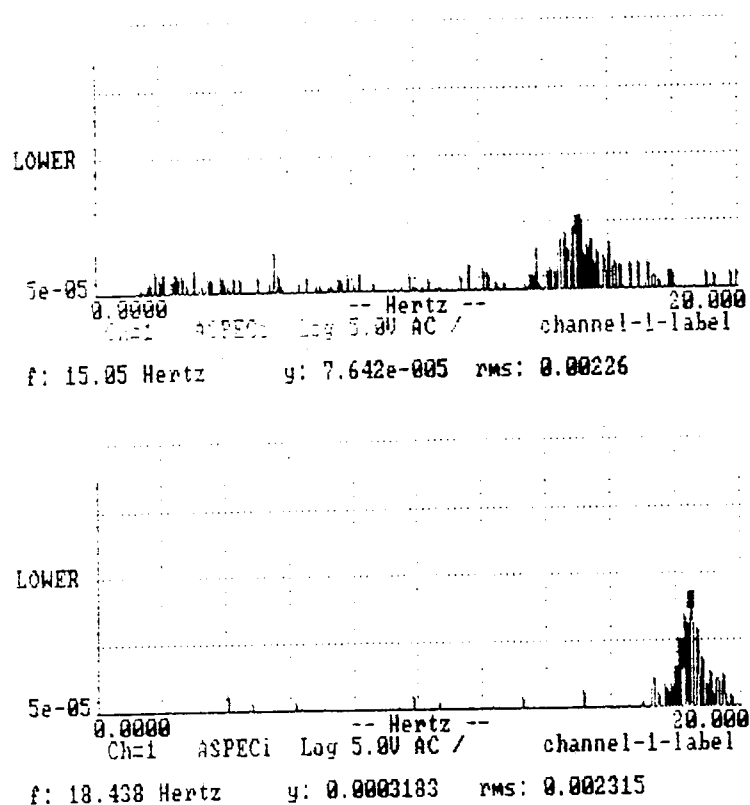


Figure 4.3.2 Spectrum analyzer data ($Re=34,000$)
with (top) and without (bottom) end cavities

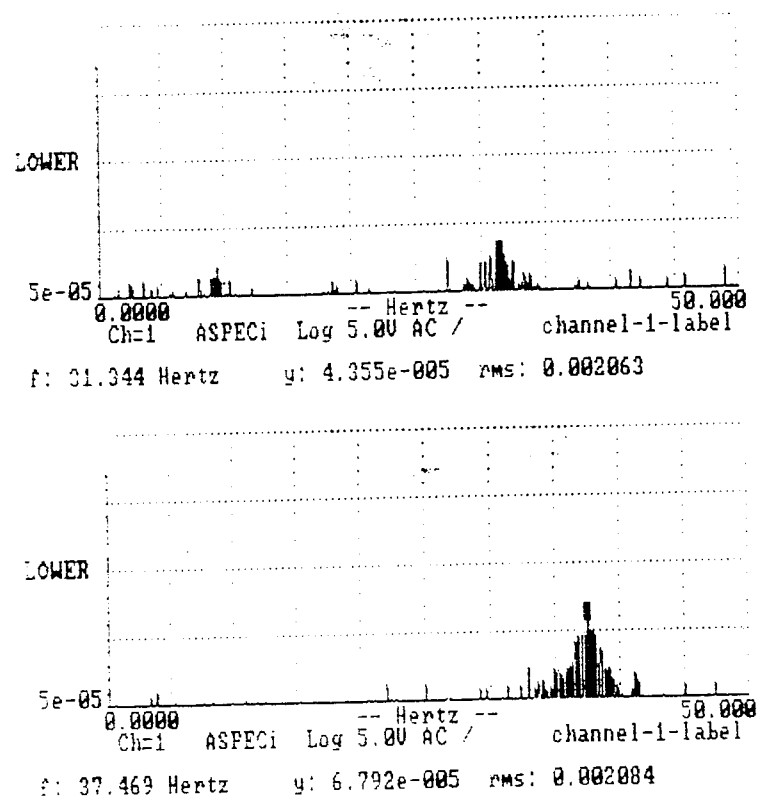


Figure 4.3.3 Spectrum analyzer data ($Re=74,000$)
with (top) and without (bottom) end cavities

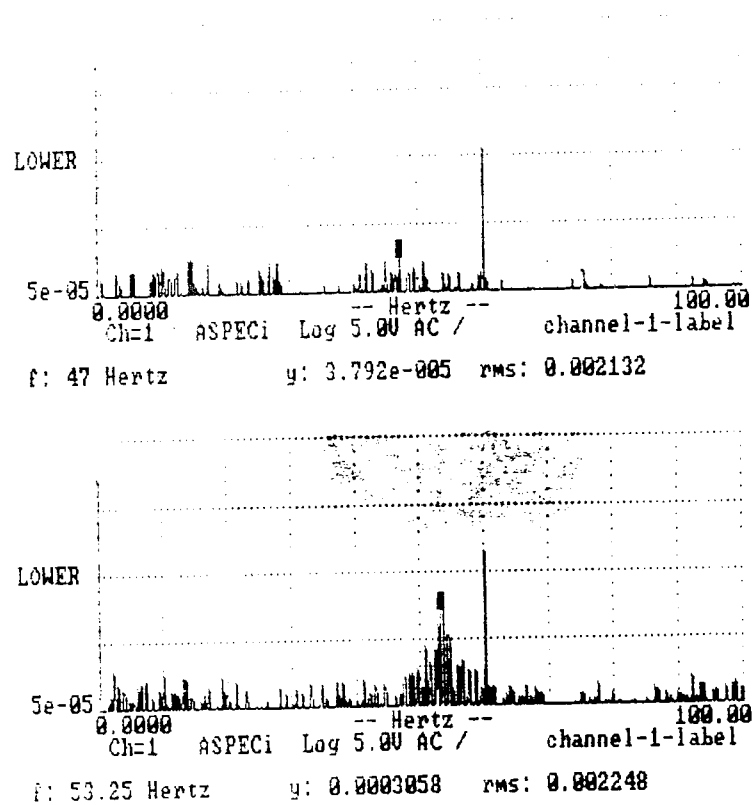


Figure 4.3.4 Spectrum analyzer data ($Re=106,000$)
with (top) and without (bottom) end cavities

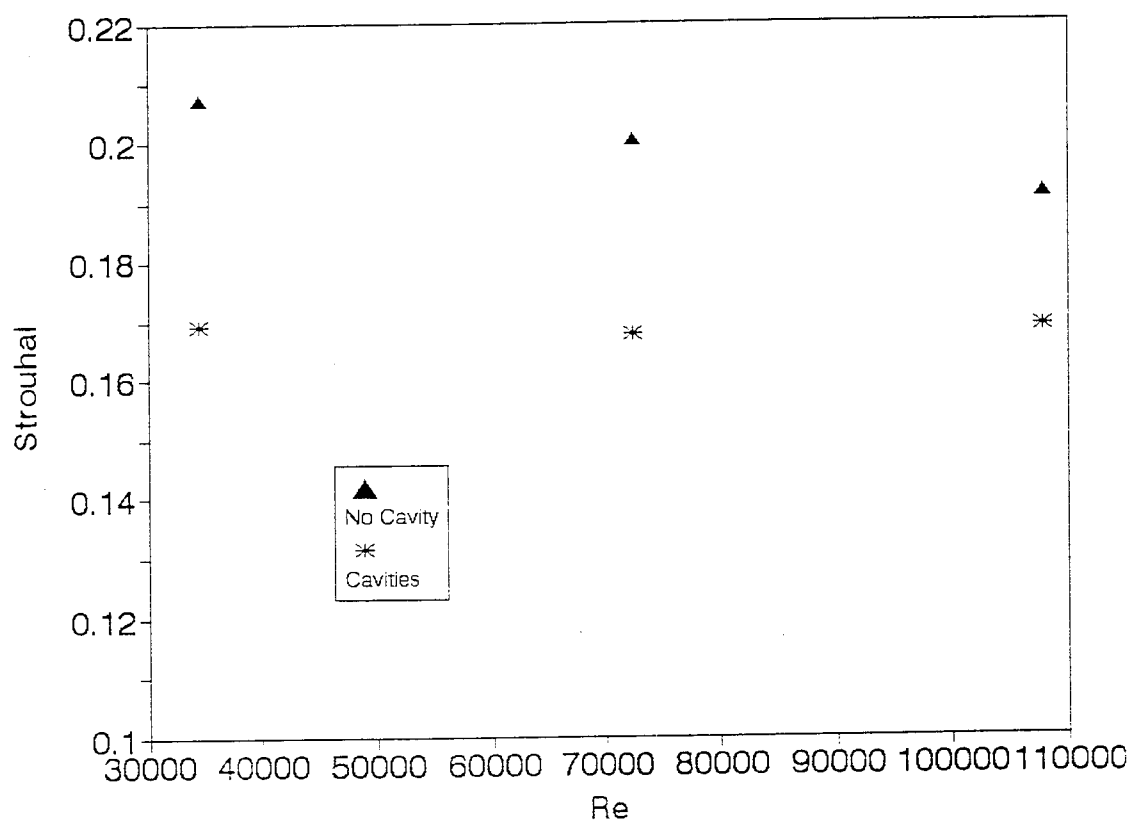
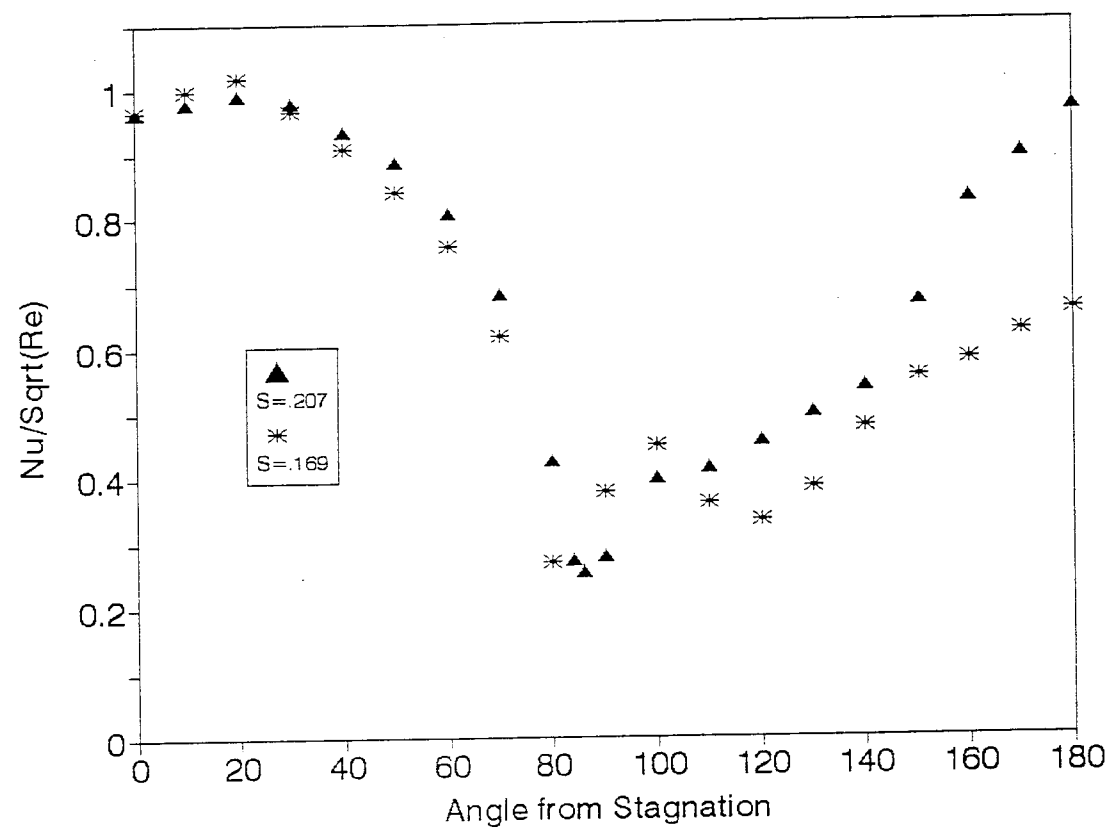


Figure 4.3.5 Strouhal number for cylinder with and without end cavities

A heat transfer comparison is shown in Figure 4.3.6. The data influenced by the end cavities has a second maximum and second minimum like Meel (1962), and Schmidt and Wenner's (1943) 250 mm data. Although, when the vortex shedding is natural (no end cavities), the data is like Schmidt and Wenner (100 mm), and that of Kraabel (1982). The separation point is more distinct and moves slightly forward (to 80°) when the cylinder is influenced by the end cavities. This is additional evidence that the weaker vortices have less unsteady influence upstream. The measurements also show that the heat transfer in the wake region decreases, when the shedding frequency decreases. This conclusion seems physically sound. With so many influences, it is not surprising that the wake region heat transfer isn't well understood. We feel that other unsteady factors could have contaminated previous data. Future heat transfer work on periodic separated wakes should include shedding frequency measurements.

As mentioned earlier, the data in the wake region should correlate with $\text{Nu}/\text{Re}^{2/3}$. This would increase $\text{Nu}/\text{Re}^{1/2}$ as Reynolds number grows larger. The present data behaves in the opposite manner. All transient methods require the flow to develop around the body. The development time has to be very short compared to the total amount of time for the transient. Kurkal and Munukutla (1989) solved a transient flat plate problem numerically and found that the velocity divided by the distance is approximately the amount of time required for the local heat transfer rates to become steady. This result would suggest that the flow development time is very short, indeed



4.3.6 Strouhal number effect on local heat transfer ($\text{Re}=34,000$)

it probably is for most of the cylinder. Although, the amount of time required for the wake region vortices to develop and become periodic may be much longer. Our low Reynolds number results closely agree with most data in the wake region, but at higher Reynolds Number, the data appears low. This may be due to the fact that the test duration is much shorter at higher Reynolds number because the heat transfer is much higher. Therefore, the flow development time (after the removal of the shroud) may become a significant percentage of the test time. This would produce time averaged results which do not correctly represent the steady periodic time average. It should be noted that any transient technique may exhibit this problem when measuring separated boundary layers or any other flow which develops slow.

In summary, the shroud technique was used to measure the local heat transfer for a cylinder in cross-flow. Heat transfer measurements in the laminar region are in very good agreement with earlier research. The heat transfer measurements of the separation point show that this region moves forward as Reynolds number increases (86° at $Re=34,000$ to 78° at $Re=110,000$). The measurements in the separated wake region provided new insight into unsteady effects. Free-stream turbulence, tunnel blockage, surface roughness, aspect ratio, model diameter, boundary conditions, and unsteady effects were considered. For high Reynolds number, the heat transfer on the rear stagnation point is too low using the transient method because the flow development time for this region is too long. It was found that the vortex shedding frequency is very sensitive to outside influences and can drastically change the results in the wake region.

This is probably why previous researchers have had very poor agreement in the wake region (although, their data usually matched one of two profiles). Future heat transfer work on periodic separated wakes should include shedding frequency measurements. These results show that the shroud technique can be effective and accurate if used properly.

CHAPTER 5 LAMINAR FLOW OVER A FLAT PLATE

This chapter describes the investigation of laminar flow over a flat plate. Laminar flow over a flat plate is one of the most widely studied flows because it can give insight into more complicated flows. This chapter provides an in depth study utilizing analytical, numerical, and experimental solutions.

Analytical solutions over a flat plate are well known and reviewed. Three numerical codes were written to solve for the laminar flow over a flat plate with different thermal boundary conditions. The three different thermal boundary conditions are a uniform temperature wall, constant heat flux, and an unsteady wall temperature simulating transient methods.

Experimental tests were performed using a gold-film heated-coating method (uniform heat flux) and the shroud technique (transient). This allows for a direct comparison of the two different techniques.

Finally, the analytical, numerical, and experimental solutions are all compared to fully understand the flow-field and the experimental methods.

5.1 Background

Flow over a flat plate is characterized by the buildup of a viscous velocity boundary layer as the flow interacts with the plate. If the plate and fluid are at different temperatures, a thermal boundary layer will also exist. The velocity boundary layer and its profile will dictate the shear stress, while the temperature profile will define the heat

transfer to or from the plate. The velocity and temperature profiles are dependent on the type of boundary layer (laminar, transitional, or turbulent). For the present study, the Reynolds numbers are less than 500,000, therefore we expect to have laminar flow over the entire length of the plate.

The classical solution to the laminar boundary layer equations is known as the Blasius solution. This was named after H. Blasius who earned his Ph.D. working under Prandtl in 1908 (Anderson, 1991). Blasius transformed the boundary layer equations to produce a similarity solution. He used a streamfunction to satisfy continuity and applied a similarity variable to momentum reducing it to an ordinary differential equation. The ordinary differential equation is integrated to obtain the boundary layer velocity profile. The velocity gradient at the surface is proportional to the shear stress. In terms of a coefficient of friction, his solution is:

$$C_f = \frac{.664}{\sqrt{Re_x}}$$

Pohlhausen (1921, details in Schlichting) furthered this theory by analyzing the energy equation and the thermal boundary layer. Assuming the wall has a uniform temperature, the energy equation can be treated in a similar fashion. The energy equation is dependent on the velocity solution, but once the velocity profile is known, the energy equation can be approximately solved to get the temperature profile. The heat transfer is proportional to the temperature gradient at the surface. The result for the local Nusselt number for laminar flow over a uniform temperature flat plate is:

$$Nu_x = .332 \sqrt{Re_x} Pr^{4/3}$$

This solution is only good for a uniform temperature plate. Baxter and Reynolds (1958) duplicated this solution for a uniform temperature flat plate and they also solved many other thermal boundary conditions. They showed that the solution for a uniform heat flux plate is:

$$Nu_x = .453 \sqrt{Re_x} Pr^{4/3}$$

While the solution for a linear wall temperature starting at the leading edge is:

$$Nu_x = .535 \sqrt{Re_x} Pr^{4/3}$$

These solutions show that the heat transfer for laminar flow over a flat plate is very dependent on the thermal boundary conditions. The heat transfer for the uniform heat flux is 36% greater, while the linear wall temperature is 61% greater than the uniform wall temperature solution. From these results, it is clear that the heat transfer coefficient increases as the wall temperature profile deviates from the uniform temperature condition. The wall temperature profiles are shown for different thermal boundary conditions in Figure 5.1.1. For comparison, the wall temperatures were determined by picking a given point to hold constant (in this case, 40° C at $Re_{ex}=120,000$), while applying the theoretical solutions. It can be seen that the wall temperature is proportional to the square root of x for the uniform heat flux boundary condition and is proportional to x (by definition) for the linear wall temperature. Therefore, as the wall temperature deviates further from the uniform condition, the heat transfer becomes larger than the uniform wall temperature solution.

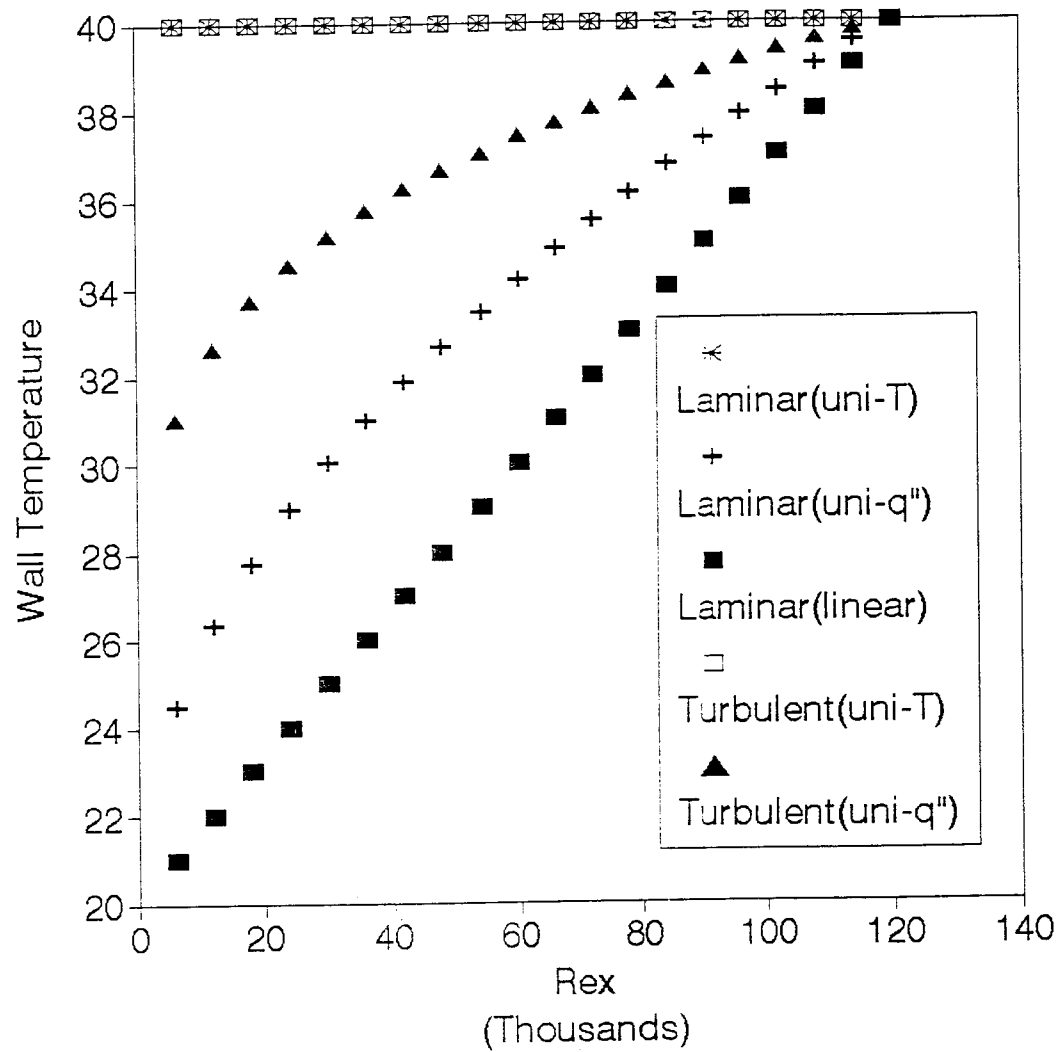


Figure 5.1.1 Effect of thermal boundary condition on wall temperature

The heat transfer for turbulent flow over a flat plate can be determined using integral methods. Taylor et al. (1989) is an outstanding paper investigating the difference between uniform wall temperature and uniform heat flux boundary conditions for turbulent boundary layers. Kays and Crawford (1980) showed the turbulent uniform temperature plate solution is:

$$Nu_x = .0296 Re_x^{4/5} Pr^{1/3}$$

While the solution for a uniform heat flux boundary condition is:

$$Nu_x = .0308 Re_x^{4/5} Pr^{1/3}$$

For a turbulent boundary layer, the heat transfer for the uniform heat flux boundary condition is only 4% larger than the uniform wall temperature. The thermal boundary condition is not as important for the turbulent boundary layer. This is because the wall temperature profile more closely matches the uniform wall temperature, while for laminar uniform heat flux conditions, the wall temperature profile is quite different (Figure 5.1.1). For the turbulent boundary layer, the heat transfer coefficient is inversely proportional to $x^{1/5}$, while the heat transfer coefficient is inversely proportional to $x^{1/2}$ in a laminar boundary layer. This produces larger wall temperature differences and heat transfer coefficient gradients for the laminar boundary layer, thus amplifying the effect of different thermal boundary conditions.

Transient techniques produce unsteady thermal boundary conditions depending on the flow geometry and the length of the transient. We would expect that an unsteady temperature plate (like a transient method) would yield different results than a uniform

wall temperature and the solution would be dependent on the wall temperature transients. O'Brien et al. (1986), and Baughn et al. (1989) compared the difference between transient and uniform heat flux techniques in the stagnation region of a cylinder. They didn't find a significant difference between methods. This is expected because it is impossible for upstream boundary conditions to effect the stagnation point and the heat transfer coefficient is relatively constant in the region very near the stagnation point. They refer to the transient method as being very much like a uniform wall temperature technique, but in the stagnation region it would also be very much like a uniform heat flux technique because of its independence of thermal boundary conditions. Downstream of the stagnation point, the results may or may not be like a uniform temperature technique, they would be very dependent on the nondimensional transient temperature (T^*) used in the test, which like most other transient work was not reported. The uniform wall temperature boundary condition is compared to a uniform heat flux on a cylinder in cross-flow by Baughn and Sanei (1991). They found the results to be the same at the stagnation point, followed by increasing heat transfer for the uniform heat flux technique moving away from the stagnation point, and nearly twice the heat transfer at the separation point. Again, this shows the greatest differences between techniques in the region where the heat transfer coefficient exhibits large gradients. Kim et al. (1993) numerically showed that impinging jet local heat transfer is independent of the thermal boundary condition within 2.5 diameters of the jet, this would be expected in this region because the flow is similar to a stagnation region.

A lot of work has been done investigating the effect of free-stream turbulence on flat plate heat transfer. Kestin (1966) concluded that free-stream turbulence had no

effect on turbulent boundary layers and laminar boundary layers with zero pressure gradient, although he found turbulence to increase the heat transfer on flat surfaces with laminar boundary layers and favorable pressure gradients. Junkhan and Serovy (1967) had similar results. Simonich and Bradshaw (1978) found that free-stream turbulence did in fact increase the heat transfer produced by a turbulent boundary layer (roughly 5% per percent of turbulence). Blair (1983) also found turbulence to increase the heat transfer in turbulent boundary layers (20% increase at 6% turbulence). Other studies agreed with these findings including MacMullin et al (1989) who used a circular wall jet, and Young et al (1992) who used jet grid turbulence. Gostelow and Blunden (1989) studied the turbulence effect on adverse pressure gradient transition and showed that the transition location did not change much, but the transition length was greatly reduced by turbulence. Rivir et al. (1994) showed that the minimum heat transfer exists at the location of boundary layer separation and is 60% less than the zero pressure gradient level. Sugawara et al. (1988) used a transient technique for measuring flat plate heat transfer. They found that turbulence did not increase the heat transfer in the zero pressure gradient laminar region, but their heat transfer levels were 44% higher than theory or other experiments. From the conclusions of the present work, we believe this increase in heat transfer is probably due to the transient method and its resulting thermal boundary conditions.

The present study numerically and experimentally investigated the effect of thermal boundary conditions on laminar flat plate heat transfer. Three numerical codes are used to solve for the laminar flow over a flat plate with different thermal boundary conditions (uniform temperature wall, constant heat flux, and an unsteady wall

temperature simulating transient methods). Experimental tests were performed using a gold-film heated-coating (uniform heat flux) method and the shroud technique (transient). This allowed for a direct comparison of the different techniques.

5.2 Numerical Solutions

In order to compare the different experimental techniques, we must have accurate known solutions for any type of thermal boundary condition. This section explains the computational fluid dynamics code which was written to solve for laminar flow over a flat plate. The code needs to be able to solve for various thermal boundary conditions. The code was first written and compared to the exact solution for a uniform wall temperature (Blasius solution). This will confirm the code is accurate and can match a known solution. Further test cases can then be run with uniform heat flux or mixed thermal boundary conditions.

The governing equations for this problem are the incompressible boundary layer equations (Schlichting, 1968). The Reynolds numbers are relatively low, therefore the flow will be laminar. The continuity equation is:

$$\frac{\partial u}{\partial x} + \frac{\partial v}{\partial y} = 0$$

The x-momentum equation is:

$$u \frac{\partial u}{\partial x} + v \frac{\partial u}{\partial y} = - \frac{1}{\rho} \frac{\partial P}{\partial x} + v \frac{\partial^2 u}{\partial y^2}$$

Where the pressure gradient term will equal zero for a flat plate. The y-momentum equation tells us there isn't a pressure difference across the boundary layer in the y direction.

$$\frac{\partial P}{\partial y} = 0$$

Due to our low speed, viscous dissipation can be ignored and the energy equation reduces to:

$$u \frac{\partial T}{\partial x} + v \frac{\partial T}{\partial y} = \alpha \frac{\partial^2 T}{\partial y^2}$$

These equations must be solved numerically to determine the velocity and temperature boundary layers. The continuity and momentum equations are independent of the energy equation (assuming constant properties), therefore they are decoupled and can be solved by themselves. The energy equation is dependent (coupled) on the velocity field and requires the solution from the continuity and momentum equations before it can be solved.

The solution method for the velocity boundary layer is one detailed in Anderson et al. (1984). An extension of this technique suggested by Byerley (1990) is used for the energy equation to solve for the temperature profile. The method is an explicit method. The equations are parabolic, therefore the equations can be marched down the plate without iteration.

In our tests, the flow region is 4 inches long. For a velocity range of 6.5 to 21.5 m/s, we would expect the boundary layer to be no greater than .0025 m thick at the end of the plate. The thermal boundary layer will be slightly thicker (because the Prandtl

number is less than 1), so the grid is extended to .003 m. 101 grid points are used in the y direction to gain accuracy. The step in the x direction is dependent on the stability requirements and is generally very small.

The nodes along the wall are initialized with zero velocity and a fixed elevated temperature. The first column (free-stream air) and the top row of nodes are initialized to free-stream velocity and temperature values. The code starts at the second column, first row, and calculates the u-velocity using the discretized x-momentum equation.

$$u_j^n \frac{(u_j^{n+1} - u_j^n)}{\Delta x} + v_j^n \frac{u_{j+1}^n - u_{j-1}^n}{2\Delta y} = \nu \frac{(u_{j+1}^n - 2u_j^n + u_{j-1}^n)}{(\Delta y)^2}$$

The unknown (u_j^{n+1}) is solved for. The continuity equation is used to determine the v-velocity component (v_j^{n+1}).

$$\frac{v_j^{n+1} - v_{j-1}^{n+1}}{\Delta y} + \frac{u_j^{n+1} + u_{j-1}^{n+1} - u_j^n - u_{j-1}^n}{2\Delta x} = 0$$

The energy equation looks very similar to the x-momentum equation. It is discretized in a similar manner to determine the temperature (T_j^{n+1}).

$$u_j^n \frac{(T_j^{n+1} - T_j^n)}{\Delta x} + v_j^n \frac{T_{j+1}^n - T_{j-1}^n}{2\Delta y} = \alpha \frac{(T_{j+1}^n - 2T_j^n + T_{j-1}^n)}{(\Delta y)^2}$$

The three unknowns are solved for at each node moving up a column in the y direction. Once the column is finished, the code decides the step size in the x direction from stability. The stability requirement is:

$$\frac{2\alpha\Delta x}{u_j^n(\Delta y)^2} \leq 1$$

This requirement is from the energy equation and is more severe than the stability requirements from continuity or momentum. The code marches in the x-direction until the end of the plate is reached.

Once the entire velocity and temperature field is known, shear stress and heat transfer can be calculated. For the uniform wall temperature case, the numerical results can be compared to the exact theoretical results. The uniform wall temperature code calculated the coefficient of friction (C_f) and the local Nusselt number based on x (Nu_x). These results are compared to the theoretical solutions in Figure 5.2.1 and Figure 5.2.2. The numerical results are very good. The coefficient of friction is accurate within 3 digits, while the local Nusselt number is good to 2 digits. These results are very encouraging and suggest accurate solutions will be available for mixed thermal boundary conditions.

The next case to be examined is a wall with a uniform heat flux. For this boundary condition, the code needs to be modified. The x-momentum and continuity

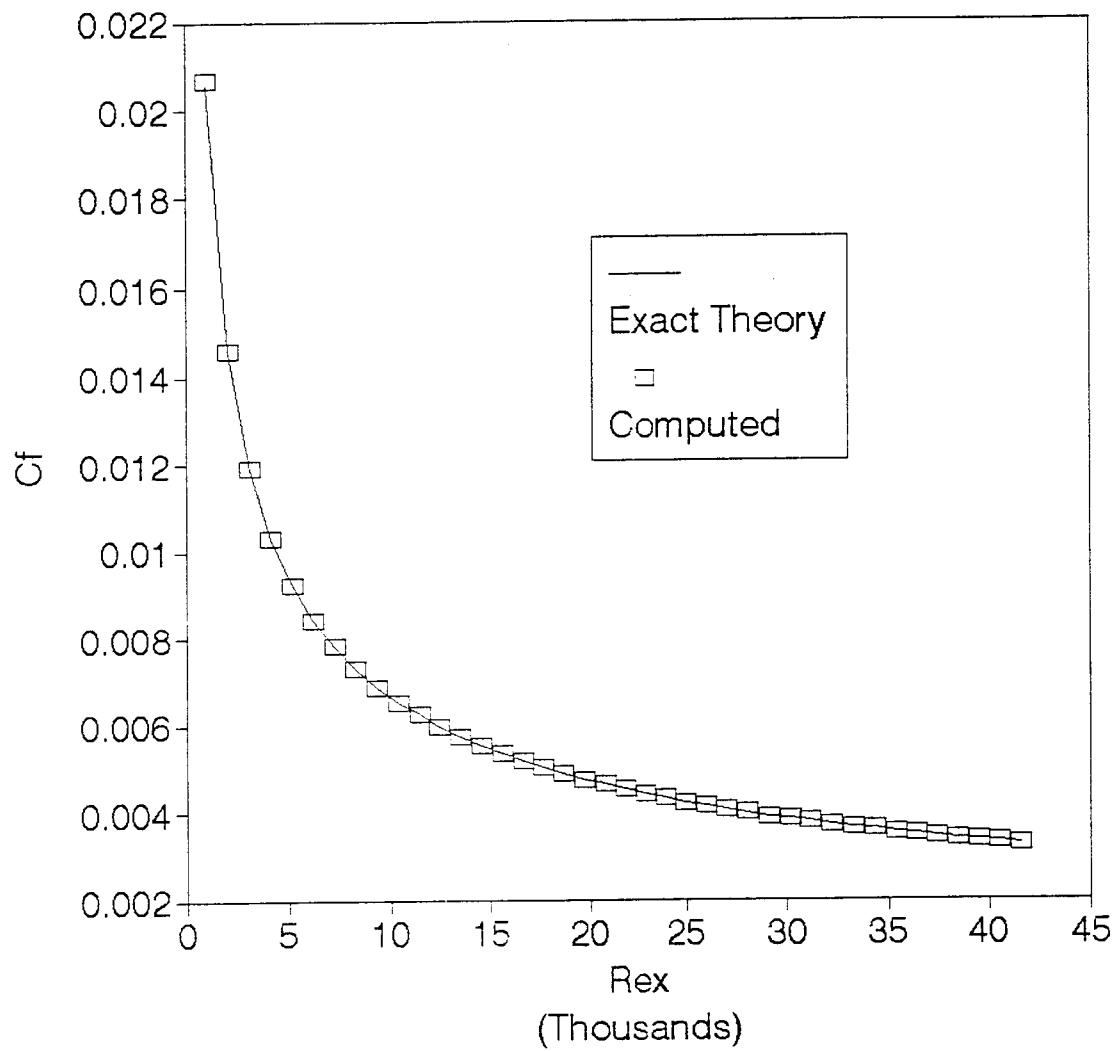


Figure 5.2.1 Computed vs exact coefficient of friction on a flat plate

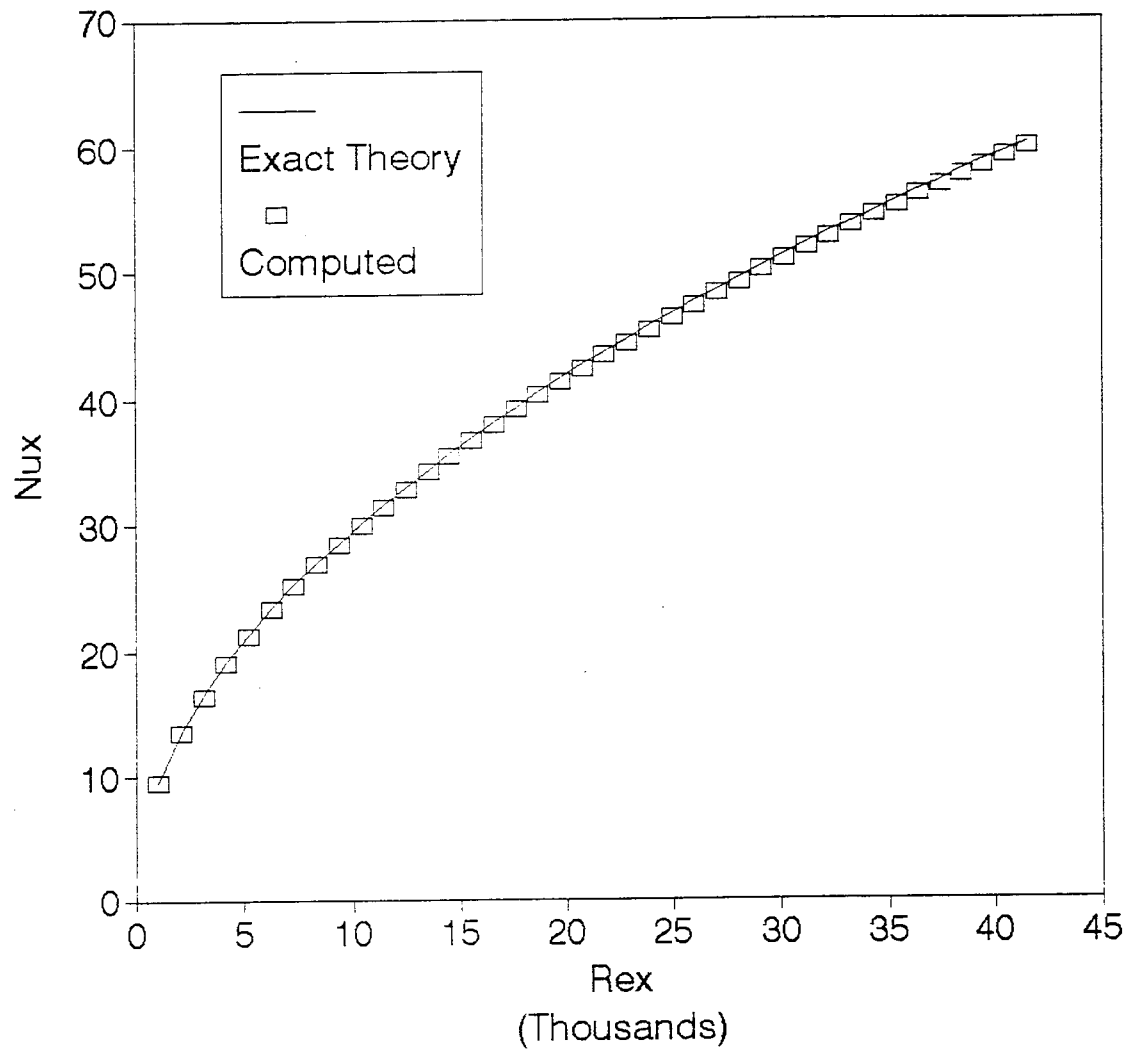


Figure 5.2.2 Computed vs exact local Nusselt number on a flat plate

equations will remain unchanged, therefore, the velocity boundary layer will not be effected. The thermal boundary condition at the wall will now be:

$$q'' = k_f \frac{T_{j=1} - T_{j=2}}{\Delta y} = \text{Constant}$$

Where $T_{j=1}$ is the wall temperature and is an unknown. It is clear this equation contains two unknown temperatures. The solution method needs to be modified in order to solve for the temperature profile. The velocities are solved for, like before, by marching up a column. To solve for the temperatures, the energy equation is solved while marching back down the column. The last equation to be solved is the thermal boundary condition and this equation determines the local wall temperature. The local wall temperature along with the free-stream temperature is used to determine the local heat transfer coefficient and Nusselt number.

The results for the constant heat flux are compared to the uniform wall temperature in Figure 5.2.3. As expected, near the beginning of the plate, the results are similar. The results diverge as the history of the thermal boundary condition grows longer. The local Nusselt number for the constant heat flux is 36% larger than the uniform temperature solution and this increase is independent of location. The local Nusselt number is independent of the magnitude of the heat flux, although, the local wall temperature is not. A typical local wall temperature is shown in Figure 5.2.4. For this uniform heat flux boundary condition, the wall temperature is very low near the beginning of the plate because the heat transfer rate is very high. The overall shape of the wall temperature curve would stay the same for different levels of heat flux, but the magnitude of the wall temperature would change.

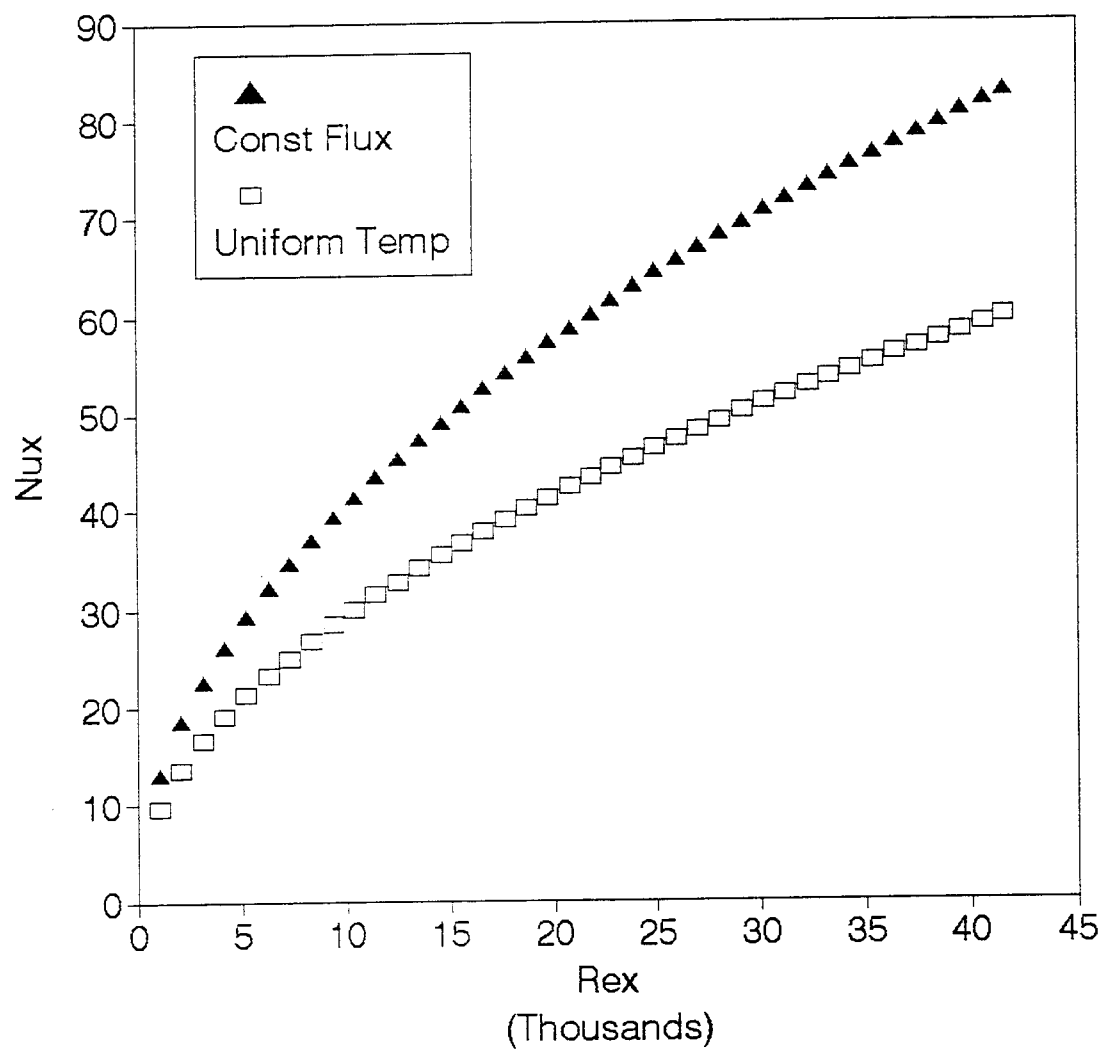


Figure 5.2.3 Uniform temperature vs. constant heat flux boundary conditions

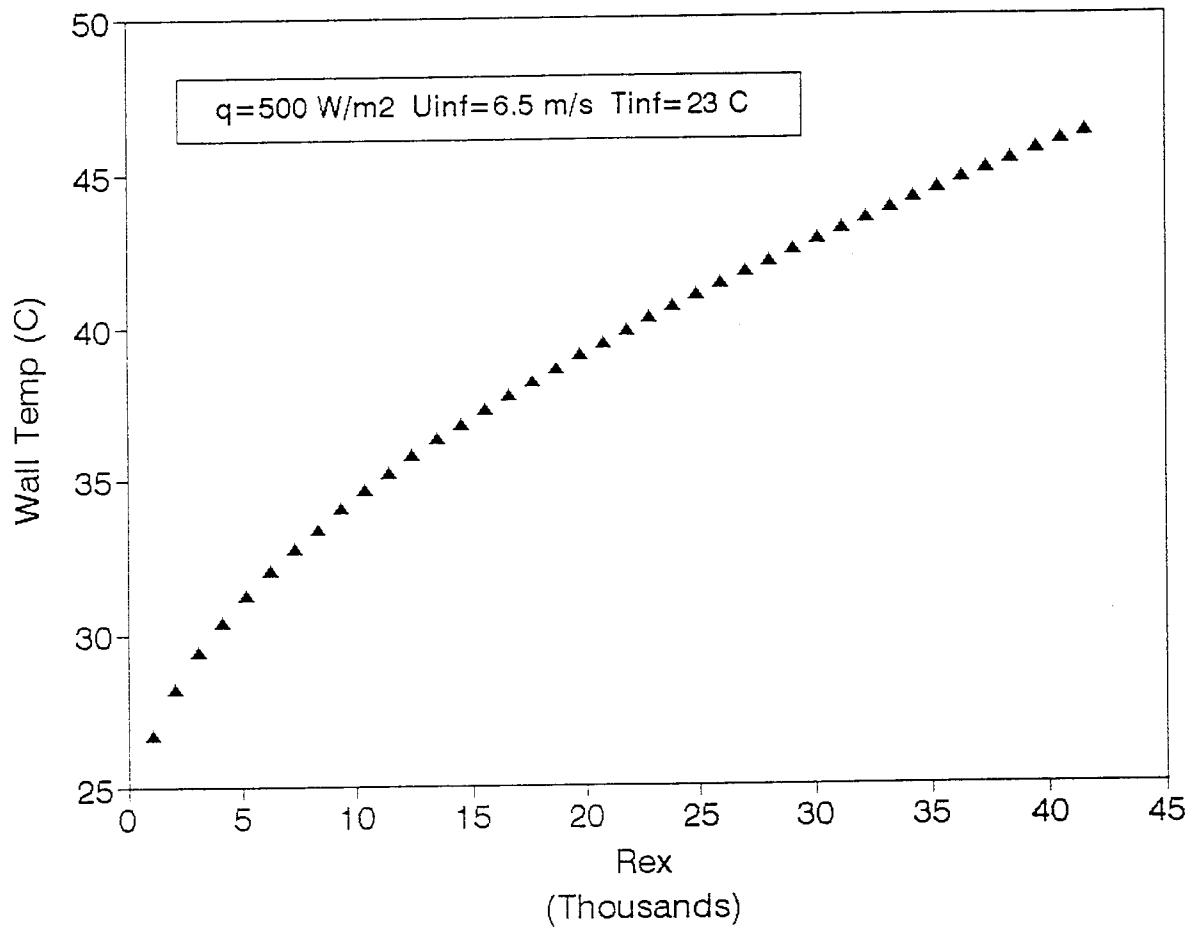


Figure 5.2.4 Wall temperature for a constant heat flux boundary condition

This code provided very good results for both the uniform wall temperature and the constant heat flux boundary conditions, now it can be applied it to unconventional thermal boundary conditions. The shroud technique produces a boundary condition which is neither a uniform wall temperature nor a constant heat flux. Changes to the code are required in order to simulate this unsteady boundary condition provided by the transient shroud technique. The uniform wall temperature code was modified to allow for the wall temperature to be a known variable. The code first runs with the wall temperature equal to the starting temperature of the model in the shroud technique. From this, the local heat transfer coefficients are determined. Since each location on the plate has different heat transfer, the local wall temperatures will change at different rates over time. The wall temperatures are calculated by locally allowing each node to cool according to its heat transfer coefficient over a small time step. A time averaged heat transfer coefficient is used in this 1-D transient update. Appendix L shows that this simplified wall temperature update gives good results, but this code could be improved by finite-differencing the wall conduction. The code marches in time, running updated wall temperatures for each time step. This would be considered a pseudo-unsteady scheme, because the fluid mechanics are calculated assuming steady-state and the wall temperatures are varied with time. This is permissible because the time scale for conduction is much greater than the time scale for convection. Kurkral and Munukutla (1989) showed that the boundary layer responds very fast (on the order of u/x), as compared to the transient for the wall temperatures (L^2/α). This technique is effective but slow, the code takes roughly 2 days to run on a Intel 486-33 based machine.

The results are shown in Figure 5.2.5. As a reference, the steady-state uniform wall temperature and constant heat flux solutions are also shown on this plot. The local Nusselt number is highly dependent on the nondimensional temperature (T^*) used in the transient method. As expected, the closer the nondimensional temperature is to 1.0, the more the transient method acts like a uniform wall temperature method. Although even at $T^*=.9$, the results are still quite different. Lower T^* 's require longer transients and the heat transfer increases because the plate cools further from its initial uniform wall temperature. This allows cool air to reach further down the plate (because the front of the plate has already cooled) and effectively "shorten the plate" which increases the downstream heat transfer. This is a very important finding and it has ramifications on any data collected using transient techniques. Downstream, the plot shows the transient solutions elevated, although following the general shape of the uniform wall temperature solution. These results resemble a uniform wall temperature wall with an unheated starting length.

Most transient methods assume that the local heat transfer coefficients are constant over time. The heat transfer coefficient time history is plotted for three locations on the plate in Figure 5.2.6. This clearly shows that the local heat transfer coefficients are far from being constant during the transient. Five data points are plotted at each location and they correspond to the time for each location to reach $T^*= 1.0, .9, .8, .7$, and $.6$. This also shows the extreme difference in the length of each transient for different distances down the laminar boundary layer. This is caused by the large gradients in heat transfer coefficient (it is proportional to $1/\sqrt{Rex}$). The gradients are more shallow in a turbulent boundary layer because the heat transfer coefficient is

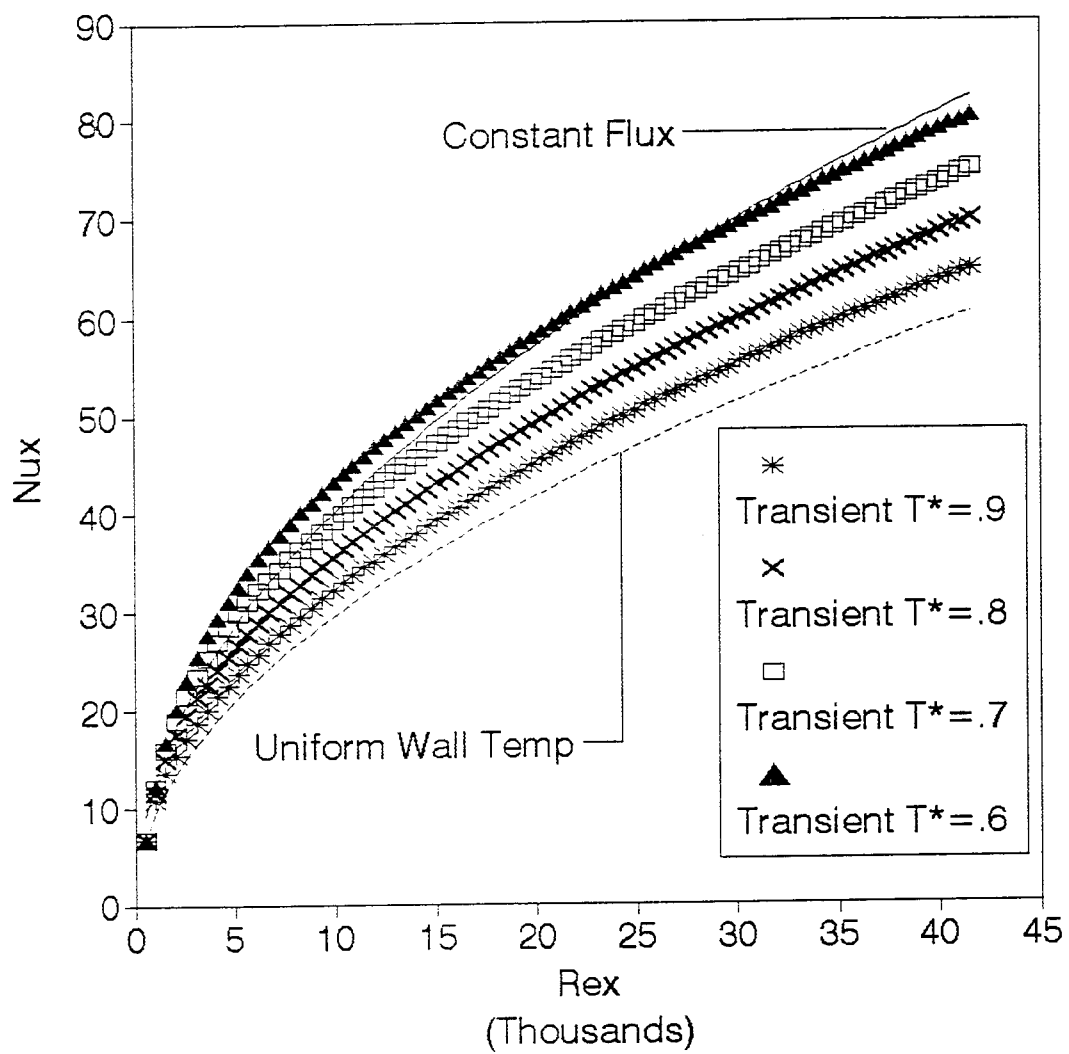


Figure 5.2.5 Nondimensional temperature effect on transient heat transfer

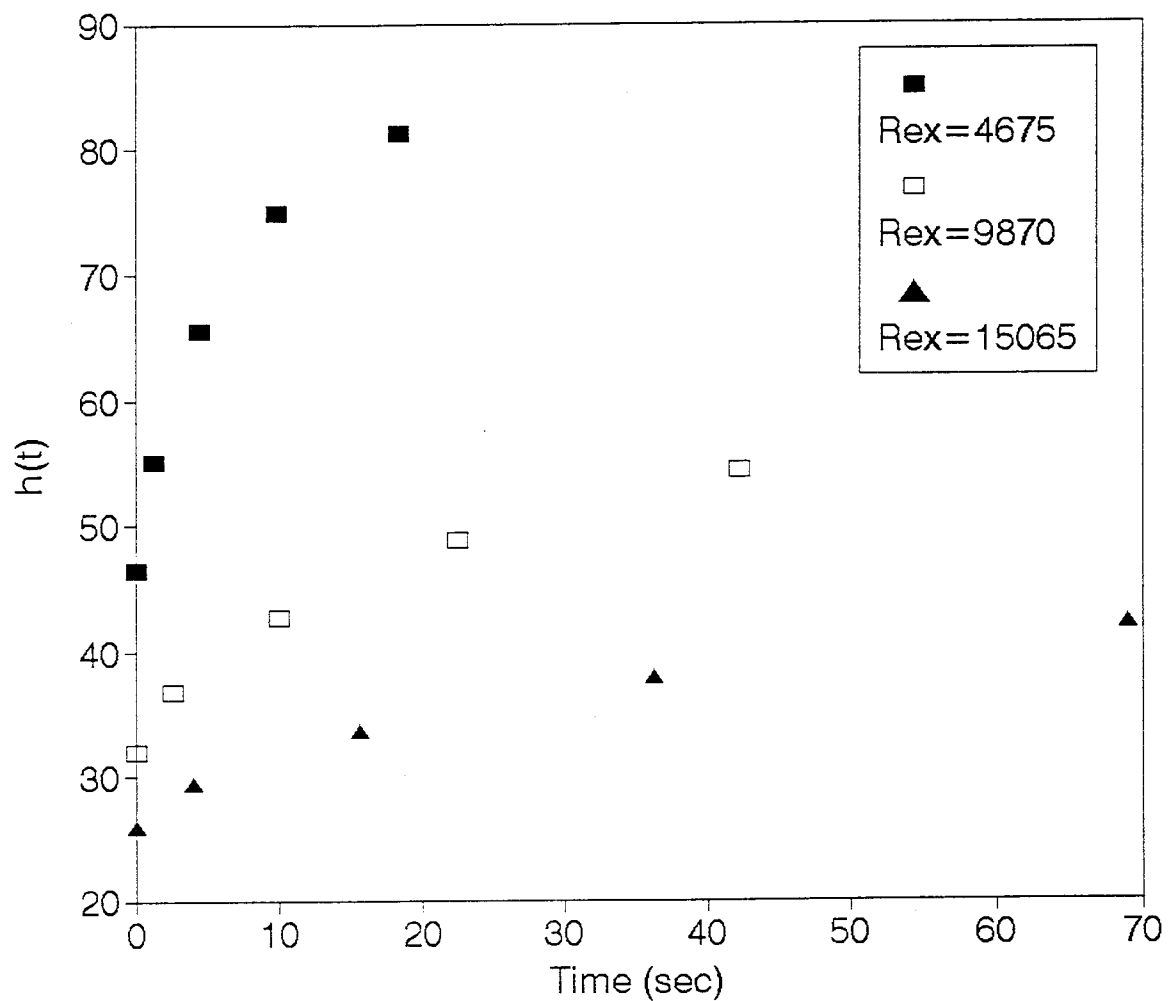


Figure 5.2.6 Variation of local heat transfer coefficient over time

proportional to $1/Rex^{1/5}$, therefore, we wouldn't expect to see such a large transient effect in a turbulent boundary layer.

These numerical results prove that it is very important to fully understand the thermal boundary conditions and their effect on the measured Nusselt number. Transient methods further complicate this issue and require extra attention.

5.3 Results for the Shroud Technique

This section discusses the experimental results for a laminar boundary layer over a flat plate using the shroud technique. We would like to determine the effect of Reynolds number and the nondimensional temperature (T^*) used in the transient method.

A flat plate model was constructed from Plexiglas .25" thick, 4" wide, and 28" long to completely span the tunnel. A sharp leading edge was formed by milling the backside of the front edge at a 30° angle. The test portion of the Plexiglas model was air brushed with black paint followed by liquid crystals. The flat plate model was mounted in the shroud technique apparatus. For a laminar boundary layer to form, the test side of the flat plate needs to be parallel or slightly windward to the free-stream flow. If the flat surface is at all leeward, a separation bubble forms near the leading edge and the flow is turbulent downstream of the reattachment point. To ensure a laminar boundary layer, the present tests were performed with the flat surface 1° windward.

In the present and many other transient techniques, you must choose the magnitude of the temperature difference between the ambient air, model, and model

starting temperatures. These variables show up in the data reduction in the form of a nondimensional temperature T^* .

$$T^* = \frac{T_{LC} - T_\infty}{T_o - T_\infty}$$

The numerical results showed that the choice of nondimensional temperature will effect the resulting heat transfer coefficients. When T^* equals 1.0, the starting temperature and the data collection (liquid crystal) temperature would be the same. This would be equivalent to an isothermal wall, but this couldn't be used in a transient test, because the time between the start and the end of the test would obviously be zero. Therefore, all of the runs require the starting temperature to be measurably higher than the liquid crystal temperature. Although, the downstream data is influenced by the upstream boundary conditions. This would suggest that we would want to run each test at T^* very near 1.0, but this causes the uncertainty of the measurement to go up. Therefore, we have to balance the desire of an isothermal wall to that of low uncertainty, but in the end, we need to fully understand this transient effect and its influence on the measurement.

The flat plate laminar boundary layer heat transfer was measured using the shroud technique with four different nondimensional temperatures ($T^* = .6, .7, .8$, and $.9$) and a free-stream velocity of 6.7 m/s . These results are shown in Figure 5.3.1. Also shown in this figure is the theoretical heat transfer for the uniform wall temperature and constant heat flux boundary conditions. As expected, the higher the nondimensional temperature, the closer the measurements are to the uniform wall temperature solution. The graph also shows how dependent the heat transfer is on the transient

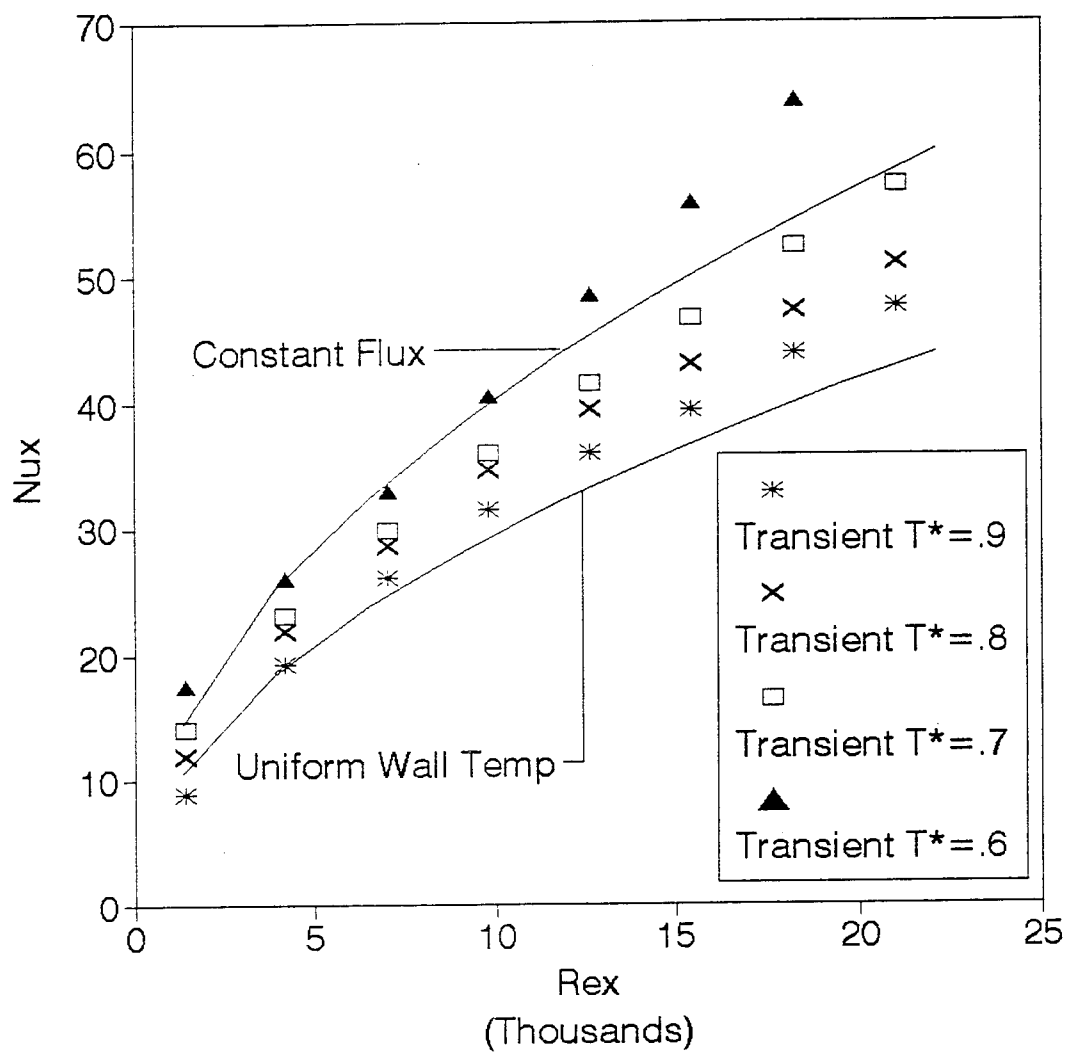


Figure 5.3.1 Effect of the transient nondimensional temperature

nondimensional temperature (T^*). The heat transfer measurements increase as the nondimensional temperature decreases. This is caused by the front region of the plate cooling faster than the rear region, therefore, longer transients (lower T^*) allow air passing over the cool front region to reach the rear region and increase the heat transfer. It should be noted, that the ($T^*=.6$) data diverges near the end of the plate. This is due to the long transients required to take the $T^*=.6$ data in these locations. The long transient allows the 1-D semi-infinite substrate assumption to break down and this causes the calculated heat transfer to increase further. The $T^*=.6$ data was included to show the overall effect of T^* , but in practice, T^* 's this low should not be used. For more detail on this effect, wall thickness sensitivity is analyzed in Appendix F.

The effect of Reynolds number was also determined using the shroud technique. The flat plate was tested using two different speeds (6.7 and 20 m/s), and in both cases the data was collected using $T^*=.8$. The results are shown in a log-log plot in Figure 5.3.2. As expected, as Reynolds number increases the heat transfer increases with a slope of 1/2 decade/decade. This data confirms laminar boundary layer theory which predicts the heat transfer to increase at a rate proportional to the square root of the Reynolds number.

The heat transfer measurements on the flat plate using the shroud technique provide insight into laminar boundary layers and transient methods in general. The results show how dependent the heat transfer measurements are on the nondimensional temperature used in the transient method. The selection of the transient nondimensional temperature has a direct impact on the results and should always be reported in transient research. It is most important when trying to interpret

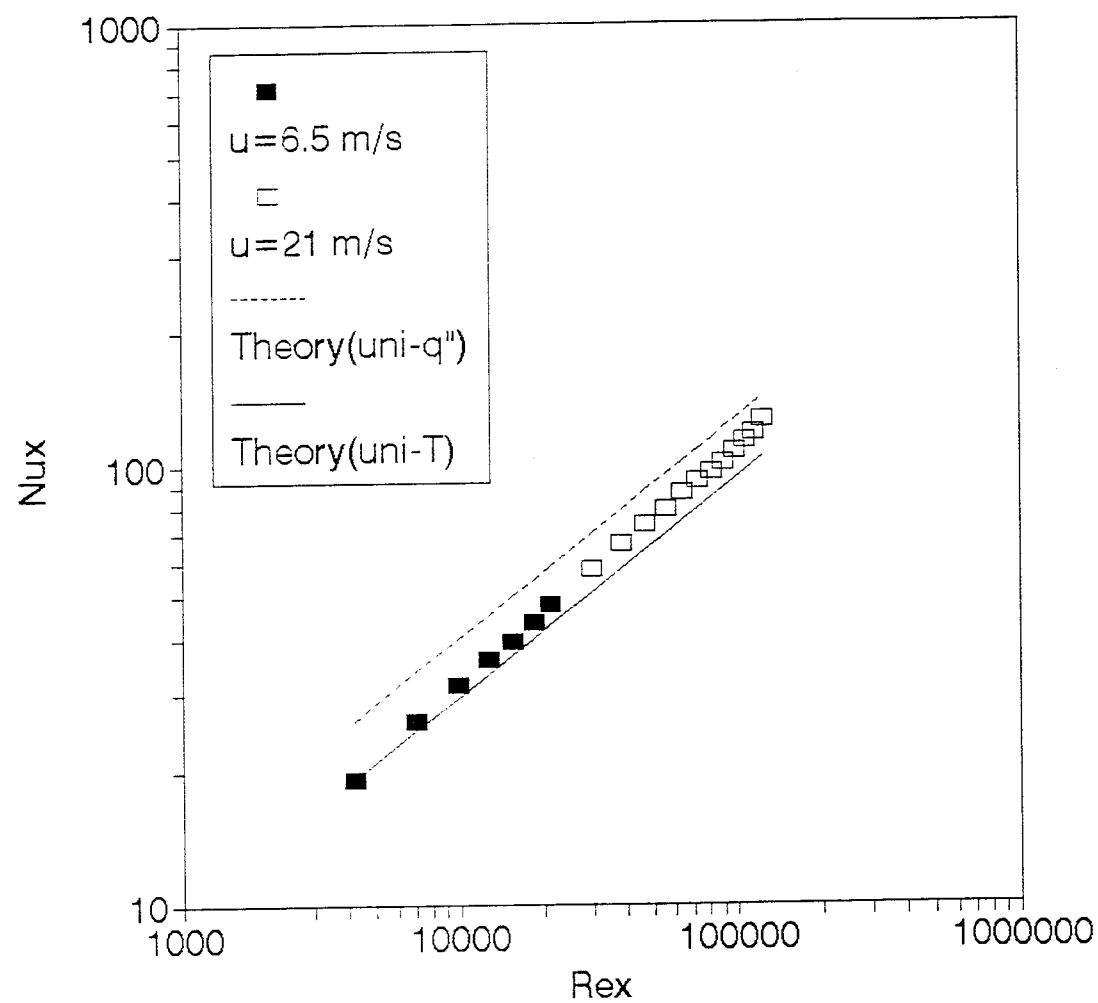


Figure 5.3.2 Effect of Reynolds number (Transient $T^*=.8$)

measurements from transient techniques as compared to other methods. The shroud technique measurements on a flat plate also confirmed that the heat transfer is proportional to the square root of the Reynolds number in a laminar boundary layer.

5.4 Results for the Gold-Film Heated-Coating Method

This section discusses the experimental results for laminar boundary layer flow over a flat plate using the gold-film heated-coating method. We would like to determine the effect of the uniform heat flux boundary condition on the heat transfer measurements. In addition, the Reynolds number effect will be confirmed.

A flat plate model was constructed from .25" thick ponderosa pine four inches wide and a length of 24" to completely span the wind tunnel. Wood was chosen for its strength and low thermal conductivity. The test side of the wood was planned flat and the front edge was cut on the backside to form a sharp 30° leading edge. A .007" thick polyester sheet (6.375" x 3.859") with a thin uniform layer of vacuum deposited gold was applied to the center portion of the wood using spray adhesive. The flat plate gold film was from a different lot than the turbine blade gold film. The flat plate gold film had a resistivity of 2.29 Ohms/square. A thin strip of copper tape was attached to the top and bottom of the gold film. Electrical contact was ensured using silver paint at the junction between the copper bus bars and the gold film. The gold film was air brushed with black paint followed by liquid crystals. For a laminar boundary layer to form, the test side of the flat plate needs to be parallel or slightly windward to the free-stream flow. If the flat surface is at all leeward, a separation bubble forms near the leading edge and the flow is turbulent downstream of the reattachment point. To ensure a

laminar boundary layer, the present tests were performed with the flat surface 1° windward.

The experimental results are plotted in Figure 5.4.1 for a free-stream velocity of 6.7 m/s. For comparison, the theoretical solutions for constant heat flux and uniform temperature boundary conditions are also shown on this graph. The experimental data matches theory for the first half of the plate. The measured heat transfer is slightly higher than theory on the rear of the plate. The trailing edge is blunt, with a square cut .25" thick. The blunt trailing edge causes the flow to deviate from a theoretical "flat plate". This was also observed in the transient measurements. These flat plate measurements were performed first, and because of this trailing edge effect, only experimental measurements (for either method) from the first portion of the plate were used for a comparison with theory.

The effect of Reynolds number was also measured using the gold-film heated-coating method. The flat plate was tested using two different tunnel velocities (6.7 and 21 m/s). The results are shown in a log-log plot in Figure 5.4.2. The Reynolds number effect is the same as what was observed using the shroud technique (although the magnitude is different because the boundary condition is not the same). The slope of the plot is 1/2 decade/decade, therefore, the heat transfer increases at a rate proportional to the square root of the Reynolds number. This again confirms laminar boundary layer theory.

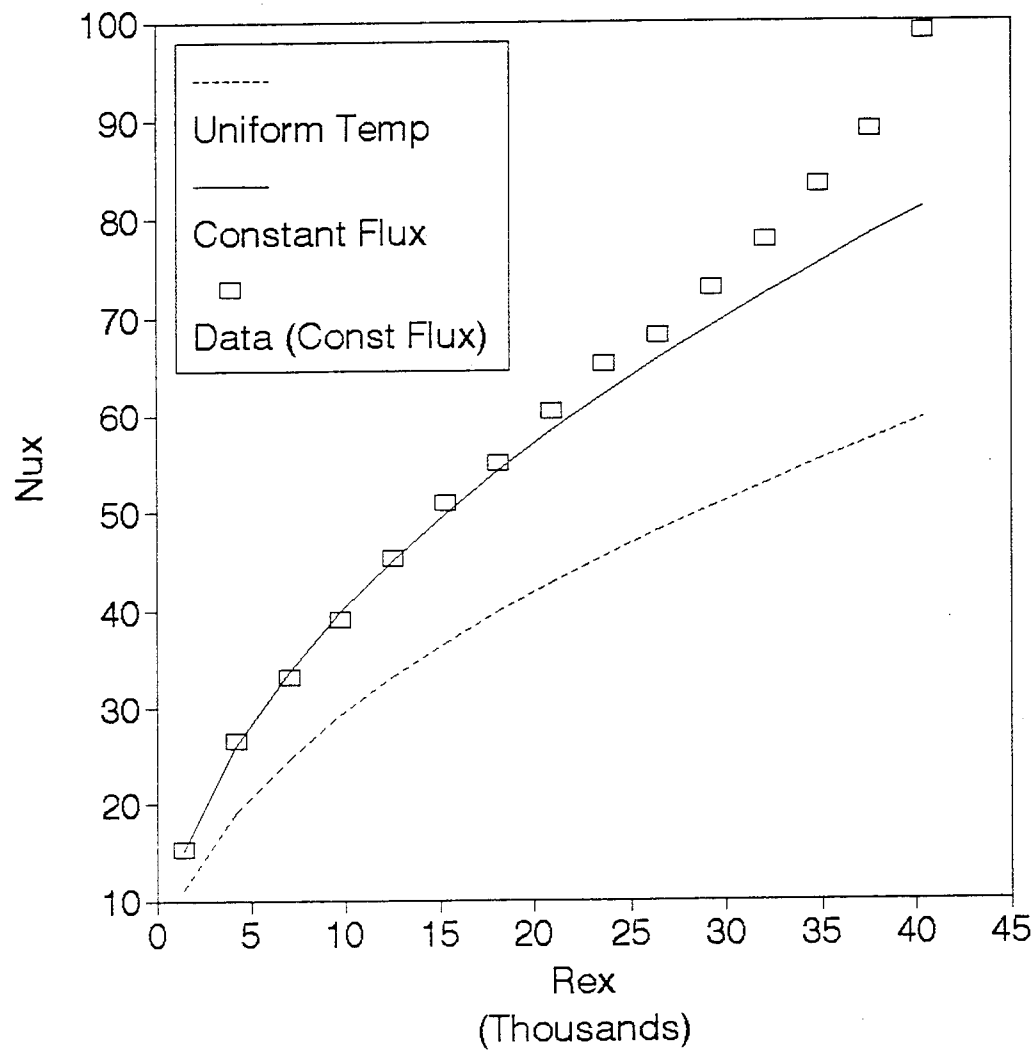


Figure 5.4.1 Laminar flat plate heat transfer (uniform heat flux)

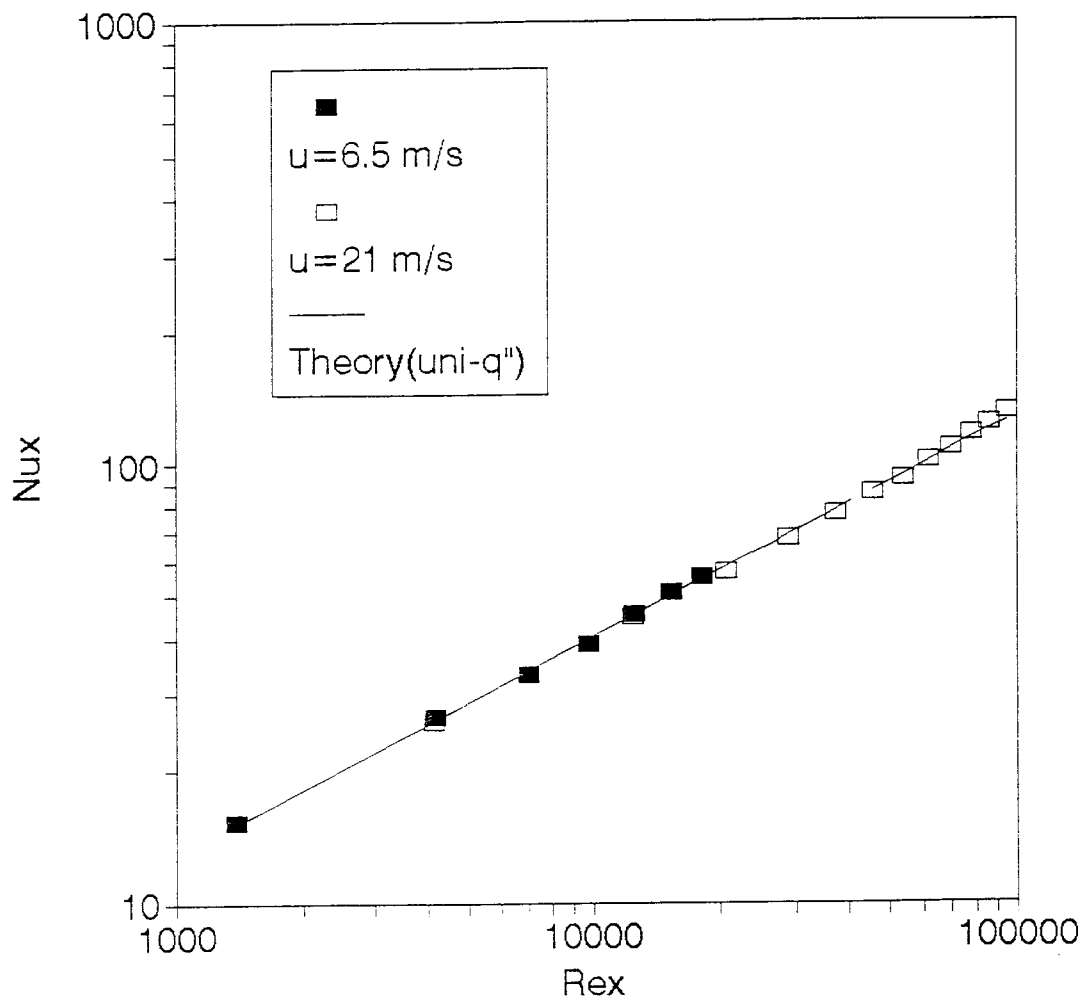


Figure 5.4.2 Effect of Reynolds number (uniform heat flux)

5.5 Comparison, Correlation and Discussion

This section compares the numerical and experimental results for laminar flow over a flat plate with all three types of thermal boundary conditions: uniform wall temperature, uniform heat flux, and the transient wall temperature.

The transient numerical results are compared to the transient experimental results in Figures 5.5.1 and 5.5.2. For reference, the theoretical solutions for a uniform wall temperature and a constant heat flux are also shown on these plots. Figure 5.5.1 compares the $T^*=.9$ and $T^*=.7$ transients. For clarity, a separate plot (Figure 5.5.2) is used for the $T^*=.8$ and $T^*=.6$ results. The experimental results compare very favorably to the numerical solutions. More importantly, the trends are the same, showing higher heat transfer as the nondimensional temperature decreases. The experimental $T^*=.6$ data diverges past $R_{ex}=15,000$. This is caused by excessively long transients which prevent the flat plate model from behaving like a 1-D semi-infinite solid (see Appendix F).

The transient results are very different than other thermal boundary conditions, therefore, a correlation between transient and other results would be valuable. Since a transient test starts at a uniform temperature, a correlation between transient and uniform wall temperature solutions seems logical. Analyzing the numerical data shows that the transient results are dependent on Reynolds number as well as the nondimensional temperature (T^*). The numerical results were chosen to develop a correlation because

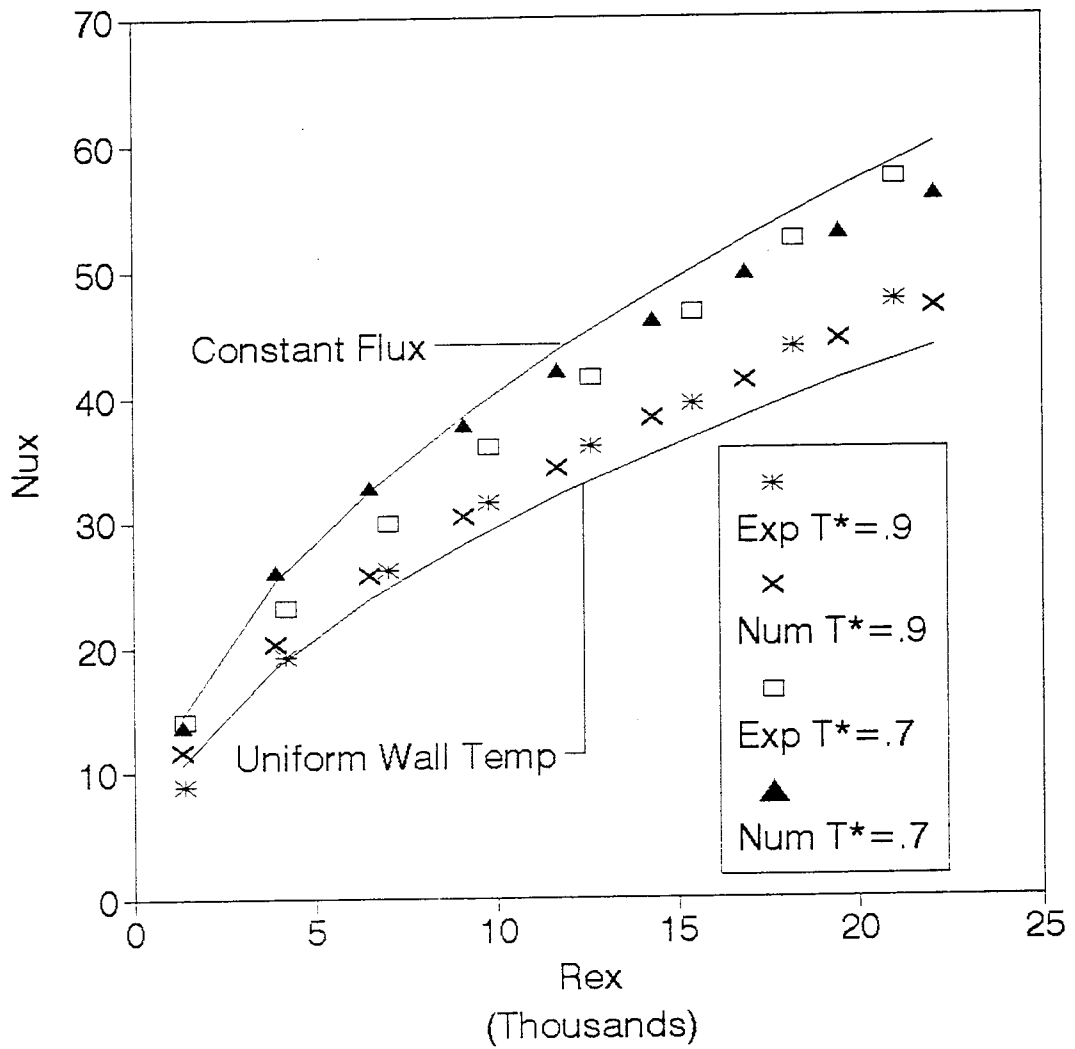


Figure 5.5.1 Numerical solutions compared to experimental ($T^* = .9$ and $.7$)

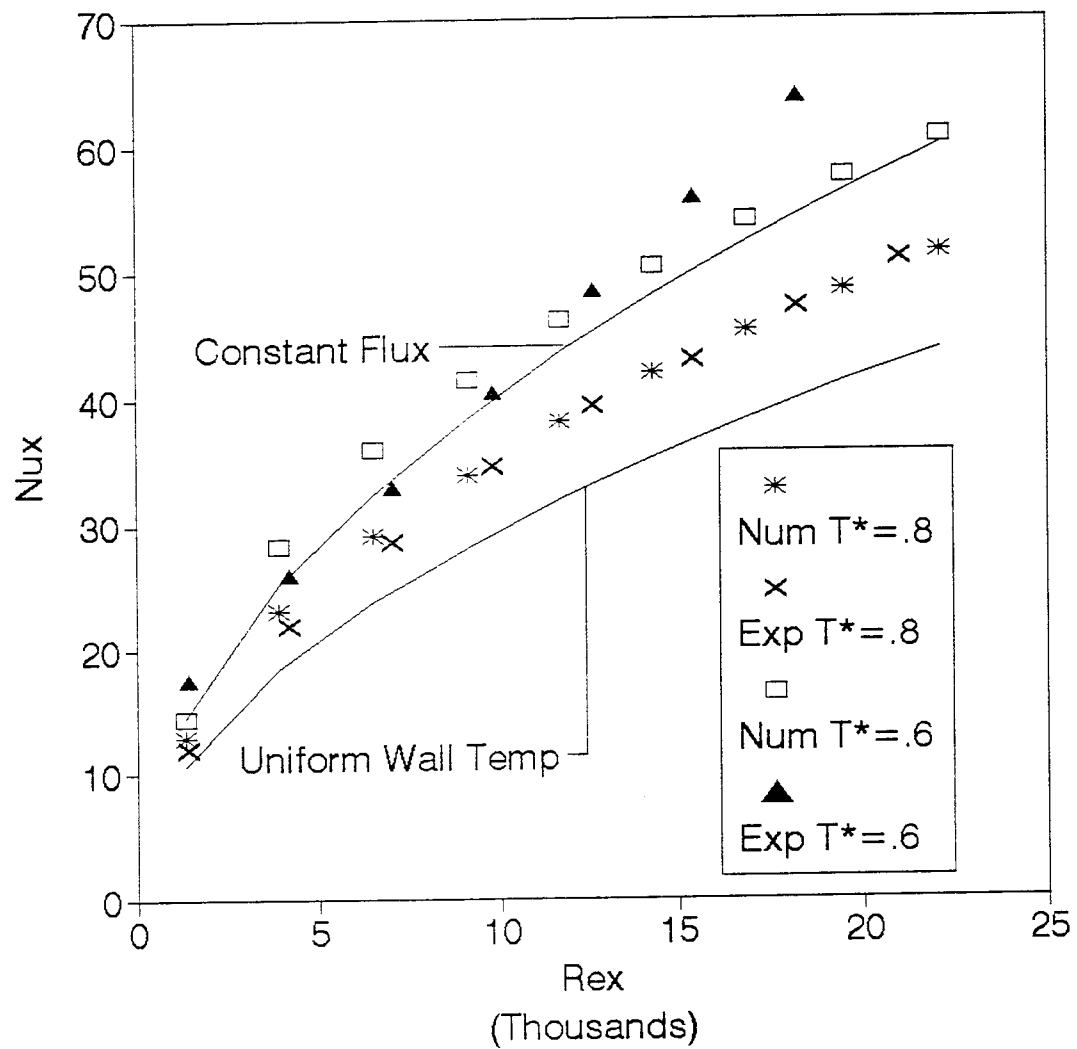


Figure 5.5.2 Numerical solutions compared to experimental ($T^* = .8$ and $.6$)

they are more uniform, though they show the same trends as the experimental data. The following correlation is suggested.

$$Nu_x = Nu_{x*}(T^*)^{\frac{4.9}{Re_x^2}}$$

The transient Nusselt number (Nu_{x*}) is scaled to be equivalent to the uniform wall temperature solution (Nu_x). The correlation is primarily dependent on the transient nondimensional temperature (T^*). It is also a weak function of Reynolds number. This correlation corrected the numerical transient data to be within 1.5% of the theoretical uniform wall temperature solution. This is shown in Figure 5.5.3. This correlation can be applied for Reynolds numbers greater than $700/(T^*)^4$ and is shown to be good up to 40,000, but since it is such a weak function of Reynolds number, it may be good up to 500,000.

This correlation was also applied to the experimental data and the results are shown in Figure 5.5.4. The correlation does a very good job matching the uniform wall temperature solution and reducing the transient solutions to a common solution which is independent of the transient nondimensional temperature. The ($T^*=.6$) data is slightly high further down the plate because the longer transients cause the semi-infinite assumption to be violated.

Overall it can be said that the type of thermal boundary condition for laminar flat plate flow has a profound effect on the local heat transfer measurement. The uniform heat flux boundary condition increases the heat transfer 36% over that of a uniform wall

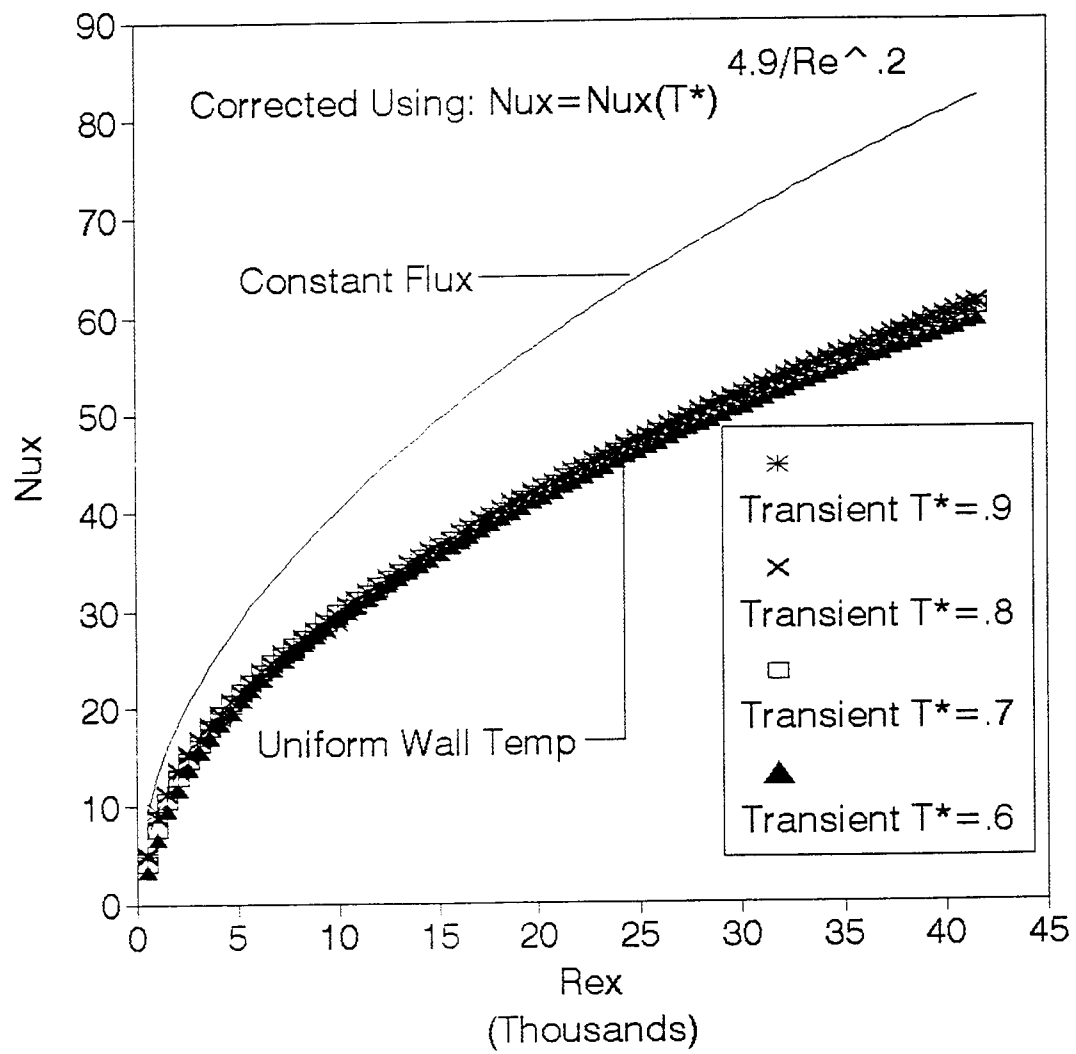


Figure 5.5.3 Transient numerical results corrected by correlation

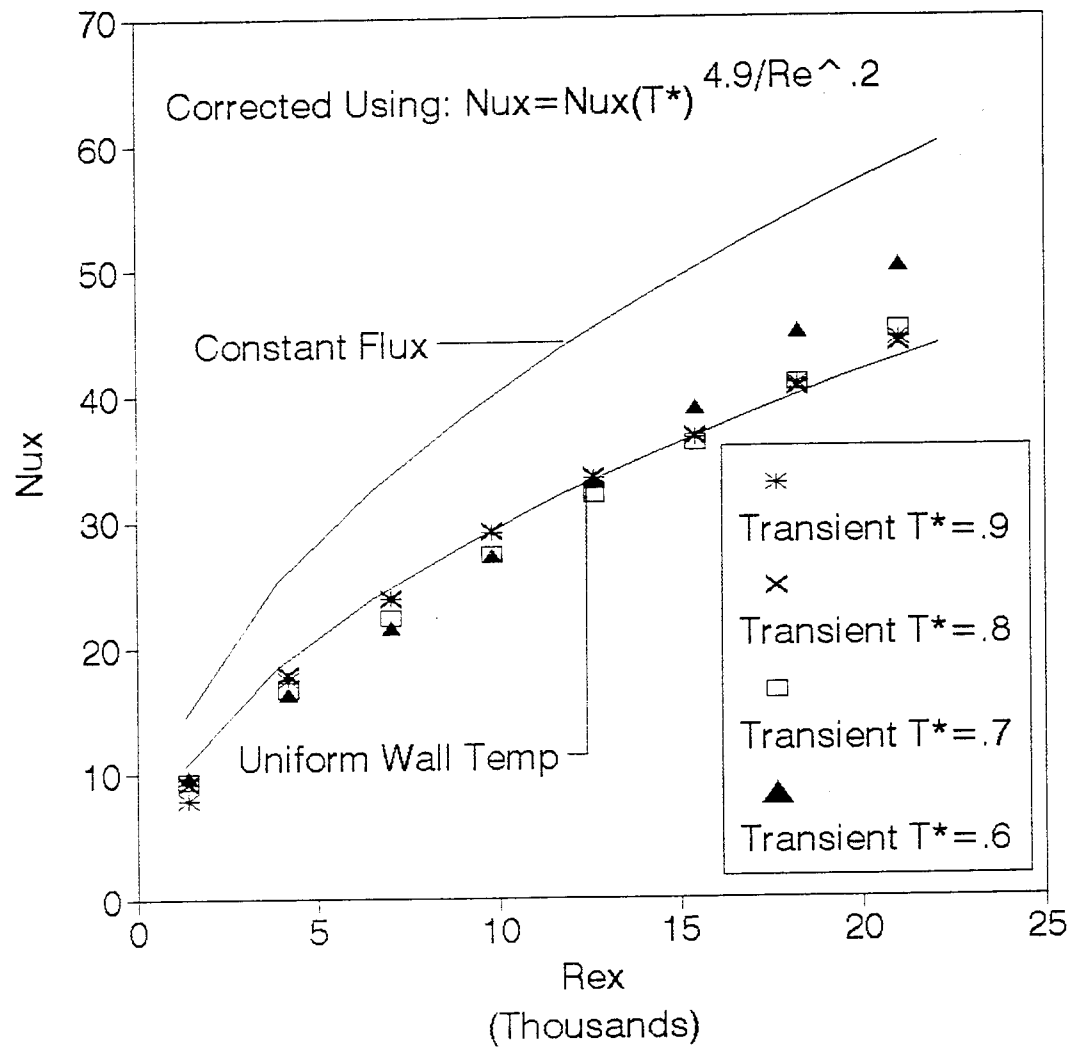


Figure 5.5.4 Transient experimental results corrected by correlation

temperature. Transient methods always measure higher heat transfer than uniform wall temperature conditions, although the amount is dependent on the nondimensional temperature (T^*) used in the transient method. The heat transfer gradients also play a major role in transient measurements. Theoretically, if some geometry could provide a uniform heat transfer coefficient, uniform wall temperature and uniform heat flux methods would give the same result. In addition, under these conditions the local wall temperatures would be equal during a transient test and the resulting transient measurement would be equivalent to the uniform wall temperature and uniform heat flux methods. This is evident near the stagnation point on a cylinder where all three techniques give similar solutions. Transient methods diverge further from uniform wall temperature solutions as the heat transfer gradients increase. The laminar boundary layer is a good example of this because the heat transfer is proportional to $1/\sqrt{R_{ex}}$. Transient methods would not be as different for turbulent boundary layers because they have a more shallow heat transfer gradient (proportional to $1/R_{ex}^2$). Theoretically this is evident when comparing the uniform wall temperature and constant heat flux turbulent boundary layer solutions. The integral solutions (Incropera and DeWitt, 1990) show that the local heat transfer for the uniform heat flux boundary condition is only 4% larger than the uniform temperature solution. Whereas there was a 36% difference between these two solutions for a laminar boundary layer.

This chapter demonstrated the importance of the thermal boundary condition which is imposed by different methods to measure local heat transfer. It is imperative that the method be considered when comparing or using local heat transfer data.

CHAPTER 6 TURBINE BLADE IN A LINEAR CASCADE

In this chapter, the results for local heat transfer measurements on a turbine blade in a linear cascade are reported. Because the linear cascade turbine blade model is two-dimensional a heated-coating method can be used to provide accurate measurements with known thermal boundary conditions. It was determined that the gold-film heated-coating method is best suited for these measurements. The effect of free-stream turbulence intensity ranging from the clean tunnel condition (1%) up to very high grid turbulence (25%) is presented. In addition, the effect of Reynolds number (67,500 to 144,000) is also examined. The cascade results are also compared to rotating rig and Air Force Academy linear cascade results measured on the same turbine blade shape.

6.1 Background

Since the development of the gas turbine engine, improvements in engine efficiency have been gained through improvements to individual engine components. Over the last forty years the turbine stage has gained much of this attention, and recently, most of the research has been on understanding and improving turbine blade cooling and materials.

An actual turbine rotor blade is three dimensional and rotates in an extreme (high temperature and turbulence) environment. Due to these practical limitation, fundamental research on turbine blades is not performed in operating gas turbine engines. Instead, different approaches are used to simplify and separate the different aspects of the turbine

stage. The two different general approaches are cascade (linear and annular) and rotating facilities. The cascade and rotating facilities can further be categorized depending on there use of steady-state or transient testing techniques. A general overview of the history of turbine testing is included. For additional background and much more detail about computational techniques, the outstanding review by Simoneau and Simon (1993) should be consulted.

Cascade testing is generally the simplest model of the gas turbine flow path. Gostelow (1984) defines a cascade to be "an infinite row of equidistant similar bodies". "The cascade plane is obtained by viewing along the blade axis... a cut is made along the streamline and then viewed in a direction parallel to the blade axis or stacking line" (Gostelow, 1984). A linear cascade is formed if this "cut" is unrolled to form a two-dimensional row of blades. An annular cascade is axis-symmetric and "consists of a row of blades mounted between two co-axial surfaces of revolution" (Gostelow, 1984). Testing similarity is improved, although the difficulty is increased when rotation is added. Some rotating facilities are developed from actual hardware, but most are geometrically similar large scale models. Both cascade and rotating facilities can operate under steady-state or transient running conditions. The literature history is easiest to discuss when categorized. This discussion shall group the following types of tests: steady-state cascade, transient cascade, steady-state rotating, and transient rotating.

Steady-state linear cascade research started with very early work by Wilson and Pope (1954). The United Technologies Research Center (UTRC) group started important test cases using a now "famous" blade shape in a linear cascade [Langston et al. (1977) and Graziani (1980)], later they used this shape in rotating tests. Detailed

aerodynamic measurements were performed on the Langston geometry at Virginia Polytechnic Institute [Moore and Ransmayr (1984a, 1984b), Moore and Adhye (1985), Moore and Moore (1985), and Moore et al. (1986)]. Heat transfer data was collected on the Langston geometry at NASA Lewis [Hippensteele et al. (1985), Boyle and Russell (1990)] and numerical computations were performed by Boyle (1991). Priddy and Bayley (1988) investigated the effect of turbulence on turbine blade heat transfer. Turbulence and wake effects were also studied in the linear cascade test facility at the Institute of Thermal Turbomachinery (ITS), Karlsruhe, Germany by Dullenkopf et al. (1991), and Dullenkopf and Mayle (1994). At Detroit Diesel Allison, Nealy et al. (1984) and York et al. (1984) investigated the heat transfer on nozzle guide vanes.

Transient cascade experiments have been performed at Oxford's isentropic light piston tunnel. This facility has been used for transient heat transfer tests on a linear cascade by Schultz et al. (1980) and wake effects by Ashworth et al. (1985). An annular cascade section was added to the Oxford tunnel and transient heat transfer tests were performed on nozzle guide vanes by Wedlake et al. (1989), and Harasgama and Wedlake (1991).

In addition to their linear cascade work, the UTRC group performed many investigations using a steady-state rotating facility with Langston's mean blade geometry [Dring et al. (1986), Blair et al. (1989a), Blair et al (1989b), and Blair (1994)]. At MIT, a rotating blowdown tunnel which operates under some transient and steady-state conditions was used to measure turbine blade heat transfer and compared to Oxford's cascade data (Guenette et al. 1989). A new rotating facility is being run at Pennsylvania State University and is discussed in Lakshminarayana et al. (1992).

Dunn and Stoddard (1979) began an impressive amount of research carried out in a shock tube driven transient rotating facility developed at Calspan. Heat transfer tests were performed on the Garrett TFE 731-2 [Dunn and Stoddard (1979), Dunn and Hause (1982), Dunn et al. (1984a, 1984b), and Dunn (1990)], Teledyne CAE 702 HP [Dunn and Chupp (1988), and Dunn et al. (1989)], and the Rocketdyne Space Shuttle [Dunn et al. (1994)] engines in this facility. Oxford is also performing transient rotational tests. Their heat transfer technique and instrumentation is explained by Ainsworth et al. (1989).

The type of facility (cascade vs. rotating) is not important when considering the method for measuring heat transfer, but the facilities operating condition (transient versus steady-state) must be considered. Most transient facilities use a method developed by Schultz and Jones (1973). These methods use a resistance gage to measure the surface temperature and a circuit which is an electrical equivalent to the semi-infinite conduction equation to directly measure heat flux. This method or one based on the same idea was used in all of the following tests: Schultz et al. (1980), Ashworth et al. (1985), Ainsworth et al. (1989), Wedlake et al. (1989), Harasgama and Wedlake (1991), Dunn and Stoddard (1979), Dunn and Hause (1982), Dunn et al. (1984a, 1984b), and Dunn (1990), Dunn and Chupp (1988), and Dunn et al. (1989), and Dunn et al. (1994). These techniques have the ability to give high frequency heat transfer fluctuations. Guenette et al. (1989) developed a similar transient method but it used two temperature sensitive resistance gages with an insulating material between them. Like the other methods, this gage uses the outer temperature for high frequency

data, but this gage uses a temperature difference across a known insulating resistance to measure low frequency heat transfer.

Steady-state cascade and rotating facilities use other methods to measure heat transfer. Wilson and Pope (1954) used individually heated nichrome strips to create a uniform temperature, the local heat transfer could then be determined on each strip. Turner (1971) developed a technique which used cooling tubes running through a turbine blade model. The surface temperatures and the advected energy across each tube were measured. These measurements were then used as boundary conditions solving Laplace's equation for conduction inside the blade, the local heat transfer was determined by the local conduction surface temperature gradient. Similar methods were later used by Nealy et al. (1984), York et al. (1984), Dullenkopf et al. (1991), and Dullenkopf and Mayle (1994). Like the present method, many techniques produce a known uniform heat flux from the surface by passing current through a resistive material. The local surface temperatures are then measured to determine the local heat transfer. Graziani (1980), Dring et al. (1986), Blair et al. (1989a), Blair et al (1989b), and Blair (1994) used this technique with thermocouples to measure surface temperature. Like the present method, Hippensteele et al. (1985), and Boyle and Russell (1990) used liquid crystals to measure surface temperature.

6.2 Linear Cascade Apparatus

A linear cascade facility was developed by adding a turning cascade section onto an existing UC/Davis wind tunnel. The wind tunnel is open loop and is driven by a 50 HP constant speed motor operating a centrifugal compressor. A 16 to 1 stilling chamber

with screens is used upstream of the wind tunnel nozzle to reduce free-stream turbulence. Adjustable vanes on the compressor allow for a variable speed from 6 to 14 m/s with the cascade section attached. The clean tunnel free-stream turbulence was measured with a hot-wire to be approximately 1.0% (see Appendix I). The wind tunnel is open loop and without the cascade section has an exit area of 24 x 40 inches. The cascade section (with an inlet of 24 x 40 inches) is mated to the exit flange of the existing tunnel. The wind tunnel and attached cascade section is shown in Figure 6.2.1.

The cascade geometry is shown in Figure 6.2.2 and its measured parameters are listed in Table 6.2.1. The x-axis is defined to be in the axial direction. Cascade angles are defined relative to the y-axis. The cascade angles are the same as used by Langston et al. (1977) and Graziani et al. (1980), although, there tunnel used four blades with a rather low aspect ratio of approximately 1.0. Gostelow (1984) suggests an aspect ratio of 4.0 to achieve two-dimensional flow in a turbine cascade. The present cascade has seven blades (nine blades including the end walls) with an aspect ratio of 3.52. Due to the favorable pressure gradient through the turbine cascade, boundary layer bleeds are not required (Gostelow, 1984). With an aspect ratio of 1.0, Graziani (1980) found the pressure surface to be essentially two-dimensional, but the suction surface was still dependent on the inlet boundary layer size. Ports are located in the top of the cascade for aerodynamic measurements. The ports are located one axial chord upstream for free-stream measurements and 40% axial chord downstream for wake measurements. Periodicity is achieved by making fine adjustments to the tailboard. The present study used a turbine airfoil shape with a very long history, it was first used in cascade tests

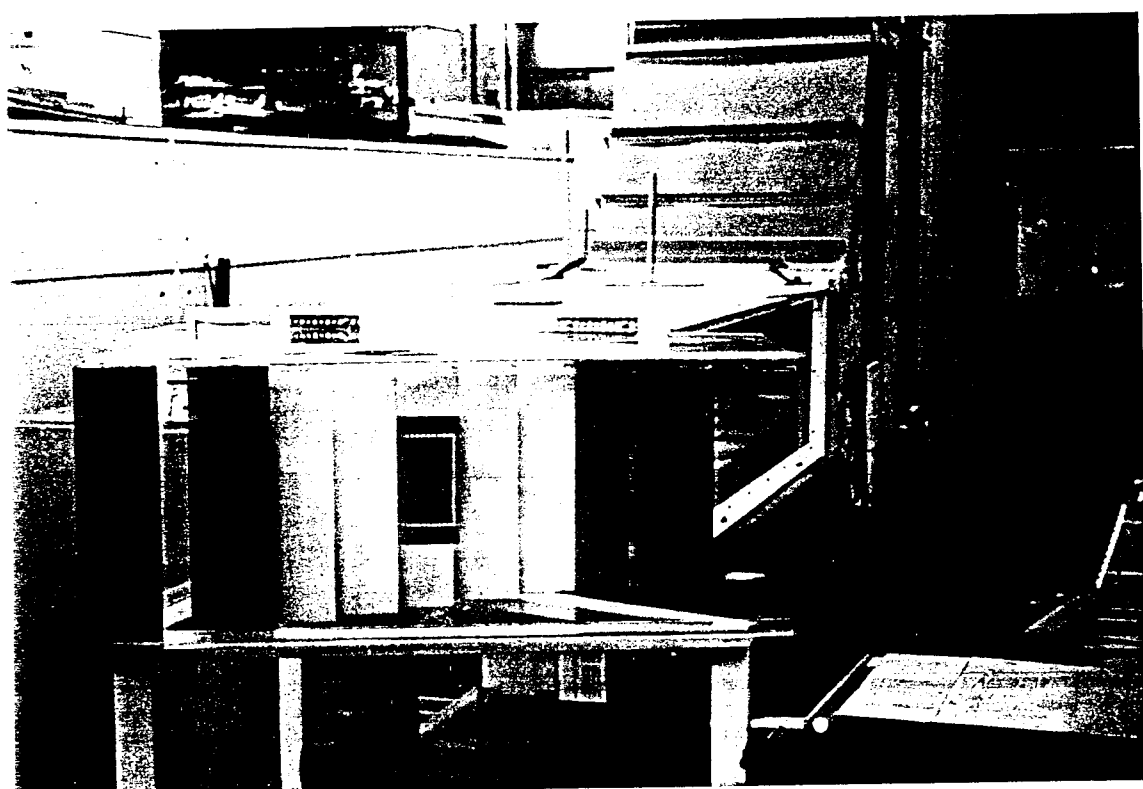


Figure 6.2.1 Wind tunnel with attached cascade section

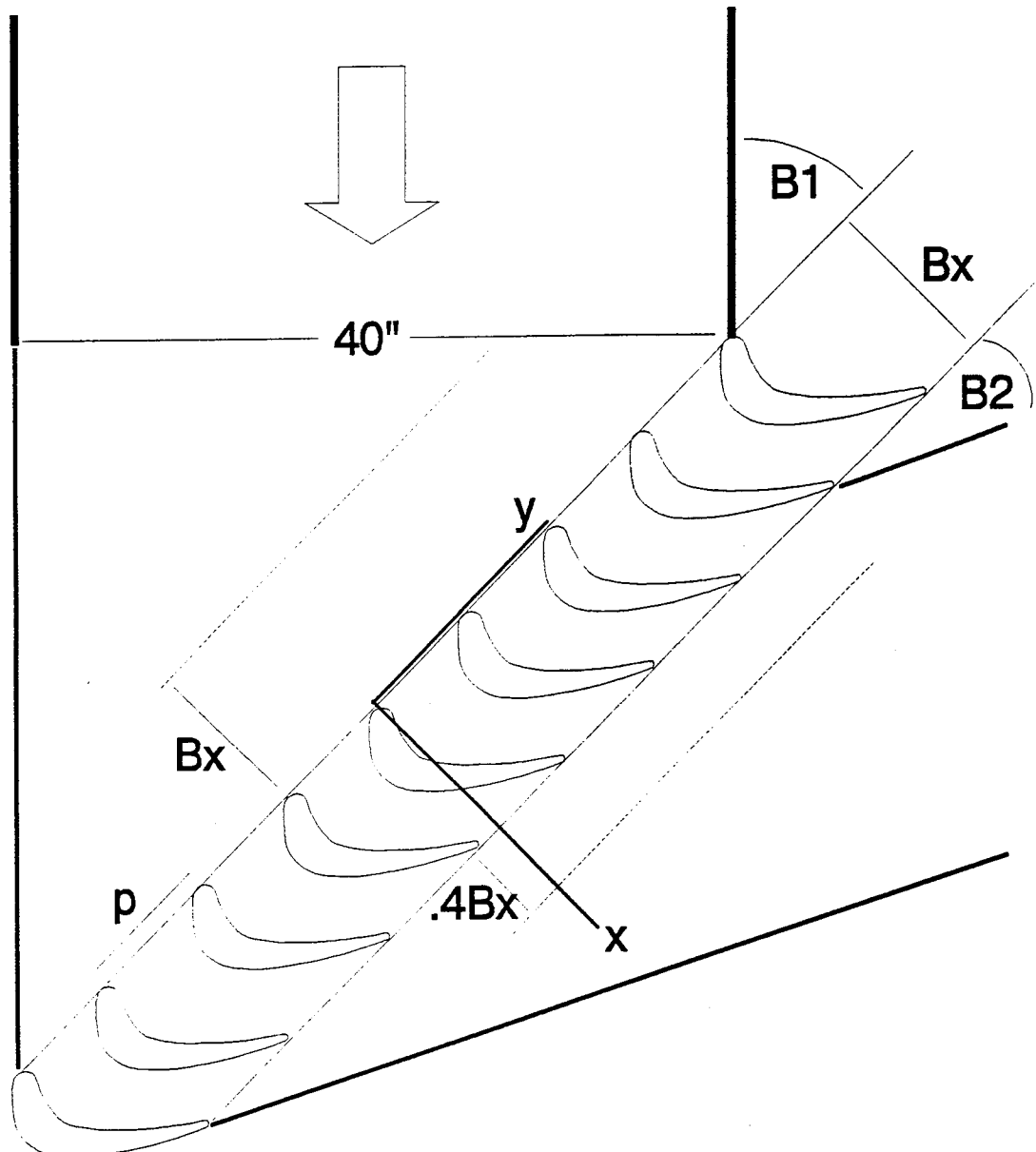


Figure 6.2.2 Linear cascade geometry

Table 6.2.1 Cascade Geometry

Axial Chord (Bx)	6.82"
Pitch (p)	6.25"
Pitch/Axial Chord (p/Bx)	.92
Aspect Ratio (Span/Axial Chord)	3.52
Inlet Camber Angle	42°
Exit Camber Angle	26°
Air Inlet Angle (β_1)	44.7°
Air Exit Angle (β_2)	26°

by Langston et al. (1977). It is also geometrically similar to the mean blade geometry used in rotating tests by Dring et al. (1986) and Blair et al. (1989a, 1989b). The turbine blade shape is shown in Figure 6.2.3, this blade shape is 7.5% larger than the mean geometry of Dring et al. (1986) and Blair et al. (1989a, 1989b). The physical coordinates of the turbine blade are listed in Appendix M. The turbine blade shape is that of a heavily loaded machine with a design flow coefficient of .78, stage loading coefficient of 2.8, and 34% static pressure reaction (Blair et al. 1989a, 1989b). The turbine blade has an inlet mean camber line of 42° and an exit mean camber line is 26° . The air inlet angle is 44.7° , therefore the blade is operating at -2.7° of incidence. The axial chord is 6.82 inches and blade pitch is 6.25 inches. Locations on the turbine blade were measured relative to a geometric zero which is determined by placing a straight edge across the concave portion of the turbine blade. The tangent point near the leading edge is used as the reference point ($s=0$). Note, this location is not the stagnation point, although, this reference location is easier to duplicate and is consistent with Blair et al. (1989a, 1989b). The turbine blades were hot-wire cut from 2 lb/ft³ polystyrene. The test blade is shown in the cascade row in Figure 6.2.4. Further details about the turbine blade construction are given in section 3.2. Heat transfer tests were performed on the center blade using the gold-film heated-coating method.

A turbulence generating grid is used in selected test cases to simulate the high level of turbulence which exists in operating gas turbine engines. Grid turbulence theory and correlations provided by Baines and Peterson (1951), and Roach (1987) were used to design a square-mesh array of square bars. The grid was fabricated from redwood and a photograph of the grid in the cascade is shown in Figure 6.2.5. The square bar

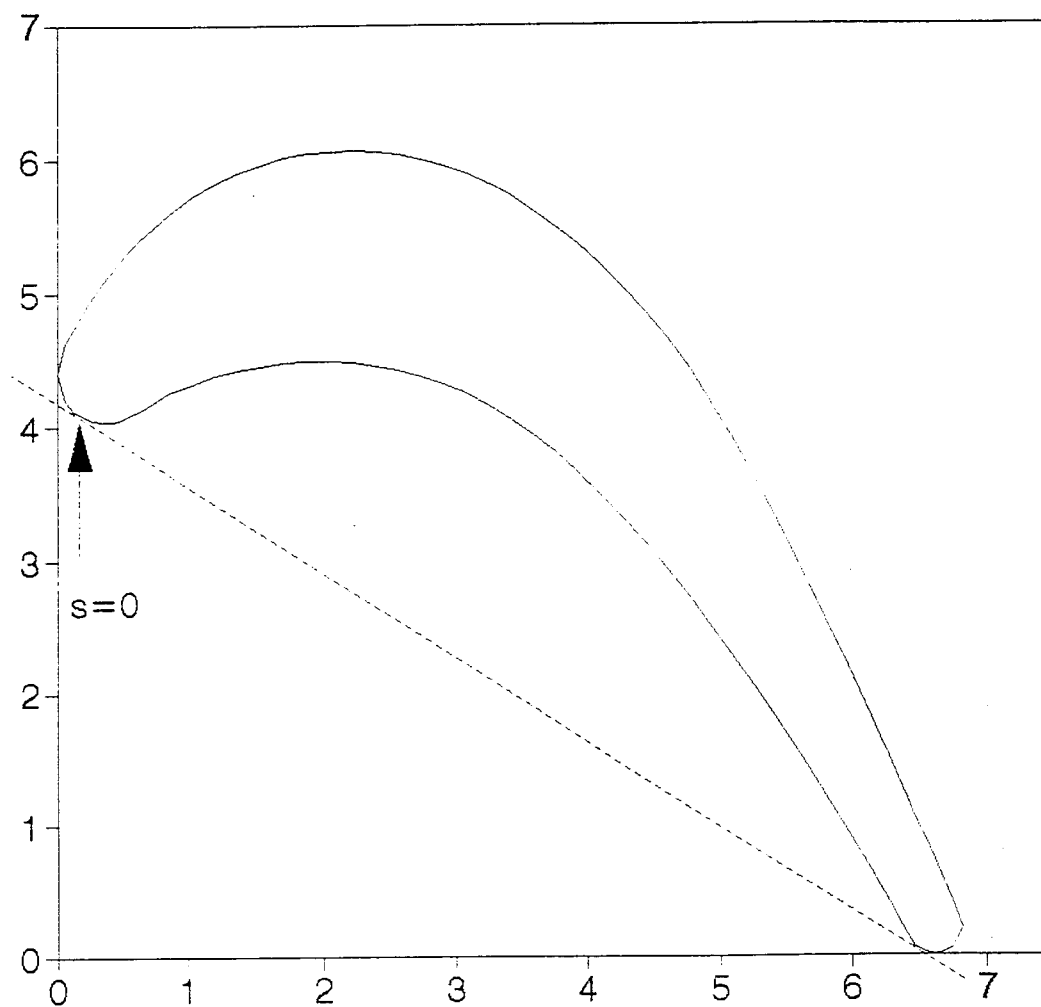


Figure 6.2.3 Turbine blade geometry

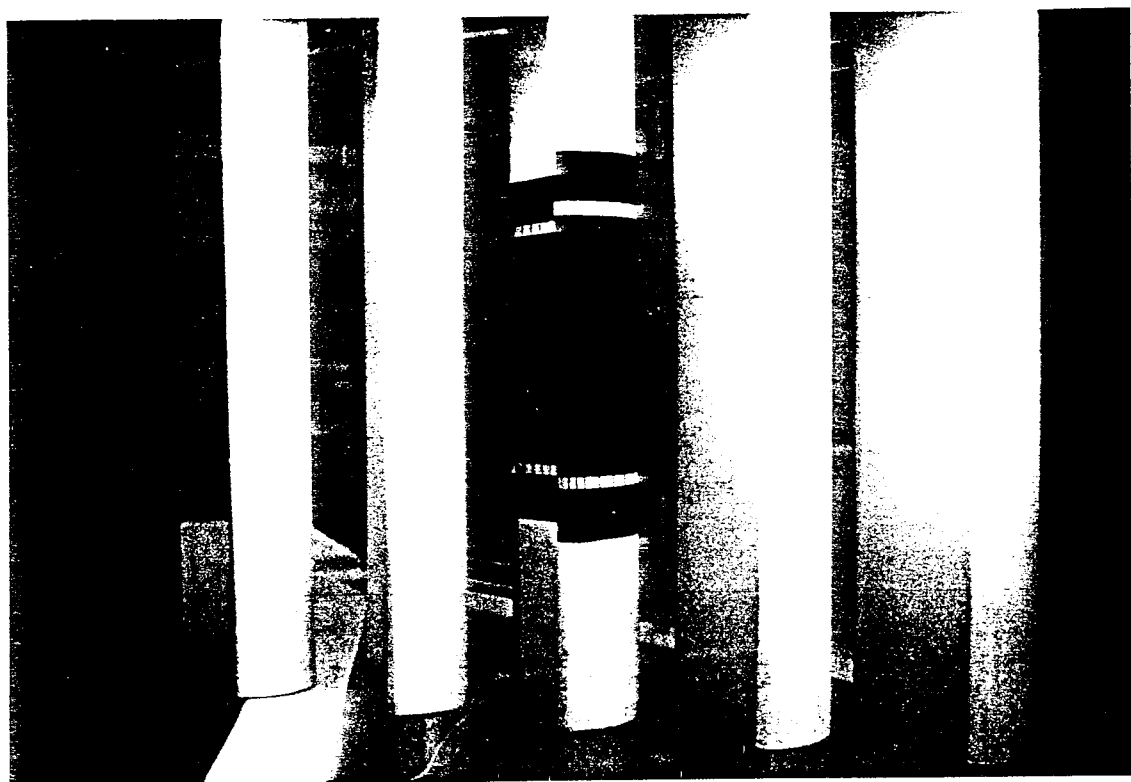


Figure 6.2.4 Heat transfer turbine blade in the cascade



Figure 6.2.5 Turbulence grid in the cascade tunnel

width is 1.5 inches and the bar centerline-to-centerline is 6.0 inches. By placing the grid 45 inches upstream, the grid is designed to produce 10% turbulence intensity at the leading edge of the test blade. Grid turbulence decays as it travels downstream and the grid is placed perpendicular to the flow, therefore due to the cascade angle, the turbulence level is slightly different for each blade in the cascade. Eddy scales increase as the grid turbulence decays downstream. Assuming the turbulence to be isotropic and homogeneous, the turbulence length scales can be estimated using theory (Roach, 1987). The grid turbulence macro-scale is estimated to be 1.6 inches and is independent of free-stream velocity. The micro-scale is estimated to be .28 inches (at 6 m/s) and .20 inches at 12 m/s.

6.3 Aerodynamic Results

Aerodynamic tests were performed to characterize the linear turbine blade cascade. Measurements were performed 1.0 axial chord length in front of the blade row and .4 axial chord length in the wake of the row. A 24 inch width along the y-axis (which spans roughly five blades) was traversed at each location. Velocity, turbulence intensity, and flow angle were measured at each location. Two Reynolds numbers based on inlet conditions were used which represent the lowest and highest operating conditions for the tunnel. Each Reynolds number was used with and without the turbulence grid in place.

The free-stream velocities were measured using a pitot-static tube and a micro-manometer. The results for both Reynolds number with and without the grid are shown

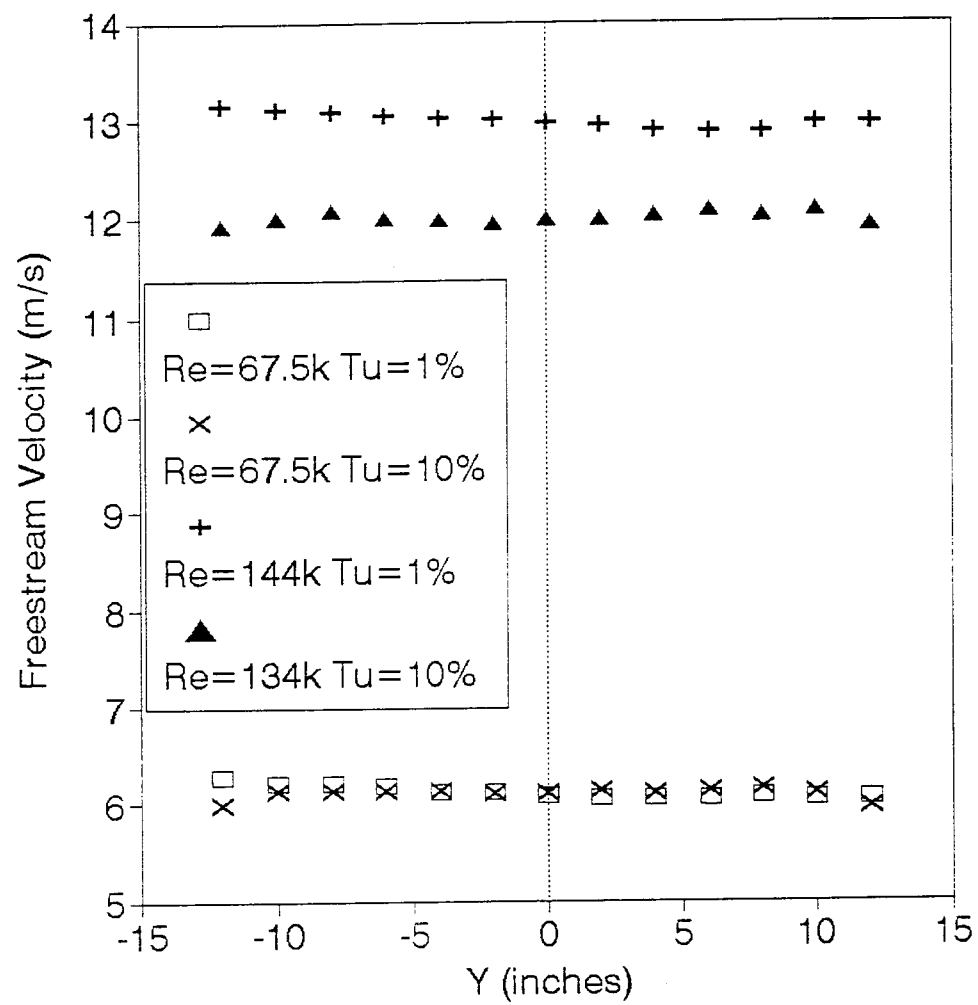


Figure 6.3.1 Free-stream velocity

in Figure 6.3.1. With the grid at the highest Reynolds number, the pressure drop across the grid limited the tunnel's maximum velocity to roughly 12 m/s. Without the grid at the highest Reynolds number, the tests were performed at 13 m/s to match the velocity used by Byerley and Baughn (1994) in the USAF Academy cascade tunnel. Ideally, the flow would be constant across the tunnel for each case. Adjustments to the tailboard were made to produce nominally uniform velocity across the cascade. The tailboard setting providing the most uniform velocity was determined to be 5 inches from the wall blade. In each case without the grid, it is evident that there is a shallow velocity gradient across the tunnel (high to low in the positive y direction). This is also the case with the grid, although it is harder to discern because the measurements pickup variations of velocity caused by the grid. The grid produces wakes and jets which mix as they travel downstream. Due to the angle of the cascade, the measurement locations move closer to the grid as y increases.

Free-stream turbulence intensity was measured using a TSI constant temperature hot-film anemometer. A .002 inch diameter platinum hot-film sensor (TSI 1210-20) was used operating at an overheat ratio of 2.0. Data was collected at 1000 Hz using a 12 bit (10 V range) analog-to-digital board. The uncertainty of the hot-film measurements was estimated to be 5%. See Appendix I for data reduction and further detail about the hot-film calibration. The free-stream turbulence intensity is shown in Figure 6.3.2. Without the grid in place, the turbulence level is independent of velocity and is nominally 1%. With the grid, the plot shows the natural decay of the turbulence as it travels downstream. Due to the angle of the cascade, the measurement locations are

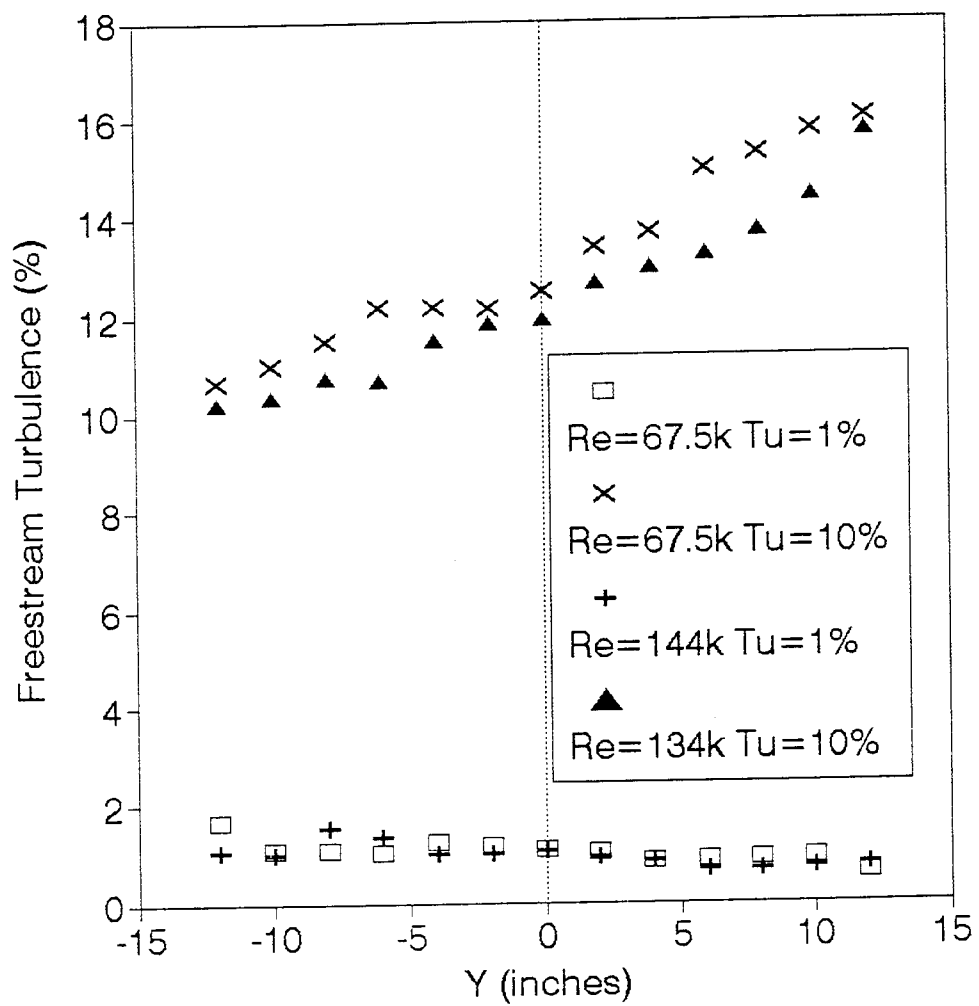


Figure 6.3.2 Free-stream turbulence

closer to the grid as the y location goes up. The turbulence intensity at the leading edge of the test blade can be extrapolated from these results. Viewed perpendicular to the flow, the -12 inch (y) location is 1 inch upstream of the test blade. Therefore, it can be seen from this graph that the test blade turbulence intensity is nominally 10% (grid design theory correctly predicted this result).

Wake velocity measurements were taken using the TSI constant temperature hot-film anemometer. The static pressure on a pitot-static tube is very sensitive to flow angularity, therefore, a pitot-static tube was not used in the wake of the blades. The wake velocities are plotted in Figure 6.3.3. In all four cases, the velocity deficit is evident behind the five center blades. The center region (between the center three blades) shows very good symmetry, although, the upstream velocity gradient is more evident in this plot due to the acceleration of the flow. The wake velocities are lower in the far positive y -direction as compared to the far negative y -direction. The favorable pressure gradient across the cascade produces a velocity increase through the cascade. Based on the hot-film measurements and a spatial average of the wake velocities, on average the exit velocity is 65% larger than the free-stream velocity. Many researchers use cascade exit conditions to normalize their results. To base the present Reynolds numbers on exit conditions they must be increased by 65%.

The turbulence intensity of the wake flow was also measured using the hot-film sensor and is plotted in Figure 6.3.4. The region right behind each blade is evident in this plot by the high turbulence intensity produced in the shearing wake of the blade. The 8% turbulence in these regions is insensitive to upstream turbulence intensity. The flow between the blades accelerates through the cascade which dampens the turbulence

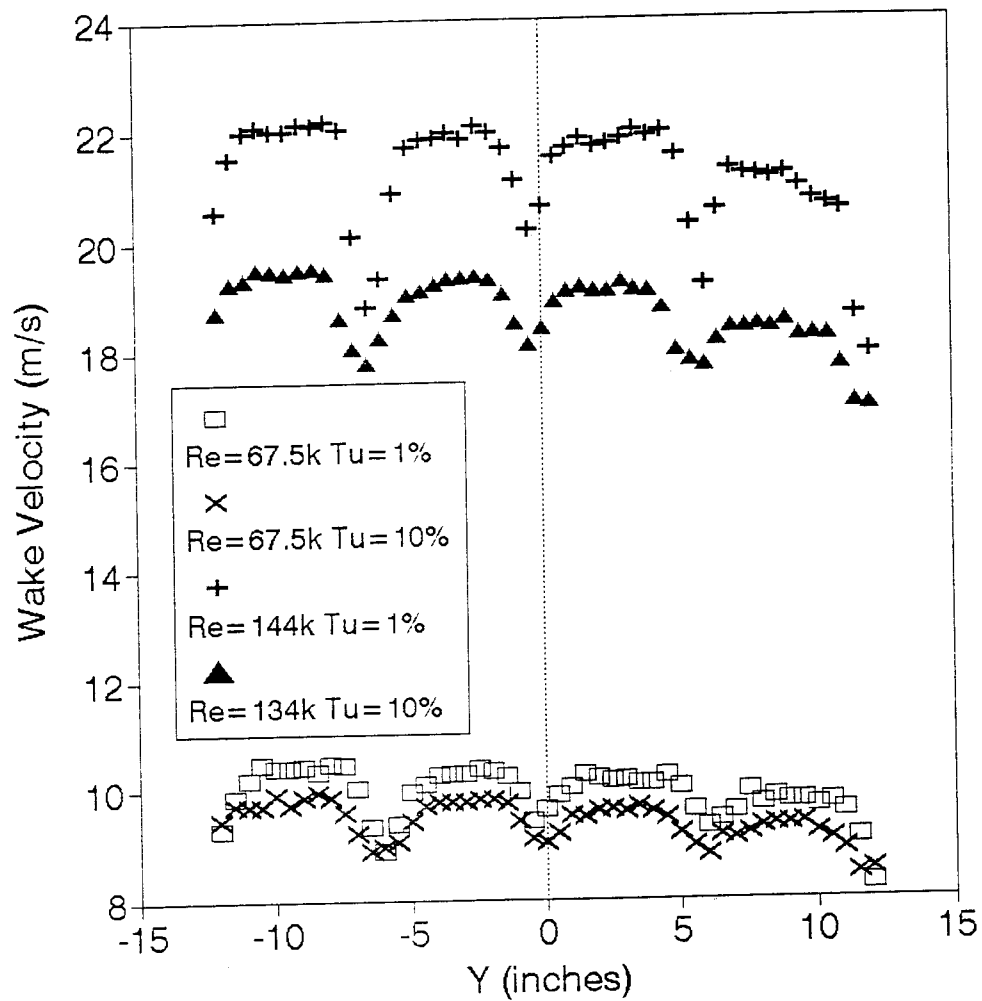


Figure 6.3.3 Wake velocity

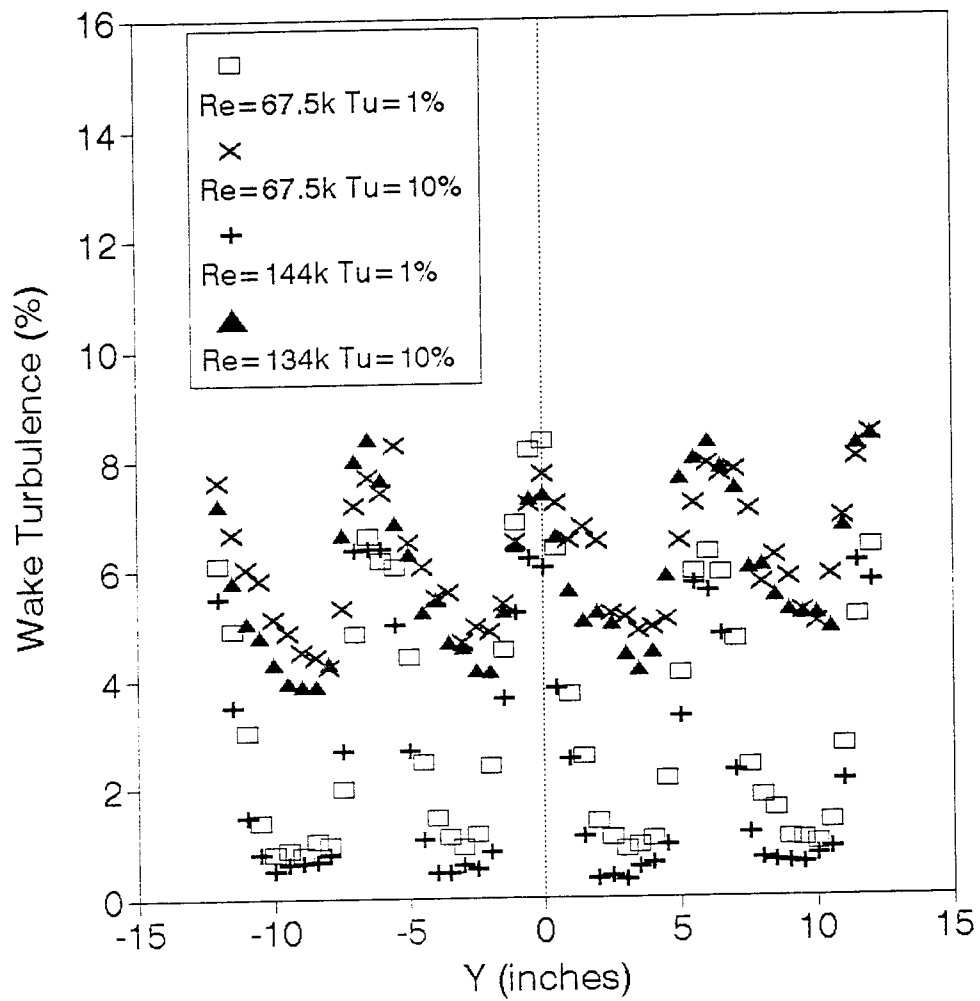


Figure 6.3.4 Wake turbulence

(without the grid, the turbulence intensity drops to .5% from a free-stream value of 1%). With the grid, the turbulence between the blades drops from a free-stream value of 10% to 4%. With the grid this is due to two effects, the natural decay of the grid turbulence and the acceleration of the flow. The turbulence intensities are independent of Reynolds number in all cases.

The flow angularity of the wake region was measured using a pressure nulling wedge probe. This technique is estimated to be accurate to 1° . A typical wake flow angle plot is shown in Figure 6.3.5. Due to the resolution of the measurement, these results do not tell us very much. The flow changes direction slightly (from roughly 27° to 26°) in the wake of each blade. The interesting feature is that the flow nominally exits the cascade at 26° (relative to the y-axis), which is the design camber angle for this turbine blade airfoil.

6.4 Results for the Gold-Film Heated-Coating Method

The present investigation sought to understand the Reynolds number and free-stream turbulence intensity effect on the local heat transfer around a turbine blade shape. The gold-film heated-coating method using liquid crystals was chosen for the complex, although two-dimensional shape of the turbine blade cascade. Four primary conditions were tested, low and high Reynolds number, with and without the turbulence generating grid. In addition to the four primary cases, the effect of very high turbulence levels was determined by placing the grid very near the cascade section. For clarity, the very high turbulence results are presented at the end of this chapter.

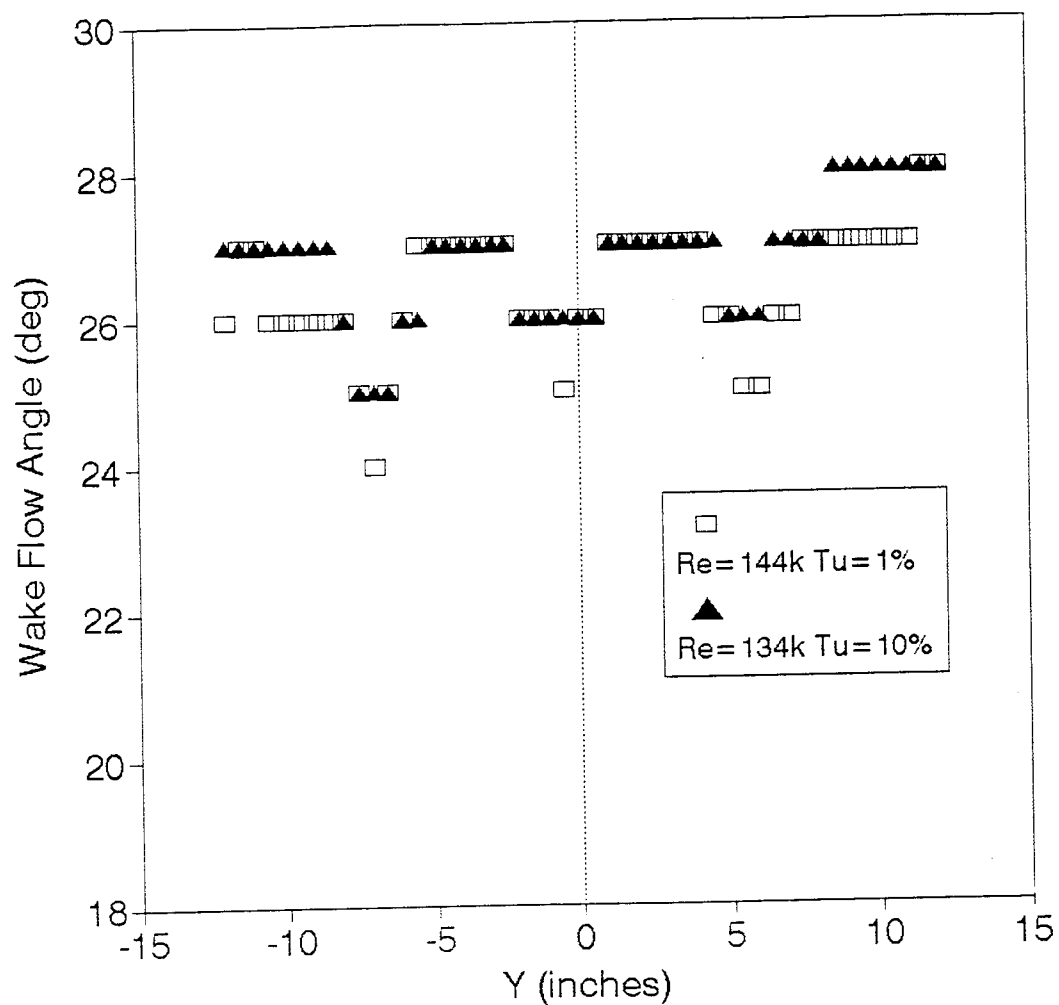


Figure 6.3.5 Wake flow angle

The general shape of the local heat transfer distribution is primarily driven by geometry, therefore, lets first discuss a typical heat transfer plot (Figure 6.4.1). The leading edge is cylindrical in shape and the heat transfer behaves very much like the forward region of a cylinder in cross-flow. The highest heat transfer exists at the stagnation point of the leading edge ($s/Bx=.03$). The flow accelerates rapidly around the cylindrical leading edge and the boundary layer grows. The growing boundary layer decreases the local heat transfer very rapidly from $s/Bx=.03$ to .15 (on the suction surface) and $s/Bx=.03$ to -.11 (on the pressure surface). On the suction surface, the flow continues to accelerate from $s/Bx=.15$ to roughly 1.0 and the heat transfer decreases much like laminar flow over a flat plate. The favorable pressure gradient helps the boundary layer stay laminar. The flow goes through an adverse pressure gradient as it decelerates from roughly $s/Bx=1.0$ to the end of the suction surface. If the boundary layer is still laminar, the adverse pressure gradient will either help the boundary layer to transition or cause it to separate. Boundary layer transition causes the heat transfer to increase in the transition region, followed by decreasing levels as the fully turbulent boundary layer grows. If the boundary layer separates, the heat transfer would be very low in the separated region. Going back to the end of the cylindrical leading edge on the pressure surface, the flow decelerates slightly over a short region (from $s/Bx=-.11$ to -.22), so the laminar boundary layer grows and the heat transfer decreases. In some cases (with the grid) the laminar boundary layer transitions to turbulent in this region, causing the heat transfer to increase. From $s/Bx=-.22$ to the end of the pressure surface, the flow encounters extreme concave curvature. If the boundary layer is turbulent, the concave surface holds the heat transfer relatively constant at turbulent levels. When the

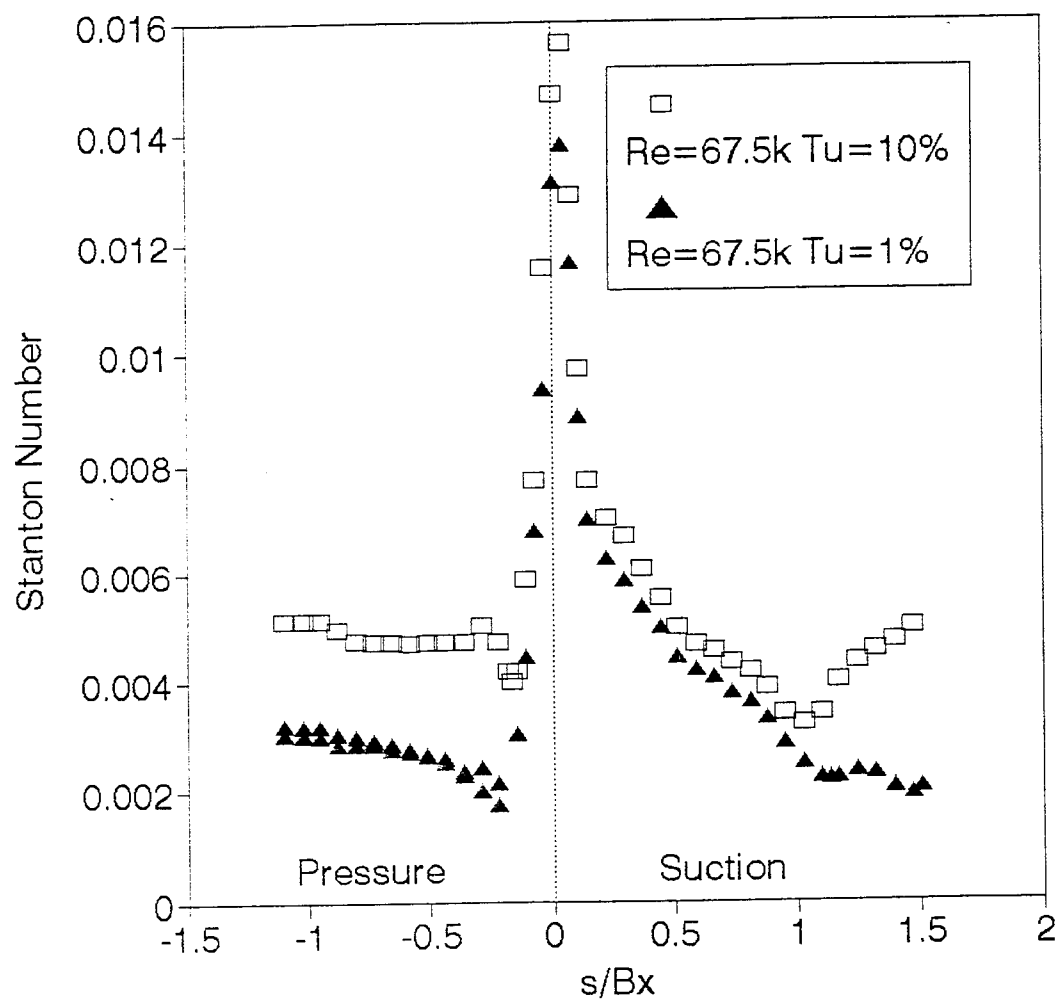


Figure 6.4.1 Effect of grid turbulence ($Re=67,500$)

boundary layer is still laminar, the concave curvature region has spanwise variation in the heat transfer which could be caused by Taylor-Gortler (discussed in the next section) vortices which form and enhance the heat transfer, but the overall level is still below that of a turbulent boundary layer.

The effect of turbulence on the local heat transfer (at 67,500 Reynolds number) is shown in Figure 6.4.1. The grid turbulence increases the heat transfer by 13% at the stagnation point. This is consistent with Lowery and Vachon (1975), and the many others who have investigated turbulence effects on the stagnation region of a cylinder. On the suction surface, the laminar boundary layer grows and the heat transfer decreases, although the grid elevates the heat transfer by roughly 12% over that of the clean tunnel case. The heat transfer distributions have different magnitudes, but the same shape until $s/Bx=1$. At this location, the heat transfer distributions change dramatically. With the grid, the boundary layer transitions to turbulent and the resulting heat transfer increases. Without the grid, the heat transfer has two minimums, both at very low heat transfer levels. Because of the low Reynolds number and turbulence level, it was suspected that one of these minimums was boundary layer separation. A technique suggested by Baughn and Rivir (1994) was tried to non-intrusively determine the flow direction. A 20 mW Helium-Neon laser was used in conjunction with the gold film heater. Power was applied to the gold film to bring this location very near, but below ,the liquid crystal color play temperature. The location of interest was then further heated using the laser. The laser heated a very small circle above the liquid crystal color play temperature. The laser was then turned off and the color shape was observed. The laser produced a hot spot which advected in the direction of the surface

flow and this flow direction was detected by a "tail" of color from the circle. We shall refer to this as the "liquid crystal thermal tuft." The thermal tuft showed that the flow continued down the blade at the first minimum, but didn't seem to have any direction at the second minimum. This would suggest that the second minimum is boundary layer separation. Now looking at the pressure side heat transfer distributions, the two curves show decreasing heat transfer as the laminar boundary layer grows from the stagnation point to $s/Bx=-.16$ (although, the grid increases the heat transfer by an average of 23% in this region). At $s/Bx=-.16$, the grid case heat transfer increases due to boundary layer transition, while the clean tunnel heat transfer continues to decrease until $s/Bx=-.22$. With the grid, the concave curvature and turbulent boundary layer produce fairly constant high levels of heat transfer on the rest of the pressure surface. Without the grid, spanwise variation of the local heat transfer coefficient was evident by liquid crystal "color fingers". A photograph showing the "color fingers" is shown in Figure 6.4.2. These variations in the data are presented in the plot by showing both the maximum and minimum heat transfer for any location. This could possibly be Taylor-Gortler vortices which form on the concave portion of the pressure surface. The high heat transfer regions are produced by downflow between vortices and the low heat transfer regions are formed by upflow. Taylor-Gortler vortices have been found on concave surfaces by many investigators. Blair et al. (1979) measured spanwise variation of dynamic pressure, Han and Cox (1983) took high speed smoke photographs, and Priddy and Bayley (1988) used laser-Doppler anemometer to show the presence of Taylor-Gortler vortices on a turbine blade. Crane and Sabzvari (1989) used a uniform heat flux liquid crystal technique to measure the heat transfer and visualize the Taylor-

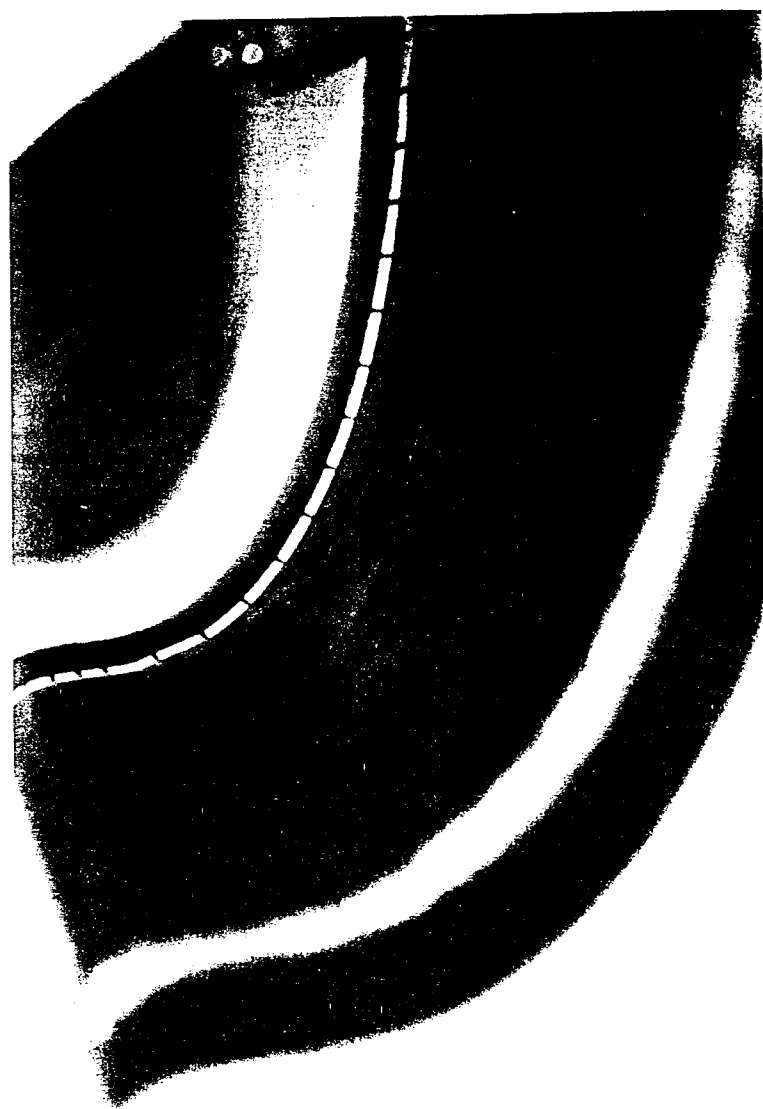


Figure 6.4.2 Spanwise heat transfer variation on the pressure surface

Gortler vortices on the concave section of a water tunnel. The present method is very sensitive and its visual nature allows this region to be captured better than most methods, although its sensitivity may be showing slight spanwise variation which is not meaningful. Overall on the concave portion of the pressure surface, the grid produced a turbulent boundary layer which has nearly two times more heat transfer than the low turbulence case. At much higher Reynolds number, but without grid turbulence, Graziani (1980) also measured heat transfer levels consistent with a turbulent boundary layer on the pressure surface.

The effect of grid turbulence on the local heat transfer (at 134,000-144,000 Reynolds number) is shown in Figure 6.4.3. For these data at slightly different Reynolds number, the difference in Stanton number can be misleading because it is inversely proportional to velocity, while laminar heat transfer is proportional to the square-root of velocity and turbulent heat transfer is proportional to velocity to the .8 power. Therefore for the present study, in these cases when the Reynolds number is not exactly matched, the "quoted" differences in heat transfer are adjusted for the square-root of velocity (the plotted values are not adjusted). At the higher Reynolds number, the grid turbulence produces some of the same effects as seen at the lower Reynolds number. The turbulence increases the stagnation point heat transfer by 17% (compared to 13% at $Re=67,500$). For a fixed increase in turbulence, Lowery and Vachon (1975) also found higher percentage changes to the stagnation heating for larger Reynolds numbers. On the suction surface, the heat transfer is elevated in the laminar boundary layer growth region (an average of roughly 16%). The laminar percentage increase is slightly less than the increase at stagnation, which is also the case at the lower Reynolds

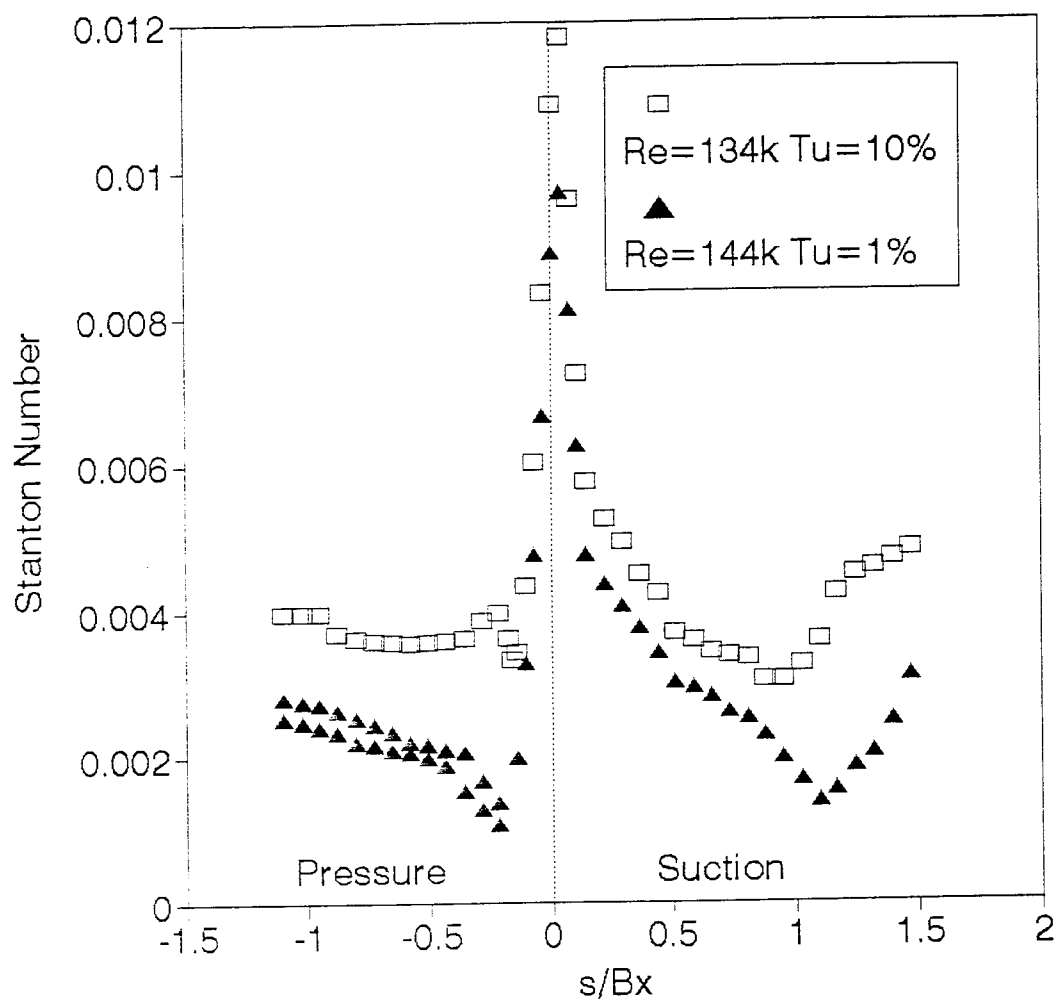


Figure 6.4.3 Effect of grid turbulence ($Re=134,000$)

number. This would agree with Kestin (1966), and Junkhan and Serovy (1967) who showed that turbulence increases the heat transfer for laminar boundary layers with favorable pressure gradients. For these higher Reynolds numbers, both sets of data show boundary layer transition (no separation). The grid turbulence advances the transition location to $s/Bx=92$, as compared to $s/Bx=1.1$ for the clean tunnel condition. Dullenkopf and Mayle (1994) also showed that added turbulence advances the boundary layer transition location on the suction surface. On the pressure surface, again the low turbulence case produced what appear to be Taylor-Gortler vortices, while the grid case shows boundary layer transition with heat transfer nearly twice as high.

The effect of Reynolds number is shown for the clean tunnel low turbulence runs in Figure 6.4.4. Again, the magnitude of the Stanton number can be somewhat misleading when comparing different Reynolds number, because it is inversely proportional to velocity, while laminar heat transfer is proportional to the square-root of velocity. This makes the Stanton number higher for the lower speed cases, therefore the shape of these plots should be considered, rather than the magnitude. Without the grid in place, the heat transfer profiles are very similar. On the pressure surface, the laminar boundary layer grows with decreasing heat transfer from the stagnation point, until the Taylor-Gortler vortices form on the concave curvature region. On the suction side, the profiles are similar as the laminar boundary layer grows out past $s/Bx=1$, then the profiles are quite different. The boundary layer transitions to turbulent at the higher Reynolds number, while the boundary layer separates at the lower Reynolds number.

The Reynolds number effect for the grid and corresponding high turbulence level is shown in Figure 6.4.5. In this case, the general trends are identical. On the pressure

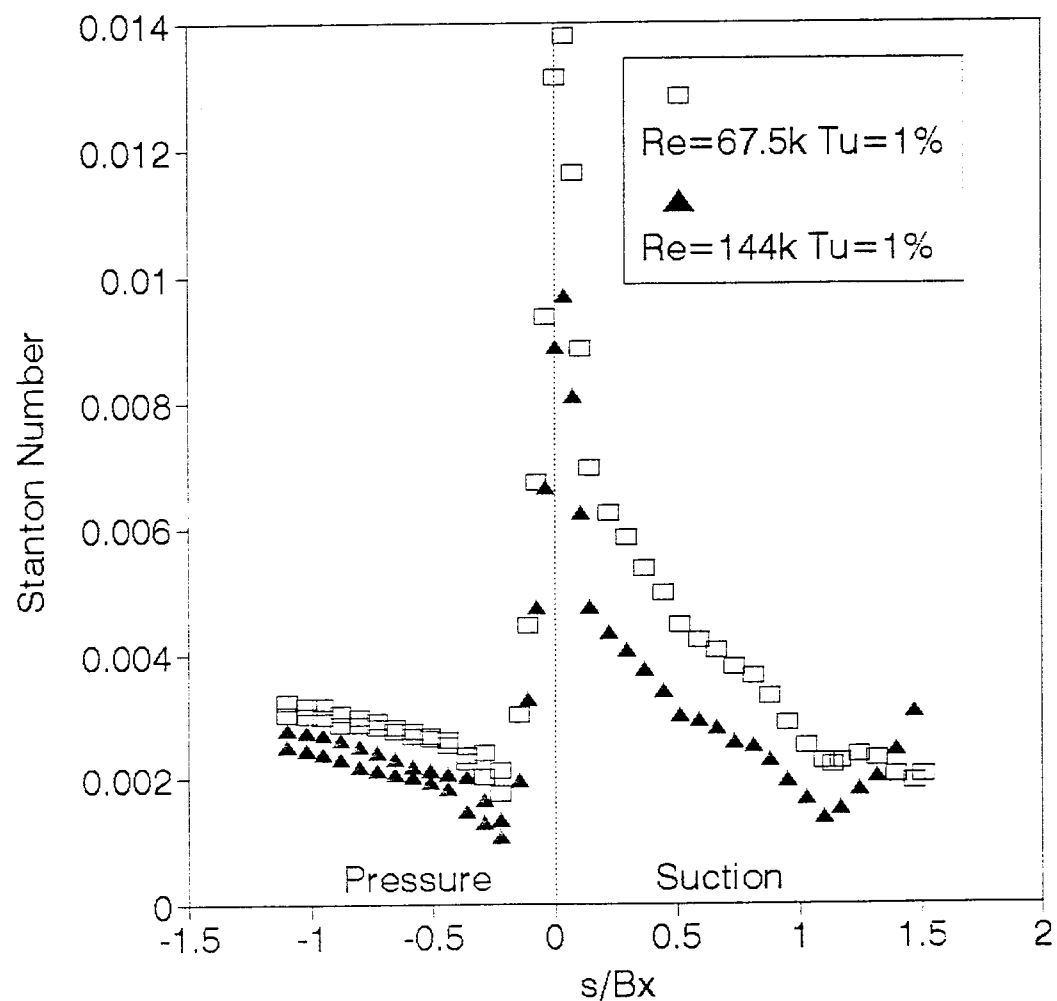


Figure 6.4.4 Effect of Reynolds number (without grid)

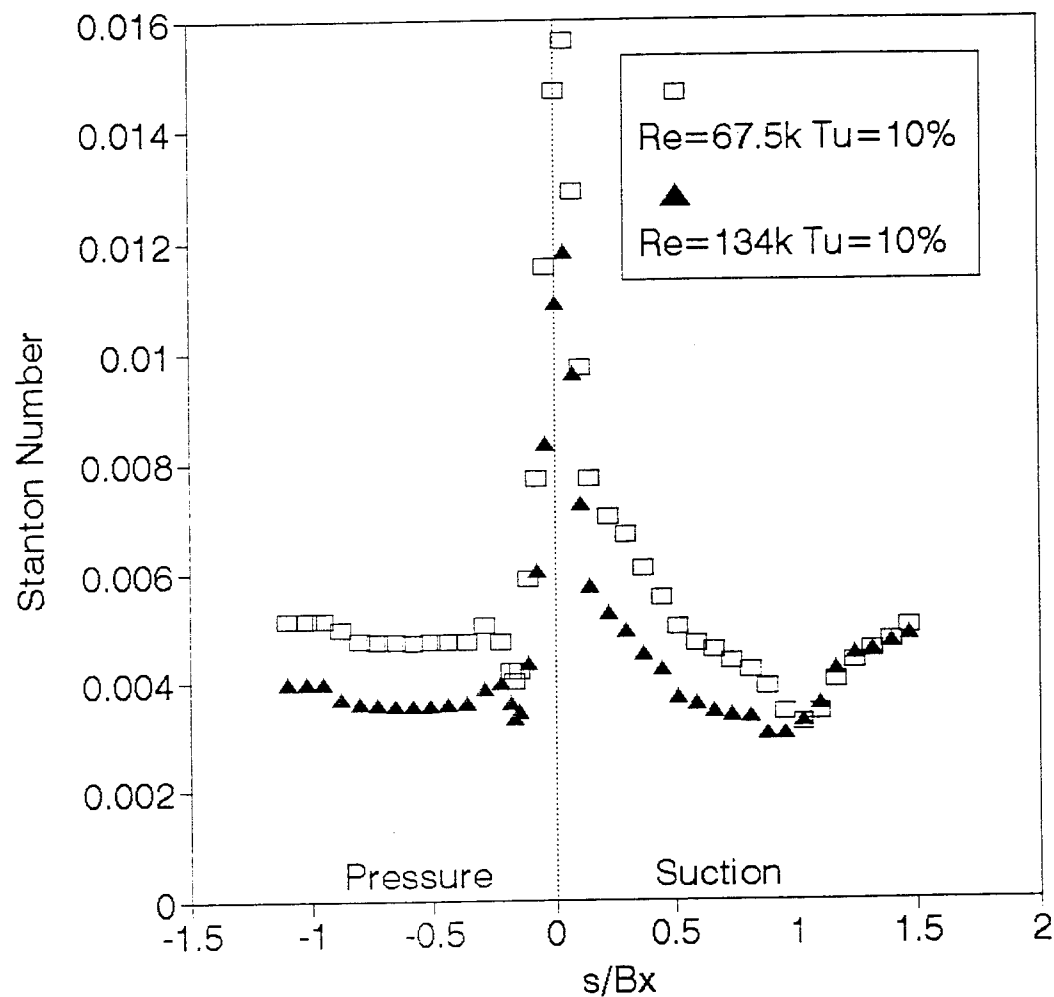


Figure 6.4.5 Effect of Reynolds number (with grid)

surface, the laminar boundary layer grows with decreasing heat transfer from the stagnation point, followed by boundary layer transition and high levels of relatively constant heat transfer along the concave portion of the pressure surface. For both cases on the suction surface, the laminar boundary layer transitions to turbulent near $s/Bx=1$. Although, the transition location is moved slightly forward ($s/Bx=.92$) for the higher Reynolds number, while the beginning of transition is $s/Bx=1.03$ at the lower Reynolds number. Overall, higher Reynolds number does not change the general shape of the heat transfer distributions, but it does make the grid turbulence effects more pronounced.

6.5 Extreme Grid Turbulence

There is interest in the effect of very high turbulence levels (greater than 20%) on turbine blade heat transfer. Therefore, data was collected using the present grid placed very near the cascade section. These results are separated from the rest of the data because using a grid to produce this level of turbulence is somewhat questionable. Grid turbulence decays as it travels downstream, therefore the high levels of turbulence will decay rapidly around the blade. In addition, the grid must be placed very close to the cascade to produce these levels of turbulence, this short distance doesn't allow the grid jets and wakes time to fully mix which results in non-uniform velocities. Even with the added difficulties, we felt local heat transfer results for very high turbulence levels would be useful.

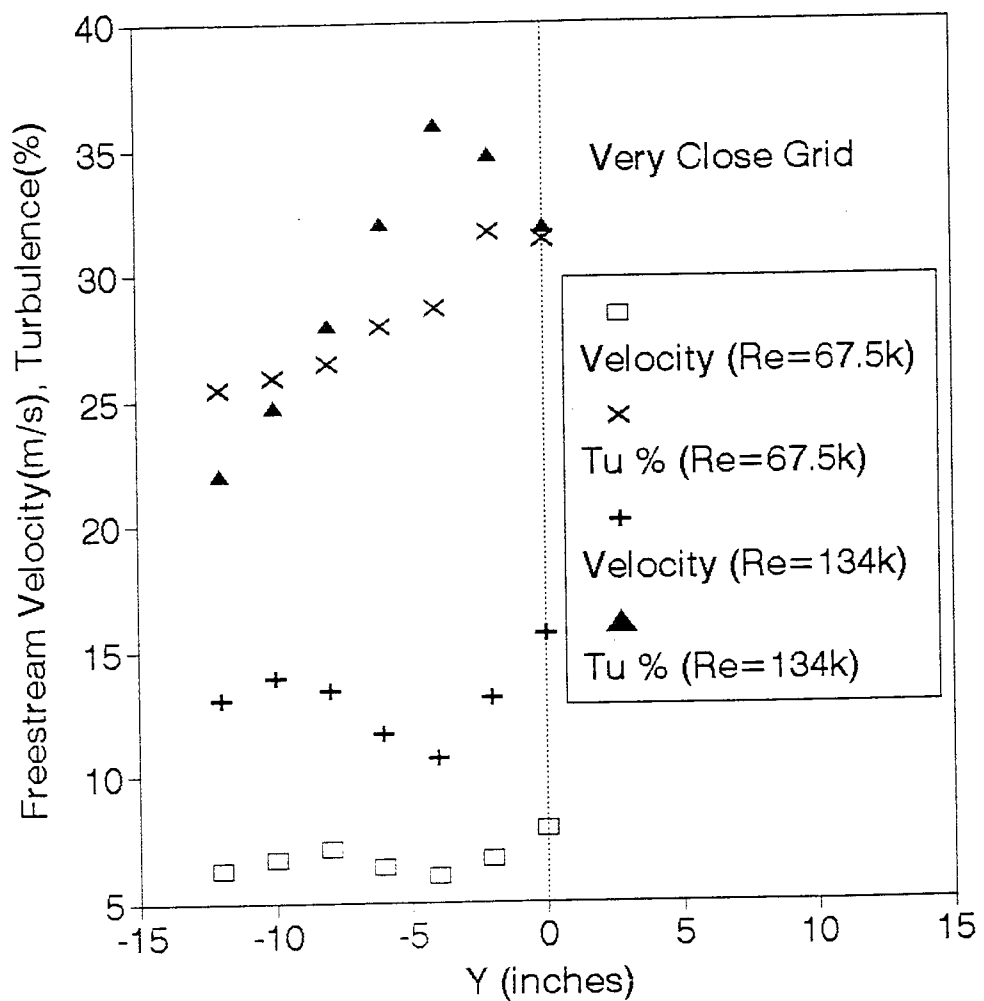


Figure 6.5.1 Free-stream velocity and turbulence for close grid

The grid was placed at the beginning of the cascade section (20.5 inches upstream of the test blade) in order to produce very high levels of turbulence. The free-stream velocity and turbulence intensities were measured and are shown in Figure 6.5.1. The measuring ports are located one axial chord up from the cascade row, which is 9.5 inches closer to the grid. Data was only collected for negative y values because the measuring ports get very close to the grid as the port locations move upstream with positive y values. For both Reynolds numbers, the velocities are very non-uniform showing low points behind grid bars and high velocities between bars. Due to the angle of the measuring ports, the turbulence intensity decay is evident on both curves. The turbulence intensity at the leading edge of the test blade can be estimated by knowing that it is located 1 inch further downstream (but, of course, in the center of the tunnel) of the $y=-12$ location. Therefore, the turbulence intensity is approximately 25% for $Re=67,500$ and 21% for $Re=134,000$.

The local heat transfer for the very high turbulence case (25%) is compared to the earlier grid turbulence (10%) at $Re=67,500$ in Figure 6.5.2. The profiles have the same overall shape, although the heat transfer is higher for the 25% turbulence case. At stagnation, the heat transfer is 14% higher. On the suction surface, the higher turbulence case has on average 23% higher heat transfer in the laminar boundary layer growth region and the transition location moves forward to $s/Bx=.92$ from $s/Bx=1.03$. On the pressure surface, both cases show a laminar boundary layer transitioning at $s/Bx=-.18$. The higher turbulence level increases the heat transfer by roughly 33% everywhere on the pressure surface. Blair et al. (1989b) also measured heat transfer levels on the pressure surface to be larger than fully turbulent predictions would suggest.

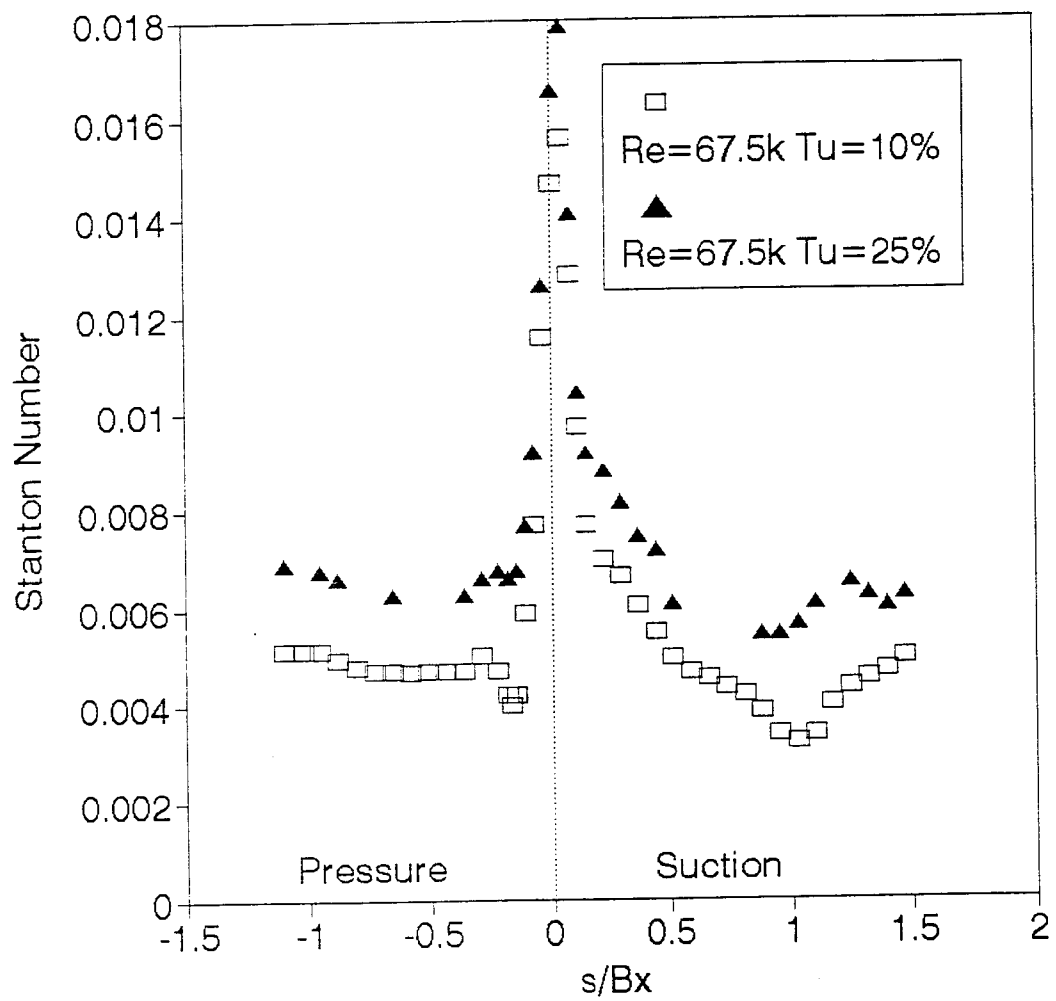


Figure 6.5.2 Effect of very high turbulence ($Re=67,500$)

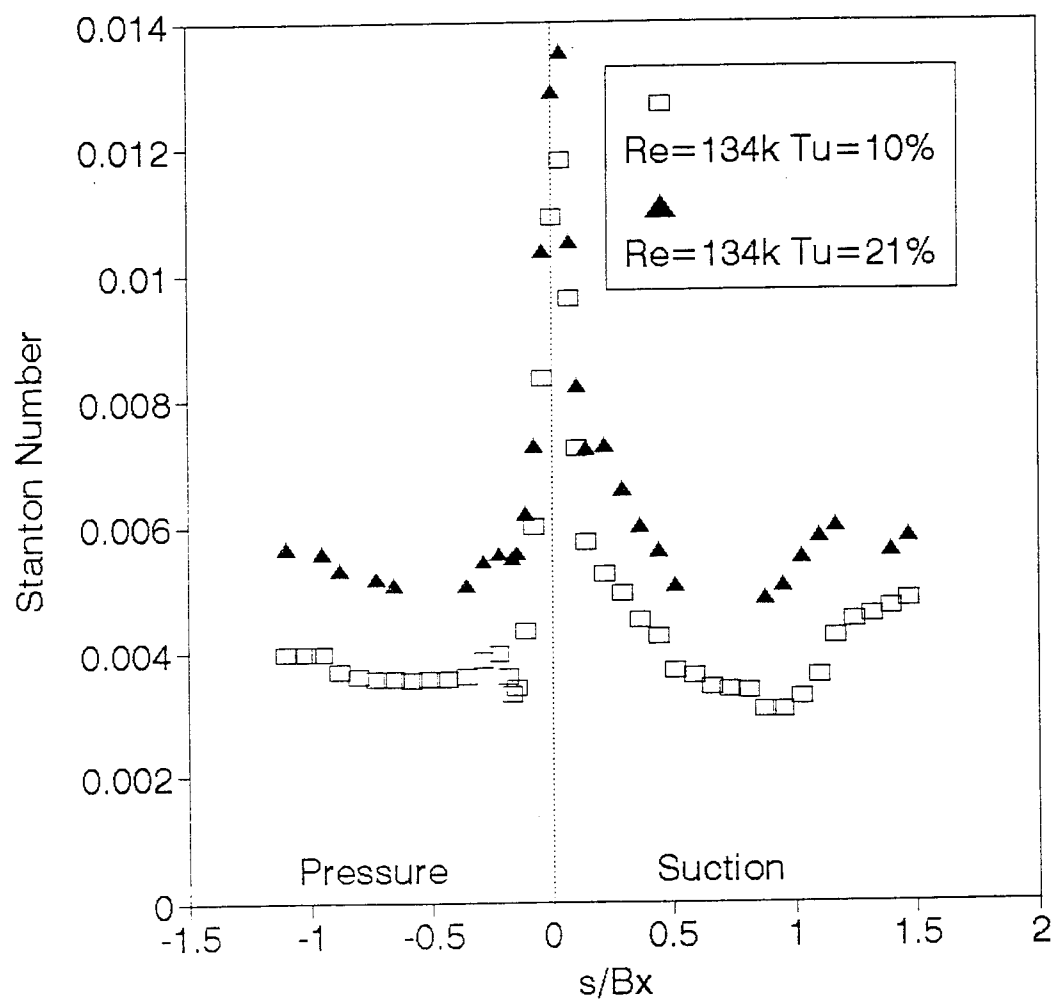


Figure 6.5.3 Effect of very high turbulence ($Re=134,000$)

On a different blade shape, Dullenkopf and Mayle (1994) measured turbulence induced large increases to the pressure side heat transfer, though they concluded that their pressure side boundary layer was laminar.

The local heat transfer for the very high turbulence case (21%) is compared to the earlier grid turbulence (10%) at $Re=134,000$ in Figure 6.5.3. Again, the profiles have the same overall shape, although the heat transfer is higher for the 21% turbulence case. The high turbulence case increases the heat transfer by 15% at the stagnation point, an average 33% on the suction side laminar region, and nearly a constant 42% on the entire pressure side. On the suction surface, the higher turbulence case moves the transition location forward to $s/Bx=.88$ from $s/Bx=.92$. On the pressure surface, both cases show a laminar boundary layer transitioning at $s/Bx=-.16$.

The high level turbulence produced by the close grid is too non-uniform to draw absolute conclusions, although some general thoughts are: turbulence effects are Reynolds number dependent showing larger heat transfer increases at higher Reynolds number, the location of boundary layer transition is slightly advanced by adding further turbulence, and the pressure surface heat transfer level is most effected by further turbulence.

6.6 Comparison of Cascade and Rotating Data

The question of using a linear cascade to model the complex process of a rotating machine can always be debated. Guenette et al. (1989) concluded that rotating midspan data is largely two-dimensional and that cascade data (Ashworth et al., 1985) is qualitatively the same, though 50% differences existed in some regions. Therefore,

in the present investigation, it was important to have a test case to compare with the cascade data. As mentioned earlier, a complete set of rotating tests for the same blade geometry was performed by Blair's group over the last decade. Most of their results are for Reynolds numbers higher than the present investigation, although, they did perform one set of tests which was not included in Blair et al. (1989b), but was listed in Tabular form in Dring et al. (1986). The present investigation nearly matched their condition by running $Re=134,000$ and 10% turbulence.

Blair et al. (1989b) used a 1 1/2 stage (stator, rotor, stator) rotating rig. They looked at Reynolds number and turbulence effects. They found that adding a grid didn't effect their rotor results very much because the stator wakes produce turbulence which interact with the rotor. This grid versus no grid effect on rotating results can be seen from Dring's (1986) lowest Reynolds number (200,000 based on exit conditions) data plotted in Figure 6.6.1. For comparison with the present investigation, their Stanton number has been adjusted for inlet conditions by multiplying it by the velocity ratio. In their original form, Dring's results are based on exit conditions. The test specifications for the present cascade are compared to Dring et al. (1986) in Table 6.6.1.

A comparison of Dring's (1986) rotating test to the present results is shown in Figure 6.6.2. Both tests used a 10% grid. The results are nearly identical near the stagnation region and on the pressure surface. Previous comparisons (Blair et al. 1989b versus Graziani 1980) on the pressure surface showed the cascade data being too low. On the suction surface the results are the same up to boundary layer transition. The transition location for the rotating test is further forward ($s/Bx=.473$) than the cascade test ($s/Bx=.92$). This was also true at higher Reynolds number in Blair's (1989b)

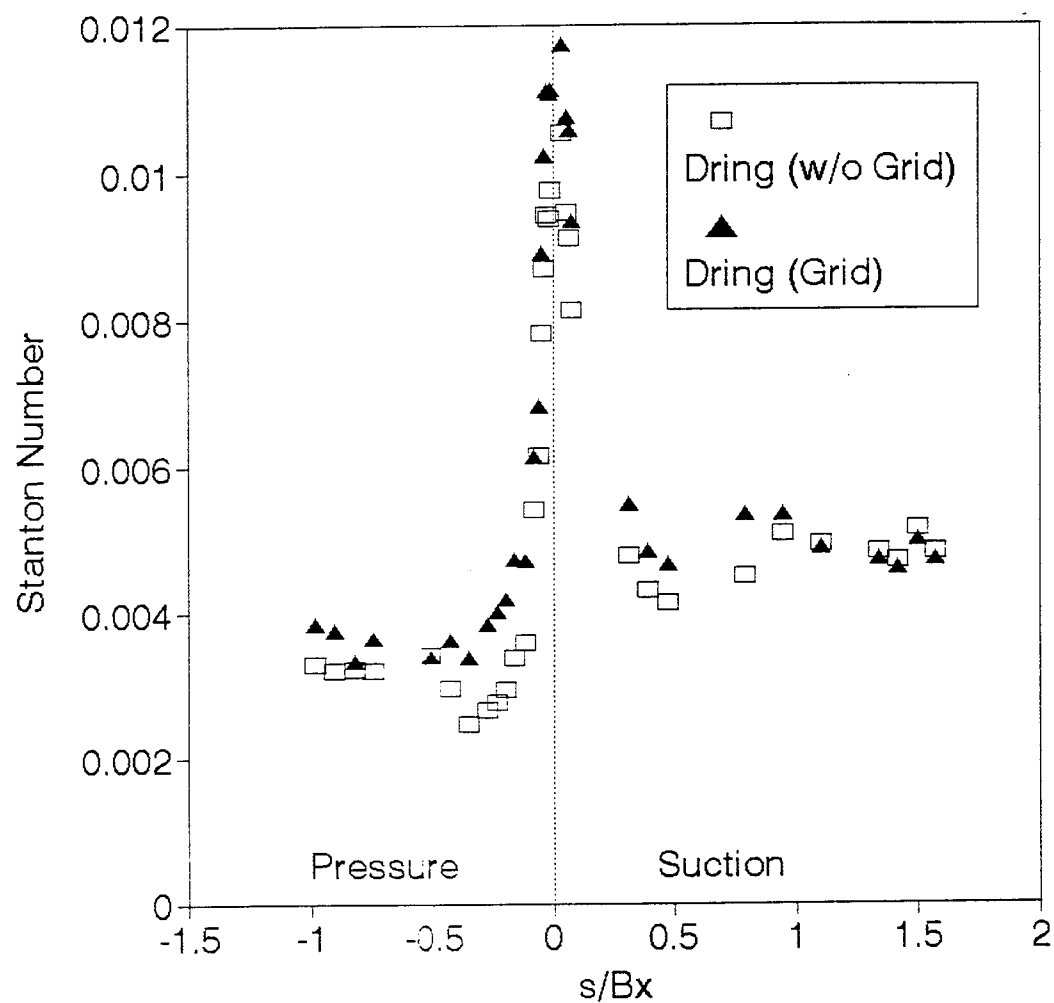


Figure 6.6.1 Grid effect on Dring's rotating tests

Table 6.6.1 Present cascade and UTRC test specifications

	Present Cascade	UTRC Rotating Rig
Axial Chord (B_x)	6.82"	6.34"
Pitch/Axial Chord (p/B_x)	.92	.96
Aspect Ratio	.95	3.52
Inlet Camber Angle	42°	42°
Exit Camber Angle	26°	26°
Air Inlet Angle	44.7°	40°
Exit Velocity	19.8 m/s	19.6 m/s

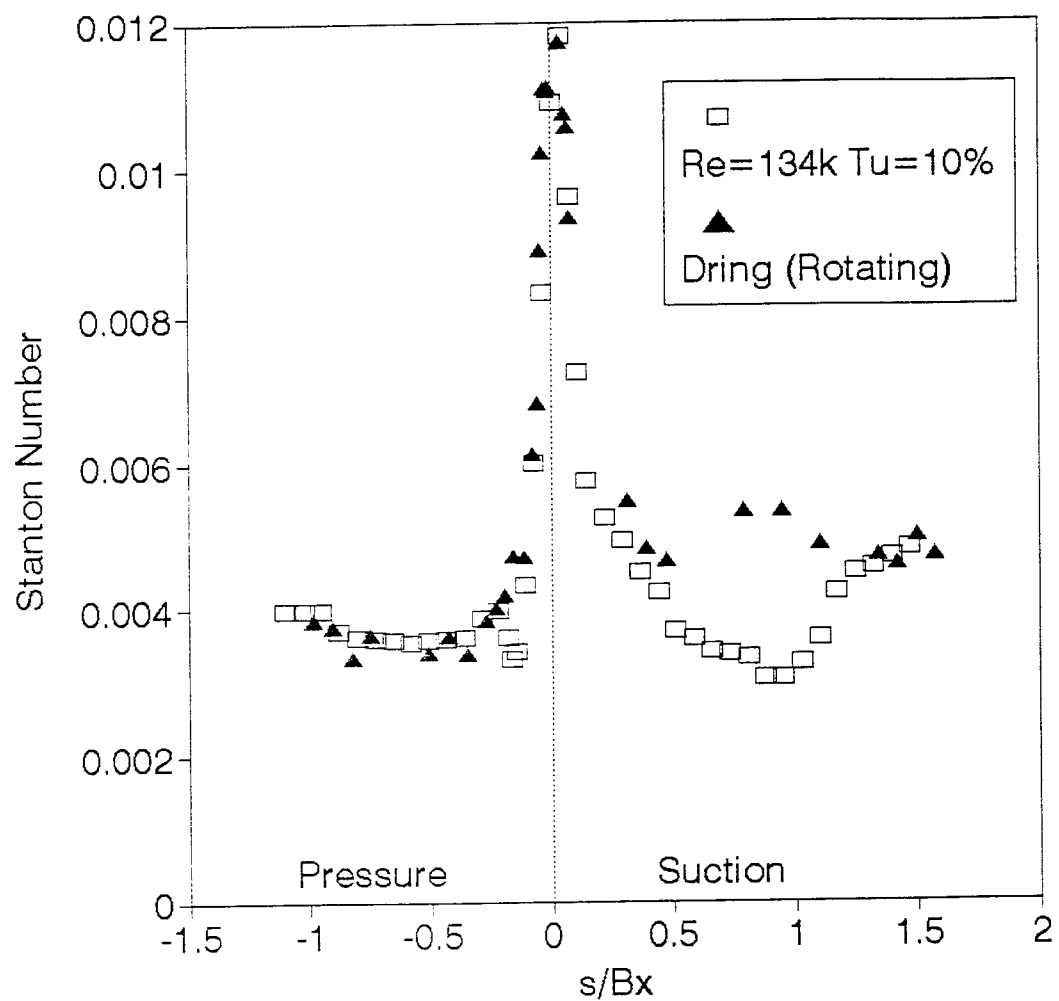


Figure 6.6.2 Comparison of cascade and rotating rig results

comparison with cascade data by Graziani et al. (1980). This difference could have many sources, some possibilities would be: stator wake turbulence, three dimensional effects, or surface roughness differences. The max-to-min surface roughness for Dring's (1986) rotating data is 51 microns (Blair, 1994), while the present model surface roughness is estimated to be 10 microns. At low Reynolds number, Blair (1994) showed that increasing the surface roughness can advance the suction side transition location. After both boundary layers have become fully turbulent at the end of the suction side, it is interesting that the heat transfer levels are the same, even though the boundary layers transitioned at different locations.

6.7 Comparison with USAF Academy Results

A turbine blade with the same geometry as the present study was built at UC/Davis with the gold-film in the same fashion as the present study. It was then tested by Byerley and Baughn (1994) in the USAF Academy Cascade Wind Tunnel. The Air Force tunnel is closed loop, has a minimum speed of 13 m/s, and operates at roughly 7000 feet altitude. A comparison of the UC/Davis and the USAF Academy cascade tunnels is shown in Table 6.7.1. In the present tunnel configuration, the pitch (distance between blades) of the Air Force cascade is 7.75 inches and its air inlet angle (β_1) is 49° . The UC/Davis pitch is 6.25 inches and the air inlet angle is 44.7° , both of these more closely match experiments by Langston et al (1979), Graziani et al. (1980), Dring et al. (1986), and Blair et al. (1989a, 1989b). The other major difference between facilities involves the turbulence grid, the Air Force grid is placed parallel to the cascade

Table 6.7.1 Cascade tunnel comparison

	UC/Davis	USAF Academy
Operation	Open Loop	Closed Loop
Blade Pitch	6.25"	7.75"
Pitch/Axial Chord	.92	1.14
Grid relative to Free-stream Velocity	Perpendicular	Angled
Turbulence (clean,grid)	1% 10%	.5% 9%
Re (clean,grid)	144,000 134,000	122,000 122,000

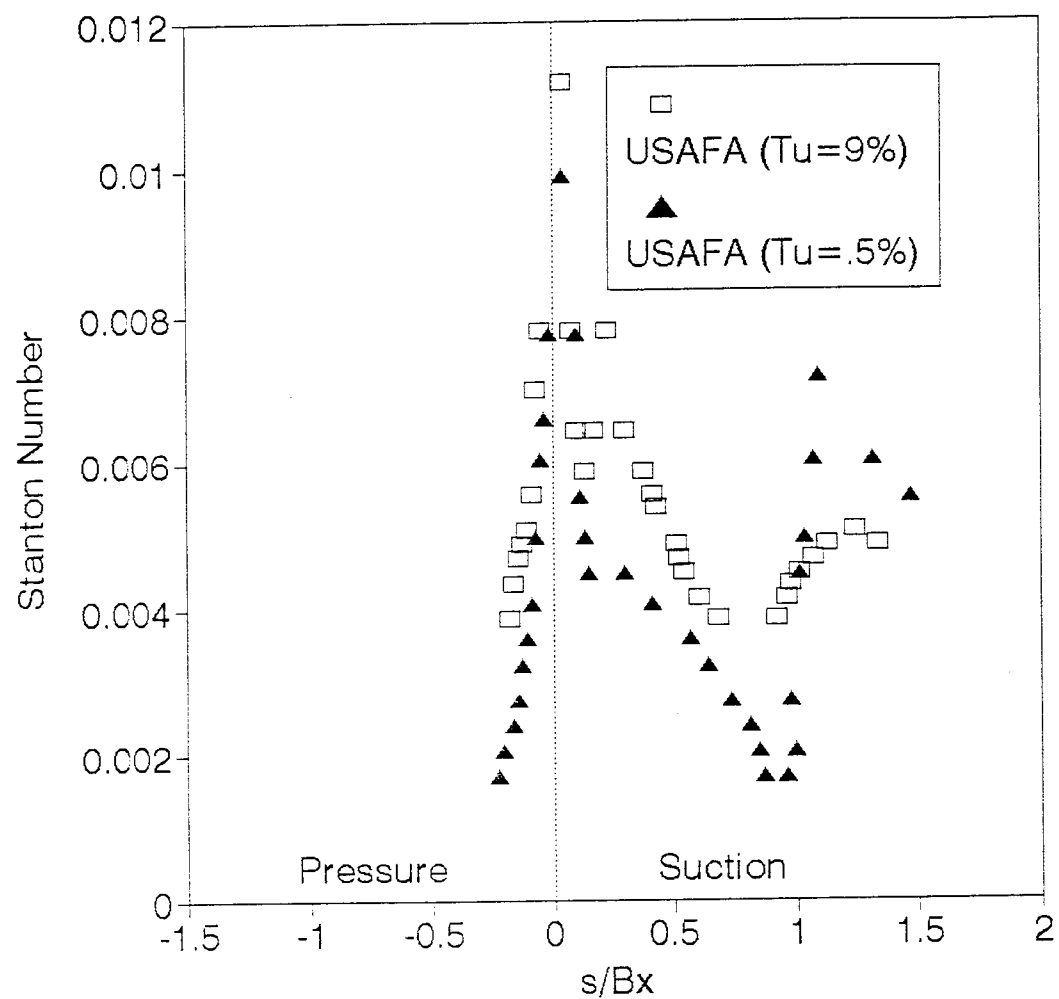


Figure 6.7.1 Effect of Turbulence on USAFA Turbine Cascade

row, therefore it is at an angle relative to the free-stream flow. The UC/Davis grid is placed perpendicular to the free-stream flow, therefore it is at an angle relative to the cascade row.

Two sets of data were collected in the Air Force tunnel. Data was collected with and without the turbulence grid at 13 m/s ($Re=122,000$). These results are shown in Figure 6.7.1. The grid turbulence had a major effect on the magnitude and the general profile of the heat transfer distributions in the Air Force tunnel. At the stagnation point, 9% grid turbulence increased the heat transfer by 13%. Very limited data was collected on the pressure surface, but the results show that the grid increased the heat transfer in this region at least 29% and at some points as much as 81%. The suction surface profile changed dramatically. Without the grid, the heat transfer decreases as a laminar boundary layer grows from the stagnation point up to $s/B_x=.921$. At this point, the laminar boundary layer appears to separate, followed by very high heat transfer where the boundary layer reattaches at $s/B_x= 1.09$. With grid turbulence, the Air Force heat transfer results show a minimum at $s/B_x=.132$ and a maximum at $s/B_x=.226$. This profile is either caused by an overspeed of the flow on the suction side or a very weak separation region followed by laminar reattachment. After $s/B_x=.226$ with the grid, the heat transfer behaves like a growing laminar boundary layer. With higher turbulence, the laminar boundary layer does not separate at $s/B_x=.921$, instead it transitions to turbulent with a gradual rise in heat transfer followed by a decrease when the boundary becomes fully turbulent.

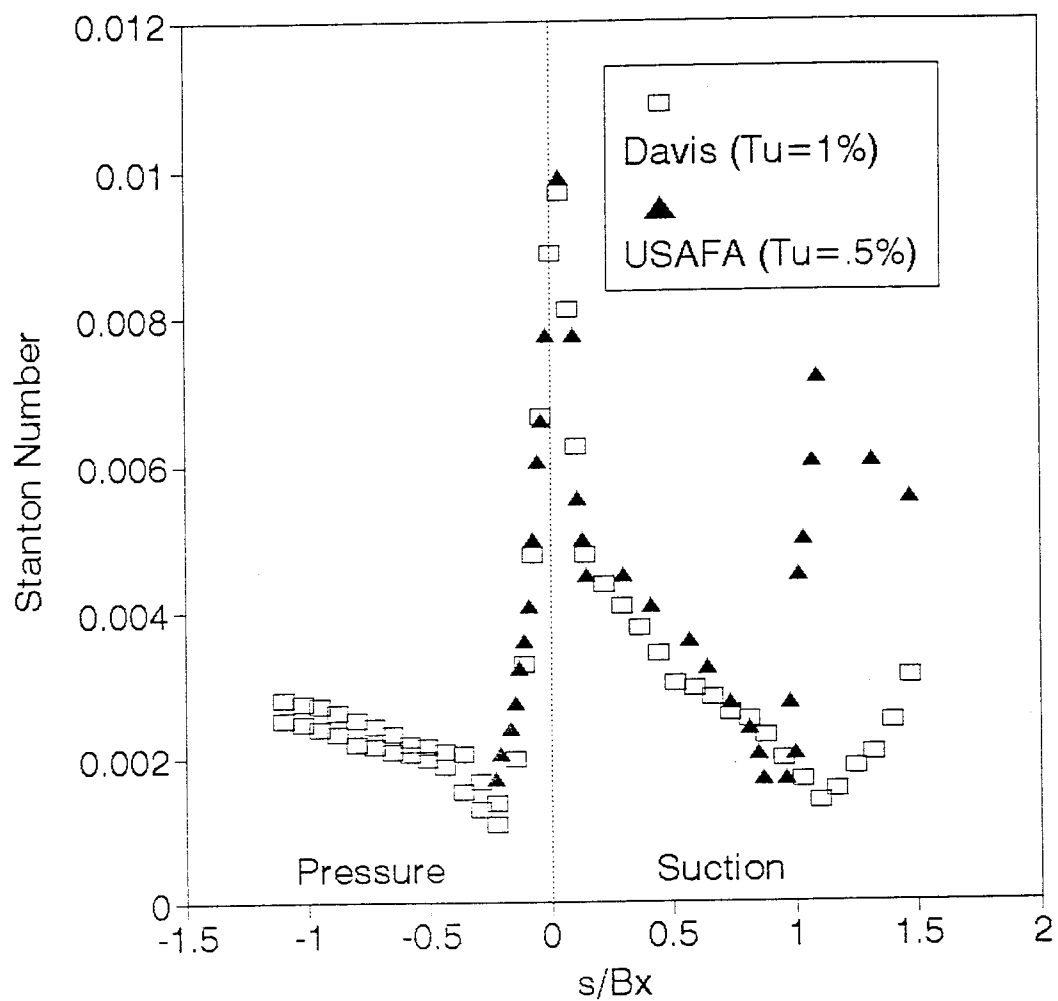


Figure 6.7.2 Comparison of UC/Davis and USAFA results (no grid)

The USAF Academy turbine blade heat transfer is compared to the UC/Davis results for the clean tunnel configuration in Figure 6.7.2. The results are nearly identical everywhere except beyond the $s/B_x = .921$ location on the suction surface. At this point, the Air Force results show boundary layer separation followed by very high heat transfer at reattachment. The UC/Davis results show boundary layer transition to turbulent. The difference is attributed to the larger blade spacing and pitch/axial chord of the Air Force cascade. As the turbine blades are moved farther apart, the flow separates because it is unable to navigate the large turning angle.

The Air Force and UC/Davis results are also compared with grid turbulence in Figure 6.7.3. These results are at slightly different free-stream velocities (12 m/s at UC/Davis and 13 m/s at USAFA), therefore due to the inverse relation of Stanton number to velocity, the results do not match at the stagnation point, but the profiles can still be compared. The grid turbulence didn't change the heat transfer distribution at UC/Davis, but it did increase the heat transfer everywhere on the blade. The grid turbulence had a dramatic effect on the Air Force heat transfer distribution. A minimum ($s/B_x = .132$) and maximum ($s/B_x = .226$) formed on the suction surface. This combination could be a slight overspeed on the suction surface or a weak separation point followed by laminar reattachment (these possibilities are considered in the next paragraph). After the maximum, the heat transfer appears to be of laminar magnitude. The laminar boundary layer then transitions to turbulent at nearly the same location as the UC/Davis results ($s/B_x \sim 1$). These major differences can possibly be explained by the angled grid in the Air Force tunnel.

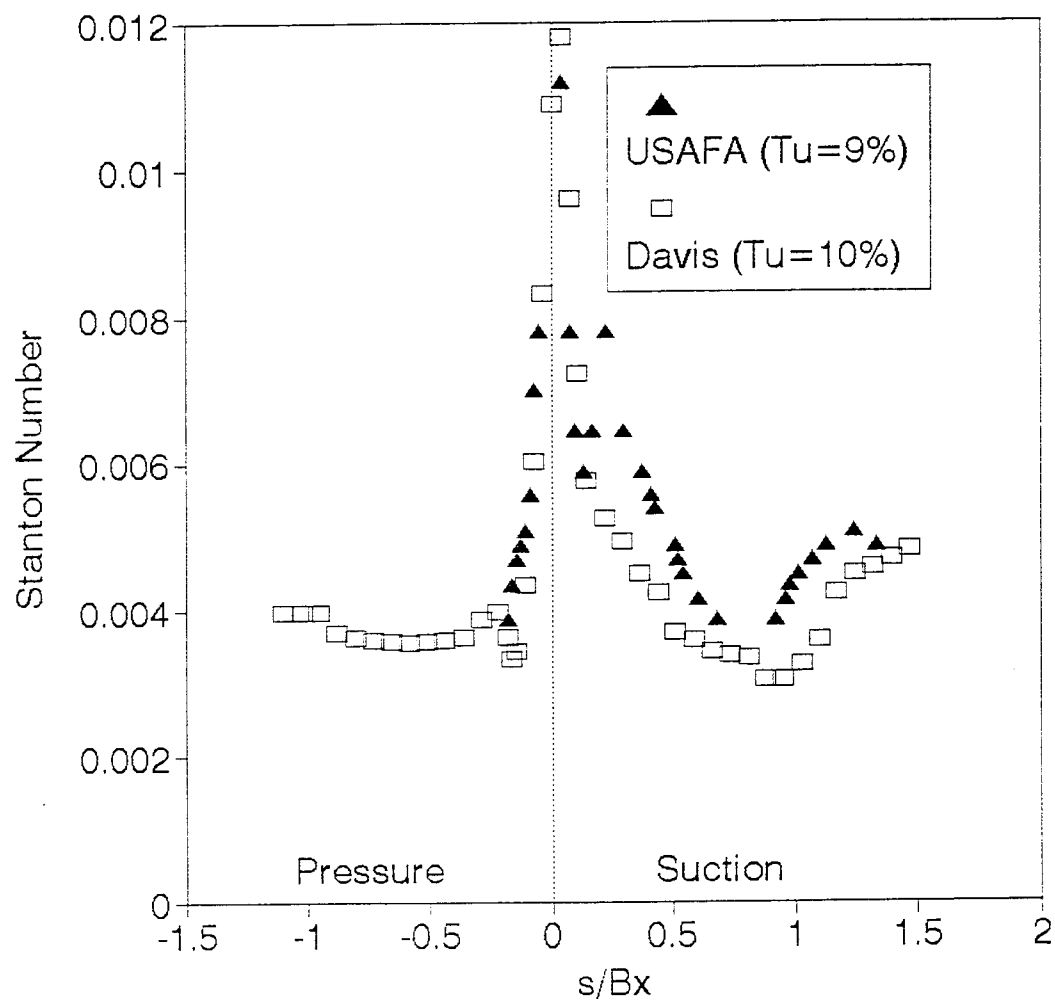


Figure 6.7.3 Comparison of UC/Davis and USAFA results (with grid)

At UC/Davis, the question of flow angularity was investigated in a very simple manner. The test blade was purposely misaligned in the normal cascade row and the resulting minimum and maximum heat transfer was measured. These results are presented in Table 6.7.1. As the blade was turned towards negative incidence angles the heat transfer in the $s/B_x = .17$ region would become very flat which was evident by a very broad color band of liquid crystals. When the deviation angle reached 2.8° , a minimum/maximum pair started to appear. This pair had very different characteristics depending on the angle. From 2.8° up to 6.3° , the minimum was very broad and the resulting maximum wasn't extreme. We believe this is caused by the flow rapidly accelerating (overspeed) and then slowing. When the deviation angle reached 6.3° , the minimum became very narrow resembling a line and the maximum grew larger with ever increasing angle. The minimum may now represent a separation line with the liquid crystal color play becoming very narrow. The maximum represents either overspeed at smaller angles or possibly reattachment if the boundary layer separates at large angles. Because of local differences in the separation point, the separation line was sometimes not straight as you looked at the blade. Without viewing the Air Force minimum, it is difficult to discern which case they may have had, but with the maximum heat transfer 31% higher than the minimum, it is possibly overspeed. It is very likely that their angled grid produced the maximum/minimum pair by changing the flow direction slightly.

Table 6.7.2 Flow angle effect on suction side heat transfer

Deviation Angle	Minimum Visual	Minimum (s/B_x)	Maximum (s/B_x)	Max/Min Heat Transfer
-4.2°	Broad	.17	.24	12%
-7°	Narrow	.15	.29	61%
-9.1°	Narrow	.15	.29	350%

6.8 Discussion

The present study investigated the effect of Reynolds number and turbulence intensity on turbine blade local heat transfer. The results were very good showing interesting features of the turbine blade heat transfer distribution.

Turbulence intensity has the largest effect on the local heat transfer. Increasing the turbulence intensity from 1% to 10% has many effects at both Reynolds numbers. The stagnation point heat transfer increases (13% at $Re=67,500$ and 17% at $Re=134,000$), and the suction side laminar boundary layer heat transfer increases (an average of 12% at $Re=67,500$ and 16% at $Re=134,000$). At $Re=67,500$, without the grid (1% turbulence) the suction side boundary layer separates near the end of the blade, while the boundary layer transitions to turbulent at $s/Bx=1.03$ with the grid (10% turbulence). At $Re=134,000$, the grid turbulence causes the suction side boundary layer transition location to move forward from $s/Bx=1.1$ to $s/Bx=.92$. The turbulence has a profound effect in the concave curvature region of the pressure surface. At 1% turbulence, Taylor-Gortler vortices possibly form in the laminar boundary layer, the vortices cause the heat transfer to be vary spanwise. With 10% turbulence, the Taylor-Gortler vortices are not present and the heat transfer nearly doubles due to the boundary layer transitioning to turbulent.

The effect of Reynolds number on the results were different with and without the grid. Without the grid, the suction side boundary layer separated at $Re=67,500$ and it transitioned to turbulent at $Re=134,000$. With the grid, the suction side boundary layer transition point moved forward (from $s/Bx=1.03$ to .92) with increasing Reynolds number. The pressure side showed what appeared to be Taylor-Gortler vortices for both

Reynolds numbers without the grid and were fully turbulent with the grid. The results also showed that the effect of turbulence was sensitive to Reynolds number. This was evident by the larger percentage increases in heat transfer (for the highest Reynolds number case) at any location when the grid was added. This type of Reynolds number turbulence effect has been measured by many investigators for the stagnation region of a cylinder.

The effect of very high turbulence intensities (greater than 20%) was investigated with the grid very close to the cascade. This data should be viewed knowing that the turbulence is decaying very rapidly and this close grid produced non-uniformities in the upstream conditions. The very high turbulence results have the same overall distribution as the 10% turbulence profiles, although the higher turbulence levels increase the heat transfer everywhere on the turbine blade. Compared to the 10% turbulence data, the stagnation point heat transfer increases (14% at $Re=67,500$ and 15% at $Re=134,000$), the entire pressure side turbulent boundary layer heat transfer increases (33% at $Re=67,500$ and 42% at $Re=134,000$), the suction side laminar boundary layer heat transfer increases (an average of 23% at $Re=67,500$ and 33% at $Re=134,000$), and the suction side boundary layer transition location moves forward slightly ($s/Bx=1.03$ to .92 at $Re=67,500$ and $s/Bx=.92$ to .88 at $Re=134,000$). These are sizeable increases and the data shows that the effect of turbulence is amplified at higher Reynolds number, this is especially true on the pressure surface.

The cascade data compares very favorably to data collected in a rotating rig by Dring et al. (1986). The stagnation, laminar boundary layer, and pressure surface heat transfer is nearly identical. The boundary layer transition location on the suction surface

is advanced in the rotating tests, although after transition, both heat transfer levels are the same by the end of the suction surface. This excellent comparison with rotating tests makes the present cascade results more valuable due to the simple nature of the technique.

The results were also compared to tests performed in the USAF Academy Cascade tunnel. The results were generally the same at low turbulence levels, although the Air Force data showed boundary layer separation on the rear portion of the suction side. This is probably caused by larger blade spacing in the Air Force tunnel. With grid turbulence, the Air Force results were quite different with a maximum and minimum near the front of the suction surface. It is suggested that this is caused by negative flow incidence produced by their grid which is installed at an angle relative the free-stream flow. It is unclear if their maximum/minimum is flow overspeed or flow separation and laminar reattachment.

CHAPTER 7 CONCLUSIONS AND RECOMMENDATIONS

The present study is multi-faceted, investigating different local heat transfer measuring techniques, experimentally studying a cylinder in cross-flow, laminar flow over a flat plate, and a turbine blade in a linear cascade tunnel and numerically studying the effect of the thermal boundary condition on a laminar boundary layer. Many conclusions can be drawn from this work.

- The shroud technique has the flexibility to be applied to three-dimensional shapes.
- The transient shroud technique works very well when the flow develops quickly, such that the amount of time for the flow to development is very short as compared to the transient heat transfer. This was shown in the stagnation through separation region on the cylinder in cross-flow. On the other hand, this method gave mixed results in the wake region where the flow development time is longer.
- Transient results can be strongly dependent on the transient nondimensional temperature when the upstream conditions exhibit large heat transfer gradients.

- The accuracy of the results for the shroud technique are highly dependent on the accurate measurement of surface temperature, liquid crystal calibration, and the initial uniformity of the model temperature. Any error in these factors can produce errors using this method.
- The gold-film heated-coating method is robust and less sensitive to temperature measurement and liquid crystal calibration.
- The gold-film heated-coating method can only be applied to two-dimensional shapes because the gold film must be attached to the model surface. In addition, the gold film can be difficult to work with and can easily be damaged.
- The experimental data for the cylinder in cross-flow (except in the wake region) agreed quite well with previous work. The boundary layer separation point on the cylinder moves slightly forward as the Reynolds number increases (86° at $Re=34,000$ to 78° at $Re=110,000$).
- Unsteady outside influences can interact with the natural vortex shedding from the cylinder. The heat transfer in the wake region decreases as the shedding frequency decreases.

- Numerical codes accurately calculated the local heat transfer for laminar flow over a flat plate for uniform wall temperature, uniform heat flux, and unsteady transient wall temperature boundary conditions.
- The experimental uniform heat flux measurements agreed with theory and numerical solutions for laminar flow over a flat plate.
- The local heat transfer for laminar flow is very dependent on the thermal boundary conditions. For laminar flow over a flat plate, the uniform heat flux boundary condition produces 36% higher heat transfer than the uniform temperature boundary condition. The transient method produces wall temperatures which change over time, which cause the thermal boundary condition to change over time. This produces an integrated average heat transfer depending on the length of the transient. When the transient starts, the heat transfer is equivalent to the uniform wall temperature solution because the surface is at a uniform temperature, but the heat transfer increases over time yielding results sometimes greater than a uniform heat flux boundary condition (the final result is dependent on the transient nondimensional temperature and the Reynolds number). A correlation was developed to adjust the transient results to uniform temperature boundary conditions.
- The shroud technique method produces experimental results which closely match the predicted numerical transient solutions for laminar flow over a flat plate.

- Considering the complex, but two-dimensional shape, of the turbine blade and the requirement for accurate heat transfer measurements, it was concluded that the gold-film heated-coating method was best suited for the turbine blade in a linear cascade tunnel.
- Increasing the free-stream turbulence intensity using a grid had many influences on the turbine blade heat transfer. The heat transfer increased everywhere on the turbine blade including the stagnation point and in the laminar region on the suction surface. The pressure side heat transfer increased the most because the grid caused the boundary layer to become fully turbulent, without the grid, the pressure side possibly exhibited Taylor-Gortler vortices. The grid turbulence also caused the suction side boundary layer transition point to move forward.
- The effect of Reynolds number on the turbine blade results were different with and without the grid. Without the grid, the suction side boundary layer separated at $Re=67,500$ and it transitioned to turbulent at $Re=134,000$. With the grid, the suction side boundary layer transition point moved forward with increasing Reynolds number. Without the grid on the pressure side the heat transfer was lower and possibly showed Taylor-Gortler vortices for both Reynolds numbers, with the grid the heat transfer was at fully turbulent levels.

- The turbulence effects were also dependent on Reynolds number. For every location on the turbine blade, larger percentage increases in heat transfer were produced by the grid when being tested at the higher Reynolds number.
- Increasing the free-stream turbulence from 10% to above 20% continued to elevate the heat transfer everywhere on the turbine blade, with the largest difference on the pressure side.
- The cascade data compares very favorably to data collected in a rotating rig by Dring et al. (1986). The stagnation, laminar boundary layer, and pressure surface heat transfer is nearly identical. The boundary layer transition location on the suction surface is advanced in the rotating tests, although after transition, both heat transfer levels are the same by the end of the suction surface.
- Purposely misaligning the test blade to produce small changes in flow angle produces local maximum and minimum heat transfer near the leading edge on the suction surface.
- The laser liquid crystal thermal tuft is a simple and non-intrusive method for determining flow direction.
- Turbine blade cascade testing is a simple and accurate method for determining mean geometry local heat transfer.

Although the present study was as comprehensive as possible, every investigation uncovers some new items which can not be treated to their fullest extent. Therefore, the following recommendations are suggested for further work to be performed in the future.

- The numerical code to predict transient heat transfer coefficients for laminar flat plate flow could be improved. Appendix L showed that the wall temperature update using a time average heat transfer coefficient could in the worst case produce a 5% error. This could be eliminated if the code ran in parallel with another code which solved the transient wall conduction problem at the same time. This was not done in the present study because of additional memory requirements and the significant increase in complexity for a little increase in accuracy. Though, the error is real and a better solution would shed more light on transient heat transfer measurements.
- The effects of turbine blade solidity should be investigated using the present cascade. In addition, complete local heat transfer distributions for misaligned test blades should be considered.
- The turbine blade cascade tunnel could be improved by increasing the size of the turbine blades. The present apparatus has nine blades which is more than necessary to ensure periodicity. Larger blades would allow for higher Reynolds number testing and better spacial resolution on the turbine blade.

- The laser liquid crystal thermal tuft method has limitless applications and it should be improved and the results quantified. Not only could it be used to predict flow direction, but a complete investigation could use it to predict turbulent or laminar boundary layer types. The method could be optimized by using a short burst high power laser with a wide band liquid crystal near room temperature. In addition, the power and duration of the laser and resulting color transient could possibly be used in order to measure local heat transfer.

REFERENCES

- Achenbach, E. 1968, "Distribution of Local Pressure and Skin Friction around a Circular Cylinder in cross-flow up to $Re=5 \times 10^6$," *Journal of Fluid Mechanics*, Vol. 34, pp. 625-639.
- Achenbach, E. 1975, "Total and Local Heat Transfer from a Smooth Circular Cylinder in Cross-Flow at High Reynolds Number," *Int. Journal of Heat and Mass Transfer*, Vol 18, pp. 1387-1396.
- Achenbach, E. 1977, "The Effect of Surface Roughness on the Heat Transfer from a Circular Cylinder to the Cross Flow of Air," *Int. Journal of Heat and Mass Transfer*, Vol. 20, pp. 359-369.
- Ainsworth, R. W., Allen, J. L., Davies, M. R. D., Doorly, J. E., Forth, C. J. P., Hilditch, M. A., Oldfield, M. L. G., and Sheard, A. G. 1989, "Developments in Instrumentation and Processing for Transient Heat Transfer Measurement in a Full-Stage Model Turbine," *ASME Journal of Turbomachinery*, Vol. 111, pp. 20-27.
- Anderson, D. A., Tannehill, J. C., and Pletcher, R. H. 1984, *Computational Fluid Mechanics and Heat Transfer*. Hemisphere Publishing Company, New York, pp. 333-335.
- Anderson, J. D. 1991, *Fundamentals of Aerodynamics*. McGraw-Hill inc., New York, pp. 725.
- Andraka, C. E., and Diller, T. E. 1985, "Heat Transfer Distribution Around a Cylinder in Pulsating Cross-flow," ASME Paper 85-GT-67.
- Ashworth, D. A., LaGraff, J. E., Scultz, D. L., and Grindrod, K. J. 1985, "Unsteady Aerodynamic and Heat Transfer Processes in a Transonic Turbine Stage," *Journal of Engineering for Gas Turbines and Power*, Vol. 107, pp. 1022-1030.
- Baines, W. D., and Peterson, E. G., 1951, "An Investigation of Flow Though Screens", *Transactions of ASME*, Vol 73, pp. 467-480.
- Barbi, C., Favier, D., Maresca, C., and Telionis, D. 1986, "Vortex Shedding and Lock-On of a Circular Cylinder in Oscillatory Flow," *Journal of Fluid Mechanics*, Vol. 170, pp 527-544.
- Baughn, J. W., Takahashi, R. K., Hoffman, M. A., and McKillop, A. A. 1985, "Local Heat Transfer Measurements using an Electrically Heated Thin Gold-Coated Plastic Sheet," *ASME Journal of Heat Transfer*, Vol. 107, pp 953-959.

Baughn, J. W., Elderkin, M. J., and McKillop, A. A. 1986, "Heat Transfer From a Single Cylinder, Cylinders in Tandom, and Cylinders in the Entrance Region of a Tube Bank with a Uniform Heat Flux," *Transactions of the ASME*, Vol. 108, pp. 386-391.

Baughn, J. W., Ireland, P. T., Jones, T. V., and Saniei, N. 1989, "A Comparison of the Transient and Heated-Coating Methods for the Measurements of the Local Heat Transfer Coefficients on a Pin Fin," *ASME Journal of Heat Transfer*, Vol. 111, pp 877-881.

Baughn, J. W., and Saniei, N. 1991, "The Effect of the Thermal Boundary Condition on Heat Transfer From a Cylinder in Cross-flow," *Journal of Heat Transfer*, Vol. 113, pp 1020-1022.

Baughn, J. W., and Yan, X. 1991, "An Insertion Technique Using the Transient Method with Liquid Crystals for Heat Transfer Measurements in Ducts", National Heat Transfer Conference, Minneapolis, MN.

Baughn, J. W. and Rivir, R. B., personal communication, 1994.

Baxter, D. C., and Reynolds, W. C. 1958, "Fundamental Solutions for Heat Transfer from Nonisothermal Flat Plates," *Journal of the Aeronautical Sciences*, Vol. 25, pp. 403-404.

Blair, M. F. 1983, "Influence of Free-Stream Turbulence on Turbulent Boundary Layer Heat Transfer and Mean Profile Development," *ASME Journal of Heat Transfer*, Vol. 105, pp 33-50.

Blair, M. F., Dring, R. P., and Joslyn, H. D. 1989a, "The Effects of Turbulence and Stator/Rotor Interactions on Turbine Heat Transfer: Part 1-Design Operating Conditions," *ASME Journal of Turbomachinery*, Vol. 111, pp. 87-96.

Blair, M. F., Dring, R. P., and Joslyn, H. D. 1989b, "The Effects of Turbulence and Stator/Rotor Interactions on Turbine Heat Transfer: Part 2-Effects of Reynolds Number and Incidence," *ASME Journal of Turbomachinery*, Vol. 111, pp. 97-103.

Blair, M. F. 1994, "An Experimental Study of Heat Transfer in a Large-Scale Turbine Rotor Passage," *ASME Journal of Turbomachinery*, Vol. 116, pp. 1-13.

Blevins, R. D., 1990, *Flow-Induced Vibration*, Van Nostrand Reinhold, New York.

Boyle, R. J., and Russell, L. M. 1990, "Experimental Determination of Stator Endwall Heat Transfer," *Journal of Turbomachinery*, Vol. 112, pp. 547-557.

Boyle, R. J. 1991, "Navier-Stokes Analysis of Turbine Blade Heat Transfer," *Journal of Turbomachinery*, Vol. 113, pp. 392-403.

- Byerley, A., personal communication, Heat Transfer Course Notes, 1990.
- Byerley, A., and Baughn, J. W., to be published test results, 1994.
- Camci, C., Kim, K., Hippensteele, S. A., and Poinsatte, P. E. 1991, "Convective Heat Transfer at the Curved Bottom Surface of a Square to Rectangular Transition Duct using a new Hue Capturing Based Liquid Crystal Technique," *Fundamental Experimental Measurements in Heat Transfer*, ASME HTD-Vol. 179, pp. 7-22.
- Camci, C., Kim, K., and Hippensteele, S. A. 1992, "A New Hue Capturing Technique for the Quantitative Interpretation of Liquid Crystal Images Used in Convective Heat Transfer Studies," *ASME Journal of Turbomachinery*, Vol. 114, pp. 765-775.
- Ching, C. Y., and O'Brien, J. E. 1991, "Unsteady Heat Flux in a Cylinder Stagnation Region with High Free-stream Turbulence," *Fundamental Experimental Measurements in Heat Transfer*, ASME HTD-Vol. 179, pp. 57-66.
- Clifford, R. J., Jones, T. V., and Dunne, S. T. 1983, "Techniques for Obtaining Detailed Heat Transfer Coefficient Measurements Within Gas Turbine Blade and Vane Cooling Passages," *ASME Paper 83-GT-58*.
- Crane, R. I., and Sabzvari, J. 1989, "Heat Transfer Visualization and Measurement in Unsatble Concave-Wall Laminar Boundary Layers," *ASME Journal of Turbomachinery*, Vol. 111, pp. 51-56.
- Dring, R. P., Blair, M. F., and Joslyn, H. D., 1986, "The Effects of Inlet Turbulence and Rotor Stator Interactions on the Aerodynamic and Heat Transfer of a Large-Scale Rotating Turbine Model, Vol II- Heat Transfer Data Tabulation, 15% Axial Spacing," NASA CR 179467, UTRC-R86-956480-2.
- Dullenkopf, K., Schulz, A., and Wittig, S. 1991, "The Effect of Incident Wake Conditions on the Mean Heat Transfer of an Airfoil," *Journal of Turbomachinery*, Vol. 113, pp. 412-418.
- Dullenkopf, K., and Mayle, R. E. 1994, "The Effects of Incident Turbulence and Moving Wakes on the Laminar Heat Transfer in Gas Turbines," *ASME Journal of Turbomachinery*, Vol. 116, pp. 23-28.
- Dunne, S. T. 1983, "A Study of Flow and Heat Transfer in Gas Turbine Cooling Passages," D. Phil. Thesis, Oxford University, Oxford, UK.
- Dunn, M. G., Rae, W. J., and Holt, J. L. 1984a, "Measurement and Analyses of Heat Flux Data in a Turbine Stage: Part 1-Description of Experimenatal Apparatus and Data Analysis," *Journal of Engineering for Gas Turbines and Power*, Vol. 106, pp. 229-233.

- Dunn, M. G., Rae, W. J., and Holt, J. L. 1984b, "Measurement and Analyses of Heat Flux Data in a Turbine Stage: Part 2-Discussion of Results and Comparison with Predictions," *Journal of Engineering for Gas Turbines and Power*, Vol. 106, pp. 234-240.
- Dunn, M. G., and Chupp, R. E. 1988, "Time-Averaged Heat-Flux Distributions and Comparison with Prediction for the Teledyne 702 HP Turbine Stage," *Journal of Turbomachinery*, Vol. 110, pp. 51-56.
- Dunn, M. G., Seymour, P. J., Woodward, S. H., George, W. K., and Chupp, R. E. 1989, "Phase-Resolved Heat-Flux Measurements on the Blade of a Full-Scale Rotating Turbine," *Journal of Turbomachinery*, Vol. 111, pp. 8-19.
- Dunn, M. G. 1990, "Phase and Time-Resolved Measurements of Unsteady Heat Transfer and Pressure in a Full-Stage Rotating Turbine," *Journal of Turbomachinery*, Vol. 112, pp. 531-538.
- Dunn, M. G., Kim, J., Civinskas, K. C., and Boyle, R. J. 1994, "Time-Averaged Heat Transfer and Pressure Measurements and Comparison with Prediction for a Two-Stage Turbine," *Journal of Turbomachinery*, Vol. 116, pp. 14-22.
- Dwyer, H. A., and McCroskey, W. J. 1973, "Oscillating Flow over a Cylinder at Large Reynolds Number," *Journal of Fluid Mechanics*, Vol. 61, 1973, pp. 753-767.
- Elderkin, M. J. , "Measurements of Local Heat Transfer Coefficients in Air for Staggered and In-Line Banks," Master's Thesis, University of California Davis.
- Fergason, J. L. 1964, "Liquid Crystals," *Scientific American*, Vol 211, pp. 76-85.
- Frössling, N. 1958, "Evaporation, Heat Transfer, and Velocity Distribution in Two-Dimensional and Rotationally Symmetrical Laminar Boundary Layer Flow," NACA TM-1432.
- Gostelow, J. P., and Blunden, A. R. 1989, "Investigation of Boundary Layer Transition in an Adverse Pressure Gradient," ASME *Journal of Turbomachinery*, Vol. 111, pp. 366-375.
- Gostelow, J. P., 1984, *Cascade Aerodynamics*, Pergamon Press, Oxford, England.
- Giedt, W. H. 1949, "Investigation of Variation of Point Unit Heat Transfer Coefficient Around a Cylinder Normal to an Air Stream," *Transactions of the ASME*, Vol. 71, pp. 375-381.

- Graziani, R. A., Blair, M. F., Taylor, J. R., and Mayle, R. E. 1980, "An Experimental Study of Endwall and Airfoil Surface Heat Transfer in a Large Scale Turbine Blade Cascade," *Journal of Engineering for Power*, Vol. 102, pp. 257-267.
- Guenette, G. R., Epstein, A. H., Giles, M. B., Haimes, R. and Norton, R. J. G. 1989, "Fully Scaled Transonic Turbine Rotor Heat Transfer Measurements," *Journal of Turbomachinery*, Vol. 111, pp. 1-7.
- Han, L. S., and Cox, W. R. 1983, "A Visual Study of Turbine Blade Pressure-Side Boundary Layers," *Journal of Engineering for Power*, Vol. 105, pp. 47-52.
- Handbook of Industrial Materials* 1992, Elsevier Advanced Technology, Oxford, UK.
- Handbook of Mathematical Functions* 1970, Department of Commerce, National Bureau of Standards, Washington, D. C.
- Hinze, J. O. 1975, *Turbulence*, McGraw-Hill, New York.
- Hippensteele, S. A., Russell, L. M., and Torres, F. J. 1985, "Local Heat-Transfer Measurements on a Large Scale-Model Turbine Blade Airfoil using a Composite of a Heater Element and Liquid Crystals," *Journal of Engineering for Gas and Power*, Vol. 107, pp. 953-960.
- Hippensteele, S. A., and Poinsatte, P. E. 1993, "Transient Liquid-Crystal Technique used to Produce High-Resolution Convective Heat-Transfer-Coefficient Maps," NASA TM 106083.
- Harasgama, S. P., and Wedlake, E. T. 1991, "Heat Transfer and Aerodynamics of a High Rim Speed Turbine Nozzle Guide Vane Tested in the RAE Isentropic Light Piston Cascade (ILPC)," *Journal of Turbomachinery*, Vol. 113, pp. 384-391.
- Hiwada, M., Niwa, K., Kumada, M., and Mabuchi, I. 1979, "Effects of Tunnel Blockage on Local Mass Transfer from a Circular Cylinder in Cross Flow," *Heat Transfer, Japanese Research*, Vol. 8-3, pp. 37-50.
- Hiwada, M., and Mabuchi, I. 1982, "Flow Behavior and Heat Transfer around a Circular Cylinder at High Blockage Ratios," *Heat Transfer, Japanese Research*, pp. 17-39.
- Ibrahim, M. B. 1985, "Turbulence Effects on Fluid Flow and Heat Transfer Near Stagnation Point of a Circular Cylinder." ASME Paper 85-HT-59.
- Igarashi, T. 1984, "Correlation between Heat Transfer and Fluctuating Pressure in Separated Region of a Cylinder," *Int. Journal of Heat and Mass Transfer*, Vol. 27, pp. 927-937.

Incropera, F. P., and DeWitt D. P. 1990, *Introduction to Heat Transfer*, John Wiley and Sons, New York.

Ireland, P. T., and Jones, T. V. 1985, "The Measurement of Local Heat Transfer Coefficients in Blade Cooling Geometries," *AGARD Conference Proceedings No. 390*, Paper 28.

Ireland, P. T., and Jones, T. V. 1986, "Detailed Measurements of Heat Transfer On and Around a Pedestal in Fully Developed Passage Flow," *Proceedings. 8th International Heat Transfer Conference*, Vol. 3, pp. 975-980.

Ireland, P. T. 1987, "Internal Cooling of Turbine Blades," D. Phil. Thesis, Oxford University, Oxford, UK.

Jones, T. V. 1977, "Heat Transfer, Skin Friction, Total Temperature and Concentration Measurements," *Measurements of Unsteady Fluid Dynamic Phenomena*, Richards B. E., ed., McGraw Hill, pp. 63-102.

Jones, T. V., and Hippensteele, S. A. 1987, "High-Resolution Heat-Transfer-Coefficient-maps Applicable to Compound Surfaces Using Liquid Crystals in a Transient Wind Tunnel," *Development in Experimental Technique in Heat Transfer and Combustion*, ASME HTD-Vol. 71, pp. 1-9.

Junkhan, G. H., and Serovy, G. K. 1967, "Effects of Free-Stream Turbulence and Pressure Gradient on Flat-Plate Boundary-Layer Velocity Profiles and on Heat Transfer," *Journal of Heat Transfer*, pp. 169-176.

Kays, W. M., and Crawford, M. E. 1980, *Convective Heat and Mass Transfer*, McGraw-Hill, New York.

Kestin, J. 1966, "The Effect of Free-Stream Turbulence on Heat Transfer Rates," *Advances in Heat Transfer*, Vol. 3, pp. 1-31.

Kidd, S. R., Sinha, P. G., Barton, J. S., and Jones, J. D. C. 1991, "Fibre optic Fabry-Perot sensors for high speed heat transfer measurements," *S.P.I.E.*, Vol. 1504, pp. 180-190.

Kim, K., Wiedner, B., and Camci, C., 1993, "Fluid Dynamics and Convective Heat Transfer in Impinging Jets Through Implementation of a High Resolution Liquid Crystal Technique, Part II: Navier-Stokes Computation of Impulsively Starting Heat Transfer Experiments," International Symposium on Air-Breathing Engines, Tokyo, Japan.

Klein, E. J. 1968, "Liquid Crystals in Aerodynamic Testing," *Aeronautics and Astronautics*, Vol. 6, pp. 70-73.

- Kraabel , J. S., McKillop, A. A., and Baughn, J. W. 1982, "Heat Transfer to Air from a Yawed Cylinder," *Int. Journal of Heat and Mass Transfer*, Vol. 25, pp. 409-418.
- Kurkal, K. R., and Munukutla, S. 1989, "Thermal Boundary Layer Due to Sudden Heating of Fluid," *Journal of Thermophysics*, Vol. 3 No. 4, pp. 470-472.
- Langston, L. S., Nice, M. L., and Hooper, R. M. 1977, "Three-Dimensional Flow within a Turbine Cascade Passage," *Journal of Engineering for Power*, Vol. 99, pp. 21-28.
- Lakshminarayana, B., Camci, C., Halliwell, I., and Zaccaria, M., 1992, "Investigation of Three Dimensional Flow Field in a Turbine including Rotor/Stator Interaction, Part1: Design Development and Performance of the Research Facility," American Institute of Aeronautics and Astronautics.
- Lebouche, M., and Martin, M. 1975, "Convection Forcee Autour Du Cylindre; Sensibilite Aux Pulsations De L'Ecoulement Externe," *Int. Journal of Heat and Mass Transfer*, Vol. 18, pp. 1161-1175.
- Lowery, G. W., and Vachon, R. I. 1975, "The Effect of Turbulence on Heat Transfer from Heated Cylinders," *Int. Journal of Heat and Mass Transfer*, Vol. 18, pp. 1229-1242.
- Mabuchi, M., Hiwada, M., and Kumada, M. 1974, "Some Experiments associated with Heat Transfer Mechanism in Turbulent Separated Region of a Cylinder," 5th Heat Transfer Conference, Tokyo, Japan, Vol. 2, pp. 315.
- MacMullin, R., Elrod, W., and Rivir, R. 1989, "Free-stream Turbulence From a Circular Wall Jet on a Flat Plate Heat Transfer and Boundary Layer Flow," ASME *Journal of Turbomachinery*, Vol. 111, pp. 78-86.
- Mancuso, T., and Diller, T. E.. 1991, "Time-Resolved Heat Flux Measurements in Unsteady Flow," *Fundamental Experimental Measurements in Heat Transfer*, ASME HTD-Vol. 179, pp. 67-74.
- Mayle, R. E., Blair, M. F., and Kopper, F. C. 1979, "Turbulent Boundary Layer Heat Transfer on Curved Surfaces," ASME *Journal of Heat Transfer*, Vol. 101, pp 521-525.
- Meel, D. A. 1962, "A Method for the Determination of Local Convective Heat Transfer from a Cylinder placed Normal to an Air Stream," *Int. Journal of Heat and Mass Transfer*, Vol. 5, pp. 715-722.
- Metzger, D. E., and Larson, E. E. 1986, "Use of Melting Point Surface Coatings for Local Convective Heat Transfer Measurements in Rectangular Channel Flows With 90-Degree Turns," ASME *Journal of Heat Transfer*, Vol. 108, pp 48-54.

Metzger, D. E., Bunker, R. S., and Bosch, G. 1991, "Transient Liquid Crystal Measurement of Local Heat Transfer on a Rotating Disk With Jet Impingement," ASME *Journal of Turbomachinery*, Vol. 113, pp. 52-59.

Moffat, R. J. 1990, "Experimental Heat Transfer," *Proceedings of the Ninth International Heat Transfer Conference*, Jerusalem, Israel.

Moore, J., and Ransmayr, A. 1984a, "Flow in a Turbine Cascade: Part 1- Losses and Leading-Edge Effects," *Journal of Engineering for Gas Turbines and Power*, Vol. 106, pp. 401-408.

Moore, J., and Ransmayr, A. 1984b, "Flow in a Turbine Cascade: Part 2- Measurement of Flow Trajectories by Ethylene Detection," *Journal of Engineering for Gas Turbines and Power*, Vol. 106, pp. 409-413.

Moore, J., and Adhye, R. Y. 1985a, "Secondary Flows and Losses Downstream of a Turbine Cascade," *Journal of Engineering for Gas Turbines and Power*, Vol. 107, pp. 961-968.

Moore, J., and Moore, J. G. 1985b, "Performance Evaluation of Linear Turbine Cascades Using Three-Dimensional Viscous Flow Calculations," *Journal of Engineering for Gas Turbines and Power*, Vol. 107, pp. 969-975.

Moore, J., Shaffer, D. M., and Moore, J. G. 1987, "Reynolds Stresses and Dissipation Mechanisms Downstream of a Turbine Cascade," *Journal of Turbomachinery*, Vol. 109, pp. 258-267.

Nealy, D. A., Mihelic, M. S., Hylton, L. D., and Gladden, H. J. 1984, "Measurements of Heat Transfer Distribution over the Surfaces of Highly Loaded Turbine Guide Vanes," *Journal of Engineering for Gas Turbines and Power*, Vol. 106, pp. 149-158.

Newman, L. B., Sparrow, E. M., and Eckert, E. R. G. 1972, "Free-Stream Turbulence Effects on Local Heat Transfer from a Sphere," *Journal of Heat Transfer*, Feb., pp 7-16.

O'Brien, J. E., and VanFossen, G. J. Jr. 1985, "The Influence of Jet-Grid Turbulence on Heat Transfer from the Stagnation Region of a Cylinder in Cross-flow," ASME Paper 85-HT-58.

O'Brien, J. E., Simoneau, R. J., LaGraff, J. E., and Morehouse, K. A. 1986, "Unsteady Heat Transfer and Direct Comparison for Steady-State Measurements in a Rotor-Wake Experiment", *Proceedings, 8th International Heat Transfer Conference*, San Francisco, pp. 1243-1248.

O'Brien, J. E. 1990, "Effects of Wake Passing on Stagnation Region Heat Transfer," ASME *Journal of Turbomachinery*, Vol. 112, pp. 522-530.

- Perdichizzi, A., and Dossena, V. 1993, "Incidence Angle and Pitch-Chord Effects on Secondary Flows Downstream of a Turbine Cascade," *Journal of Turbomachinery*, Vol. 115, pp. 383-391.
- Pohlhausen, E. 1921, "Der Wärmeaustausch zwischen festen Körpern und Flüssigkeiten mit kleiner Reibung und kleiner Wärmeleitung," *ZAMM*, Vol 1, pp. 115.
- Priddy, W. J., and Bayley, F. J. 1988, "Turbulence Measurements in Turbine Blade Passages and Implications for Heat Transfer," *Journal of Turbomachinery*, Vol. 110, pp. 73-79.
- Reda, D. C. 1991, "Observation of Dynamic Stall Phenomena Using Liquid Crystal Coatings," *AIAA Journal*, Vol. 29, No. 2, pp. 308-310.
- Reda, D. C., and Aeschliman, D. P. 1992, "Liquid Crystal Coating for Surface Shear-Stress Visualization in Hypersonic Flows," *Journal of Spacecraft and Rockets*, Vol. 29, No. 2, pp. 155-158.
- Richardson, P. D. 1963, "Heat and Mass Transfer in Turbulent Separated Flows," *Chemical Engineering Science*, Vol. 18, pp. 149-155.
- Rivir, R. B., Johnston, J. P., and Eaton, J. K. 1994, "Heat Transfer on a Flat Surface Under a Region of Turbulent Separation," *ASME Journal of Turbomachinery*, Vol. 116, pp. 57-62.
- Roach, P. E., 1987, "The Generation of Nearly Isotropic Turbulence by Means of Grids," *Heat and Fluid Flow*, Vol. 8, No 2, pp 82-92.
- Roby, J. L. 1993, "Measurement of Local Heat Transfer in Smooth and Ribbed Ducts using the Insertion Technique and Liquid Crystals," Master's Thesis, University of California Davis.
- Russell, L. M., Thurman, D. R., Simonyi, P. S., Hippensteele, S. A., and Poinsatte, P. E. 1993, "Measurements and Computational Analysis of Heat Transfer and Flow in a Simulated Turbine Blade Internal Cooling Passage," NASA TM 106189.
- Schlichting, H. 1968, *Boundary-Layer Theory*, McGraw-Hill, New York.
- Schmidt, S., and Wenner, K. 1943. "Heat Transfer over the Circumference of a Heated Cylinder in Transverse Flow." NACA-TM-1050.
- Schultz, D. L., and Jones, T. V. 1973. "Heat Transfer Measurements in Short Duration Hypersonic Facilities." Agardograph No. 165.

Schultz, D. L., Oldfield, M. L. G., and Jones, T. V. 1980, "Heat Transfer Rate and Film Cooling Effectiveness Measurements in a Transient Cascade," AGARD CP-281.

Sieverding, C. H. 1985, "Recent Progress in the Understanding of Basic Aspects of Secondary Flows in Turbine Blade Passages," *Journal of Engineering for Gas Turbines and Power*, Vol. 107, pp. 248-257.

Simoneau, R. J., and Simon, F. F. 1993, "Progress Towards Understanding and Predicting Heat Transfer in the Turbine Gas Path," *International Journal of Heat and Fluid Flow*, Vol. 14, No. 2, pp. 106-128.

Simonich, J. C., and Bradshaw, P. 1978, "Effect of Free-Stream Turbulence on Heat Transfer through a Turbulent Boundary Layer," *ASME Journal of Heat Transfer*, Vol. 100, pp. 671-677.

Son, J. S., and Honratty, T. J. 1969, "Velocity Gradients at the Wall for Flow Around a Cylinder at Reynolds Numbers from 5×10^3 to 1×10^5 ," *Journal of Fluid Mechanics*, Vol. 35, pp. 353-368.

Sparrow, E. M., Stahl, T. J., and Traub, P. 1984, "Heat Transfer Adjacent to the Attached End of a Cylinder in Cross-flow," *Int. Journal of Heat and Mass Transfer*, Vol. 27, pp. 233-242.

Sugawara, S., Sato, T., Komatsu, H., and Osaka, H. 1988, "Effect of Free-stream Turbulence on Flat Plate Heat Transfer," *Int. Journal of Heat and Mass Transfer*, Vol. 31, pp. 5-12.

Taylor, R. P., Coleman, H. W., Hosni, M. H., and Love, P. H. 1989, "Thermal Boundary Condition Effects on Heat Transfer in the Turbulent Incompressible Flat Plate Boundary Layer," *Int. Journal of Heat and Mass Transfer*, Vol. 32, pp. 1165-1174.

Turner, A. B. 1971, "Local Heat Transfer Measurements on a Gas Turbine Blade," *Journal Mechanical Engineering Science*, Vol. 13, pp. 1-12.

Wedlake, E. T., Brooks, A. J., and Harasgama, S. P. 1989, "Aerodynamic and Heat Transfer Measurements on a Transonic Nozzle Guid Vane," *Journal of Turbomachinery*, Vol. 111, pp. 36-42.

West, G. S., and Apelt, C. J. 1982, "The Effects of Tunnel Blockage and Aspect Ratio on the Mean Flow Past a Circular Cylinder with Reynolds Numbers between 10^4 and 10^5 ," *Journal of Fluid Mechanics*, Vol. 114, pp. 361-377.

Wilson, D. G., and Pope, J. A. 1954, "Convective Heat Transfer to Gas Turbine Blade Surfaces," *Proceedings Institutional Mechanical Engineering*, Vol. 168, pp. 861-874.

Yan, X. 1993, "A Preheated-Wall Transient Method using Liquid Crystals for the Measurement of Heat Transfer on External Surfaces and Ducts," PhD Dissertation, University of California Davis.

York, R. E., Hylton, L. D., and Mihelc, M. S. 1984, "An Experimental Investigation of Endwall Heat Transfer and Aerodynamics in a Linear Vane Cascade," *Journal of Engineering for Gas Turbines and Power*, Vol. 106, pp. 159-167.

Young, C. D., Han, J. C., Huang, Y., and Rivir, R. B. 1992, "Influence of Jet-Grid Turbulence on Flat Plate Turbulent Boundary Layer Flow and Heat Transfer," ASME *Journal of Heat Transfer*, Vol. 1114, pp 65-72.

Zukauskas, A. 1972, *Advances in Heat Transfer*, Vol. 8, Academic Press, N.Y., pp. 93-159.

APPENDICES

Appendix A Shroud Heater and Control Program

The data acquisition and control program for the shroud was written in BASIC and it uses an Omega A/D Card connected to an IBM AT computer. The data acquisition card measures the output of four K type thermocouples. One measures the air temperature, two measure the test object temperature, and one is used as an extra/reference temperature. Digital outputs are used to control a fan and a 100 W light bulb. The program measures the test object and air temperature and compares them to a desired set temperature. 5 V DC digital output signals are sent to solid state relays (which switch 110 V AC) in order to control the fan and light bulbs.

Thermocouples are a common, but sometimes difficult way to measure temperature. Thermocouples exhibit very small sensitivity to changes in temperature, therefore their output is quite often less than a millivolt. Many A/D boards with 12 bits of resolution are not capable of measuring these small voltages very accurately. Therefore, an A/D board with 16 bits of resolution and a ± 25 mV range was used. This produces a quantization resolution of:

$$\delta = \frac{50mV}{2^{16}} = 0.000763mV$$

Using the sensitivity of a K type thermocouple, one can turn the quantization resolution into a temperature resolution:

$$\Delta T = 0.000763 \text{mV} \cdot 24.713 \frac{\text{C}^\circ}{\text{mV}} = 0.019^\circ\text{C}$$

This shows that the Omega A/D board is capable of making these small measurements. Special limit of error K type thermocouples (from the same spool of wire) were used. The temperature measuring system was calibrated against a platinum resistance thermometer (see Appendix B) which is traceable back to the International Temperature Standard of 1990 (ITS-90).

The data acquisition and control software is self documenting, but it was written in BASICA, therefore awkward structure was sometimes unavoidable. Once the program is started, the A/D card is initialized and set to 16 bit resolution, ± 25 mV range, and the digital I/O's are set to output mode. The screen is then drawn. The screen is broken in to three regions: menu items, software outputs, and a real time temperature vs. time graph. A data file is then opened for data output.

The software runs in a continuous loop measuring temperatures and comparing them to the set temperature, to decide if the light bulb and fan should be on. The program calls the card to take voltage measurements from the thermocouples. The card uses an internal thermistor in order to reference the junction box temperature. The AM1 subroutine is called, which returns each thermocouple temperature. Each temperature is then adjusted for any bias and/or thermistor error. When the test sample temperature reaches the set point temperature, the light bulb is shut off. The fan should run all the time to minimize any temperature gradients within the apparatus, although, the fan is adding a small amount of energy to the container. Therefore, the fan is switched off if the average temperature is 0.1°C higher than the set temperature. In practice, the light

bulb rapidly kicks on and off when the steady state is reached, and the air within the apparatus keeps circulating. On/Off signals are sent to the screen informing the user of the fan and light bulb status.

The temperature measurements can be considered quasi-static because they change very slowly (the entire process is from 1 to 4 hours). Therefore, rapid data acquisition wasn't required. Some random noise is generated by trying to measure the temperature of moving air. To avoid the random noise in the voltage measurements, the "low noise" setting on the card was used which incorporates "boxcar" averaging of the data. A software interrupt ("ON TIMER") is used every minute to plot the data to a real time graph. Keyboard interrupts are used if the user wants to change the set temperature, print the data, or quit the program.

A listing of the program is included in the following pages.

```

3      HEATER CONTROL PROGRAM
5
10     ROBERT J. BUTLER
20
30   THIS PROGRAM DRIVES THE OMEGA WB-AAI-B DATA ACQ CARD TO HEAT AND
40   CONTROL THE TEMPERATURE OF THE TEST APPARATUS. THE PROGRAM
50   USES ANALOG CHANNELS 2,3,4 AND 5 TO MEASURE THE TEMPERATURE OF FOUR
60   SPECIAL LIMIT OF ERROR K TYPE THERMOCOUPLES. THE CHANNELS ARE
70   SET TO 16 BIT ACCURACY AND CH #5 THERMOCOUPLE IS USED AS AN EXTRA
80   TEMP. THE PROGRAM ALSO CONTROLS TWO RELAYS WHICH SWITCH A LIGHT
90   BULB ON OR OFF DEPENDING ON THE MEASURED VS DESIRED TEMPERATURE
AND
100  ONE RELAY CONTROLS A FAN. DATA IS AUTOMATICALLY SAVED TO A FILE AND
110  PLOTTED ON THE SCREEN. THE PROGRAM ALLOWS FOR THE USER TO CHANGE
THE
120  SET POINT OR PRINT THE TEMPERATURE AND TIME DATA. LINES 150-240 ARE
130  USED TO LET THE PROGRAM KNOW WHERE THE AM1 SUBROUTINE EXISTS IN
MEMORY.
140  .....
145
150 DATA
&H50,&HE8,&H18,&H00,&H3D,&HFF,&HFF,&H74,&H0C,&H58,&HFA,&HB8,&H59,&H47,&HC
D,&H60,&H90,&H90,&HCA,&H06,&H00,&HB8,&HFF,&HFF,&H5D,&HCA,&H06,&H00,&H56,&H
06,&HB8,&H00,&H00,&H8E,&HC0,&H26,&HA1,&H80,&H01,&H3D,&H00,&H00,&H74,&H1A,&H
8B,&HF0,&H26
160 DATA
&HA1,&H82,&H01,&H3D,&H00,&H00,&H74,&H0F,&H8E,&HC0,&H26,&H8A,&H04,&H3C,&H3
D,&H75,&H06,&H07,&H5E,&HB8,&H00,&H00,&HC3,&HB8,&HFF,&HFF,&H07,&H5E,&HC3.0
170 DIM A%(7), VOLT(7), DIG%(7), SET%(7)
180 DEF SEG . APROG$ = SPACE$(80): APROG1$ = SPACE$(80)
190 A% = VARPTR(APROG$): AX% = VARPTR(APROG1$)
200 AM1 = PEEK(A% + 1) + PEEK(A% + 2) * 256: AM2 = PEEK(AX% + 1) + PEEK(AX% + 2) *
256
210 RESTORE 150
220 FOR A = 0 TO 76
230 READ A%: POKE A + AM1, A%: POKE A + AM2, A%
240 NEXT: POKE AM2 + 19, 16: POKE AM2 + 26, 16
250
251 'SET CARD TO USE THE FIRST 5 CHANNELS
252 C$ = "N" + CHR$(0)
253 SET%(0) = 5
254 CALL AM1(SET%(0), VOLT(0), C$)
260
270 'SET THE CARD TO 16 BIT RESOLUTION AND LOW NOISE
280 C$ = "A" + CHR$(0)
290 SET%(1) = 18: SET%(2) = 18: SET%(3) = 18: SET%(4) = 18

```

```

300 CALL AM1(SET%(0), VOLT(0), C$)
310 '
320 'SET CHANNEL RANGES TO 50 mV AND SPECIFY TYPE K T/C
330 C$ = "r" + CHR$(0)
340 SET%(1) = 22: SET%(2) = 22: SET%(3) = 22: SET%(4) = 22
341 CALL AM1(SET%(0), VOLT(0), C$)
342 '
350 'SET 150 ms DELAY BETWEEN READINGS (INTEGER*.03)
351 C$ = "d" + CHR$(0)
352 SET%(0) = 5000
353 CALL AM1(SET%(0), VOLT(0), C$)
360 '
370 'SET THE DIGITAL I/O'S TO OUTPUT MODE
371 C$ = "S" + CHR$(0)
373 SET%(0) = 1: SET%(1) = 1: SET%(2) = 1
375 CALL AM1(SET%(0), VOLT(0), C$)
376 '
380 'CALIBRATE CARD
381 C$ = "c" + CHR$(0)
382 CALL AM1(DIG%(0), VOLT(0), C$)
383 '
384 'MAIN MENU AND SCREEN SETUP
385 SCREEN 2, 0
386 CLS
387 LINE (0, 0)-(639, 0)
388 LINE (0, 170)-(639, 170)
389 LINE (0, 199)-(639, 199)
390 LINE (0, 0)-(0, 199)
391 LINE (180, 0)-(180, 170)
392 LINE (639, 0)-(639, 199)
393 LINE (250, 10)-(250, 145)
394 LINE (250, 145)-(610, 145)
395 LOCATE 11, 25: PRINT "TEMP"
396 LOCATE 21, 53: PRINT "MINUTES"
397 LOCATE 20, 43: PRINT "60"      120      180      240"
398 LOCATE 2, 29: PRINT "60"
399 LOCATE 5, 29: PRINT "50"
400 LOCATE 9, 29: PRINT "40"
401 LOCATE 13, 29: PRINT "30"
402 LOCATE 17, 29: PRINT "20"
408 LOCATE 23, 6: PRINT "T: SET TEMPERATURE"
409 LOCATE 23, 34: PRINT "D: TAKE DATA"
410 LOCATE 23, 64: PRINT "Q: QUIT"
411 LOCATE 3, 8: PRINT "FAN : "
412 LOCATE 6, 5: PRINT "HEATER : "
413 LOCATE 10, 3: PRINT "REF TEMP : "
414 LOCATE 12, 3: PRINT "AIR TEMP : "
415 LOCATE 14, 3: PRINT "MODEL #1 : "
416 LOCATE 16, 3: PRINT "MODEL #2 : "
417 LOCATE 18, 3: PRINT "SET TEMP : "
418 PSET (248, 10): PSET (248, 40): PSET (248, 70): PSET (248, 100): PSET (248, 130)
419 PSET (340, 146): PSET (430, 146): PSET (520, 146): PSET (610, 146)
420 '

```

```

421 'SET TIMER TO PLOT DATA AND CALIBRATE EVERY MINUTE
422 ON TIMER(60) GOSUB 940
423 TIMER ON
424 MINUTES% = 0
425 OPEN "TEMP.DAT" FOR OUTPUT AS #1
426 PRINT #1, "AIR", "MODEL #1", "MODEL #2", "REF"
430 '
432 'MAIN LOOP UNTIL USER PRESSES "Q" (LOOP=0)
433 LOOP=1
434 WHILE LOOP
435   CHOICE$ = INKEY$
436   IF (CHOICE$ = "T") OR (CHOICE$ = "t") THEN GOSUB 928
437   IF (CHOICE$ = "D") OR (CHOICE$ = "d") THEN GOSUB 968
438 '
450 ' CALL THE CARD TO READ ANALOG TEMPERATURE
451   C$ = "m" + CHR$(0)
452   CALL AM1(A%(0), VOLT(0), C$)
453 ' CALIBRATE TEMPERATURES
457   AIR = VOLT(1) + .02
458   MOD1 = VOLT(2) + .03
459   MOD2 = VOLT(3)
460   REF = VOLT(4)
461   AVGTEMP = (MOD1 + MOD2) / 2!
470 '
471   LOCATE 10, 14: PRINT USING "##.##"; REF
472   LOCATE 12, 14: PRINT USING "##.##"; AIR
473   LOCATE 14, 14: PRINT USING "##.##"; MOD1
474   LOCATE 16, 14: PRINT USING "##.##"; MOD2
475   LOCATE 18, 14: PRINT USING "##.##"; SETTEMP
476 '
477 ' DECIDE IF FAN AND WHICH LIGHT BULBS SHOULD BE ON
478   IF AVGTEMP < SETTEMP THEN DIG%(1) = 1 ELSE DIG%(1) = 0 'HEATER
479   DIG%(0) = 0 'EXTRA RELAY
480   IF AVGTEMP < SETTEMP + .1 THEN DIG%(2) = 1 ELSE DIG%(2) = 0 'FAN
481 '
482 ' SEND DIG% DATA TO FAN AND LIGHT BULB SWITCHES
483   C$ = "O" + CHR$(0)
484   CALL AM1(DIG%(0), VOLT(0), C$)
485   LOCATE 3, 14
486   IF DIG%(2) = 1 THEN PRINT "ON" ELSE PRINT "OFF"
487   LOCATE 6, 14
488   IF DIG%(1) = 1 THEN PRINT "ON" ELSE PRINT "OFF"
489 '
490 ' IF THE USER PRESSES Q THE PROGRAM QUILTS
491   IF (CHOICE$ = "Q") OR (CHOICE$ = "q") THEN LOOP=0
492 WEND
493 CLOSE #1
494 'BEFORE QUITING MAKE SURE THE FAN AND LIGHT BULBS ARE OFF
495 DIG%(0) = 0: DIG%(1) = 0: DIG%(2) = 0
496 C$ = "O" + CHR$(0)
497 CALL AM1(DIG%(0), VOLT(0), C$)
498 END
499 '

```

```
927 '
928 'SUBROUTINE TO CHANGE THE TEMPERATURE SET POINT
929 LOCATE 18, 3: INPUT "SET TEMP : ", SETTEMP
938 RETURN
939 '
940 'SUBROUTINE TO PLOT DATA AND CALIBRATE CARD EVERY MINUTE
941 C$ = "c" + CHR$(0)
942 CALL AM1(DIG%(0), VOLT(0), C$)
951 Y1% = -3 * AVGTEMP + 190
953 YSET% = -3 * SETTEMP + 190
954 MINUTES% = MINUTES% + 1
955 X% = 3 * MINUTES% / 2 + 250
956 PSET (X%, Y1%): PSET (X%, YSET%)
957 RETURN
958 '
960 'SUBROUTINE TO SEND DATA TO A FILE
962 PRINT #1, USING "###.##      "; AIR; MOD1; MOD2; REF
966 RETURN
967 '
968 'SUBROUTINE TO SET TIMER FOR DATA COLLECTION AND SHUT OFF FAN/HEATER
969 'SET TIMER TO COLLECT DATA EVERY 3 SECONDS
970 ON TIMER(3) GOSUB 960
971 TIMER ON
972 SETTEMP = 0
979 RETURN
```

Appendix B Thermocouple Calibration

Four special limit of error K type thermocouples were used to measure temperature. The thermocouples were connected to a IBM-AT computer through a Omega 16 bit A/D card. The A/D card was controlled by the data acquisition and control program described in Appendix A. The card used an internal thermistor to compensate for the reference junction temperature. This calibration was performed to bias each channel and correct for any bias in the reference temperature.

The thermocouples were exposed to their normal operating temperatures (15° to 40° C) using a Rosemount constant temperature bath. In accordance with The International Temperature Scale of 1990, a platinum resistance thermometer is required in this temperature range as a known calibrated temperature. A four-wire Rosemount platinum resistance thermometer was used with a HP DVM. At each set point, temperatures were measured through the data acquisition program (with all the channel bias's equal to zero) and the resistance of the PRT was recorded. The results are shown in Table B.1 and are plotted in Figure B.1.

From these results it is clear the A/D card does a very good job compensating for the reference junction temperature and the thermocouples are very near standard. A slight bias in each channel can be corrected for depending on the normal operating temperature for that channel. The Ref and Air temperature channels operate near 20° C, while the two model temperature channels are usually around 40° C. The following bias for each channel was chosen:

Table B.1 Thermocouple calibration

PRT (Ohms)	PRT (C)	Ref Temp (C)	Air Temp (C)	Mod #1 Temp(C)	Mod #2 Temp(C)
27.469	19.12	19.13	19.12	19.12	19.10
28.026	24.63	24.61	24.59	24.56	24.59
28.483	29.16	29.16	29.15	29.10	29.12
29.051	34.79	34.81	34.80	34.74	34.77
29.473	38.99	39.04	39.04	38.96	39.01

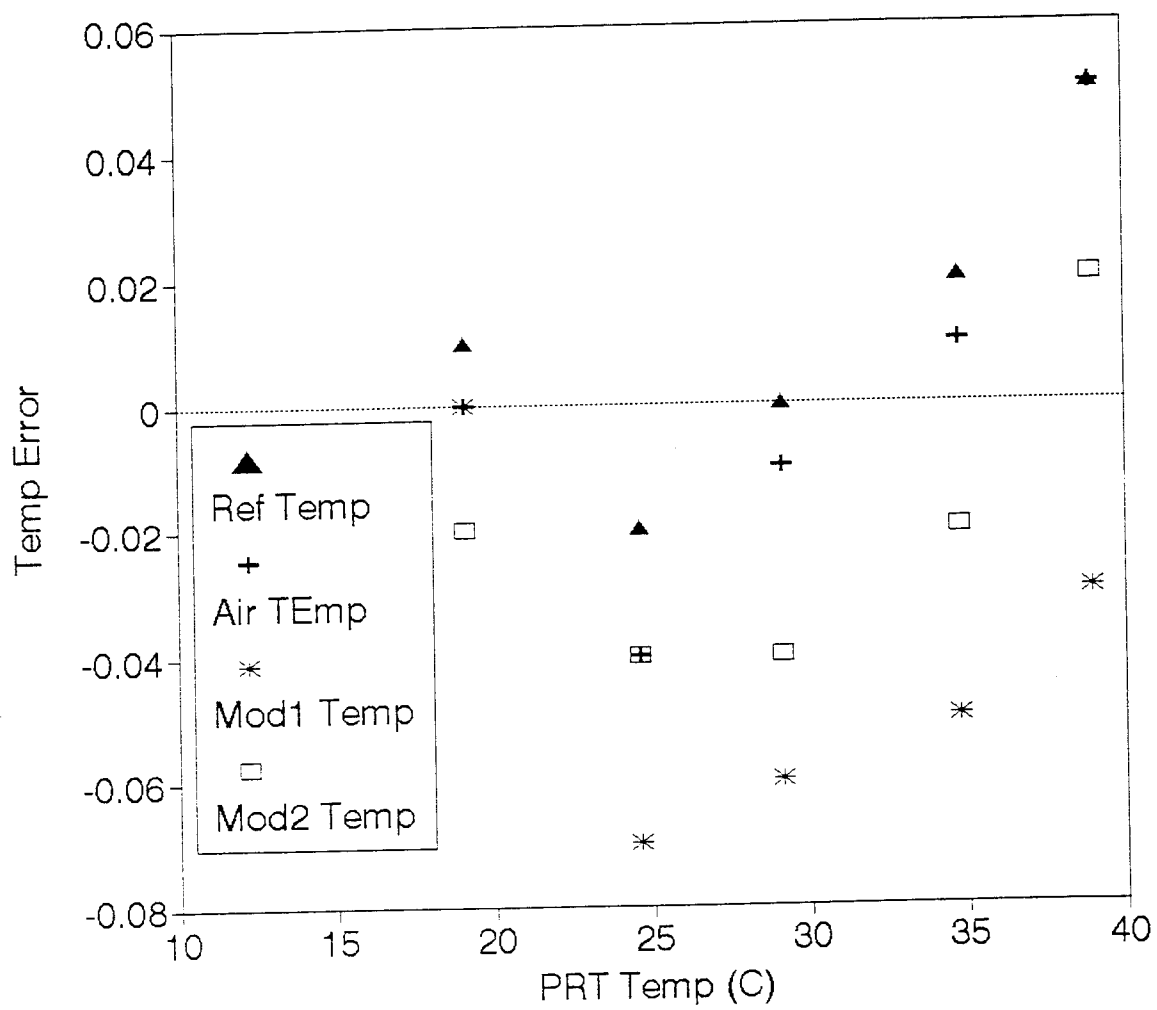


Figure B.1 Thermocouple calibration

$$T_{ref} = T_{ef} + 0.00$$

$$T_{air} = T_{air} + 0.02$$

$$T_{mod1} = T_{mod1} + 0.03$$

$$T_{mod2} = T_{mod2} + 0.00$$

These corrections are applied in the data acquisition program to further reduce the uncertainty of temperature measurements. A final uncertainty of $\pm 0.1^\circ \text{C}$ is attributed to the thermocouple temperature measurements.

Appendix C Liquid Crystal Calibration

Pure liquid crystals are thick clear (at most temperatures) liquids. Although, they do have properties of both liquid and solid crystalline states (Yan 1992). For our purpose, their most important feature allows them to be used as a temperature sensor because they reflect incident white light at different frequencies depending on their temperature. A detailed review of liquid crystals is given in Moffat (1990), but the most important information is included here.

Reinitzer (1888) an Austrian biologist, first discussed liquid crystals more than one-hundred years ago. It was much longer before liquid crystals made an impact on experimental engineering. Fergason (1964) understood and documented the use of liquid crystals. He also used liquid crystals as temperature sensor in many tests. In addition to being sensitive to temperature, liquid crystals are also color sensitive to shear and were used by Klein (1968) to visualize turbulent boundary layer transition.

Liquid crystals come in three types: smectic, nematic, and cholesteric. Each type of liquid crystal has a different molecular structure. In smetic and nematic liquid crystals, the molecules are "stacked on end" (Moffat, 1990). The molecules in cholesteric liquid crystals are layered, with each layer being slightly rotated relative to the layer above and below. This unique arrangement of cholesteric liquid crystals makes them more sensitive to outside influences. Temperature, shear, and other factors alter the alignment of the layers of molecules. The altered molecular arrangement reflects incident light differently, thus altering the color appearance of the material.

Their sensitivity to temperature is a very nice attribute, but they are also sensitive to shear, viewing angle, and they degrade from exposure to the environment and ultra-

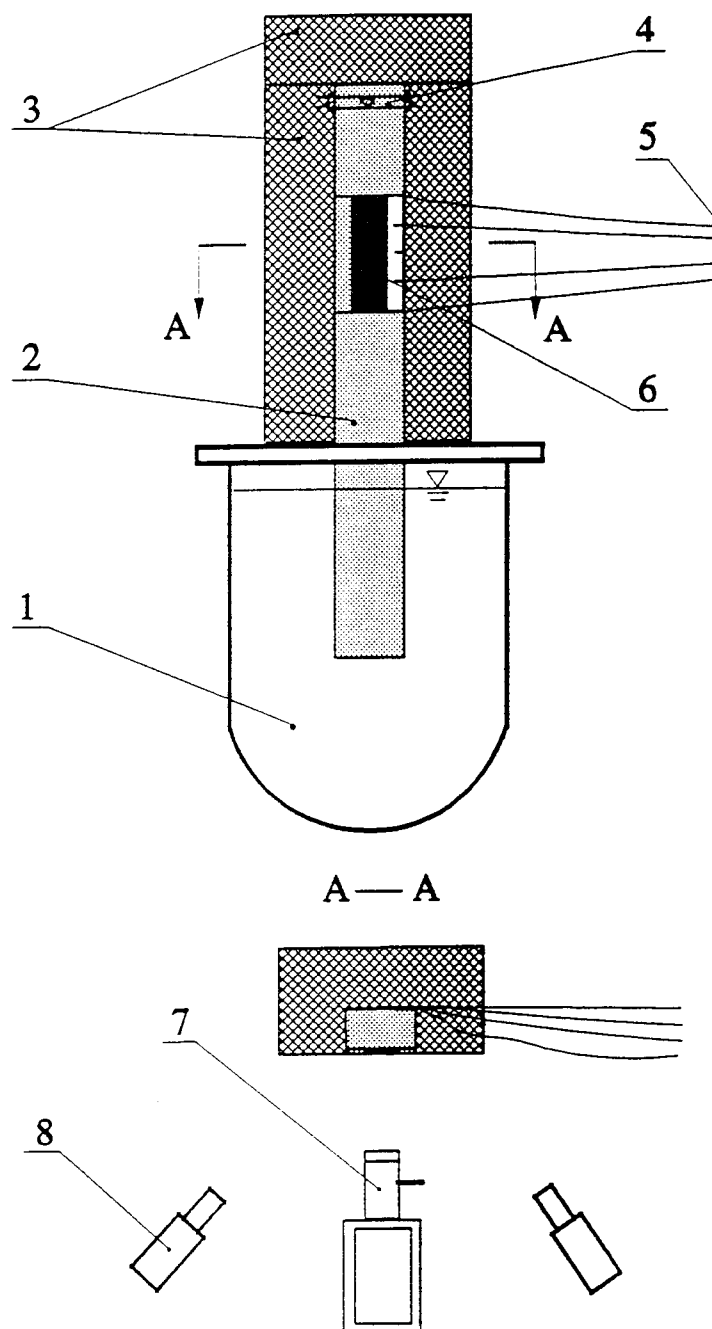
violet light, which has hampered their application for many years. More recently, cholesteric liquid crystals have been encapsulated in 10-30 micron diameter spheres. The encapsulated liquid crystals are more stable and less sensitive to viewing angle and shear, therefore, they are ideal for heat transfer experiments. Encapsulated liquid crystals are also easier to work with and different temperature range encapsulated liquid crystals can be combined to form a mixture with several event temperatures, without changing the properties of each individual temperature range.

Two different temperature range encapsulated cholesteric liquid crystals were used in this study. The liquid crystals are manufactured by Hallcrest and have specification numbers R35C1W and R40C1W. The event temperature for a particular liquid crystal refers to the temperature at which the liquid crystal appears yellow and the bandwidth (color play) refers to the range of temperatures which must occur for the color to span the spectrum (red, yellow, green, and blue). The event temperatures can be low or high and the bandwidth can be broad or narrow, depending on the composition. For the present experiments, the event temperature is selected when sizing the model for a particular experiment and the bandwidth is chosen to be very narrow to reduce the uncertainty of the measurements. The specification number is supplied by the manufacturer to give an approximate color play for the liquid crystals. In one case, R35C1W tells us that the red color first appears at about 35° C and the color band is approximately 1° C wide. This information is fine, but our technique requires a more rigorous calibration of the liquid crystals.

Two methods were used to calibrate the liquid crystals used in this study. The first method was developed by Yan (1993). He built a calibration rig (see Figure C.1)

which provided a linear temperature gradient through an aluminum bar with a cross-section of 1" x 1.5" x 16". Two resistance heaters (30 W) provided a uniform heat flux to one end of the calibration bar. The other end of the bar was held at a constant temperature using the Rosemount calibration bath. All sides of the calibration bar were insulated with styrofoam. In the middle of the bar, a four inch section was sprayed with black paint and the liquid crystals to be calibrated. In this four inch region, four special limit of error type K thermocouples were mounted. The thermocouple data was collected using a HP-3421A data acquisition system. The heater power was adjusted so the liquid crystal color band would form in the four inch region sprayed with liquid crystals. A linear temperature profile would be established when the calibration bar reached steady-state. A video camera recorded the color image on a VHS tape, while thermocouple data was collected. Using calibration marks on the bar to reference the thermocouple locations, the temperature of the center of the yellow color band could be determined. This method yielded the yellow region of the R35C1W liquid crystals to be $35.75^{\circ}\text{ C} \pm 0.13^{\circ}\text{ C}$ and the R40C1W liquid crystals to be $40.15 \pm .15^{\circ}\text{ C}$.

The author felt this method was reliable, but not practical because it took so long to perform and couldn't provide periodic checks of the liquid crystal calibration. Therefore, an easier method was considered and tested. The new method was based on the same principles as Yan's method. A long thin aluminum bar was used (.125" x .5" x 10"). On one side of the bar, a very small (.01") hole was drilled .05" deep.



- | | |
|------------------------------|--------------------|
| 1. Constant Temperature Bath | 5. Liquid Crystals |
| 2. Aluminum Bar | 6. Thermocouples |
| 3. Insulations | 7. Video Camera |
| 4. Heaters | 8. Illuminators |

Figure C.1 Liquid crystal calibration rig (from Yan)

The leads of a special limit of error type K thermocouple were stripped .05" and placed inside the drilled hole. The hole was closed by lightly flat punching around the hole. This arrangement formed an intrinsic thermocouple junction very near the surface of the aluminum bar. Voltage signals from the intrinsic thermocouple were collected by the data acquisition and control program (Ref Temp channel) described in Appendix A. The intrinsic thermocouple/bar was calibrated against the platinum resistance thermometer and the results are shown in Table C.1. This method has the advantage of using the same hardware to measure calibration temperatures as the actual heating apparatus. The intrinsic thermocouple/bar calibration against the PRT shows that it does not require a bias. The temperatures are within the resolution of the A/D card.

The calibration bar is then placed inside a plexiglas duct to allow viewing, but reduce any radiation and/or conduction errors. The plexiglas duct is heated to very near the calibration temperature and then the duct ends are insulated. From outside the duct, a temperature gradient is created in the calibration bar by heating one end. A temperature reading is taken when the intrinsic thermocouple is between each color of the liquid crystal color band. This calibration was performed before each test not only to check the liquid crystals, but to also check the temperature measuring system. Typical results for the two different liquid crystals are shown in Table C.2.

Table C.1 Intrinsic Thermocouple Calibration

PRT (ohms)	PRT Temp (C)	Intrinsic T/C (Ref Channel)
29.278	37.05	37.04
29.180	36.07	36.09
29.081	35.09	35.11

Table C.2 Liquid crystal calibration

	Black	Red	Yellow	Green
R35C1W	35.40	35.85	35.95	35.40
R40C1W	39.75	40.05	40.15	40.55

The center of the yellow color bands were determined to be 35.9° C and 40.10° C for the two different liquid crystals. This is in very good agreement with Yan's method. The data reduction for the transient method found it easiest to determine the location between the yellow and the red color bands. From this calibration, the yellow-red calibration temperature is 35.85° C for the R35C1W liquid crystals used in the transient cylinder study Moffat (1990) found the liquid crystal calibration temperature to be stable over roughly a year, but the color would fade as the liquid crystals deteriorated.

Appendix D Shroud Technique Data Reduction

The model colors are recorded on a VHS video tape for the shroud technique. The amount of time for each location to reach the liquid crystal event temperature is measured from the timer on the tape. The time and other measured parameters are entered into a data reduction spreadsheet. An example of the spreadsheet is shown in Table D.1. The top left region of the spreadsheet contains all of the measured and fixed values. The upper right portion of the spreadsheet holds flow properties which were calculated from the measured and fixed values. The measured parameters are: static pressure, free-stream ("static"- see Appendix J) temperature, model initial temperature, and manometer height. The fixed/calibrated values are: the model diameter, the liquid crystal event temperature, square root of the thermal properties of the model, and the model surface's emissivity.

The calculations are very straight forward, but are included for completeness. The air density is calculated using the perfect gas law:

$$\rho = \frac{P}{RT}$$

The viscosity of the air is calculated using Sutherland's equation:

$$\mu = \frac{1.458 \cdot 10^{-6} (T+273)^{1.5}}{(T+273+110.4)}$$

Table D.1 Transient method data reduction spreadsheet

P=	30 in Hg	d8	rho=	1.1971851
T=	23.71 C		mu=	1.83E-05
To=	39.26 C		K=	0.0260565
delta h=	0.119 in oil		V=	6.8019374
D=	0.076556 m		Re=	34058.783
Tlc=	35.85 C		T*=	0.7807074
pCpK^.5=	575		gamma=	0.2362104
emmis=	0.85			
to=	2.67	delta t	h	Nu Nu/Re^.5
0	6.9	4.23	60.592862	178.02621 0.9646492
10	6.8	4.13	61.387577	180.36114 0.9773012
20	6.7	4.03	62.211691	182.78245 0.9904212
30	6.8	4.13	61.387577	180.36114 0.9773012
40	7.16	4.49	58.652325	172.32478 0.9337555
50	7.63	4.96	55.539862	163.18013 0.8842045
60	8.26	5.59	52.000595	152.78151 0.8278587
70				
80				
80				
90				
100				
110				
120				
130				
140				
150				
160				
170				
180				

The air's thermal conductivity is interpolated from data using:

$$k_f = 7.4 \cdot 10^{-5} T + 0.024302$$

The velocity is measured using a pitot-static probe connected to an oil micromanometer capable of resolving 0.001 inches of oil. The oil has a specific gravity of 0.934. Since the Mach number is very low ($M \sim 0.06$), the Bernoulli equation applies.

$$P_o - P = \frac{1}{2} \rho V^2$$

And the hydrostatic equation for the manometer is:

$$P_o - P = \rho_{oil} g \Delta h$$

Combining, determines the velocity to be:

$$V = \sqrt{\frac{2 \rho_{oil} g \Delta h}{\rho}}$$

The Reynolds number based on diameter and the nondimensional temperature (T^*) are calculated based on their definitions.

$$Re = \frac{\rho V D}{\mu}$$

$$T^* = \frac{T_{LC} - T_\infty}{T_o - T_\infty}$$

The solution for one-dimensional conduction into a semi-infinite solid is:

$$T^* = e^{\gamma^2} \operatorname{erfc}(\gamma)$$

The only unknown is γ , but this step is tricky because there isn't an explicit solution. The spreadsheet data reduction is quite nice for this step because it is used to invert this function and solve for γ (see Appendix K for further details). For each location on the model (shown down the left hand side of the spreadsheet), the time at the event temperature is entered. The difference between the event temperature and the initial time is calculated and used in:

$$h_T = \frac{\gamma \sqrt{\rho C_p k}}{\sqrt{t}}$$

in order to calculate the total heat transfer coefficient. The heat transfer coefficient for convection is determined by subtracting the heat transfer coefficient due to radiation, which is:

$$h_r = \epsilon \sigma (T_{LC} + T_\infty) (T_{LC}^2 + T_\infty^2)$$

Where the temperatures are absolute and σ is the Stefan-Boltzmann constant. The Nusselt number is finally calculated using its definition.

$$Nu = \frac{hD}{k_f}$$

For this type of testing, a spreadsheet is ideal for reducing the data and plotting routines are included for easy analysis.

Appendix E Gold-Film Heated-Coating Data Reduction

The gold-film heated-coating method has very straight forward data reduction. An example of the data reduction spreadsheet is shown in Table E.1. The top left region of the spreadsheet contains all of the measured and fixed values. The upper right portion of the spreadsheet holds flow properties which were calculated from the measured and fixed values. The measured parameters are: static pressure, free-stream ("static"- see Appendix J) temperature, and manometer height. The fixed values are the length, width, and resistivity of the gold, the liquid crystal temperature, and the model surface's emissivity.

The air density, viscosity, thermal conductivity, and velocity are calculated using the same equations as were shown in Appendix D. The axial turbine blade chord length is used to calculate the Reynolds number based on inlet conditions.

The voltage across the gold film is adjusted to increase or decrease the surface temperatures. The power supply is set in order to produce the color yellow from the liquid crystals at any location from which data is being collected. When steady state is reached, the current, voltage, and free-stream temperature are recorded for that location. Each line of the spreadsheet is for different streamline distances along the surface. The local heat transfer coefficient is determined by:

$$h = \frac{q_c'''}{(T_{LC} - T_\infty)}$$

The adiabatic wall temperature is used in this equation as the reference temperature (T_∞). In this case, a thermocouple exposed to the free-stream tunnel air is used to

Table E.1 Gold-film heated-coating data reduction spreadsheet

P= 29.88 in Hg No Grid rho= 1.1793197kg/m^3
 T= 27 C mu= 1.846E-05 N s/m^2
 T lc= 40.1 C k air= 0.0263 W/mK
 delta h= 0.43 in oil V= 13.027415m/s
 L= 18.375 in Bx= 6.82 in
 W= 8 in Recx= 144170.31
 R"= 2.49 Ohms/SQ
 emmis= 0.85

s	s/Bx	Current	Volt	T inf	h	St
-7.5	-1.099707	3.05	17.47	27.5	38.953222	0.0025178
-7.5	-1.099707	3.19	18.33	27.5	43.134355	0.0027881
-7	-1.026393	3.02	17.27	27.5	38.081674	0.0024615
-7	-1.026393	3.17	17.17	27.5	42.525564	0.0027487
-6.5	-0.953079	2.98	17.05	27.5	36.933011	0.0023872
-6.5	-0.953079	3.15	18.06	27.5	41.920601	0.0027096
-6	-0.879765	2.95	16.88	27.5	36.081565	0.0023322
-6	-0.879765	3.1	17.75	27.5	40.424947	0.0026129
-5.5	-0.806452	2.87	16.4	27.5	33.853158	0.0021882
-5.5	-0.806452	3.05	17.47	27.5	38.953222	0.0025178
-5	-0.733138	2.84	16.22	27.5	33.0333	0.0021352
-5	-0.733138	3	17.16	27.5	37.505428	0.0024242
-4.5	-0.659824	2.81	16.05	27.5	32.222057	0.0020827
-4.5	-0.659824	2.95	16.88	27.5	36.081565	0.0023322
-4	-0.58651	2.78	15.86	27.5	31.419429	0.0020309
-4	-0.58651	2.87	16.4	27.5	33.853158	0.0021882
-3.5	-0.513196	2.74	15.65	27.5	30.362659	0.0019625
-3.5	-0.513196	2.84	16.22	27.5	33.0333	0.0021352
-3	-0.439883	2.69	15.35	27.4	28.79322	0.0018611
-3	-0.439883	2.81	16.05	27.5	32.222057	0.0020827
-2.5	-0.366569	2.46	14	27.4	23.168728	0.0014976
-2.5	-0.366569	2.78	15.86	27.5	31.419429	0.0020309
-2	-0.293255	2.31	13.12	27.4	19.771241	0.001278
-2	-0.293255	2.56	14.55	27.4	25.55243	0.0016516
-1.5	-0.219941	2.16	12.23	27.4	16.587432	0.0010722
-1.5	-0.219941	2.36	13.41	27.4	20.879994	0.0013496
-1	-0.146628	2.797	15.92	27	30.457496	0.0019687
-0.75	-0.109971	3.37	19.31	27.9	50.557166	0.0032679
-0.5	-0.073314	3.98	22.97	28	73.363595	0.004742
-0.25	-0.036657	4.66	27.12	28	102.64482	0.0066346

measure temperature (T_∞). For this very low Mach number flow, the measured temperature is within 0.1° C of the total, static, and adiabatic wall temperatures (this measurement is analyzed in more detail in Appendix J). The heat flux due to convection (q_c'') is determined by subtracting radiation and conduction losses from the local heat flux (q'').

$$q_c'' = q'' - \epsilon \sigma (T_{LC}^4 - T_\infty^4) - q_L''$$

The local heat flux (q'') can be calculated many ways. It is desirable to account for the temperature sensitivity of the gold surface, therefore simply using the product of current and voltage divided by the surface area can yield a small error. Because this method requires data to be collected at a constant temperature associated with the color yellow from the liquid crystals, the local resistance of the gold is fixed at 40° C . Assuming the current density is uniform through the model allows for the local heat flux to be calculated using:

$$q'' = \frac{i^2 R_{40}}{lw} = \frac{i^2 (R_{40}'' / w)}{lw} = \frac{i^2 R_{40}''}{w^2}$$

The current, length and width of the gold are measured. The resistance of the gold at 40° C (R_{40}) is expressed in terms of the resistance per square (R''). The resistance per square is a common way to express the resistance of surface coatings and it is simply the resistance of any size square piece (note: due to scaling of the electrical path, any size square piece will have the same resistance). The actual resistance of a rectangular piece is proportional to its length and inversely proportional to its width. The resistance of the gold sample was measured using a four-wire arrangement at 25° C to be

5.63 Ohms. Baughn et al. (1985) measured the temperature coefficient of the gold coating to be .0011 (1/C°). Therefore, the resistance of the coating would be $R_{40} = 5.63(1+.0011(40-25)) = 5.72$ Ohms at 40° C. Accounting for the dimensions of the gold yields $R''_{40} = R_{40}(w/l) = 2.49$ Ohms/square. Since the data already includes the voltage, it is interesting to reduce the data using the current/voltage product method. If everything is in order, the current/voltage product method should give slightly lower (less than 1%) results when the average blade temperature is below 40° C (at low heat transfer locations). The current/voltage product method will produce higher results (up to 3%) when the average blade temperature is higher than 40° C (at high heat transfer locations). At some locations, the two methods will give the same result because the average blade temperature is equal to 40° C.

The conduction losses (q_L'') can be shown to be negligible for the turbine blade because the model is heated from both sides and is made from polystyrene. The conduction losses can not be ignored on the relatively thin wooden flat plate model, but the losses can be measured fairly accurately. Thermocouple measurements were taken on the opposing side of the flat plate model for each liquid crystal location. This allowed for an estimation of the conduction loss using Fourier's conduction law:

$$q_L'' = -k_w \frac{(T_{LC} - T_w)}{L_w}$$

The Stanton number is finally calculated using its definition:

$$St = \frac{h}{\rho C_p V}$$

Appendix F Model Wall Thickness Sensitivity

Many transient methods use an assumption of conduction through a 1-D semi-infinite solid with a convective boundary condition. This brings up many questions. Does the body really behave like a 1-D solid? Does the finite thickness of the body effect the results of the data reduction? These are legitimate questions which need to be addressed.

The thickness of the Plexiglas model needs to be considered before a test is planned. The allowable thickness is dependent on the level of heat transfer and the nondimensional temperature T^* for a particular test. Most of the tests of the present study were performed with $T^*=0.8$. The magnitude of the heat transfer varies quit a bit, therefore a broad range is considered.

To determine the sensitivity of the wall thickness, three Plexiglas slabs are used which are 1/16, 1/8, and 1/4 inches thick. For this study, the slab will start with a uniform elevated temperature (39.125°C) and one side will be exposed to a convective boundary condition ($T_\infty=23^\circ\text{C}$). The boundary condition on the other wall will be natural convection ($5 \text{ W/m}^2\text{K}$). An insulated condition could have been chosen, but natural convection would be the worst case. A finite-difference code was written to solve the unsteady conduction problem until the outside wall temperature reaches the liquid crystal temperature ($T_{LC}=35.9^\circ\text{C}$). The code determines the amount of time it takes for each slab to reach the liquid crystal temperature for heat transfer coefficients ranging from 20 to 120 $\text{W/m}^2\text{K}$.

The code was written to solve the unsteady energy equation:

$$\rho C_p \frac{\partial T}{\partial t} V = kA \frac{\partial T}{\partial x} - hA(T - T_\infty)$$

The convective term is only used for the nodes at each wall. The slab is grid with 253 nodes. Numbers 1 and 253 are free-stream temperature, therefore number 2 is the outside wall, while number 252 is the inside wall. For time and spatial accuracy, a backward Euler implicit method is used. This produces a tridiagonal matrix of the following form:

$$\begin{array}{ccccccccc} & & & & & T_1 & & T_\infty \\ 1 & 0 & 0 & 0 & 0 & & & \\ A & B & C & 0 & 0 & T_2 & & D \\ & & & & & & & \\ 0 & * & * & * & 0 & \downarrow & = & \downarrow \\ 0 & 0 & A & B & C & T_{252} & & D \\ 0 & 0 & 0 & 0 & 1 & T_{253} & & T_\infty \end{array}$$

The matrix coefficients A, B, C, and D can be determined by discritizing the energy equation. The form of the equation depends on the type of node. For the interior nodes with only conduction, the equation is:

$$-\frac{k_{i-1/2}}{\Delta x} T_{i-1}^{n+1} + \left(\frac{\rho C_p \Delta x}{\Delta t} + \frac{k_{i-1/2}}{\Delta x} + \frac{k_{i+1/2}}{\Delta x} \right) T_i^{n+1} - \frac{k_{i+1/2}}{\Delta x} T_{i+1}^{n+1} = \frac{\rho C_p \Delta x}{\Delta t} T_i^n$$

The exterior nodes have convection on the surface and the node volume is half the size of an interior node. The outer surface equation (node #2) is:

$$\left(\frac{\rho C_p \Delta x}{2 \Delta t} + \frac{k_{i+1/2}}{\Delta x} + h \right) T_i^{n+1} - \frac{k_{i+1/2}}{\Delta x} T_{i+1}^{n+1} = \frac{\rho C_p \Delta x}{2 \Delta t} T_i^n + h T_{i-1}^n$$

The inner surface with natural convection (node #252) is:

$$-\frac{k_{i-1/2}}{\Delta x} T_{i-1}^{n+1} + \left(\frac{\rho C_p \Delta x}{2\Delta t} + \frac{k_{i-1/2}}{\Delta x} + h_n \right) T_i^{n+1} = \frac{\rho C_p \Delta x}{2\Delta t} T_i^n + h_n T_{i+1}^n$$

The code ran 18 times while varying the heat transfer coefficient for all three slab thicknesses. The results are shown in Table F.1.

The program determines the amount of time it takes the surface to cool to the liquid crystal temperature. Ideally, this would equal the amount of time our 1-D model would require. A comparison is shown in Figure F.1. This shows that the 1/4" slab performs very well for the whole range of heat transfer coefficients. The 1/16" slab diverges from the model at low heat transfer rates. In practice, the time is used to calculate a heat transfer coefficient using our 1-D model. If this is done, the result can be compared to the actual heat transfer coefficient which was used in the code. If the plate has adequate thickness, the heat transfer coefficients will be equal. This plot is shown in Figure F.2. At very high heat transfer, the plate can be very thin and there isn't a detrimental impact on the solution. Although, at low heat transfer the transients are very long and the 1/16" slab is too thin, while the 1/8" slab is marginal. This analysis shows how the model's wall thickness can artificially play a role in the results of transient test techniques. The code used in this analysis is listed at the end of this Appendix.

Table F.1 Wall Thickness Sensitivity

1/16" Thick Plexiglas

h	time (1-D)	actual time	actual h
20	36.91	21.67	26.1
40	9.23	8.50	41.7
60	4.10	4.10	60.0
80	2.31	2.33	79.6
100	1.48	1.49	99.6
120	1.02	1.03	119.7

1/8" Thick Plexiglas

h	time (1-D)	actual time	actual h
20	36.91	31.90	21.5
40	9.23	9.29	39.9
60	4.10	4.12	59.8
80	2.31	2.31	79.9
100	1.48	1.48	99.9
120	1.02	1.03	119.9

1/4" Thick Plexiglas

h	time (1-D)	actual time	actual h
20	36.91	36.90	20.0
40	9.23	9.25	39.9
60	4.10	4.11	59.9
80	2.31	2.31	79.9
100	1.48	1.48	99.9
120	1.02	1.03	119.9

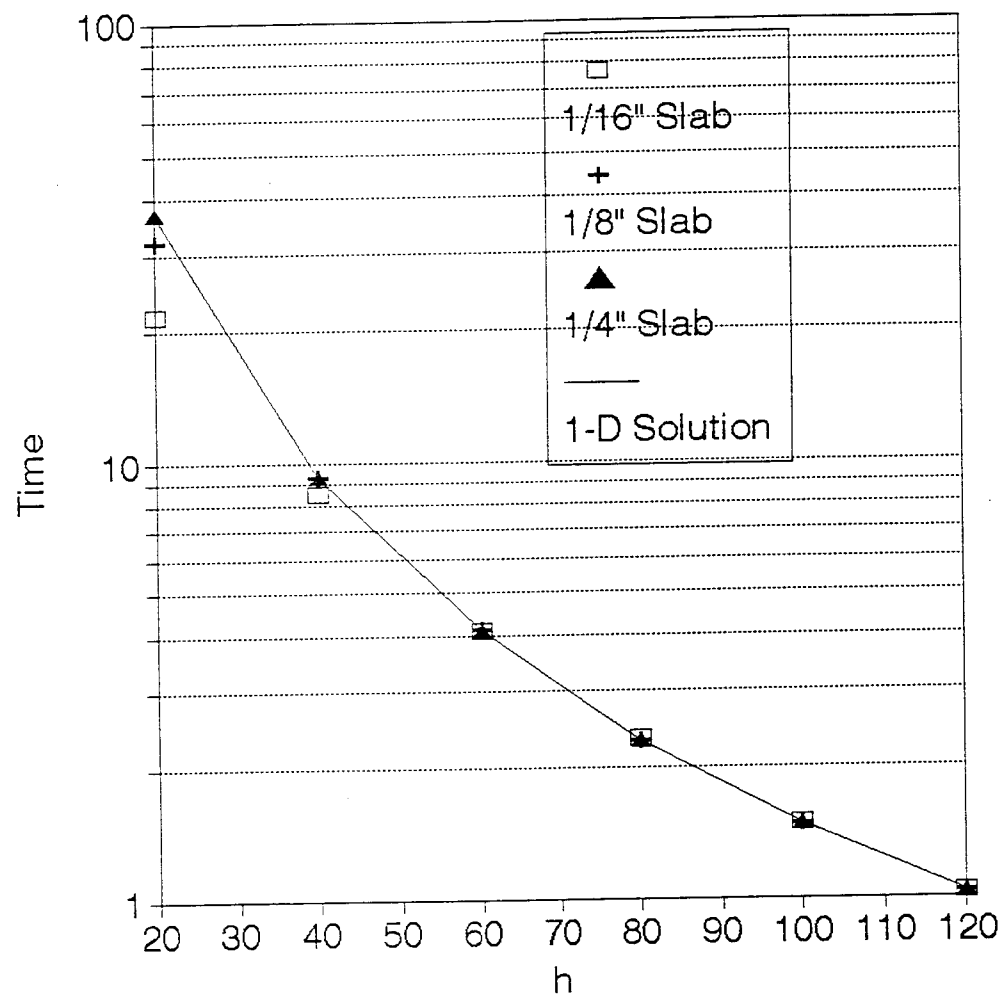


Figure F.1 Effect of wall thickness on transition time

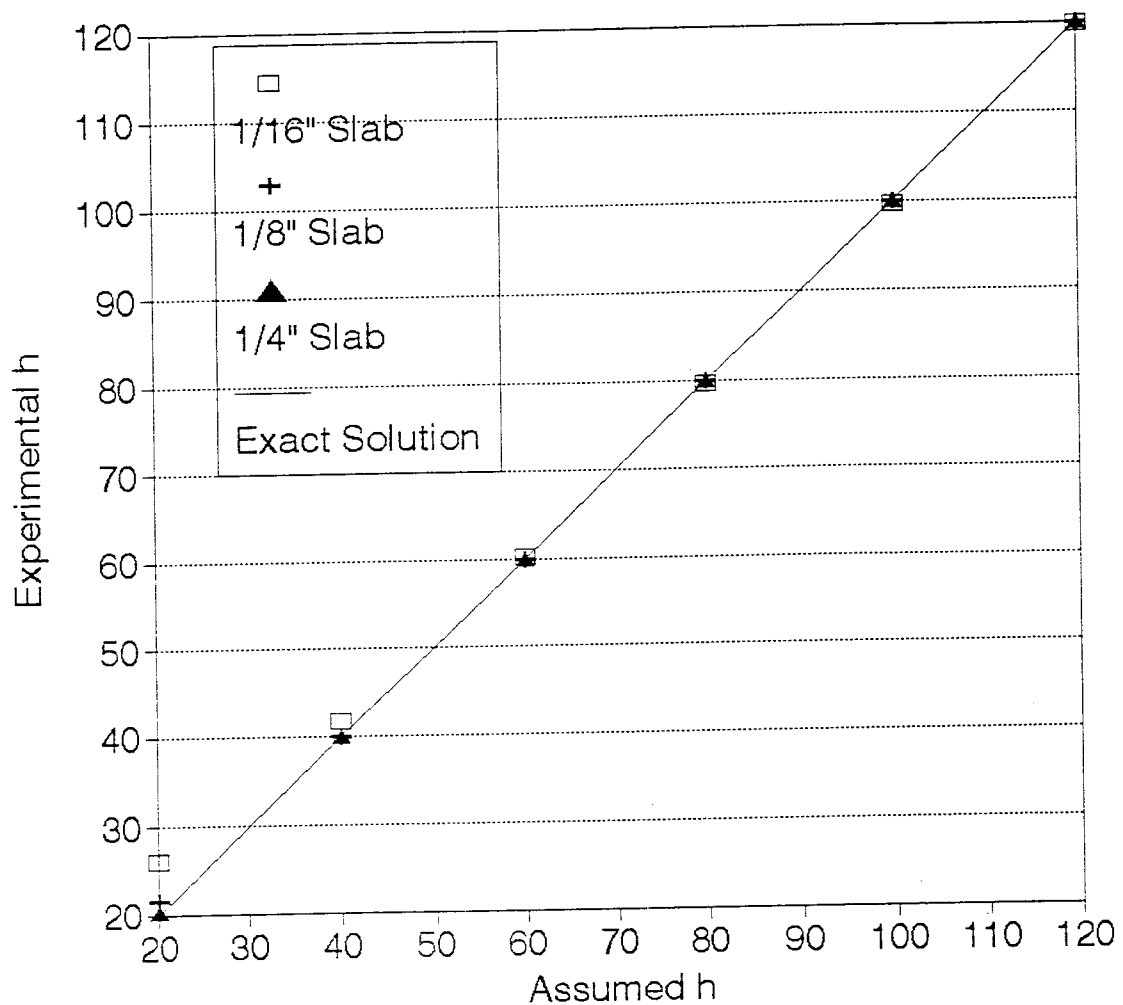


Figure F.2 Effect of wall thickness on calculated heat transfer coefficient

C ROBERT J. BUTLER

C THIS PROGRAM SOLVES THE UNSTEADY HEAT CONDUCTION FOR A
 C SLAB (1/16, 1/8, AND 1/4" THICK) WITH CONVECTIVE BOUNDARY
 C CONDITIONS ($h=20-120$) ON ONE SIDE AND NATURAL CONVECTION ON
 C THE OTHER SIDE ($h=5$). THE SLAB HAS THERMAL PROPERTIES OF
 C PLEXIGLAS AND STARTS AT 39.125 C AND THE PROGRAM RUNS UNTIL
 C THE SURFACE REACHES 35.9 C ($T^*=.80$), WHILE THE Free-stream IS
 C 23 C. THE PROGRAM USES A BACKWARD EULER IMPLICIT METHOD.

```

DIMENSION A(253),B(253),C(253),D(253),T(253),TOLD(253)
INTEGER I,J,N,IMAX
REAL A,B,C,D,T,TOLD,TIME,RHO,K,CP,DELTAX,DELTAT,H,HI
OPEN (UNIT=6,FILE='THICK.DAT',STATUS='UNKNOWN')
HI=5
IMAX=253
RHO=1190
CP=1462.3
K=.19
DO 1 N=1,6
H=N*20.0
DO 5 J=1,3
DELTAX=2***(J-1)*.0015875/250.0
DELTAT=DELTAX**2*RHO*CP/(2*K)
TIME=0
      print *,deltax,H
C INITIALIZE THE I.C. AND B.C.'S
DO 10 I=1,253
      T(I)=39.125
10    CONTINUE
      T(1)=23
      A(1)=0
      B(1)=1
      C(1)=0
      D(1)=23
      T(253)=23
      A(253)=0
      B(253)=1
      C(253)=0
      D(253)=23

```

```

C ITERATE UNTIL THE SURFACE (T(2)) IS LESS THAN 35.90
DO WHILE (T(2) .GT. 35.90)
    TIME=TIME+DELTAT
    DO 51 I=1,253
        TOLD(I)=T(I)
51    CONTINUE
C     CALCULATE MATRIX
    DO 60 I=2,252
        IF (I .EQ. 2) THEN
            A(I)=0
            B(I)=+K/DELTAX+CP*RHO*DELTAX/(2*DELTAT)+H
            C(I)=-K/DELTAX
            D(I)=CP*RHO*DELTAX*TOLD(I)/(2*DELTAT)+H*TOLD(I-1)
        ELSE IF (I .EQ. 252) THEN
            A(I)=-K/DELTAX
            B(I)=+K/DELTAX+CP*RHO*DELTAX/(2*DELTAT)+HI
            C(I)=0
            D(I)=CP*RHO*DELTAX*TOLD(I)/(2*DELTAT)+HI*TOLD(I+1)
        ELSE
            A(I)=-K/DELTAX
            B(I)=+2.0*K/DELTAX+CP*RHO*DELTAX/(DELTAT)
            C(I)=-K/DELTAX
            D(I)=CP*RHO*DELTAX*TOLD(I)/(DELTAT)
        ENDIF
60    CONTINUE
        CALL TRIDIA (IMAX,A,B,C,D)
        DO 35 I=1,253
            T(I)=D(I)
35    CONTINUE

        END DO

        WRITE(6,*) DELTAX,T(2),H,TIME

5    CONTINUE

1    CONTINUE

CLOSE (UNIT=6,FILE='THICK.DAT')
END

```

```
SUBROUTINE TRIDIA(IX,P,Q,R,S)
DIMENSION P(IX),Q(IX),R(IX),S(IX)
P(1)=0
RM=0
SM=0
R(IX)=0
C   DIRECT SWEEP
    DO 1 I=1,IX
        QI=Q(I)-P(I)*RM
        QINV=1.0/QI
        RM=R(I)*QINV
        SM=(S(I)-P(I)*SM)*QINV
        R(I)=RM
        S(I)=SM
1   CONTINUE
C   INVERSE SWEEP
    DO 2 IC=2,IX
        I=IX+1-IC
        S(I)=S(I)-R(I)*S(I+1)
2   CONTINUE
    RETURN
    END
```

Appendix G Model Size and Thermal Property Determination

When applying the shroud technique, it is very important to analyze the level of heat transfer to be measured in order to properly choose the heat transfer model's size and thermal properties. The transient technique works best when there is a balance between the heat transfer penetration depth and the amount of time the transient takes for the surface to reach the liquid crystal temperature. If the heat transfer penetrates the model too much, back side boundary conditions and two dimensional conduction will make the surface not behave like the one-dimensional model that we have assumed. This would suggest limiting the amount of time allowed for the model to cool. But, if the time is too short, time resolution creates large uncertainties in the measurement. All of these factors need to be considered before conducting transient heat transfer tests.

When examining an experimental setup, we have two major choices which will effect the penetration depth and the amount of time until liquid crystal transition. First, the size of the model can be changed in order to slow down or speed up an experiment. Secondly, the thermal properties of the model can be picked to alter the transient time. For this example, a cylinder in cross-flow is chosen for analysis. We first need a rough estimate on the maximum and minimum heat transfer coefficient expected on the model. Sometimes this step must be an educated guess, but for the cylinder, we know the maximum heat transfer to be about $Nu = .95\sqrt{Re}$ and the minimum to be $Nu = .25\sqrt{Re}$. We would like our model to be constructed from extruded Plexiglas because they are easy to find and are inexpensive. Therefore, we will look at the effect of different size

models. Note, in many cases the size will be fixed and the flexible variables are the thermal properties of the model. From the transient data reduction we know:

$$h = \frac{\gamma \sqrt{\rho C_p k}}{\sqrt{t}}$$

From the definition of Nusselt number:

$$Nu = \frac{hD}{k_f}$$

Substituting and solving for the time (t), yields:

$$t = \frac{\gamma^2 \rho C_p k D^2}{x^2 Re k_f^2}$$

Where x is either .25 or .95, depending if we are calculating the maximum or minimum time required for the transient. Applying this equation to Plexiglas cylinders of 2, 3, and 4 inch diameters, with wind tunnel speeds ranging from 7 to 21 m/s, gives the results shown in Table G.1 and Figure G.1.

Table G.1 Cylinder diameter analysis

Diameter=2"

Velocity (m/s)	Reynolds Number	Maximum Time	Minimum Time
7.0	22379	39.3	2.72
14.0	44758	19.6	1.36
21.0	67137	13.1	.91

Diameter=3"

Velocity (m/s)	Reynolds Number	Maximum Time	Minimum Time
7.0	33569	58.9	4.08
14.0	67137	29.4	2.04
21.0	100705	19.6	1.36

Diameter=4"

Velocity (m/s)	Reynolds Number	Maximum Time	Minimum Time
7.0	44758	78.5	5.44
14.0	89515	39.3	2.72
21.0	134273	26.2	1.81

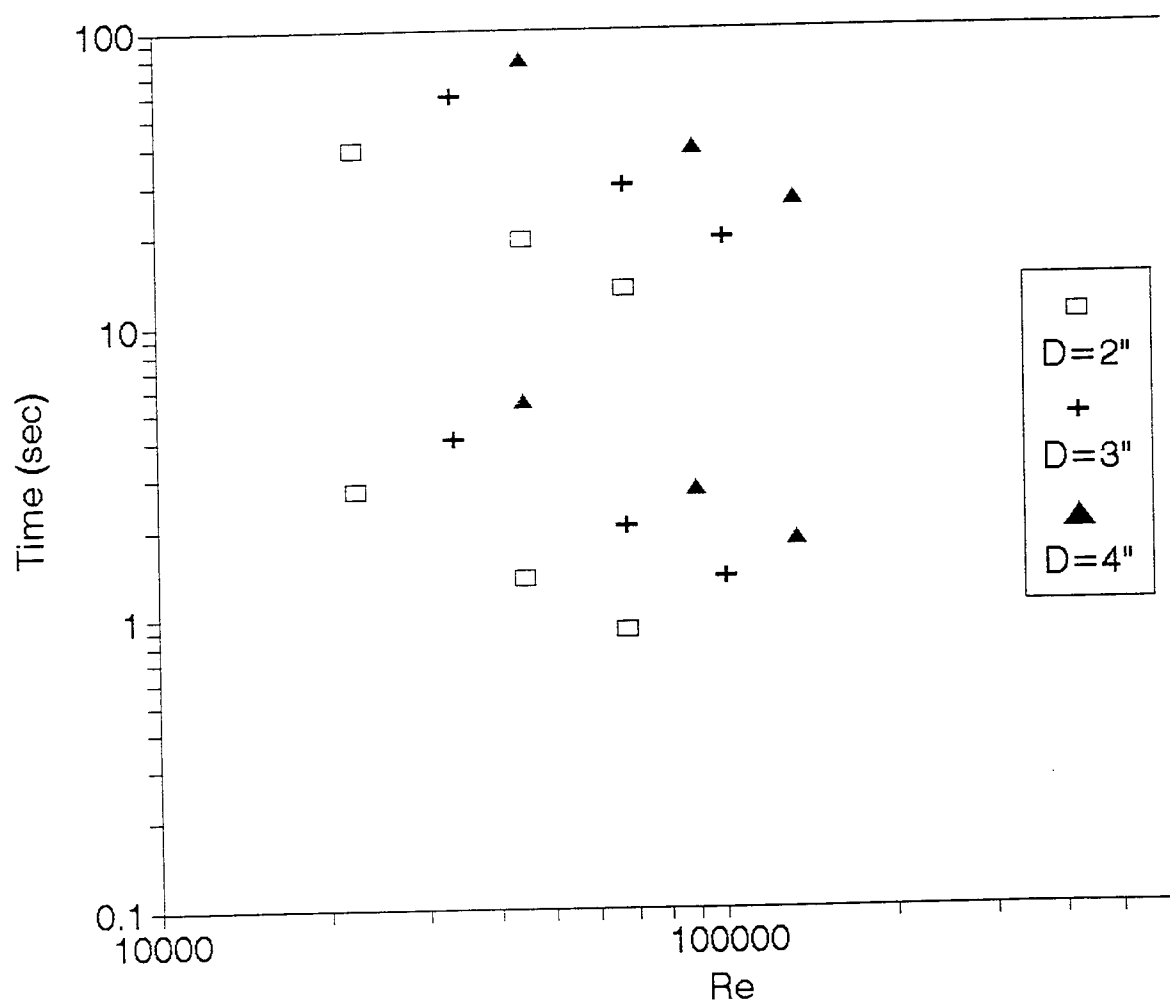


Figure G.1 Cylinder diameter analysis

This analysis determines the Reynolds number range available and the transient time required for the location of lowest and highest heat transfer. The transient time should be no greater than 60 seconds or the one-dimensional model breaks down. On the other end of the spectrum, we would like the transient time to be greater than one second for good time resolution with the video system (30 frames per second) and flow development time. The graph shows that the 4 inch cylinder responds too slowly at the lowest Reynolds number and the 2 inch cylinder responds too fast at the highest Reynolds number. Therefore, the 3 inch cylinder was chosen. This is an example of creating a good test situation when using the shroud technique. Keep in mind that in many heat transfer environments, we may have to change the model material for a more significant impact on the transient.

Appendix H Liquid Crystal and Paint Thickness Sensitivity

The shroud technique uses black paint and liquid crystals on the surface of the model, but does not account for them in the data reduction. The data reduction assumes conduction through a 1-D semi-infinite piece of Plexiglas with a convective boundary condition. This Appendix analyzes the ramifications of the paint and liquid crystal on the surface of the model.

This analysis is complicated by the fact that we do not know the exact thickness nor the thermal properties of the black paint and liquid crystal material. Although, educated approximate ranges can be considered for both. While painting the cylinder, a separate flat plate was sprayed with black paint and liquid crystals. A small region was cleaned and the depth of the paint/liquid crystals was measured with a depth micrometer to be less than or equal to .001". This will be used as the upper limit for this analysis. Unsteady conduction through a solid is governed by the thermal properties of the material. These properties are usually grouped as the $\sqrt{\rho C_p k}$. The value of $\sqrt{\rho C_p k}$ for Plexiglas is 575. An educated guess can be made for the paint and liquid crystals by looking at values for other material. Other material properties are shown in Table H.1.

Table H.1 Thermal properties for various materials

Material	$\sqrt{\rho C_p k}$
Plexiglas	575
Hard Rubber	618
Oil	495
Paper	474

The liquid crystals are a greasy organic material encapsulated in polymer spheres. It would be very difficult to determine the exact value for the paint/liquid crystal layers, therefore a range will be considered. The thermal properties ($\sqrt{\rho C_p k}$) will be varied from 475 to 675. This range is a larger than first appears, because this is a square root of the properties. The effect of the paint/liquid crystals will also depend on the level of heat transfer and the nondimensional temperature T^* for a particular test. Most of the tests of the present study were performed with $T^*=0.8$. The magnitude of the heat transfer varies quite a bit, therefore a broad range needs to be considered.

For this model, a 1/8" thick slab of Plexiglas will start with a uniform elevated temperature (39.125°C) and one side will be exposed to a convective boundary condition ($T_\infty=23^\circ \text{C}$). The side with convection will also have a thin layer of material with different thermal properties to simulate the paint/liquid crystals. Natural convection ($5 \text{ W/m}^2\text{K}$) will be imposed for the boundary condition on the other wall. A finite-difference code solves the unsteady conduction problem until the outside wall temperature reaches the liquid crystal temperature ($T_{LC}=35.9^\circ \text{C}$). The code determines the amount of time it takes for the slab to reach this temperature, for heat transfer coefficients ranging from 20 to 120 $\text{W/m}^2\text{K}$, paint/liquid crystal thicknesses of .0005 to .001", and for thermal properties of the paint/liquid crystals of 475, 575, and 675.

The code solves the unsteady energy equation:

$$\rho C_p \frac{\partial T}{\partial t} = kA \frac{\partial T}{\partial x} - hA(T - T_\infty)$$

The convective term is only used for the nodes at each wall. The slab is grid with 253 nodes. Numbers 1 and 253 are free-stream temperature, therefore number 2 is the

outside wall, while number 252 is the inside wall. The distance between nodes is .0005", therefore the code allows for variable thermal properties between the first three nodes. For time and spatial accuracy, a backward Euler implicit method is used. This produces a tridiagonal matrix of the following form:

$$\begin{array}{ccccccccc}
 & & & & & T_1 & & T_\infty \\
 1 & 0 & 0 & 0 & 0 & & & \\
 A & B & C & 0 & 0 & T_2 & & D \\
 0 & \times & \times & \times & 0 & \downarrow & = & \downarrow \\
 0 & 0 & A & B & C & T_{252} & & D \\
 0 & 0 & 0 & 0 & 1 & T_{253} & & T_\infty
 \end{array}$$

The matrix coefficients A, B, C, and D can be determined by discretizing the energy equation. The form of the equation depends on the type of node. For the interior nodes with only conduction, the equation is:

$$-\frac{k_{i-1/2}}{\Delta x}T_{i-1}^{n+1} + \left(\frac{\rho C_p \Delta x}{\Delta t} + \frac{k_{i-1/2}}{\Delta x} + \frac{k_{i+1/2}}{\Delta x}\right)T_i^{n+1} - \frac{k_{i+1/2}}{\Delta x}T_{i+1}^{n+1} = \frac{\rho C_p \Delta x}{\Delta t}T_i^n$$

The exterior nodes have convection on the surface and the node volume is half the size of an interior node. The outer surface equation (node #2) is:

$$\left(\frac{\rho C_p \Delta x}{2\Delta t} + \frac{k_{i+1/2}}{\Delta x} + h\right)T_i^{n+1} - \frac{k_{i+1/2}}{\Delta x}T_{i+1}^{n+1} = \frac{\rho C_p \Delta x}{2\Delta t}T_i^n + hT_{i-1}^n$$

The inner surface with natural convection (node #252) is:

$$-\frac{k_{i-1/2}}{\Delta x}T_{i-1}^{n+1} + \left(\frac{\rho C_p \Delta x}{2\Delta t} + \frac{k_{i-1/2}}{\Delta x} + h_n\right)T_i^{n+1} = \frac{\rho C_p \Delta x}{2\Delta t}T_i^n + h_nT_{i+1}^n$$

The code ran 36 times while varying the heat transfer coefficient, paint/liquid crystal thickness, and paint/liquid crystal properties. The results are shown in Table H.2.

Table H.2 Paint/Liquid Crystal Thickness Sensitivity

.0005" Thick Paint/Liquid Crystal

h	No Pnt/LC $\sqrt{\rho C_p}k=575$		Paint/LC $\sqrt{\rho C_p}k=475$		Paint/LC $\sqrt{\rho C_p}k=675$	
	time	h	time	h	time	h
20	31.90	21.5	31.85	21.5	32.0	21.5
40	9.28	39.9	9.21	40.0	9.33	39.8
60	4.12	59.8	4.07	60.2	4.16	59.6
80	2.31	79.9	2.27	80.6	2.34	79.4
100	1.48	99.9	1.45	101.0	1.50	99.2
120	1.03	119.9	1.00	121.5	1.04	118.9

.001" Thick Paint/Liquid Crystal

h	No Pnt/LC $\sqrt{\rho C_p}k=575$		Paint/LC $\sqrt{\rho C_p}k=475$		Paint/LC $\sqrt{\rho C_p}k=675$	
	time	h	time	h	time	h
20	31.90	21.5	31.74	21.6	32.05	21.5
40	9.28	39.9	9.12	40.2	9.38	39.7
60	4.12	59.8	4.01	60.7	4.19	59.4
80	2.31	79.9	2.23	81.4	2.37	79.0
100	1.48	99.9	1.41	102.2	1.52	98.5
120	1.03	119.9	.97	123.2	1.06	118.0

The program determines the amount of time it takes for the surface to cool to the liquid crystal temperature. Ideally, the different thermal properties of the paint/liquid crystals wouldn't have a large effect and the amount of time for the different cases would be nearly equal to the time for the case when the slab is solid Plexiglas ($\sqrt{\rho C_p k} = 575$). A comparison is shown in Figure H.1. The paint/liquid crystal thickness has a much larger effect than expected. Previously it was thought to have no effect at all. The layer of paint and liquid crystal material has the most dramatic effect when the heat transfer is very high and most of the unsteady conduction takes place near the surface. If the paint/liquid crystal layer reaches thicknesses on the order of .001", the error could be on the order of 3% at high heat transfer coefficients. This assumes thermal properties for the paint/liquid crystal material which may or may not be realistic. If the thermal properties of the paint/liquid crystal material falls outside the considered range, the error would be larger. On the other hand, the properties could be very similar to Plexiglas, therefore, producing no effect at all.

This analysis showed how the paint/liquid crystal thickness can artificially play a role in the result of transient test methods. The code used for this study is listed at the end of the Appendix.

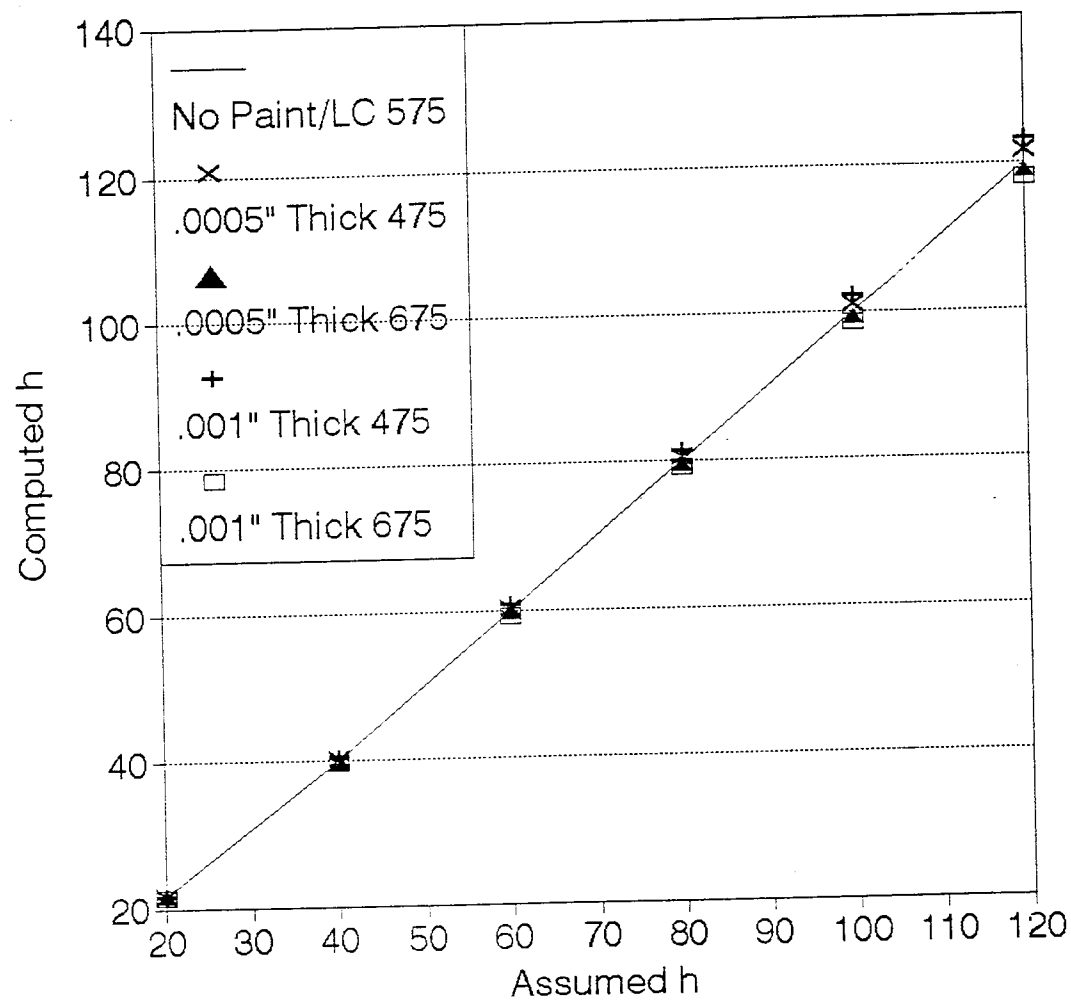


Figure H.1 Effect of paint/liquid crystal thickness on the heat transfer

C

ROBERT J. BUTLER

C THIS PROGRAM SOLVES THE UNSTEADY HEAT CONDUCTION FOR A
 C SLAB (1/8" THICK) WITH CONVECTIVE BOUNDARY CONDITIONS
 C (h=20-120) ON ONE SIDE AND NATURAL CONVECTION ON THE OTHER
 C SIDE (h=5). THE SLAB HAS THERMAL PROPERTIES OF PLEXIGLAS AND
 C STARTS AT 39.125 C AND THE PROGRAM RUNS UNTIL THE SURFACE
 C REACHES 35.9 C (T*=.80), WHILE THE Free-stream IS 23 C. THE AREA
 C BETWEEN NODES #2 THRU #4 HAS VARIABLE THERMAL PROPERTIES
 C TO ALLOW A COMPARISON OF LIQUID CRYSTAL AND PAINT
 C THICKNESSES OF .0005 AND .001". THE THERMAL PROPERTIES ARE
 C VARIED FROM (RHO Cp k)^{.5}=475,575,675. THE PROGRAM USES A
 C BACKWARD EULER IMPLICIT METHOD.

```

DIMENSION A(253),B(253),C(253),D(253),T(253),TOLD(253),KLC(4)
INTEGER I,J,M,N,IMAX
REAL A,B,C,D,T,TOLD,TIME,RHO,K,CP,DELTAX,DELTAT
P      ,H,HI,KLC,RCPK
OPEN (UNIT=6,FILE='DEPTH.DAT',STATUS='UNKNOWN')
HI=5
IMAX=253
RHO=1190
CP=1462.3
K=.19
KLC(4)=.19
DELTAX=.003175/250.0
DELTAT=DELTAX**2*RHO*CP/(2*K)
DO 1 N=1,6
H=N*20.0
DO 2 M=1,2
DO 5 J=1,3
RCPK=475+100*(J-1)
TIME=0
      print *,M*.0005,RCPK,H
DO 6 I=1,3
      KLC(I)=RCPK**2/(CP*RHO)
6   CONTINUE
IF (M .EQ. 1) THEN
      KLC(3)=.19
ENDIF

```

```

C INITIALIZE THE I.C. AND B.C.'S
DO 10 I=1,253
      T(I)=39.125
10    CONTINUE
      T(1)=23
      A(1)=0
      B(1)=1
      C(1)=0
      D(1)=23
      T(253)=23
      A(253)=0
      B(253)=1
      C(253)=0
      D(253)=23

C ITERATE UNTIL THE SURFACE (T(2)) IS LESS THAN 35.90
DO WHILE (T(2) .GT. 35.90)
      TIME=TIME+DELTAT
      DO 51 I=1,253
          TOLD(I)=T(I)
51    CONTINUE
C     CALCULATE MATRIX
      DO 60 I=2,252
          IF (I .EQ. 2) THEN
              A(I)=0
              B(I)=+KLC(2)/DELTAX+CP*RHO*DELTAX/(2*DELTAT)+H
              C(I)=-KLC(2)/DELTAX
              D(I)=CP*RHO*DELTAX*TOLD(I)/(2*DELTAT)+H*TOLD(I-1)
          ELSE IF (I .EQ. 252) THEN
              A(I)=-K/DELTAX
              B(I)=+K/DELTAX+CP*RHO*DELTAX/(2*DELTAT)+HI
              C(I)=0
              D(I)=CP*RHO*DELTAX*TOLD(I)/(2*DELTAT)+HI*TOLD(I+1)
          ELSE IF (I .EQ. 3 .OR. I .EQ. 4) THEN
              A(I)=-KLC(I-1)/DELTAX
              B(I)=+(KLC(I-1)+KLC(I))/DELTAX+CP*RHO*DELTAX/(DELTAT)
              C(I)=-KLC(I)/DELTAX
              D(I)=CP*RHO*DELTAX*TOLD(I)/(DELTAT)
          ELSE
              A(I)=-K/DELTAX
              B(I)=+2.0*K/DELTAX+CP*RHO*DELTAX/(DELTAT)
              C(I)=-K/DELTAX
              D(I)=CP*RHO*DELTAX*TOLD(I)/(DELTAT)
          ENDIF
60    CONTINUE

```

```

      CALL TRIDIA (IMAX,A,B,C,D)
      DO 35 I=1,253
          T(I)=D(I)
35      CONTINUE

      END DO

      WRITE(6,*) H,M*.0005,RCPK,TIME

5      CONTINUE

2      CONTINUE

1      CONTINUE

      CLOSE (UNIT=6,FILE='DEPTH.DAT')
      END

      SUBROUTINE TRIDIA(IX,P,Q,R,S)
      DIMENSION P(IX),Q(IX),R(IX),S(IX)
      P(1)=0
      RM=0
      SM=0
      R(IX)=0
C      DIRECT SWEEP
      DO 1 I=1,IX
          QI=Q(I)-P(I)*RM
          QINV=1.0/QI
          RM=R(I)*QINV
          SM=(S(I)-P(I)*SM)*QINV
          R(I)=RM
          S(I)=SM
1      CONTINUE
C      INVERSE SWEEP
      DO 2 IC=2,IX
          I=IX+1-IC
          S(I)=S(I)-R(I)*S(I+1)
2      CONTINUE
      RETURN
      END

```

Appendix I Hot-Wire Calibration and Measurement

Three different types of hot-wire measurements were used in the present study. The turbine blade testing used a constant temperature hot-film sensor. The hot-film probe was used in two different orientations which required separate calibrations. In addition, a constant current hot-wire was used to measure the vortex shedding frequency of the cylinder in cross-flow.

Upstream and downstream velocity and turbulence intensity measurements were required for the turbine blade aerodynamic tests. A TSI 1210-20 hot-film sensor was used in conjunction with a TSI constant temperature system. Data was collected at 1000 Hz using a 12 bit A/D board and IBM AT computer. The data collection and reduction program is listed at the end of this appendix. The upstream measurements were taken with the probe inserted down through the top of the tunnel with the wire in a horizontal position (cross-flow), while the downstream measurements had the wire oriented vertically with the probe attached to a stand pointed into the flow (endflow). With this orientation, the downstream measurements were less sensitive to flow angularity. Due to flow around the hot-film sensor supports, the two different probe orientations required different calibrations.

The hot-film sensors were calibrated using two different secondary standards. At very slow speeds (0-5 m/s), a TSI 1125 Calibrator was used with the probe in cross-flow. At higher speeds (5-20 m/s), a pitot-static tube and a micromenometer was used to determine the reference velocity. The probe was calibrated in cross-flow and endflow at the higher speeds. The two hot-film calibrations are shown in Tables I.1 and I.2, and Figures I.1 and I.2.

Table I.1 Hot-film calibration (cross-flow)

V (m/s)	e (volts)	e-e0 fit	V (m/s)	% error
0	6.888	0	0.026	na
0.585	7.124	0.236	0.558	-4.632
0.902	7.215	0.327	0.909	0.774
1.265	7.289	0.401	1.254	-0.901
1.524	7.343	0.455	1.540	1.026
1.951	7.414	0.526	1.962	0.579
2.438	7.493	0.605	2.499	2.506
2.972	7.561	0.673	3.022	1.692
3.658	7.63	0.742	3.617	-1.126
4.328	7.7	0.812	4.292	-0.825
5.182	7.779	0.891	5.152	-0.573
6.05	7.85	0.962	6.024	-0.428
6.95	7.918	1.03	6.957	0.103
9.5	8.073	1.185	9.501	0.014
13	8.244	1.356	13.127	0.975
14.63	8.3	1.412	14.537	-0.635

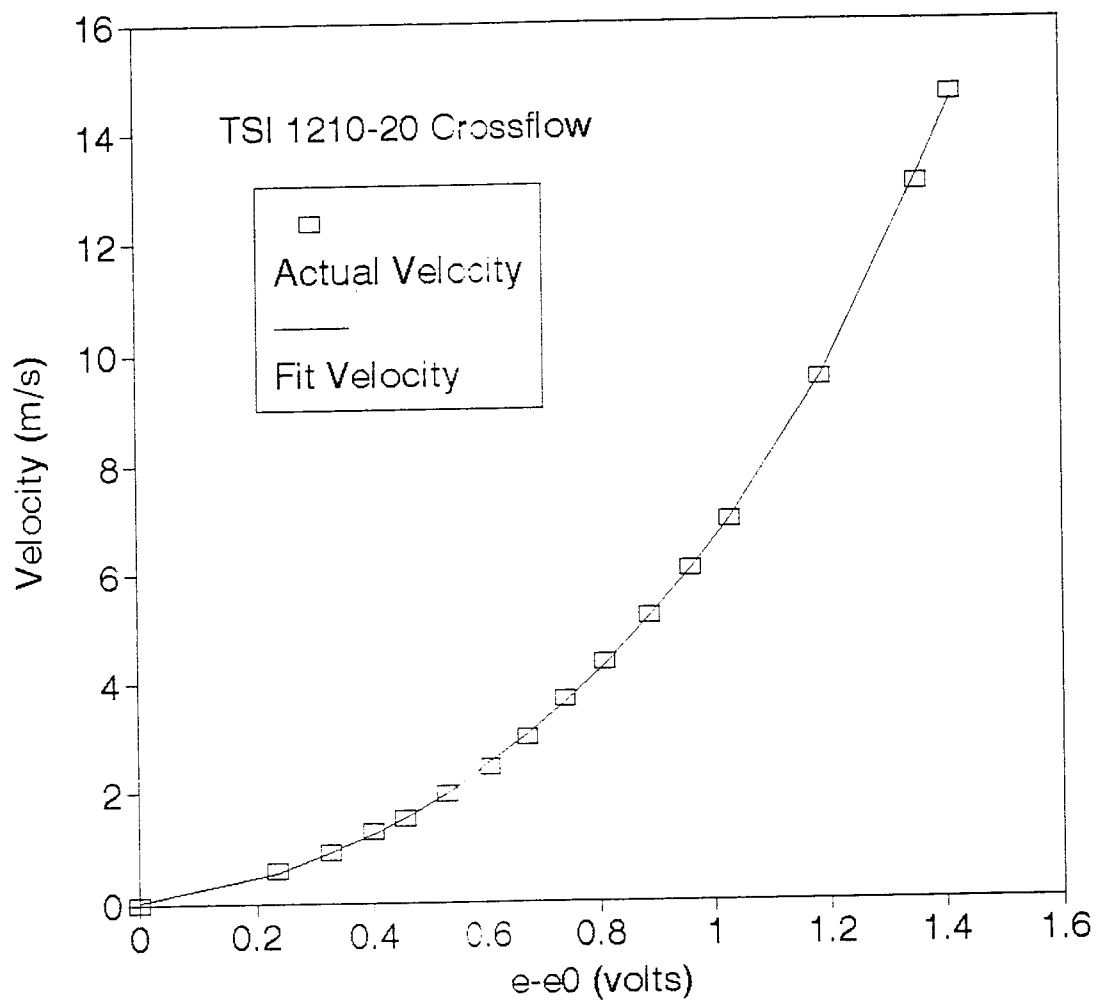


Figure I.1 Hot-film calibration (cross-flow)

Table I.2 Hot-film calibration (endflow)

V (m/s)	e (volts)	e-e0 fit	V (m/s)	% error
0	6.888	0	-0.007	na
0.585	7.124	0.236	0.598	2.235
0.902	7.215	0.327	0.913	1.184
1.265	7.289	0.401	1.226	-3.047
1.524	7.343	0.455	1.495	-1.874
1.951	7.414	0.526	1.909	-2.173
2.438	7.493	0.605	2.459	0.843
2.972	7.561	0.673	3.017	1.526
3.658	7.63	0.742	3.674	0.427
4.328	7.7	0.812	4.439	2.572
6.68	7.855	0.967	6.531	-2.226
10.04	8.05	1.162	10.040	-0.004
14.2	8.23	1.342	14.258	0.407
18.34	8.373	1.485	18.346	0.032
19.28	8.402	1.514	19.259	-0.110

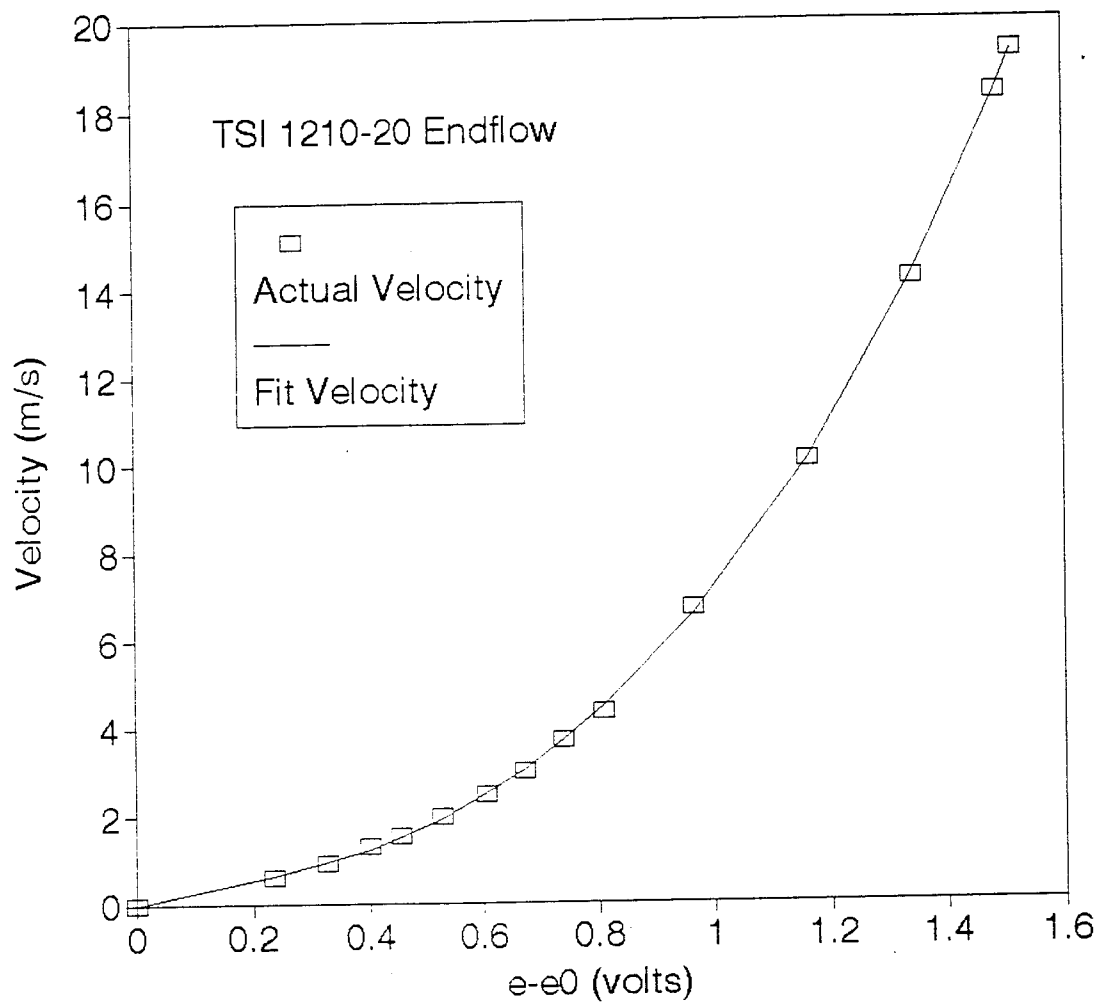


Figure I.2 Hot-film calibration (endflow)

The data was curve fit using a fourth-order polynomial. The calibration curve for the probe in cross-flow is:

$$V=1.903e^4 - 1.992e^3 + 5.571e^2 + 1.025e + .026$$

The calibration curve for the hot-film sensor in the endflow orientation is:

$$V=-.561e^4 + 5.562e^3 - .265e^2 + 2.324e - .007$$

Also shown in the tables are the percentage error produced by using the calibration curves. In the operational range, the errors associated with just the curve fit are on the order of 1%.

When measuring the heat transfer in the periodic wake region on the cylinder, it is important to measure the shedding frequency of the vortices. Outside unsteady influences like sound, pressure, or flow fluctuations can cause the periodic vortex shedding to be altered, which will directly effect the fluid mechanics and heat transfer. The shedding frequency behind the cylinder in cross-flow was measured using a simple constant current hot-wire. Constant current was provided to a TSI 0.0038 mm diameter hot-wire probe by putting it in series with 1000 Ohm resistor. A power supply was used to provide DC power. The voltage was adjusted (~26 Volts) to heat the hot-wire to roughly 250° C in still air. This setup wasn't used for velocity magnitude, therefore, a detailed calibration wasn't performed. With the probe hotter than the surrounding air, any change in flow velocity will cool the probe at different rates. This will result in the probe cooling and decreasing its resistance. Although the current is practically constant, because the probe resistance is so much smaller than the 1000 Ohm resistor. With constant current, the change in probe resistance will be seen as a change in voltage

across the hot-wire. Rapidly changing velocity due to the vortex shedding in the wake of the cylinder will cause the voltage to oscillate. This type of hot-wire will not provide extremely high frequency response, but is adequate for the present shedding frequencies up to 60 Hz. The voltage across the hot-wire was fed into a spectrum analyzer to determine the most dominate frequencies. The wires pick up 60 Hz noise from the lights and other electromagnetic interference. The 60 Hz noise is easy to see in the data and should be ignored. The amount of off frequency turbulence is heavily dependant on the probe location. The shedding frequency is easiest to measure if the probe is located where it will respond to the edge of vortices shedding from one side of the cylinder. For these tests, the probe was located 6 diameters downstream of the cylinder and 1.5 diameters from the centerline.

The code which was used for the hot-film data collection and reduction is listed at the end of this Appendix. This code was previously written by the named authors and it was modified for the present calibration.

```

C      WRITTEN BY ARASH BERUKHIM
C      MODIFIED BY NADER BAGHERI
C      MODIFIED BY J.F.K AND H.M.
C      MODIFIED BY ROBERT J. BUTLER
C
C      INTEGER*2 BUF(60000)
C      DIMENSION EV(60000)
C      INTEGER*4 COUNT,RATE,N1,N2
C      INTEGER*2 ADAPT,DEVICE,CHANLO,CTRL,MODE,N4
*   STOR,STAT,DATA
REAL DIS
CHARACTER*20 date,model
PRINT*,INPUT TODAYS DATE :'
READ*,date
PRINT*,INPUT MODEL TYPE FOR YOUR RECORD :'
READ*,model
OPEN(1,FILE='hwire.out',STATUS='unknown')
WRITE(1,*)"TESTING DATE = ", date
WRITE(1,*)"TESTING MODEL = ",model
C.....
N1=60000
N2=1000
PRINT*,ENTER THE NUMBER OF SAMPLES: '
READ*,N1
PRINT*,ENTER THE SAMPLING RATE: '
READ*,N2
WRITE(1,*)"    NUMBER OF SAMPLES = ',N1
WRITE(1,*)"    '
WRITE(1,*)"    SAMPLING FREQUENCY = ',N2
WRITE(1,*)"    '
WRITE(1,*)"Location Vave Vrms TI Veq Mean Volt RMS'
WRITE(1,*)" # (m/s) (m/s) (%) (m/s) (Volt) (Volt)'
PRINT*,***** NOTE '
PRINT*,***** TO EXIT THE PROGRAM PRESS CTRL
BREAK '
PRINT*,'
112  CONTINUE
C.....
C      PRINT*,*-*-*-*-*-*-* INPUT 1 IF YOU WISH AN E0 VALUE
C      READ*,EVALUE
C
C      PRINT*,'
C      PRINT*,'
C

```

```

C      IF (EVALUE.EQ.1) THEN
C          N1 = 60000
C          N2 = 1000
C          GO TO 115
C      ELSE
C.....
C          PRINT*,'*-*-*-*-*-*-*-' INPUT THE VALUE OF E0
C          READ*,Z
C          PRINT*' '
C          PRINT*' '
C.....
C      END IF
C.....
C.....SAMPLING LOOP
C.....
113    PRINT*,'ENTER LOCATION #'
        READ*,Y
C.....
C.. 6/8/93 (G.C.) N2=1000 FOR CALIBRATION OF IFA100 AGAINST HOT
WIRE
C
115    ADAPT=0
        DEVICE=9
        CHANLO=1
        CTRL=0
        MODE=128
        STOR=0
        COUNT=N1
        RATE=N2
        STAT=0
C
C----- DATA ACQUISITION STARTS
C
PRINT*, '** COLLECTING DATA ** '
CALL AINM(ADAPT,DEVICE,CHANLO,CTRL,MODE,STOR,
* COUNT,RATE,BUF(1),STAT)
IF(STAT.NE.0) GOTO 116
C
C----- VOLTAGE CALCULATION
C
C      ESUM=0
C      ESQSUM=0
C
C      IF (EVALUE.EQ.1) THEN
C          PRINT*' '

```

```

      PRINT*,** CALCULATING MEAN/RMS VELOCITY/Volt'
C      PRINT*,''
C      GO TO 111
C      END IF
C
C      PRINT*,''
C      PRINT*,'-- MOVE TO NEXT LOCATION --'
C      PRINT*,''
C      DO 1 I=1,N1
C      EV(I)=((BUF(I))*.0024420)
C      ESQSUM=EV(I)*EV(I) + ESQSUM
C      1 ESUM=EV(I)+ESUM
C      EAVE=ESUM/N1
C      ESQAVE=ESQSUM/N1
C      ERMSSQ = ESQAVE - EAVE*EAVE
C      ERMS=ERMSSQ**0.5
C
C----- RMS VOLTAGE CALCULATION
C
C      SDE=0
C      DO 2 I=1,N1
C2      SDE=(EV(I)-EAVE)*(EV(I)-EAVE)+SDE
C      ERMSSQ=SDE/N1
C      ERMS=ERMSSQ**.5
C
C      IF (EVALUE.EQ.1) THEN
C          PRINT*,''
C          PRINT*,'Eave = ',EAVE,' VOLTS'
C          PRINT*,'Erms = ',ERMS,' VOLTS'
C          PRINT*,''
C          PRINT*,''
C          Z = EAVE
C          EVALUE = 0
C          GO TO 113
C      END IF
C
C----- COEFFICIENTS FOR THE CALIBRATION CURVE
A=-43.979
B=222.118
C=-398.267
D=319.308
F=-92.42
C----- VELOCITY CALCULATION

```

```

C
  SUMV=0
  SUMVSQ=0
  ESUM = 0
  ESQSUM = 0
  DO 3 I=1,N1
C.....Voltage
  EV(I)=((BUF(I))* .0024420)
  ESQSUM=EV(I)*EV(I) + ESQSUM
  ESUM=EV(I)+ESUM
C.....Velocity
  E1=EV(I)-Z
  E2=E1*E1
  E3=E2*E1
  E4=E3*E1
  EV(I)=A*E4+B*E3+C*E2+D*E1+F
  SUMVSQ=SUMVSQ + EV(I)*EV(I)
  3  SUMV=EV(I)+SUMV
  VAVE=(SUMV/N1)
  VSQAVE=SUMVSQ/N1
  VRMS = (VSQAVE - VAVE*VAVE)**0.5
C
  EAVE=ESUM/N1
  ESQAVE=ESQSUM/N1
  ERMSSQ = ESQAVE - EAVE*EAVE
  ERMS=ERMSSQ**0.5
C----- RMS VELOCITY CALCULATION
C
C      SDV=0
C      DO 5 I=1,N1
C5      SDV=(EV(I)-VAVE)*(EV(I)-VAVE)+SDV
C      VRMSSQ=(SDV)/N1
C      VRMS=(VRMSSQ)**.5
C..... CALL CALIBEV(N1,Z,SUMV,BUF,EV,VAVE,VRMS)

      TI=VRMS/VAVE
      VEQ1=VAVE*((1+3*TI)/1.45)

      WRITE(6,452)VAVE,EAVE,VRMS,ERMS,VEQ1
452  FORMAT(' Vave =',1X,F6.3,' m/sec',' Eave =',1X,F6.3,' Volts',
*      /,' Vrms =',1X,F6.3,' m/sec',' Erms =',1X,F6.3,' Volts',
*      /,' Veq =',1X,F6.3,' m/sec')
      WRITE(1,106) Y,VAVE,VRMS,VI*100,VEQ1,EAVE,ERMS
106  FORMAT(5X,F6.3,3X,F7.4,5(3X,F6.3))
      PRINT*' '

```

```

      GOTO 113
116  PRINT*, 'EXECUTION ERROR'
114  STOP
      END

C      SUBROUTINE CALIBEV(N1,Z,SUMV,BUF,EV,VAVE,VRMS)
C.....CALIBRATION COEFFICIENTS
C

C.....CALIBRATION COEFFICIENTS
C      A=3.349
C      B=6.319
C      C=4.058
C      D=1.491
C      E=0.016
C
C      SUMV=0
C      DO 10 I = 1, N1
C          E1= BUF(I)*0.002442 -Z
C          E2=E1*E1
C          E3=E2*E1
C22      E4=E3*E1
C          EV(I)=A*E4+B*E3+C*E2+D*E1+E
C10      SUMV=EV(I)+SUMV
C          VAVE=(SUMV/N1)*1.013
C2      PRINT*, 'MEAN VELOCITY OBTAINED'
C.....VRMS
C
C      SDV=0
C      DO 20 J = 1, N1
C20      SDV=(EV(J)-VAVE)*(EV(J)-VAVE)+SDV
C          VRMSSQ = SDV/N1
C          VRMS= (VRMSSQ)**0.5
C      RETURN
C      END

```

Appendix J Adiabatic Wall Temperature

For many high speed flows, compressibility can play an important role in heat transfer and temperature measurements. By definition, the heat transfer is governed by Newton's law of cooling:

$$q'' = h(T_s - T_{aw})$$

When the surface temperature (T_s) reaches the adiabatic wall temperature (T_{aw}), heat transfer ceases to exist. The adiabatic wall temperature is dependant on the geometry of the body and is difficult to measure. Air temperature is measured using a thermocouple exposed to the wind tunnel air, this is referred to as the measured temperature (T_m). Due to compressibility, the free-stream temperature (T_∞) depends on the recovery factor (r) of the thermocouple. This relationship derives from the energy equation:

$$T_m = T_\infty + r \frac{v^2}{2c_p}$$

A typical recovery factor is about 60%, therefore using the most conservative and highest test speed of 21.5 m/s. the largest difference between the measured and free-stream temperature is:

$$T_m - T_\infty = 0.14^\circ C$$

Simple reasoning require the adiabatic wall temperature to be no greater than the total temperature (T_t) and no less than the free-stream temperature, thus:

$$T_{\infty} \leq T_{aw} \leq T_o$$

Through the energy equation, the total temperature is:

$$T_o = T_{\infty} + \frac{V^2}{2C_p}$$

For the most conservative case:

$$T_o - T_{\infty} = 0.23^{\circ}C$$

Since the adiabatic wall temperature is less than or equal to the total temperature, we can substitute it and change the equality to an inequality:

$$T_{aw} - T_{\infty} \leq 0.23^{\circ}C$$

Subtracting our first result ($T_m - T_{\infty} = 14^{\circ} C$) from this, leads us to the conclusion:

$$T_{aw} - T_m \leq 0.09^{\circ}C$$

This shows that the largest error produced by using the measured temperature rather than the adiabatic wall temperature is less than $0.09^{\circ} C$. This result is less than the uncertainty in the thermocouple measurements themselves and the thermocouple uncertainty. Therefore for these slow speeds, the adiabatic wall temperature does not have to be measured. It should be noted that these relations are proportional to the velocity squared, and will produce significant heat transfer errors at higher speeds.

Appendix K Inversion of the $\text{erfc}(\gamma)$ using Quattro Pro

The data reduction for the shroud technique solves for conduction through a 1-D, semi-infinite solid, with a convective boundary condition. The nondimensional surface temperature response is:

$$T^* = \frac{T_{LC} - T_\infty}{T_o - T_\infty} = e^{\gamma^2} \text{erfc}(\gamma)$$

Where $\text{erfc}(\gamma)$ is the complementary error function defined as:

$$\text{erfc}(\gamma) = 1 - \frac{2}{\sqrt{\pi}} \int_0^\gamma e^{-x^2} dx$$

And γ is related to the heat transfer coefficient, time, and the surface properties by:

$$\gamma = \frac{h\sqrt{t}}{\sqrt{\rho C_p k}}$$

In order to solve for the unknown heat transfer coefficient (h), γ must be solved for explicitly. This requires the inversion of the complementary error function, which does not have a closed form solution. Yan (1993) used a polynomial curve fit in his data reduction. This author used the power of modern computer spreadsheets which contain features that allow implicit equations to be solved automatically. The *Handbook of Mathematical Functions* (1970) gives the following equation:

$$\operatorname{erf}(\gamma) = 1 - (a_1 s + a_2 s^2 + a_3 s^3 + a_4 s^4 + a_5 s^5) e^{-\gamma^2} + \epsilon$$

$$s = \frac{1}{1 + p\gamma}$$

$$p = .3275911 \quad a_1 = .254829592 \quad a_2 = -.284496736$$

$$a_3 = 1.421413741 \quad a_4 = -1.453152027 \quad a_5 = 1.061405429$$

Where the error (ϵ) is less than 1.5×10^{-7} . This equation is for the error function and needs to be rewritten in terms of our equation and the complimentary error function.

$$T^* = \frac{T_{LC} - T_\infty}{T_o - T_\infty} = e^{\gamma^2} \operatorname{erfc}(\gamma) = e^{\gamma^2} (1 - \operatorname{erf}(\gamma))$$

$$T^* = e^{\gamma^2} (1 - \operatorname{erf}(\gamma)) = a_1 s + a_2 s^2 + a_3 s^3 + a_4 s^4 + a_5 s^5 + \epsilon e^{\gamma^2}$$

The unknown which has to be solved for is γ and it is hidden inside of s . In order for a spreadsheet to solve an implicit equation, it must be able to call the same cell it is calculating. It solves for the value of this cell (over and over) until it converges. Therefore, the unknown value must be the cell itself and this requires us to rewrite the equation one more time.

$$\gamma = \gamma - T^* + a_1 s + a_2 s^2 + a_3 s^3 + a_4 s^4 + a_5 s^5$$

This equation is entered into the spreadsheet. The equation is implicit and the spreadsheet uses the value of the cell itself, to calculate the value for the cell. The recalculation setting needs to be set for at least 10 iterations. This method was checked by comparing inverted solutions of the complementary error function to the exact solution. Results are shown in Table K.1 for the operational range of T^* 's.

Table K.1 Iterative inversion of the complementary error function

given γ	exact $\text{erf}(\gamma)$	$T^* = e^{\gamma^2} \text{erfc}(\gamma)$	iteration for γ	% error
.15	.1679959714	.850936	.15000008	5.24E-5
.20	.2227025892	.809020	.20000017	8.49E-5
.25	.2763263902	.770347	.25000018	7.38E-5
.30	.3286267595	.734599	.30000012	4.04E-5
.35	.3793820536	.701496	.35000000	1.29E-6
.40	.4283923550	.670788	.39999986	3.40E-5
.45	.4754817198	.642252	.44999974	5.80E-5

These results show that for this type of inversion of the complementary error function the error is of the order of machine accuracy. Yan's (1993) curve fit produced errors up to .28% depending on the T^* . The new method seems complex, but it is only entered into a spreadsheet one time, and then it is calculated automatically without further thought.

Appendix L Flat Plate Computational Fluid Dynamics Codes

This Appendix lists and explains the computational fluid dynamic codes which were written to solve for laminar flow over a flat plate with different thermal boundary conditions. The equations which are solved are the boundary layer equations. The continuity equation is:

$$\frac{\partial u}{\partial x} + \frac{\partial v}{\partial y} = 0$$

The x-momentum equation is:

$$u \frac{\partial u}{\partial x} + v \frac{\partial u}{\partial y} = - \frac{1}{\rho} \frac{\partial P}{\partial x} + v \frac{\partial^2 u}{\partial y^2}$$

Where the pressure gradient term equals zero for a flat plate. The y-momentum equation shows us there isn't a pressure difference across the boundary layer in the y direction.

$$\frac{\partial P}{\partial y} = 0$$

And the energy equation is:

$$u \frac{\partial T}{\partial x} + v \frac{\partial T}{\partial y} = \alpha \frac{\partial^2 T}{\partial y^2}$$

These equations must be solved numerically to determine the velocity and temperature boundary layers. The discretized version of the x-momentum equation is:

$$u_j^n \frac{(u_j^{n+1} - u_j^n)}{\Delta x} + v_j^n \frac{u_{j+1}^n - u_{j-1}^n}{2\Delta y} = \nu \frac{(u_{j+1}^n - 2u_j^n + u_{j-1}^n)}{(\Delta y)^2}$$

The unknown (u_j^{n+1}) is solved for. The continuity equation is used to determine the v-velocity component (v_j^{n+1}).

$$\frac{v_j^{n+1} - v_{j-1}^{n+1}}{\Delta y} + \frac{u_j^{n+1} + u_{j-1}^{n+1} - u_j^n - u_{j-1}^n}{2\Delta x} = 0$$

The energy equation looks very similar to the x-momentum equation. It is discretized in a similar manner to determine the temperature (T_j^{n+1}).

$$u_j^n \frac{(T_j^{n+1} - T_j^n)}{\Delta x} + v_j^n \frac{T_{j+1}^n - T_{j-1}^n}{2\Delta y} = \alpha \frac{(T_{j+1}^n - 2T_j^n + T_{j-1}^n)}{(\Delta y)^2}$$

The three unknowns are solved for at each node moving up a column in the y direction. Once the column is completed, the code decides the step size in the x direction from stability. The stability requirement is:

$$\frac{2\alpha\Delta x}{u_j^n(\Delta y)^2} \leq 1$$

This requirement is for the energy equation and is more severe than the stability requirements from continuity or momentum. The code marches down the plate until the end of the plate is reached. Once the entire velocity and temperature field is known, shear stress and heat transfer can be calculated. A listing of the uniform wall temperature code is given in the following pages.

C

ROBERT J. BUTLER

C THIS PROGRAM SOLVES THE LAMINAR BOUNDARY LAYER EQUATIONS
 C OVER A FLAT PLATE USING AN EXPLICIT METHOD DESCRIBED IN
 C ANDERSON. THE GRID HAS 101 NODES IN THE Y DIRECTION EXTENDING
 C .003 m. DELTA X IS DETERMINED FROM STABILITY. THE Free-stream
 C VELOCITY AND TEMPERATURE ARE SET. THE PLATE IS HEATED TO A
 C UNIFORM TEMPERATURE.

```
DIMENSION U(101),UN(101),V(101),VN(101),T(101),TN(101)
INTEGER J
REAL X,U,UN,V,VN,T,TN,DELTAX,NU,DELTAY,UINF,TINF,ALPHA
P      ,CF,NUX,TWALL
OPEN (UNIT=6,FILE='TEMP.DAT',STATUS='UNKNOWN')
```

```
UINF=6.5
TINF=23.0
TWALL=36.0
NU=15.89E-6
ALPHA=22.5E-6
DELTAY=.00003
DELTAX=.00001
```

C INITIALIZE

```
UN(1)=0
U(1)=0
V(1)=0
VN(1)=0
T(1)=TWALL
TN(1)=TWALL
UN(101)=UINF
TN(101)=TINF
DO 10 J=2,101
    U(J)=UINF
    V(J)=0
    T(J)=TINF
```

10 CONTINUE

C MARCH DOWN THE PLATE

X=0

SEND=.00254

DO 20 WHILE (X .LE. .1016)

X=X+DELTAX

DO 40 J=2,100

UN(J)=U(J)+DELTAX*(NU*(U(J+1)-2*U(J)+U(J-1))/DELTAY**2

P -V(J)*(U(J+1)-U(J-1))/(2*DELTAY))/U(J)

VN(J)=VN(J-1)-DELTAY*(UN(J)+UN(J-1)-U(J)-U(J-1))/(2*DELTAX)

TN(J)=T(J)+DELTAX*(ALPHA*(T(J+1)-2*T(J)+T(J-1))/DELTAY**2

P -V(J)*(T(J+1)-T(J-1))/(2*DELTAY))/U(J)

40 CONTINUE

VN(101)=VN(100)

C UPDATE VALUES

DO 50 J=1,101

U(J)=UN(J)

V(J)=VN(J)

T(J)=TN(J)

50 CONTINUE

C CALCULATE OUTPUT VALUES

IF (X .GE. SEND) THEN

SEND=SEND+.00254

CF=2*NU*U(2)/(UINF**2*DELTAY)

NUX=(TWALL-T(2))*X/((TWALL-TINF)*DELTAY)

WRITE(6,*) X,CF,NUX

ENDIF

C DETERMINE NEXT DELTAX FROM STABILITY

DELTAX=DELTAY**2*U(2)/(2*ALPHA)

20 CONTINUE

CLOSE (UNIT=6,FILE='TEMP.DAT')

END

The next code is for a uniform heat flux wall. For this code, the thermal boundary condition at the wall is:

$$q'' = k_f \frac{T_{j=1} - T_{j=2}}{\Delta y} = \text{Constant}$$

Where $T_{j=1}$ is the wall temperature and is an unknown. It is clear this equation contains two unknown temperatures. The solution method is changed to solve for the temperature profile. The velocities are solved for, like before, by marching up a column. To solve for the temperatures, the energy equation is solved while marching back down the column. The local wall temperature is determined by solving thermal boundary condition equation last. The constant heat flux code is listed in the following pages.

C ROBERT J. BUTLER

C THIS PROGRAM SOLVES THE LAMINAR BOUNDARY LAYER EQUATIONS
 C OVER A FLAT PLATE USING AN EXPLICIT METHOD DESCRIBED IN
 C ANDERSON. THE GRID HAS 101 NODES IN THE Y DIRECTION EXTENDING
 C .003 m. DELTA X IS DETERMINED FROM STABILITY. THE Free-stream
 C VELOCITY AND TEMPERATURE ARE SET. THE PLATE IS HEATED BY A
 C UNIFORM HEAT FLUX.

```

DIMENSION U(101),UN(101),V(101),VN(101),T(101),TN(101)
INTEGER J
REAL X,U,UN,V,VN,T,TN,DELTAX,NU,DELTAY,UINF,TINF,ALPHA
P      ,CF,NUX,FLUX
OPEN (UNIT=6,FILE='FLUX.DAT',STATUS='UNKNOWN')

UINF=6.5
TINF=23.0
FLUX=500
NU=15.89E-6
ALPHA=22.5E-6
DELTAY=.00003
DELTAX=.00001

C INITIALIZE
UN(1)=0
U(1)=0
V(1)=0
VN(1)=0
T(1)=FLUX*DELTAY/.0263+TINF
UN(101)=UINF
TN(101)=TINF
DO 10 J=2,101
  U(J)=UINF
  V(J)=0
  T(J)=TINF
10    CONTINUE

```

```

C MARCH DOWN THE PLATE
X=0
SEND=.00254
DO 20 WHILE (X .LE. .1016)
    X=X+DELTAX

    DO 40 J=2,100
        UN(J)=U(J)+DELTAX*(NU*(U(J+1)-2*U(J)+U(J-1))/DELTAY**2
P        -V(J)*(U(J+1)-U(J-1))/(2*DELTAY))/U(J)
        VN(J)=VN(J-1)-DELTAY*(UN(J)+UN(J-1)-U(J)-U(J-1))/(2*DELTAX)
40      CONTINUE

        DO 45 J=100,2,-1
            TN(J)=T(J)+DELTAX*(ALPHA*(T(J+1)-2*T(J)+T(J-1))/DELTAY**2
P            -V(J)*(T(J+1)-T(J-1))/(2*DELTAY))/U(J)
45      CONTINUE
        TN(1)=TN(2)+FLUX*DELTAY/.0263

        VN(101)=VN(100)
C UPDATE VALUES
        DO 50 J=1,101
            U(J)=UN(J)
            V(J)=VN(J)
            T(J)=TN(J)
50      CONTINUE

C CALCULATE OUTPUT VALUES
        IF (X .GE. SEND) THEN
            SEND=SEND+.00254
            CF=2*NU*U(2)/(UINF**2*DELTAY)
            NUX=(T(1)-T(2))*X/((T(1)-TINF)*DELTAY)
            WRITE(6,*) X,T(1),CF,NUX
        ENDIF

C DETERMINE NEXT DELTAX FROM STABILITY
        DELTAX=DELTAY**2*U(2)/(2*ALPHA)

20      CONTINUE

        CLOSE (UNIT=6,FILE='FLUX.DAT')
        END

```

The last code uses unconventional thermal boundary conditions. A transient test method produces a boundary condition which is neither a uniform wall temperature nor a constant heat flux. Changes to the uniform wall temperature code are required in order to simulate the unsteady boundary conditions imposed by transient methods. The uniform wall temperature code was modified to allow for the wall temperature to be a known variable. The code first runs with the wall temperature equal to the starting temperature of the model used in the transient method. From this, the local heat transfer coefficients are determined. The code then determines the change to each local wall temperature for a small time step. The wall temperature update could be performed several different ways. The three different methods considered were: grid the flat plate and solve two-dimensional unsteady conduction, grid each location into the plate and solve one-dimensional unsteady conduction, or use a time averaged local heat transfer coefficient and the semi-infinite one-dimensional conduction equation. Although the first two options would be more accurate, the later was chosen because the first two options create another finite-difference solution for each time step which required too much memory and time for the current machine. Since we know that the local heat transfer coefficients are not constant, this raises a question about the accuracy of using the time averaged heat transfer coefficient to update the wall temperature. A separate test code was written (included at the end of the Appendix) which compares the unsteady wall temperature response for a time varying heat transfer coefficient. The test code determines the wall temperature using a time-averaged heat transfer coefficient and a finite-differenced solution. If the time-averaged approach is reasonable for the same

varying heat transfer coefficient, the two solutions will produce the same surface wall temperature over time. The results from the test code are shown in Figure L.1. This shows that the two solutions diverge slightly over time. The critical measurement is the amount of time it takes either solution to reach any given temperature. The error produced in the local heat transfer coefficient would be proportional to the square-root of the time error. Therefore, the time-averaged approach produces a 1% error at the shortest times and greater than 4% at the longest times. This error is not small, but it was considered within the bounds of this analysis. It should be noticed that the time-averaged approach over predicts the amount of time it takes the wall to cool and this would make the heat transfer coefficients slightly low, therefore the T^* effect would be more pronounced with a more accurate wall temperature update. Using the time-averaged approach the code marches in time and runs new wall temperatures for each time step. A listing of the transient thermal boundary layer code and the test code for the wall temperature update is listed in the following pages.

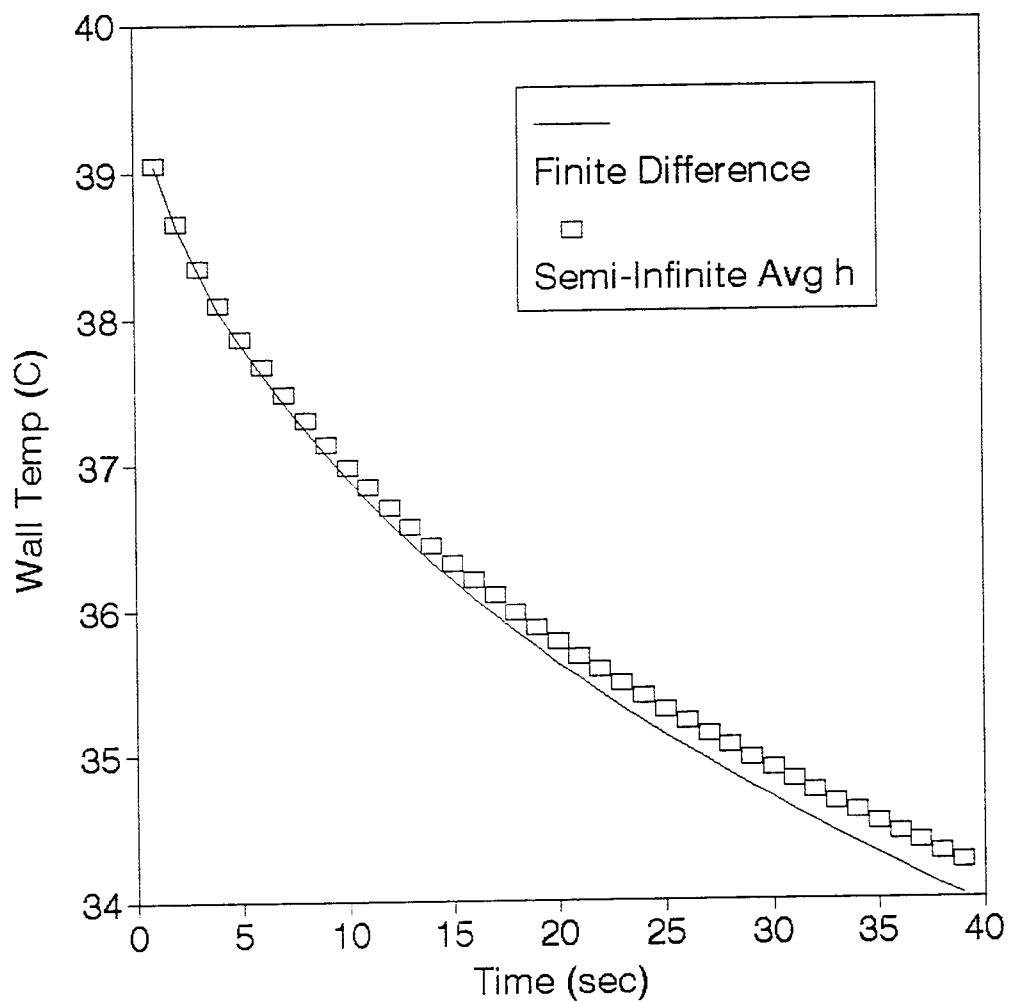


Figure L.1 Comparison of two methods for updating the wall temperature

C

ROBERT J. BUTLER

C THIS PROGRAM SOLVES THE LAMINAR BOUNDARY LAYER EQUATIONS
 C OVER A FLAT PLATE USING AN EXPLICIT METHOD DESCRIBED IN
 C ANDERSON. THE GRID HAS 101 NODES IN THE Y DIRECTION EXTENDING
 C .003 m. DELTA X IS DETERMINED FROM STABILITY. THE Free-stream
 C VELOCITY AND TEMPERATURE ARE SET. THE PLATE IS HEATED TO A
 C UNIFORM TEMPERATURE AND ALLOWED TO COOL LOCALLY LIKE A 1-D
 C SOLID OVER TIME. THE PROGRAM ACCOUNTS FOR THE LOCAL WALL
 C TEMPERATURE CHANGES.

```

DIMENSION U(101),UN(101),V(101),VN(101),T(101),TN(101)
P      ,TWALL(81),DELTA(81),H(81),HA(81),Z(81,4)
INTEGER J,N,I,Z
REAL X,U,UN,V,VN,T,TN,DELTAX,NU,DELTAY,UINF,TINF,ALPHA
P      ,NUX,TWALL,H,DELTAT,TIME,GAMMA,P,HA,TW
OPEN (UNIT=6,FILE='MIXED.DAT',STATUS='UNKNOWN')

UINF=6.5
TINF=25.0
NU=15.89E-6
ALPHA=22.5E-6
DELTAY=.00003
DELTAT=.125
TW=40.0
DO 5 I=1,81
    TWALL(I)=TW
    HA(I)=0
    Z(I,1)=0
    Z(I,2)=0
    Z(I,3)=0
    Z(I,4)=0
5     CONTINUE

C MARCH IN TIME
TIME=0
DO 15 N=1,1761
PRINT*,N
DELTAX=.00001

```

```

C INITIALIZE
UN(1)=0
U(1)=0
V(1)=0
VN(1)=0
UN(101)=UINF
TN(101)=TINF
DO 10 J=2,101
    U(J)=UINF
    V(J)=0
    T(J)=TINF
10    CONTINUE

C MARCH DOWN THE PLATE
X=0
I=1
SEND=.00127
T(1)=TWALL(2)
DO 20 WHILE (X .LE. .1016)
    X=X+DELTA(X

        DO 40 J=2,100
            UN(J)=U(J)+DELTA(X*(NU*(U(J+1)-2*U(J)+U(J-1))/DELTA(Y)**2
P            -V(J)*(U(J+1)-U(J-1))/(2*DELTA(Y))/U(J)
            VN(J)=VN(J-1)-DELTA(Y*(UN(J)+UN(J-1)-U(J)-U(J-1))/(2*DELTA(X)
            TN(J)=T(J)+DELTA(X*(ALPHA*(T(J+1)-2*T(J)+T(J-1))/DELTA(Y)**2
P            -V(J)*(T(J+1)-T(J-1))/(2*DELTA(Y))/U(J)
40    CONTINUE

        VN(101)=VN(100)

C UPDATE VALUES
DO 50 J=2,101
    U(J)=UN(J)
    V(J)=VN(J)
    T(J)=TN(J)
50    CONTINUE

C UPDATE WALL TEMP MOVING DOWN THE PLATE
IF (X .GE. SEND) THEN
    I=I+1
    SEND=SEND+.00127
    T(1)=TWALL(I)
    DELTA(I)=TWALL(I)-T(2)
ENDIF

```

```

C DETERMINE NEXT DELTAX FROM STABILITY
DELTAX=DELTAY**2*U(2)/(2*ALPHA)

20    CONTINUE

C      OUTPUT VALUES AND UPDATE WALL CONDITIONS
DO 60 I=2,81
      H(I)=.0263*DELTAX/((TWALL(I)-TINF)*DELTAY)
      NUX=H(I)*(I-1)*.00127/.0263
C      AVERAGE HEAT TRANSFER COEFFICIENT
      HA(I)=(HA(I)*(N-1)+H(I))/N
      GAMMA=HA(I)*(DELTAT*N)**.5/575
C      SERIES EXPRESSION FOR THE ERFC TERM
      P=1.0/(1.0+.3275911*GAMMA)
      TWALL(I)=TINF+(TW-TINF)
P      *(.254829592*P-.284496736*P**2+1.421413741*P**3
P      -1.453152027*P**4+1.061405429*P**5)
      IF (TWALL(I) .LE. 38.5 .AND. Z(I,1) .EQ. 0) THEN
          WRITE(6,*) ".9", (I-1)*.00127, H(I), HA(I), TIME+DELTAT
          Z(I,1)=1
      ENDIF
      IF (TWALL(I) .LE. 37.0 .AND. Z(I,2) .EQ. 0) THEN
          WRITE(6,*) ".8", (I-1)*.00127, H(I), HA(I), TIME+DELTAT
          Z(I,2)=1
      ENDIF
      IF (TWALL(I) .LE. 35.5 .AND. Z(I,3) .EQ. 0) THEN
          WRITE(6,*) ".7", (I-1)*.00127, H(I), HA(I), TIME+DELTAT
          Z(I,3)=1
      ENDIF
      IF (TWALL(I) .LE. 34.0 .AND. Z(I,4) .EQ. 0) THEN
          WRITE(6,*) ".6", (I-1)*.00127, H(I), HA(I), TIME+DELTAT
          Z(I,4)=1
      ENDIF
60    CONTINUE
      TIME=TIME+DELTAT

15    CONTINUE

      CLOSE (UNIT=6,FILE='MIXED.DAT')
END

```

C ROBERT J. BUTLER
C THIS PROGRAM SOLVES THE UNSTEADY HEAT CONDUCTION FOR A
C SLAB (1/4" THICK) WITH CONVECTIVE BOUNDARY CONDITIONS
C WHICH VARY OVER TIME H=32.02+3.07t**.53, ADIABATIC ON OTHER
C WALL. THE SLAB HAS THERMAL PROPERTIES OF PLEXIGLAS AND
C STARTS AT 40 C AND THE PROGRAM RUNS UNTIL THE SURFACE
C REACHES 34 C (T*=.60), WHILE THE Free-stream IS 25 C. THE
C PROGRAM USES A BACKWARD EULER IMPLICIT METHOD.
C THE ACTUAL 1-D SURFACE RESPONSE IS COMPARED TO AN
C AVERAGE H CALC.

```
DIMENSION A(253),B(253),C(253),D(253),T(253),TOLD(253)
INTEGER I,IMAX
REAL A,B,C,D,T,TOLD,TIME,RHO,K,CP,DELTAX,DELTAT,H,HI,
P HA,TWALL,OUTPUT,P,GAMMA
OPEN (UNIT=6,FILE='AVGH.DAT',STATUS='UNKNOWN')
HI=0
IMAX=253
RHO=1190
CP=1462.3
K=.19
HA=32.02
OUTPUT=1.0
DELTAX=.00635/250.0
DELTAT=DELTAX**2*RHO*CP/(2*K)
TIME=0
```

C INITIALIZE THE I.C. AND B.C.'S

```
DO 10 I=1,253
    T(I)=40
10    CONTINUE
    T(1)=25
    A(1)=0
    B(1)=1
    C(1)=0
    D(1)=25
    T(253)=25
    A(253)=0
    B(253)=1
    C(253)=0
    D(253)=25
```

C ITERATE UNTIL THE SURFACE (T(2)) IS LESS THAN 34.0
DO WHILE (T(2) .GT. 34.0)

```

TIME=TIME+DELTAT
H=32.02+3.04*TIME**.53
HA=(HA*TIME+H*DELTAT)/(TIME+DELTAT)
DO 51 I=1,253
    TOLD(I)=T(I)
51    CONTINUE
C    CALCULATE MATRIX
    DO 60 I=2,252
        IF (I .EQ. 2) THEN
            A(I)=0
            B(I)=+K/DELTAX+CP*RHO*DELTAX/(2*DELTAT)+H
            C(I)=-K/DELTAX
            D(I)=CP*RHO*DELTAX*TOLD(I)/(2*DELTAT)+H*TOLD(I-1)
        ELSE IF (I .EQ. 252) THEN
            A(I)=-K/DELTAX
            B(I)=+K/DELTAX+CP*RHO*DELTAX/(2*DELTAT)+HI
            C(I)=0
            D(I)=CP*RHO*DELTAX*TOLD(I)/(2*DELTAT)+HI*TOLD(I+1)
        ELSE
            A(I)=-K/DELTAX
            B(I)=+2.0*K/DELTAX+CP*RHO*DELTAX/(DELTAT)
            C(I)=-K/DELTAX
            D(I)=CP*RHO*DELTAX*TOLD(I)/(DELTAT)
        ENDIF
60    CONTINUE
        CALL TRIDIA (IMAX,A,B,C,D)
        DO 35 I=1,253
            T(I)=D(I)
35    CONTINUE

        IF (TIME .GE. OUTPUT) THEN
            OUTPUT=OUTPUT+1.0
            GAMMA=HA*(TIME)**.5/575
C            SERIES EXPRESSION FOR THE ERFC TERM
            P=1.0/(1.0+.3275911*GAMMA)
            TWALL=25+(40-25)
P            *(.254829592*P-.284496736*P**2+1.421413741*P**3
P            -1.453152027*P**4+1.061405429*P**5)
            WRITE(6,*) TIME,T(2),TWALL
            ENDIF
        END DO

        CLOSE (UNIT=6,FILE='AVGH.DAT')
    END

```

```
SUBROUTINE TRIDIA(IX,P,Q,R,S)
DIMENSION P(IX),Q(IX),R(IX),S(IX)
P(1)=0
RM=0
SM=0
R(IX)=0
C   DIRECT SWEEP
    DO 1 I=1,IX
        QI=Q(I)-P(I)*RM
        QINV=1.0/QI
        RM=R(I)*QINV
        SM=(S(I)-P(I)*SM)*QINV
        R(I)=RM
        S(I)=SM
1   CONTINUE
C   INVERSE SWEEP
    DO 2 IC=2,IX
        I=IX+1-IC
        S(I)=S(I)-R(I)*S(I+1)
2   CONTINUE
    RETURN
    END
```

Appendix M Turbine Blade Geometry

The turbine blade shape was chosen to simulate the mean geometry used in rotating tests performed by Blair et al. (1989a, 1989b). The turbine blade coordinates are listed in Table M.1. The blade shape is 7.5% larger than the mean geometry used by Blair et al. (1989a, 1989b). The turbine blade shape is that of a heavily loaded machine with a design flow coefficient of .78, stage loading coefficient of 2.8, and 34% static pressure reaction (Blair et al. 1989a, 1989b). The turbine blade has an inlet mean camber line angle of 42° and an exit mean camber line angle of 26°. The air inlet angle is 44.7°, therefore the blade is tested at -2.7° of incidence. The axial chord is designed to be 6.82 inches. Because of the hot-wire cutting process through the styrofoam, the actual axial chord is slightly shorter (ranging from 6.55 to 6.65 inches). An axial chord of 6.82 inches was used in the data reduction because this is the length the blades should be based on their curvature. The axial chord of the Air Force tunnel is 6.53 inches. The author believes the Air Force blades are the correct length but they are mounted with a trailing edge camber angle of 23.5°, therefore decreasing the axial chord. The UC Davis blade pitch is 6.25 inches. The leading and trailing edge radii are .75 and .204 inches respectively.

Table M.1 Turbine Blade Geometry

x (inch)	y lower	y upper
0.000	4.415	4.415
0.068	4.200	4.641
0.135	4.125	4.759
0.204	4.082	4.877
0.272	4.050	4.985
0.341	4.039	5.082
0.409	4.039	5.168
0.477	4.050	5.243
0.545	4.082	5.329
0.614	4.125	5.393
0.682	4.157	5.458
0.852	4.254	5.608
1.022	4.318	5.727
1.192	4.383	5.823
1.363	4.426	5.909
1.534	4.458	5.968
1.704	4.480	6.017
1.875	4.490	6.049
2.045	4.490	6.060
2.216	4.480	6.067
2.387	4.458	6.057
2.556	4.426	6.034
2.726	4.372	5.995
2.897	4.318	5.952
3.067	4.243	5.888
3.238	4.157	5.813
3.409	4.050	5.727
3.579	3.931	5.619
3.750	3.802	5.501
3.919	3.652	5.372
4.090	3.491	5.221
4.260	3.319	5.049
4.431	3.136	4.867
4.601	2.932	4.652
4.772	2.717	4.421
4.942	2.491	4.157
5.113	2.254	3.878
5.283	2.007	3.566
5.453	1.755	3.243

5.623	1.491	2.899
5.794	1.216	2.545
5.964	0.932	2.179
6.135	0.640	1.800
6.203	0.520	1.648
6.272	0.399	1.495
6.339	0.277	1.342
6.407	0.154	1.187
6.471	0.053	1.032
6.544	0.012	0.876
6.611	0.000	0.719
6.680	0.012	0.562
6.748	0.053	0.404
6.817	0.204	0.204

Appendix N Cylinder in Cross-flow Data

P=	30 in Hg	d8	rho= 1.1971851
T=	23.71 C		mu= 1.83E-05
To=	39.26 C		K= 0.0260565
delta h=	0.119 in oil		V= 6.8019374
D=	0.076556 m		Re= 34058.783
Tlc=	35.85 C		T*= 0.7807074
pCpK^.5=	575		gamma= 0.2362104
emmis=	0.85		

to=	2.67	delta t	h	Nu	Nu/Re^.5
0	6.9	4.23	60.592862	178.02621	0.9646492
10	6.8	4.13	61.387577	180.36114	0.9773012
20	6.7	4.03	62.211691	182.78245	0.9904212
30	6.8	4.13	61.387577	180.36114	0.9773012
40	7.16	4.49	58.652325	172.32478	0.9337555
50	7.63	4.96	55.539862	163.18013	0.8842045
60	8.26	5.59	52.000595	152.78151	0.8278587
70					
80					
80					
90					
100					
110					
120					
130					
140					
150					
160					
170					
180					

P=	30 in Hg	e5	rho=	1.199854
T=	23.05 C		mu=	1.827E-05
To=	39.17 C		K=	0.0260077
delta h=	0.118 in oil		V=	6.7657601
D=	0.076556 m		Re=	34011.536
Tlc=	35.85 C		T*=	0.7940447
pCpK ^{.5} =	575		gamma=	0.2188914
emmis=	0.85			
to=	3.58	delta t	h	Nu Nu/Re ^{.5}
0				
10				
20				
30				
40				
50				
60	8.64	5.06	50.526999	148.73076 0.806469
70	10.41	6.83	42.734235	125.79206 0.6820875
80	19	15.42	26.626207	78.376631 0.4249849
84	35.23	31.65	16.946514	49.883585 0.2704858
87	38.47	34.89	15.882428	46.751353 0.2535018
90	34.03	30.45	17.383087	51.168677 0.277454
100	20.72	17.14	24.975493	73.517605 0.3986376
110	19.65	16.07	25.971297	76.448844 0.4145318
120	17.35	13.77	28.492213	83.869387 0.4547685
130				
140				
150				
160				
170				
180				

P=	30 in Hg	e19	rho=	1.2049416
T=	21.8 C		mu=	1.821E-05
To=	39.18 C		K=	0.0259152
delta h=	0.12 in oil		V=	6.808437
D=	0.076556 m		Re=	34483.659
Tlc=	35.85 C		T*=	0.8084005
pCpK^.5=	575		gamma=	0.2007699
emmis=	0.85			
to=	27.79	delta t	h	Nu Nu/Re^.5
0				
10				
20				
30				
40				
50				
60				
70				
80				
84				
87				
90				
100				
110				
120	41.29	13.5	26.026262 76.884089	0.4140281
130	37.65	9.86	31.371184 92.673502	0.4990556
140	36.48	8.69	33.767992 99.753904	0.5371842
150	33.68	5.89	42.174073 124.58628	0.6709089
160	31.84	4.05	51.970674 153.52638	0.8267541
170	31.28	3.49	56.401795 166.61634	0.8972447
180	30.84	3.05	60.709032 179.34034	0.9657646

P= 30 in Hg e2 rho= 1.2016806
 T= 22.6 C mu= 1.825E-05
 To= 39.26 C K= 0.0259744
 delta h= 0.545 in oil V= 14.529261
 D= 0.076556 m Re= 73235.841
 Tlc= 35.85 C T*= 0.7953181
 pCpK^.5= 575 gamma= 0.2172625
 emmis= 0.85

to=	46.02	delta t	h	Nu	Nu/Re^.5
0	47.84	1.82	87.18489	256.96557	0.9495396
10	47.84	1.82	87.18489	256.96557	0.9495396
20	47.84	1.82	87.18489	256.96557	0.9495396
30	47.87	1.85	86.431	254.74358	0.9413289
40	48.11	2.09	80.996702	238.72673	0.8821434
50	48.24	2.22	78.428423	231.15708	0.8541721
60	48.61	2.59	72.208825	212.82566	0.7864338
70					
80					
80					
90					
100					
110					
120					
130					
140					
150					
160					
170					
180					

P=	30 in Hg	e3	rho=	1.2017619
T=	22.58 C		mu=	1.825E-05
To=	39.09 C		K=	0.0259729
delta h=	0.55 in oil		V=	14.595263
D=	0.076556 m		Re=	73577.35
Tlc=	35.85 C		T*=	0.8037553
pCpK ^{.5} =	575		gamma=	0.2065761
emmis=	0.85			
to=	26.43	delta t	h	Nu Nu/Re ^{.5}
0				
10				
20				
30				
40				
50				
60	28.86	2.43	70.786985 208.64687	0.7692009
70	30.12	3.69	56.423825 166.311	0.6131248
78	43.24	16.81	23.559811 69.443284	0.2560107
79	45.71	19.28	21.640462 63.785944	0.2351543
80	43.24	16.81	23.559811 69.443284	0.2560107
90	35.8	9.37	33.392918 98.426677	0.3628614
100	34.99	8.56	35.18737 103.71588	0.3823607
110	34.86	8.43	35.499211 104.63504	0.3857492
120	32.03	5.6	44.783015 131.99935	0.4866309
130				
140				
150				
160				
170				
180				

P=	30 in Hg	e10	rho=	1.2024942
T=	22.4 C		mu=	1.824E-05
To=	39.18 C		K=	0.0259596
delta h=	0.55 in oil		V=	14.590818
D=	0.076556 m		Re=	73634.383
Tlc=	35.85 C		T*=	0.8015495
pCpK ^{.5} =	575		gamma=	0.2093524
emmis=	0.85			
to=	49.54	delta t	h	Nu Nu/Re ^{.5}
0				
10				
20				
30				
40				
50				
60				
70				
80				
84				
87				
90				
100				
110				
120	55.91	6.37	42.286389 124.70442	0.4595592
130	54.54	5	48.425547 142.80906	0.5262783
140	53.41	3.87	55.782421 164.50481	0.6062312
150	52.8	3.26	61.262035 180.66443	0.6657824
160	51.77	2.23	75.201853 221.77357	0.8172773
170	51.67	2.13	77.072423 227.28996	0.8376063
180	51.51	1.97	80.356539 236.97496	0.8732973

P=	30 in Hg	el	rho= 1.2014774		
T=	22.65 C		mu=1.825E-05		
To=	39.31 C		K= 0.0259781		
delta h=	1.24 in oil		V= 21.917592		
D=	0.076556 m		Re= 110444.18		
Tlc=	35.85 C		T*= 0.7923169		
pCpK^.5=	575		gamma= 0.2211082		
emmis=	0.85				
to=	34.56	delta t	h	Nu	Nu/Re^.5
0	35.79	1.23	109.21674	321.85559	0.9684777
10	35.79	1.23	109.21674	321.85559	0.9684777
20	35.79	1.23	109.21674	321.85559	0.9684777
30	35.86	1.3	106.08769	312.63445	0.9407309
40	35.92	1.36	103.60024	305.30407	0.9186735
50	35.99	1.43	100.89845	297.34207	0.8947155
60	36.22	1.66	93.258588	274.82781	0.8269691
70					
80					
80					
90					
100					
110					
120					
130					
140					
150					
160					
170					
180					

P=	30 in Hg	e4	rho= 1.2019652		
T=	22.53 C		mu=1.825E-05		
To=	39.14 C		K= 0.0259692		
delta h=	1.24 in oil		V= 21.913144		
D=	0.076556 m		Re= 110501.22		
Tlc=	35.85 C		T*= 0.8019266		
pCpK ^{.5} =	575		gamma= 0.2088769		
emmis=	0.85				
to=	56.79	delta t	h	Nu	Nu/Re ^{.5}
0					
10					
20					
30					
40					
50					
60	58.55	1.76	85.120678	250.93163	0.7548695
70	59.92	3.13	62.475637	184.17514	0.5540481
75	65.72	8.93	34.780065	102.52994	0.3084375
77	70.23	13.44	27.349833	80.625979	0.2425445
80	65.86	9.07	34.468672	101.61197	0.305676
90	61.92	5.13	47.616028	140.36974	0.4222697
100	62.92	6.13	43.098357	127.05186	0.382206
110	60.98	4.19	53.26347	157.01812	0.4723525
120	59.75	2.96	64.397878	189.84182	0.571095
130					
140					
150					
160					
170					
180					

P=	30 in Hg	e17	rho=	1.204533	
T=	21.9 C		mu=	1.822E-05	
To=	39.15 C		K=	0.0259226	
delta h=	1.185 in oil		V=	21.39881	
D=	0.076556 m		Re=	108316.47	
Tlc=	35.85 C		T*=	0.8086957	
pCpK^.5=	575		gamma=	0.2004027	
emmis=	0.85				
to=	12.53	delta t	h	Nu Nu/Re^.5	
0					
10					
20					
30					
40					
50					
60					
70					
80					
84					
87					
90					
100					
110					
120	15.89	3.36	57.468921	169.72027	0.5156874
130	15.55	3.02	60.913263	179.89229	0.5465946
140	15.22	2.69	64.862874	191.55649	0.5820357
150	14.75	2.22	71.943312	212.46681	0.6455708
160	14.29	1.76	81.464011	240.58385	0.7310031
170	14.02	1.49	89.006327	262.85822	0.7986828
180	13.92	1.39	92.343089	272.71252	0.8286246

Appendix O Flat Plate Data

P=	29.65 in Hg	f9	rho=	1.1984863
T=	19.58 C		mu=	1.812E-05
To=	37.75 C		K=	0.0257768
delta h=	0.115 in oil		V=	6.6830111
L=	0.003175 m		Re=	1403.1568
Tlc=	35.85 C		T*=	0.895432
pCpK^.5=	575		gamma=	0.1010809
emmis=	0.85			
to=	46.95	delta t	h	NuxRex
0.125	47.51	0.56	72.352666	8.9118717 1403.1568 0.267158
0.375	47.98	1.03	51.953361	19.197704 4209.4704 0.3322676
0.625	48.44	1.49	42.299533	26.050734 7015.784 0.3492482
0.875	48.88	1.93	36.521316	31.488999 9822.0976 0.3567871
1.125	49.31	2.36	32.518419	36.048428 12628.411 0.3602171
1.375	49.81	2.86	29.052509	39.363229 15434.725 0.3557899
1.625	50.11	3.16	27.380444	43.842794 18241.038 0.3645237
1.875	50.45	3.5	25.751794	47.578763 21047.352 0.3682704
2.125	50.81	3.86	24.26761	50.814812 23853.666 0.369458
2.375	51.25	4.3	22.713222	53.15532 26659.979 0.3655689
2.625	51.68	4.73	21.40884	55.376668 29466.293 0.3622567
2.875	52.08	5.13	20.345815	57.639117 32272.607 0.3602904
3.125	52.48	5.53	19.400322	59.73974 35078.92 0.3581728
3.375	52.92	5.97	18.472092	61.431942 37885.234 0.3544146
3.625	53.18	6.23	17.970433	64.190526 40691.547 0.3573314

P=	29.76 in Hg	f8	rho= 1.1997789
T=	20.35 C		mu=1.816E-05
To=	39.87 C		K= 0.0258338
delta h=	0.115 in oil		V= 6.6794102
L=	0.003175 m		Re= 1401.0656
Tlc=	35.85 C		T*= 0.7940574
pCpK^.5=	575		gamma= 0.2188752
emmis=	0.85		

to=	35.78	delta t	h	NuxRex	Nu/RePr
0.125	37.27	1.49	97.710157	12.008677	1401.0656 0.3602619
0.375	39.54	3.76	59.511026	21.941895	4203.1967 0.3800464
0.625	41.61	5.83	46.730262	28.715981	7005.3278 0.385267
0.875	43.34	7.56	40.379558	34.738818	9807.4589 0.3939029
1.125	45.18	9.4	35.655979	39.439401	12609.59 0.3943957
1.375	47.21	11.43	31.832743	43.035038	15411.721 0.3892683
1.625	48.75	12.97	29.552933	47.217108	18213.852 0.3928718
1.875	50.25	14.47	27.692104	51.050811	21015.983 0.3954396
2.125	51.95	16.17	25.904662	54.123053	23818.114 0.3938048
2.375	53.35	17.57	24.63187	57.51835	26620.246 0.3958702
2.625	54.89	19.11	23.396677	60.384977	29422.377 0.3953142
2.875	56.02	20.24	22.581476	63.83158	32224.508 0.3992959
3.125	57.36	21.58	21.699033	66.670823	35026.639 0.4000267
3.375	58.06	22.28	21.270046	70.580971	37828.77 0.4075012
3.625	58.32	22.54	21.115821	75.259515	40630.901 0.4192621

P=	29.74 in Hg	f13	rho= 1.1973418
T=	20.75 C		mu=1.818E-05
To=	39.63 C		K= 0.0258634
delta h=	1.06 in oil		V= 20.299421
L=	0.003175 m		Re= 4244.8662
Tlc=	35.85 C		T*= 0.7997881
pCpK^.5=	575		gamma= 0.2115781
emmis=	0.85		

to=	7	delta t	h	NuxRex	Nu/RePr
0.125	7.56	0.56	157.17482	19.294835	4244.8662 0.3325534
0.375	8.33	1.33	100.09362	36.862585	12734.599 0.3668137
0.625	9.13	2.13	77.961558	47.85294	21224.331 0.3688451
0.875	9.8	2.8	67.307484	57.838831	29714.063 0.3767826
1.125	10.5	3.5	59.631897	65.883892	38203.796 0.3785109
1.375	11.16	4.16	54.250729	73.258223	46693.528 0.3806978
1.625	11.83	4.83	49.959316	79.729299	55183.261 0.3811243
1.875	12.4	5.4	46.956291	86.46556	63672.993 0.3847848
2.125	13.07	6.07	43.982497	91.788214	72162.726 0.3836921
2.375	13.73	6.73	41.498763	96.793651	80652.458 0.3827282
2.625	14.4	7.4	39.325432	101.37968	89142.19 0.3812955
2.875	14.83	7.83	38.08009	107.51868	97631.923 0.3864029
3.125	15.3	8.3	36.831182	113.03522	106121.66 0.3896405
3.375	15.79	8.79	35.637305	118.1209	114611.39 0.3918007
3.625	15.94	8.94	35.291603	125.63988	123101.12 0.4021137

P=	29.65 in Hg	f10	rho= 1.1951407
T=	20.40 C		mu=1.816E-05
To=	42.62 C		K= 0.0258375
delta h=	0.115 in oil		V= 6.6923585
L=	0.003175 m		Re= 1398.1708
Tlc=	35.85 C		T*= 0.6953195
pCpK^.5=	575		gamma= 0.3597627
emmis=	0.85		
to=	40.27	delta t	h NuxRex Nu/RePr
0.125	43.2	2.93	115.38159 14.178482 1398.1708 0.4257964
0.375	49.47	9.2	62.731498 23.12598 4194.5123 0.4009699
0.625	54.84	14.57	48.724977 29.937456 6990.8538 0.4020704
0.875	59.35	19.08	41.88876 36.032035 9787.1953 0.4089894
1.125	63.32	23.05	37.617827 41.60346 12583.537 0.4164669
1.375	67.12	26.85	34.452561 46.570128 15379.878 0.4216803
1.625	69.49	29.22	32.799317 52.396393 18176.22 0.4364173
1.875	72.33	32.06	31.065023 57.260637 20972.561 0.4439998
2.125	75.03	34.76	29.617429 61.87134 23768.903 0.4506479
2.375	77.25	36.98	28.547956 66.653331 26565.244 0.4592163
2.625	79.8	39.53	27.432471 70.790905 29361.586 0.4639168
2.875	82.8	42.53	26.250829 74.193199 32157.928 0.4645928
3.125	84.94	44.67	25.481696 78.281939 34954.269 0.4701797
3.375	84.27	44	25.716456 85.323393 37750.611 0.4931267
3.625	84.61	44.34	25.596659 91.216734 40546.952 0.5086837

P=	29.65 in Hg	f11	rho= 1.192502
T=	21.05 C		mu=1.819E-05
To=	46.10 C		K= 0.0258856
delta h=	0.115 in oil		V= 6.6997587
L=	0.003175 m		Re= 1394.2424
Tlc=	35.85 C		T*= 0.5908184
pCpK^.5=	575		gamma= 0.5502273
emmis=	0.85		

to=	5.93	delta t	h	NuxRex	Nu/RePr
0.125	10.49	4.56	142.57567	17.487629	1394.2424 0.5259133
0.375	23.14	17.21	70.680823	26.008083	4182.7271 0.4515761
0.625	34.38	28.45	53.732416	32.952766	6971.2118 0.4431902
0.875	41.89	35.96	47.176263	40.504854	9759.6966 0.4604063
1.125	46.9	40.97	43.845278	48.400609	12548.181 0.4851911
1.375	51.27	45.34	41.402908	55.861041	15336.666 0.5065192
1.625	54	48.07	40.049186	63.859062	18125.151 0.5326404
1.875	57.81	51.88	38.341647	70.541959	20913.636 0.5477534
2.125	61.48	55.55	36.865874	76.870366	23702.12 0.5606834
2.375	64.61	58.68	35.718241	83.239442	26490.605 0.5742957
2.625	67.88	61.95	34.613427	89.155755	29279.09 0.5850904
2.875	74.19	68.26	32.710483	92.278448	32067.574 0.5786548
3.125	74.89	68.96	32.515631	99.705173	34856.059 0.5996957
3.375	72.52	66.59	33.18769	109.90723	37644.544 0.6361033
3.625	72.12	66.19	33.304663	118.46459	40433.029 0.6615654

P= 29.8 in Hg g3 rho= 1.2028249
 T= 20.35 C mu= 1.814E-05
 T lc= 35.85 C k air= 0.0258079
 delta h= 0.113 in oil V= 6.6126848
 L= 6.375 in
 W= 3.859 in
 k sub= 0.13 W/mK
 emmis= 0.85

x	T inf	Current	Volt	h	NuxRex
0.125	20.35	2.989	11.98	124.0738	15.264098 1391.8737
0.375	20.3	2.406	9.503	71.889706	26.532552 4175.621
0.625	20.3	2.161	8.488	53.930914	33.174077 6959.3683
0.875	20.3	2.028	7.946	45.148908	38.880904 9743.1157
1.125	20.3	1.959	7.666	40.891961	45.276361 12526.863
1.375	20.25	1.908	7.455	37.644587	50.943207 15310.61
1.625	20.25	1.852	7.23	34.402816	55.020991 18094.358
1.875	20.25	1.82	7.098	32.608077	60.17381 20878.105
2.125	20.35	1.79	6.979	31.307511	65.476962 23661.852
2.375	20.35	1.749	6.813	29.050759	67.905061 26445.6
2.625	20.45	1.726	6.725	28.178436	72.799306 29229.347
2.875	20.5	1.71	6.658	27.491331	77.78837 32013.094
3.125	20.55	1.699	6.615	27.106012	83.367486 34796.842
3.375	20.6	1.689	6.578	26.785811	88.973285 37580.589
3.625	20.5	1.71	6.658	27.674509	98.734513 40364.336

P= 29.8 in Hg g4 rho= 1.2052901
 T= 19.75 C mu= 1.811E-05
 T lc= 35.85 C k air= 0.0257635
 delta h= 0.985 in oil V= 19.503481
 L= 6.375 in
 W= 3.859 in
 k sub= 0.13 W/mK
 emmis= 0.85

x	T inf	Current	Volt	h	NuxRex
0.125	20.15	3.798	15.343	210.22519	25.907387 4120.1328
0.375	20.15	3.016	11.934	121.25206	44.82799 12360.399
0.625	20.15	2.692	10.6	91.550997	56.412059 20600.664
0.875	20	2.544	9.986	78.184327	67.446064 28840.93
1.125	19.85	2.439	9.553	69.076783	76.614942 37081.196
1.375	19.85	2.36	9.229	63.194946	85.667067 45321.461
1.625	19.75	2.283	8.919	57.200238	91.63894 53561.727
1.875	19.6	2.258	8.812	54.742339	101.1937 61801.993
2.125	19.6	2.211	8.623	51.58304	108.0674 70042.258
2.375	19.6	2.181	8.503	49.625421	116.19747 78282.524
2.625	19.5	2.152	8.385	47.314212	122.44746 86522.79
2.875	19.4	2.138	8.326	46.011667	130.41714 94763.055
3.125	19.3	2.111	8.219	43.933157	135.35406 103003.32
3.375	19.2	2.111	8.219	43.582422	145.01536 111243.59
3.625	19.4	2.121	8.26	45.064044	161.05234 119483.85

Appendix P Turbine Blade Data

	29.88 in Hg	No Grid	$\rho = 1.1793197 \text{ kg/m}^3$
T=	27 C		$\mu = 1.846 \times 10^{-5} \text{ N s/m}^2$
T lc=	40.1 C		k air= 0.0263 W/mK
delta h=	0.094 in oil		V= 6.0909908 m/s
L=	18.375 in		Bx= 6.82 in
W=	8 in		Re= 67407.084
R"=	2.49 Ohms/SQ		
emmis=	0.85		

s	s/Bx	Current	Volt	T inf	h	St
-7.5	-1.099707	2.4	13.74	27.5	21.998477	0.0030412
-7.5	-1.099707	2.55	14.55	26.5	23.290593	0.0032198
-7	-1.026393	2.39	13.68	27.5	21.769223	0.0030095
-7	-1.026393	2.54	14.49	26.5	23.064893	0.0031886
-6.5	-0.953079	2.385	13.65	27.5	21.654955	0.0029937
-6.5	-0.953079	2.538	14.48	26.5	23.01986	0.0031824
-6	-0.879765	2.341	13.36	27.5	20.659715	0.0028561
-6	-0.879765	2.5	14.26	26.45	22.070784	0.0030512
-5.5	-0.806452	2.34	13.36	27.5	20.637312	0.002853
-5.5	-0.806452	2.48	14.13	26.45	21.630758	0.0029904
-5	-0.733138	2.335	13.35	27.5	20.525437	0.0028375
-5	-0.733138	2.46	14.02	26.45	21.194266	0.00293
-4.5	-0.659824	2.31	13.19	27.5	19.969651	0.0027607
-4.5	-0.659824	2.43	13.85	26.45	20.546155	0.0028404
-4	-0.58651	2.29	13.08	27.5	19.529331	0.0026998
-4	-0.58651	2.405	13.71	26.45	20.012137	0.0027666
-3.5	-0.513196	2.27	12.96	27.5	19.092839	0.0026395
-3.5	-0.513196	2.38	13.57	26.4	19.393646	0.0026811
-3	-0.439883	2.252	12.85	27.3	18.329376	0.002534
-3	-0.439883	2.362	13.46	26.3	18.842641	0.0026049
-2.5	-0.366569	2.162	12.32	27.3	16.45776	0.0022752
-2.5	-0.366569	2.274	12.94	26.3	17.059856	0.0023584
-2	-0.293255	1.98	11.27	28.4	14.613102	0.0020202
-2	-0.293255	2.12	12.08	28.4	17.571646	0.0024292
-1.5	-0.219941	1.882	10.69	28.4	12.66234	0.0017505
-1.5	-0.219941	2.02	11.49	28.4	15.437784	0.0021342
-1.25	-0.183284					
-1.125	-0.164956					
-1	-0.146628	2.493	14.23	26.5	22.015984	0.0030436
-0.75	-0.109971	2.9	16.62	26.65	32.160664	0.0044461

-0.5	-0.073314	3.47	20.06	26.75	48.841993	0.0067522
-0.25	-0.036657	4.02	23.46	26.8	67.723754	0.0093625
0	0	4.69	27.7	26.9	94.93685	0.0131246
0.25	0.0366569	4.8	28.42	26.9	99.705955	0.0137839
0.5	0.0733138	4.44	26.1	26.85	84.170624	0.0116362
0.75	0.1099707	3.92	22.83	26.8	64.123602	0.0088648
1	0.1466276	3.52	20.41	26.75	50.420759	0.0069704
1.5	0.2199413	3.358	19.38	26.7	45.198791	0.0062485
2	0.2932551	3.261	18.76	26.7	42.309368	0.0058491
2.5	0.3665689	3.138	18.04	26.7	38.767239	0.0053594
3	0.4398827	3.038	17.43	26.7	35.987817	0.0049752
3.5	0.5131965	2.9	16.62	26.65	32.160664	0.0044461
4	0.5865103	2.84	16.29	26.6	30.483902	0.0042143
4.5	0.659824	2.8	16.04	26.6	29.476141	0.0040749
5	0.7331378	2.717	15.54	26.6	27.430643	0.0037922
5.5	0.8064516	2.67	15.26	26.6	26.299641	0.0036358
6	0.8797654	2.582	14.76	26.55	24.126537	0.0033354
6.25	0.9164223					
6.5	0.9530792	2.442	13.93	26.5	20.899968	0.0028893
7	1.026393	2.313	13.16	26.5	18.180066	0.0025133
7.5	1.0997067	2.25	12.8	26.2	16.428903	0.0022712
7.75	1.1363636	2.236	12.72	26.15	16.080018	0.002223
8	1.1730205	2.25	12.8	26.2	16.428903	0.0022712
8.5	1.2463343	2.28	12.98	26.25	17.098586	0.0023638
9	1.3196481	2.269	12.91	26.2	16.801408	0.0023227
9.5	1.3929619	2.179	12.39	26.1	14.920162	0.0020626
10	1.4662757	2.14	12.17	26.1	14.194604	0.0019623
10.25	1.5029326	2.179	12.39	26.1	14.920162	0.0020626

P= 29.88 in Hg No Grid rho= 1.1793197kg/m^3
 T= 27 C mu= 1.846E-05 N s/m^2
 T lc= 40.1 C k air= 0.0263 W/mK
 delta h= 0.43 in oil V= 13.027415m/s
 L= 18.375 in Bx= 6.82 in
 W= 8 in Recx= 144170.31
 R"= 2.49 Ohms/SQ
 emmis= 0.85

s	s/Bx	Current	Volt	T inf	h	St	
-7.5	-1.099707	3.05	17.47	27.5	38.953222	0.0025178	
-7.5	-1.099707	3.19	18.33	27.5	43.134355	0.0027881	
-7	-1.026393	3.02	17.27	27.5	38.081674	0.0024615	
-7	-1.026393	3.17	17.17	27.5	42.525564	0.0027487	
-6.5	-0.953079	2.98	17.05	27.5	36.933011	0.0023872	
-6.5	-0.953079	3.15	18.06	27.5	41.920601	0.0027096	
-6	-0.879765	2.95	16.88	27.5	36.081565	0.0023322	
-6	-0.879765	3.1	17.75	27.5	40.424947	0.0026129	
-5.5	-0.806452	2.87	16.4	27.5	33.853158	0.0021882	
-5.5	-0.806452	3.05	17.47	27.5	38.953222	0.0025178	
-5	-0.733138	2.84	16.22	27.5	33.0333	0.0021352	
-5	-0.733138	3	17.16	27.5	37.505428	0.0024242	
-4.5	-0.659824	2.81	16.05	27.5	32.222057	0.0020827	
-4.5	-0.659824	2.95	16.88	27.5	36.081565	0.0023322	
-4	-0.58651	2.78	15.86	27.5	31.419429	0.0020309	
-4	-0.58651	2.87	16.4	27.5	33.853158	0.0021882	
-3.5	-0.513196	2.74	15.65	27.5	30.362659	0.0019625	
-3.5	-0.513196	2.84	16.22	27.5	33.0333	0.0021352	
-3	-0.439883	2.69	15.35	27.4	28.79322	0.0018611	
-3	-0.439883	2.81	16.05	27.5	32.222057	0.0020827	
-2.5	-0.366569	2.46	14	27.4	23.168728	0.0014976	
-2.5	-0.366569	2.78	15.86	27.5	31.419429	0.0020309	
-2	-0.293255	2.31	13.12	27.4	19.771241	0.001278	
-2	-0.293255	2.56	14.55	27.4	25.55243	0.0016516	
-1.5	-0.219941	2.16	12.23	27.4	16.587432	0.0010722	
-1.5	-0.219941	2.36	13.41	27.4	20.879994	0.0013496	
-1.25	-0.183284						
-1.125	-0.164956						
	-1	-0.146628	2.797	15.92	27	30.457496	0.0019687
	-0.75	-0.109971	3.37	19.31	27.9	50.557166	0.0032679
	-0.5	-0.073314	3.98	22.97	28	73.363595	0.004742
	-0.25	-0.036657	4.66	27.12	28	102.64482	0.0066346
	0	0	5.33	31.34	28.1	137.18054	0.0088669
	0.25	0.0366569	5.54	32.6	28.2	149.94544	0.009692

0.5	0.0733138	5.11	29.9	28.05	125.09505	0.0080858
0.75	0.1099707	4.53	26.3	28	96.690591	0.0062498
1	0.1466276	3.98	22.97	28	73.363595	0.004742
1.5	0.2199413	3.82	21.99	28	67.143727	0.00434
2	0.2932551	3.72	21.4	27.9	62.823263	0.0040607
2.5	0.3665689	3.59	20.6	27.9	58.125914	0.0037571
3	0.4398827	3.44	19.71	27.8	52.440633	0.0033896
3.5	0.5131965	3.26	18.66	27.8	46.52782	0.0030074
4	0.5865103	3.222	18.38	27.8	45.320175	0.0029294
4.5	0.659824	3.18	18.19	27.7	43.604737	0.0028185
5	0.7331378	3.07	17.53	27.7	40.261224	0.0026024
5.5	0.8064516	3.03	17.3	27.7	39.074581	0.0025257
6	0.8797654	3.03	17.25	26.6	35.465972	0.0022924
6.25	0.9164223					
6.5	0.9530792	2.84	16.14	26.6	30.483902	0.0019704
7	1.026393	2.662	15.13	26.5	25.879017	0.0016727
7.5	1.0997067	2.473	14.03	26.4	21.380311	0.001382
7.75	1.1363636					
8	1.1730205	2.571	14.6	26.4	23.556179	0.0015226
8.5	1.2463343	2.76	15.7	26.55	28.358448	0.001833
9	1.3196481	2.88	16.5	26.55	31.370573	0.0020277
9.5	1.3929619	3.127	17.84	26.6	38.133808	0.0024649
10	1.4662757	3.45	19.74	26.6	47.623422	0.0030782

P= 29.78 in Hg Grid rho= 1.1789096kg/m^3
 T= 26.1 C mu= 1.842E-05 N s/m^2
 T lc= 40.1 C k air= 0.0262334W/mK
 delta h= 0.094 in oil V= 6.0920502m/s
 L= 18.375 in Bx= 6.82 in
 W= 8 in Recx= 67551.318
 R"= 2.49 Ohms/SQ
 emmis= 0.85

s	s/Bx	Current	Volt	T inf	h	St
-7.5	-1.099707	3.17	18.17	25.9	37.149219	0.0051366
-7.5	-1.099707					
-7	-1.026393	3.17	18.17	25.9	37.149219	0.0051366
-7	-1.026393					
-6.5	-0.953079	3.17	18.17	25.9	37.149219	0.0051366
-6.5	-0.953079					
-6	-0.879765	3.12	17.86	25.9	35.813595	0.0049519
-6	-0.879765					
-5.5	-0.806452	3.07	17.55	25.9	34.499205	0.0047702
-5.5	-0.806452					
-5	-0.733138	3.06	17.49	25.9	34.238875	0.0047342
-5	-0.733138					
-4.5	-0.659824	3.06	17.49	25.9	34.238875	0.0047342
-4.5	-0.659824					
-4	-0.58651	3.05	17.44	25.9	33.979395	0.0046983
-4	-0.58651					
-3.5	-0.513196	3.06	17.49	25.9	34.238875	0.0047342
-3.5	-0.513196					
-3	-0.439883	3.06	17.49	25.9	34.238875	0.0047342
-3	-0.439883					
-2.5	-0.366569	3.06	17.49	25.9	34.238875	0.0047342
-2.5	-0.366569					
-2	-0.293255	3.14	17.96	25.9	36.345297	0.0050254
-2	-0.293255					
-1.5	-0.219941	3.12	17.85	25.3	34.153617	0.0047224
-1.5	-0.219941					
-1.25	-0.183284	2.98	17.01	25.2	30.433676	0.0042081
-1.125	-0.164956	2.92	16.67	25.2	29.000931	0.0040099
-1	-0.146628	2.98	17.01	25.2	30.433676	0.0042081
-0.75	-0.109971	3.34	19.16	26.1	42.520634	0.0058793
-0.5	-0.073314	3.76	21.69	26.2	55.801001	0.0077156
-0.25	-0.036657	4.53	26.38	26.2	83.494791	0.0115448
0	0	5.06	29.67	26.3	106.34822	0.0147047
0.25	0.0366569	5.2	30.55	26.35	113.05351	0.0156319
0.5	0.0733138	4.75	27.7	26.3	93.058877	0.0128672

0.75	0.1099707	4.18	24.19	26.2	70.268949	0.0097161
1	0.1466276	3.76	21.69	26.2	55.801001	0.0077156
1.5	0.2199413	3.61	20.75	26.1	50.603632	0.0069969
2	0.2932551	3.53	20.28	26.1	48.143196	0.0066567
2.5	0.3665689	3.38	19.39	26.1	43.678486	0.0060394
3	0.4398827	3.25	18.65	26.1	39.965864	0.0055261
3.5	0.5131965	3.17	18.14	25.5	35.990674	0.0049764
4	0.5865103	3.11	17.8	25.3	33.899766	0.0046873
4.5	0.659824	3.07	17.56	25.3	32.892513	0.004548
5	0.7331378	3.02	17.27	25.3	31.651782	0.0043765
5.5	0.8064516	2.98	17.01	25.2	30.433676	0.0042081
6	0.8797654	2.89	16.46	25.1	28.072787	0.0038816
6.25	0.9164223					
6.5	0.9530792	2.75	15.67	24.95	24.6013	0.0034016
7	1.026393	2.7	15.39	24.95	23.516609	0.0032516
7.5	1.0997067	2.75	15.67	24.95	24.6013	0.0034016
7.75	1.1363636					
8	1.1730205	2.93	16.71	25.1	29.008718	0.004011
8.5	1.2463343	3.02	17.27	25.3	31.651782	0.0043765
9	1.3196481	3.07	17.56	25.3	32.892513	0.004548
9.5	1.3929619	3.12	17.86	25.3	34.153617	0.0047224
10	1.4662757	3.17	18.14	25.5	35.990674	0.0049764

P= 29.78 in Hg Grid rho= 1.1769421kg/m^3
 T= 26.6 C mu= 1.844E-05 N s/m^2
 T lc= 40.1 C k air= 0.0262704W/mK
 delta h= 0.37 in oil V= 12.096594m/s
 L= 18.375 in Bx= 6.82 in
 W= 8 in Recx= 133736.49
 R"= 2.49 Ohms/SQ
 emmis= 0.85

s	s/Bx	Current	Volt	T inf	h	St
-7.5	-1.099707	3.77	21.58	26.4	57.022526	0.0039774
-7.5	-1.099707					
-7	-1.026393	3.77	21.58	26.4	57.022526	0.0039774
-7	-1.026393					
-6.5	-0.953079	3.77	21.58	26.4	57.022526	0.0039774
-6.5	-0.953079					
-6	-0.879765	3.65	20.85	26.4	53.103154	0.003704
-6	-0.879765					
-5.5	-0.806452	3.58	20.48	26.6	51.705834	0.0036065
-5.5	-0.806452					
-5	-0.733138	3.57	20.42	26.6	51.386442	0.0035843
-5	-0.733138					
-4.5	-0.659824	3.56	20.32	26.6	51.067943	0.0035621
-4.5	-0.659824					
-4	-0.58651	3.55	20.27	26.6	50.750338	0.0035399
-4	-0.58651					
-3.5	-0.513196	3.56	20.32	26.6	51.067943	0.0035621
-3.5	-0.513196					
-3	-0.439883	3.57	20.42	26.6	51.386442	0.0035843
-3	-0.439883					
-2.5	-0.366569	3.58	20.48	26.6	51.705834	0.0036065
-2.5	-0.366569					
-2	-0.293255	3.72	21.26	26.4	55.374048	0.0038624
-2	-0.293255					
-1.5	-0.219941	3.77	21.57	26.4	57.022526	0.0039774
-1.5	-0.219941					
-1.25	-0.183284	3.58	20.46	26.6	51.705834	0.0036065
-1.125	-0.164956	3.5	19.99	26.2	47.611695	0.003321
-1	-0.146628	3.55	20.24	26.2	49.141007	0.0034276
-0.75	-0.109971	3.89	20.27	26.6	62.050119	0.0043281
-0.5	-0.073314	4.48	25.79	26.9	86.139201	0.0060083
-0.25	-0.036657	5.21	30.25	27	119.39968	0.0083283
0	0	5.93	34.7	27	156.3228	0.0109037
0.25	0.0366569	6.16	36.17	27	169.12353	0.0117966
0.5	0.0733138	5.58	32.55	27	137.77792	0.0096102

0.75	0.1099707	4.87	28.13	27	103.62284	0.0072278
1	0.1466276	4.39	25.28	27	83.161555	0.0058006
1.5	0.2199413	4.22	24.24	27	76.423528	0.0053306
2	0.2932551	4.1	23.55	26.8	70.669168	0.0049293
2.5	0.3665689	3.96	22.68	26.6	64.504748	0.0044993
3	0.4398827	3.85	22.05	26.6	60.667128	0.0042316
3.5	0.5131965	3.65	20.86	26.4	53.103154	0.003704
4	0.5865103	3.6	20.55	26.4	51.507497	0.0035927
4.5	0.659824	3.55	20.3	26.2	49.141007	0.0034276
5	0.7331378	3.53	20.11	26.2	48.526679	0.0033848
5.5	0.8064516	3.51	20	26.2	47.915822	0.0033422
6	0.8797654	3.37	19.19	26.2	43.737002	0.0030507
6.25	0.9164223	3.34	19.02	26.2		
6.5	0.9530792	3.37	19.19	26.2	43.737002	0.0030507
7	1.026393	3.47	19.76	26.2	46.704519	0.0032577
7.5	1.0997067	3.6	20.55	26.4	51.507497	0.0035927
7.75	1.1363636					
8	1.1730205	3.85	22.05	26.6	60.667128	0.0042316
8.5	1.2463343	3.96	22.68	26.6	64.504748	0.0044993
9	1.3196481	3.99	22.85	26.6	65.570133	0.0045736
9.5	1.3929619	4.03	23.13	26.7	67.541885	0.0047111
10	1.4662757	4.08	23.37	26.7	69.36678	0.0048384

P= 29.8 in Hg 20-grid rho= 1.1793071kg/m^3
 T= 26.2 C mu= 1.842E-05 N s/m^2
 T lc= 40.1 C k air= 0.0262408W/mK
 delta h= 0.094 in oil V= 6.0910235m/s
 L= 18.375 in Bx= 6.82 in
 W= 8 in Recx= 67545.326
 R"= 2.49 Ohms/SQ
 emmis= 0.85

s	s/Bx	Current	Volt	T inf	h	St
-7.5	-1.099707	3.54	20.13	26.5	50.02469	0.0069157
-7.5	-1.099707					
-7	-1.026393					
-7	-1.026393					
-6.5	-0.953079	3.51	19.92	26.5	49.086861	0.0067861
-6.5	-0.953079					
-6	-0.879765	3.47	19.75	26.5	47.848839	0.0066149
-6	-0.879765					
-5.5	-0.806452					
-5.5	-0.806452					
-5	-0.733138					
-5	-0.733138					
-4.5	-0.659824	3.39	19.28	26.5	45.415363	0.0062785
-4.5	-0.659824					
-4	-0.58651					
-4	-0.58651					
-3.5	-0.513196					
-3.5	-0.513196					
-3	-0.439883					
-3	-0.439883					
-2.5	-0.366569	3.39	19.28	26.5	45.415363	0.0062785
-2.5	-0.366569					
-2	-0.293255	3.47	19.75	26.5	47.848839	0.0066149
-2	-0.293255					
-1.5	-0.219941	3.51	19.92	26.5	49.086861	0.0067861
-1.5	-0.219941					
-1.25	-0.183284	3.47	19.75	26.5	47.848839	0.0066149
-1.125	-0.164956					
-1	-0.146628	3.51	19.92	26.5	49.086861	0.0067861
-0.75	-0.109971	3.7	21.05	26.6	55.608225	0.0076876
-0.5	-0.073314	4	22.91	26.7	66.457748	0.0091875
-0.25	-0.036657	4.62	26.5	26.8	91.229026	0.0126121
0	0	5.24	30.32	26.9	119.88796	0.0165741
0.25	0.0366569	5.43	31.55	26.9	129.14978	0.0178545
0.5	0.0733138	4.87	28.06	26.8	101.98641	0.0140992

0.75	0.1099707	4.22	24.15	26.8	75.196109	0.0103956
1	0.1466276	4	22.91	26.7	66.457748	0.0091875
1.5	0.2199413	3.93	22.42	26.7	63.959599	0.0088422
2	0.2932551	3.79	21.63	26.7	59.095611	0.0081697
2.5	0.3665689	3.65	20.81	26.6	53.966594	0.0074607
3	0.4398827	3.59	20.42	26.6	52.026119	0.0071924
3.5	0.5131965	3.4	19.3	26	43.912097	0.0060707
4	0.5865103					
4.5	0.659824					
5	0.7331378					
5.5	0.8064516					
6	0.8797654	3.26	18.5	25.8	39.293899	0.0054322
6.25	0.9164223	3.228	18.3	25.8		
6.5	0.9530792	3.26	18.5	25.8	39.293899	0.0054322
7	1.026393	3.32	18.84	25.8	40.958818	0.0056624
7.5	1.0997067	3.4	19.29	26	43.912097	0.0060707
7.75	1.1363636					
8	1.1730205					
8.5	1.2463343	3.5	19.87	26.1	47.234747	0.00653
9	1.3196481	3.45	19.6	26	45.376948	0.0062732
9.5	1.3929619	3.39	19.24	26	43.621693	0.0060305
10	1.4662757	3.45	19.6	26	45.376948	0.0062732

P= 29.8 in Hg Grid rho= 1.1773396kg/m^3
 T= 26.7 C mu= 1.845E-05 N s/m^2
 T lc= 40.1 C k air= 0.0262778W/mK
 delta h= 0.37 in oil V= 12.094552m/s
 L= 18.375 in Bx= 6.82 in
 W= 8 in Recx= 133724.74
 R"= 2.49 Ohms/SQ
 emmis= 0.85

s	s/Bx	Current	Volt	T inf	h	St
-7.5	-1.099707	4.37	24.8	26.8	81.038421	0.0056516
-7.5	-1.099707					
-7	-1.026393					
-7	-1.026393					
-6.5	-0.953079	4.35	24.69	26.8	80.247657	0.0055964
-6.5	-0.953079					
-6	-0.879765	4.25	24.13	26.8	76.348248	0.0053245
-6	-0.879765					
-5.5	-0.806452					
-5.5	-0.806452					
-5	-0.733138	4.19	23.73	26.8	74.052131	0.0051644
-5	-0.733138					
-4.5	-0.659824	4.16	23.6	26.8	72.916315	0.0050851
-4.5	-0.659824					
-4	-0.58651					
-4	-0.58651					
-3.5	-0.513196					
-3.5	-0.513196					
-3	-0.439883					
-3	-0.439883					
-2.5	-0.366569	4.16	23.6	26.8	72.916315	0.0050851
-2.5	-0.366569					
-2	-0.293255	4.3	24.41	26.8	78.286617	0.0054597
-2	-0.293255					
-1.5	-0.219941	4.35	24.69	26.8	80.247657	0.0055964
-1.5	-0.219941					
-1.25	-0.183284					
-1.125	-0.164956	4.3	24.43	26.9	78.919071	0.0055038
-1	-0.146628	4.35	24.69	26.8	80.247657	0.0055964
-0.75	-0.109971	4.5	25.6	27.2	89.103139	0.006214
-0.5	-0.073314	4.9	28	26.9	104.13744	0.0072625
-0.25	-0.036657	5.77	33.16	27.1	148.88145	0.0103829
0	0	6.38	36.88	27.2	184.72319	0.0128825
0.25	0.0366569	6.53	37.85	27.2	193.77592	0.0135138
0.5	0.0733138	5.81	33.41	27.1	151.03015	0.0105328

0.75	0.1099707	5.16	29.54	27.1	117.95296	0.008226
1	0.1466276	4.89	27.9	26.9	103.69018	0.0072313
1.5	0.2199413	4.9	28	26.9	104.13744	0.0072625
2	0.2932551	4.67	26.65	26.9	94.081618	0.0065612
2.5	0.3665689	4.48	25.5	26.9	86.139201	0.0060073
3	0.4398827	4.39	24.95	26.6	80.543593	0.0056171
3.5	0.5131965	4.19	23.8	26.5	72.304212	0.0050425
4	0.5865103					
4.5	0.659824					
5	0.7331378					
5.5	0.8064516					
6	0.8797654	4.12	23.4	26.5	69.724852	0.0048626
6.25	0.9164223					
6.5	0.9530792	4.19	23.8	26.5	72.304212	0.0050425
7	1.026393	4.35	24.7	26.6	78.981922	0.0055082
7.5	1.0997067	4.45	25.3	26.7	83.570363	0.0058282
7.75	1.1363636					
8	1.1730205	4.51	25.69	26.7	85.989756	0.0059969
8.5	1.2463343					
9	1.3196481					
9.5	1.3929619	4.39	24.95	26.6	80.543593	0.0056171
10	1.4662757	4.45	25.3	26.7	83.570363	0.0058282